THE UNIVERSITY
of ADELAIDE

FACULTY OF SCIENCES
DEPARTMENT OF PHYSICS

Quantum transport in Josephson junctions.

Ross D. Monaghan

Supervisors:
Prof. Giuseppe TETTAMANZI
Prof. Rajib RAHMAN
Prof. Francesco GIAZOTTO

November 2022

0.1 Abstract

Josephson junctions consist of two superconductors separated by some barrier, be it superconducting, ferromagnetic, or semiconducting. The striking feature of Josephson junctions is that for a phase difference between the two superconducting reservoirs, electrical current will flow between them. To study this transport we utilise the techniques of non-equilibrium Green's functions; capable of probing the interplay between coherent quantum effects over macroscopic distances.

We begin by broadly discussing the quantum mechanical techniques required in this work, before deriving the relevant equations to be solved. We then introduce numerical discretisation and explore how in lattice systems spin-orbit coupling can produce intricate fractals in an electron's bandstructure. We then introduce a numerical algorithm which, although creates numerical instabilities, improves the speed of conventional Green's function calculations.

Finally, we study the electrical current, and the bound states which carry this current, in various Josephson junction architectures. We first compare our calculations with previous results in the literature to verify our results and demonstrate the generality of the non-equilibrium Green's functions technique. We then explore numerically the anomalous Josephson effect, where current flows even in the absence of a phase bias between the two junctions. We provide a universal condition to be satisfied for Josephson junctions to exhibit anomalous current before modelling some experimental data concerning this effect.

0.2 Declaration

I certify that this work contains no material which has been accepted for the award of any other degree or diploma in my name, in any university or other tertiary institution and, to the best of my knowledge and belief, contains no material previously published or written by another person, except where due reference has been made in the text. In addition, I certify that no part of this work will, in the future, be used in a submission in my name, for any other degree or diploma in any university or other tertiary institution without the prior approval of the University of Adelaide and where applicable, any partner institution responsible for the joint award of this degree.

I give permission for the digital version of my thesis to be made available on the web, via the University's digital research repository, the Library Search and also through web search engines, unless permission has been granted by the University to restrict access for a period of time.

I acknowledge the support I have received for my research through the provision of an Australian Government Research Training Program Scholarship.

Ross D. Monaghan.

0.3 Acknowledgements

I would like to first acknowledge my main supervisor Dr. Giuseppe Tettamanzi for giving me the opportunity to work on this project, particularly for letting me run with it even when tangents became more than tangential. Additionally, I would like to acknowledge my co-supervisors Dr. Rajib Rahman and Dr. Francesco Giazotto for their support during my candidature, especially for keeping me pointed in the right direction at the very early, and very late, stages. I thank Dr. Glenn Solomon for letting me sit through his lectures, and for the particle physics PhDs for letting me sit through their Friday talks. I would also like to acknowledge Dr. Elia Strambini for his careful reading of my thesis, and in particular his notes on improving the discussion on anomalous phase shifts.

I would like to thank my colleagues Alan, Tom, and Tyler as we muddle through condensed matter [sic: read 'learning French'] together; for continually teaching me, and for a cruel coffee dependence. My friends for suffering my thesis derived aloofness, and for the quickdraw on the corkscrew. Finally, I would like to thank my family for their continual support. For Maisy and her unshakeably soft dog ears, and to Claire for always having time and care.

Contents

Chapter 1

Introduction

Our modern understanding of fundamental physics is derived from quantum field theory, where the notion of individual particles gives way to fluctuating quantum fields. By providing the framework for the Standard Model, these techniques have been wondrously successful in describing many microscopic phenomena. Historically, however, when one turns to macroscopic problems there is generally no need for a quantum theory as the uncountably-many degrees of freedom inherent to the many-body system 'self-average'; allowing the system to be described with solely macroscopic quantities and thermodynamic relations. However, spurred on by various experimental discoveries, perhaps most strikingly with the observation of superconductivity in the early 20^{th} century, it was realised that some macroscopic systems can only understood via their quantum origins, rather than from thermodynamic properties alone. This in-part gave rise to condensed matter theory, where it is the *interactions* between the constituent particles which dominate the emergent behaviour, leading to a flourish of activity in the application of field theory to macroscopic systems.

Initially the problem of extending quantum field theory to macroscopic systems seemed troublesome; even in thermal equilibrium, time-evolution at non-zero temperatures necessitates level-crossing of eigenstates which muddies the taking of averages over an initial set of states. However, in the early sixties a number of groups independently formulated theories capable of analysing such systems. Although slightly distinct in style, they are often umbrellaed under the banner of the non-equilibrium Green's function (NEGF) formalism. Although a powerful computational tool, it sat in some obscurity until the computational horsepower of modern computers made it accessible. Indeed today the NEGF formalism is utilised in a range of applications, from semiconducting transport to relativistic heavy-ion collisions [1]. To limit the scope of this work, we will focus on the application of the NEGF formalism to coupled superconductors in a device known as a Josephson junction.

A single superconductor is a macroscopic object which is characterised by an ordering of the internal electrons into a coherent quantum state. Although possessing a myriad of interesting physics, we shall focus on an effect first noted by the British physicist Brian Josephson in the late 1960's. He theorised that if two superconductors were separated by a weak-link – in a device now known as a Josephson junction

– current would flow even in the absence of an applied voltage [2]. Although the physics is well understood for ideal Josephson junctions, when one includes the competition between superconductivity and external magnetic fields alongside spin-orbit coupling the physics becomes increasingly rich. Indeed a veritable zoo of experimental effects has been identified within the interplay of these effects – most famously the prediction of Majorana zero modes at the interfaces of the nanowire Josephson junctions [3]. Although there has been significant work in classifying and unifying these effects, namely through the use of a $SU(2)$ gauge covariant description of electron transport which we advocate in this work, there is still significant progress required. The NEGF formalism is well suited to this work; acting as a unified computational tool for the exploration of a range of transport effects.

The purpose of this thesis is to derive, and solve numerically, the central equations in the non-equilibrium Green's function formalism whilst working in a $SU(2)$ gauge covariant manner. In this way we are able to explore a number of observed transport effects in Josephson junctions – from phase slips to phase shifts. As this problem is computational in nature, we will also discuss the practical numerical issues and introduce a new algorithm to improve the efficiency of the non-equilibrium Green's function formalism. Although there are few novel physical results, the work sets the groundwork for future work with the underlying aim of classifying the zoo of spin, topological, and charge phenomenologies in these devices.

1.1 Outline of thesis

Chapters two and three.

In the second and third chapters we introduce the ideas and techniques of quantum statistical mechanics. The aim is to begin with a set of general expressions in quantum and statistical mechanics respectively, then derive the resulting expressions of the non-equilibrium Green's function formalism. There is some novelty in the discussion of an $SU(2)$ gauge covariant formulation of non-relativistic quantum mechanics; a methodology which allows for a unified description of spin effects and is not entirely present in the conventional literature. The $SU(2)$ gauge covariant non-equilibrium Green's function formalism incorporating the effects of superconductivity paves the way for unified transport calculations in Josephson junctions. We also introduce the equations we will solve throughout this work.

Chapter four and five.

In the fourth and fifth chapters we introduce the numerical and computational aspects of this work, outlining how one translates the equations of the first two chapters into matrix problems which a computer can solve. The discussion on discretisation is significantly simplified by the introduction of gauge fields in previous chapters. As an application of our discretisation, we compute the bandstructure of electrons

under both spin-orbit coupling and a magnetic field in a two-dimensional lattice. We also discuss some numerical algorithms which greatly decreases the time taken to solve the required equations. The novelty in this chapter is we introduce a new numerical technique for the inversion of tri-diagonal block matrices – the central numerical operation of the non-equilibrium Green's function formalism. We compare this method to the existing literature.

Chapters six and seven.

In the final two sections we introduce the Josephson junction and describe the procedure for computing the current through these devices. Working in a wide regime of parameters, we compare the non-equilibrium Green's functions results with known results from literature. By progressively introducing terms into our Hamiltonian we increase the richness, and the complexity, of the observed physics. The final result is numerical observations of so called φ_0-junctions – Josephson junctions with arbitrary phase shifts. We study the nature of this phase shift for a range of different junctions working in different regimes. As part of this we model some experimental data concerning anomalous phase shifts in Josephson junctions.

Chapter 2

Theoretical foundations

States at different times can be compared, either by progressing forward from the earlier time, or backward from the later time... Knowledge of the transformation function referring to a closed time path determines the expectation value of any desired physical quantity.

—J. Schwinger, *Brownian Motion of a Quantum Oscillator*

Chapter Summary

This chapter is loosely split into two central ideas: the time-evolution of quantum operators, and the statistical averaging of quantum operators. The time-evolution rests on the Heisenberg equation of motion, whose central ingredient is the Hamiltonian of the system. To this end, we begin by identifying the relevant 'Schrödinger-like' equation of motion relativistic electrons evolve under; followed by a brief discussion of the symmetries of this equation. The single particle picture is then extended to a many body description which allows for an easier description of large systems. We then embark on a discussion of non-equilibrium quantum statistical mechanics which allows one to take statistical averages of operators. The purpose will be to introduce the Green's function, which will be used throughout the thesis.

2.1 Non-relativistic quantum mechanics

Being interested in the dynamics of electrons such that we can study transport in superconducting systems, we must identify the Hamiltonian upon which the dynamics of the system are inscribed. Although the best description of electrons is the relativistic Dirac's equation, in this work we only study low-energy electron excitations, hence the relativistic nature of this equation simply adds unnecessary complication. Thus by expanding out Dirac's equation, we can isolate the non-relativistic regime as required; the final result being Pauli's equation which describes the dynamics of low-energy electrons [4].

2.1.1 Non-relativistic limit of Dirac's equation

As we are interested in the dynamics of low-energy electrons, we must identify their equation of motion. For electrons in some external scalar Φ and vector potential $\mathbf{A}$, the single particle dynamics is best described by Dirac's equation. Letting $\Psi = \begin{pmatrix}\psi\\ \chi\end{pmatrix}$ denote the electron's wavefunction, which we have decomposed into the usual particle $\psi = \begin{pmatrix}\psi_\uparrow\\ \psi_\downarrow\end{pmatrix}$ and antiparticle spinors $\chi = \begin{pmatrix}\chi_\uparrow\\ \chi_\downarrow\end{pmatrix}$, Dirac's equation can be written as [5]

$$i\hbar\frac{\partial\Psi}{\partial t} = \big[c\boldsymbol{\alpha}\cdot[-i\hbar\boldsymbol{\nabla} + e\mathbf{A}] + \beta mc^2 - e\Phi\big]\Psi \quad , \tag{2.1}$$

where e is the electron charge, $\hbar$ is the reduced Planck's constant, m the electron mass, c the speed of light, and we have represented the Dirac matrices $(\beta, \boldsymbol{\alpha})$ as

$$\boldsymbol{\alpha} = \begin{pmatrix}0 & \boldsymbol{\sigma}\\ \boldsymbol{\sigma} & 0\end{pmatrix} \qquad \beta = \begin{pmatrix}I & 0\\ 0 & -I\end{pmatrix} \quad , \tag{2.2}$$

where $\boldsymbol{\sigma}$ denotes the three vector of Pauli matrices defined as

$$\sigma_1 = \begin{pmatrix}0 & 1\\ 1 & 0\end{pmatrix} \qquad \sigma_2 = \begin{pmatrix}0 & -i\\ i & 0\end{pmatrix} \qquad \sigma_3 = \begin{pmatrix}1 & 0\\ 0 & -1\end{pmatrix} \quad .$$

Noting that $-i\hbar\boldsymbol{\nabla} + e\mathbf{A}$, the first term on the right hand side of Eq. (2.1), has units of momentum thus we can regard it as a canonical momentum which factors in the coupling of the electromagnetic field and denote it by $\boldsymbol{\Pi}$ [1]. This allows us to write Dirac's equation in the compact form

$$i\hbar\frac{\partial\Psi}{\partial t} = \big[c\boldsymbol{\alpha}\cdot\boldsymbol{\Pi} + \beta mc^2 - e\Phi\big]\Psi \quad . \tag{2.3}$$

[1] Conventionally the scalar potential is also bundled with the temporal derivative to produce a canonical 4-momentum. As we are interested in non-relativistic effects we do not need to be so strict in treating time and space on the same footing and it will become easier to keep them separate.

As we are only interested in the low-energy sector we look to expand Dirac's equation around this regime to obtain an effective non-relativistic equation of motion. To this end, by expanding Dirac's equation out in powers of $1/m$ we decouple the particle and anti-particle sectors, obtaining the following equation for the Pauli 2-spinor ψ [4]

$$\begin{aligned} i\hbar\frac{\partial\psi}{\partial t} = mc^2\psi - e\Phi\psi + \frac{e\hbar}{2m}\mathbf{B}\cdot\boldsymbol{\sigma}\psi + \frac{1}{2m}\boldsymbol{\Pi}^2\psi + \frac{e\hbar^2}{8m^2c^2}\boldsymbol{\nabla}\cdot\mathbf{E}\psi \\ + \frac{e\hbar}{8m^2c^2}[\boldsymbol{\Pi}\cdot(\boldsymbol{\sigma}\times\mathbf{E}) + (\boldsymbol{\sigma}\times\mathbf{E})\cdot\boldsymbol{\Pi}]\psi \quad . \end{aligned} \tag{2.4}$$

Note that $\mathbf{E}$ and $\mathbf{B}$ denote the classical electric and magnetic fields, and that only terms up to $\mathcal{O}\big((1/m)^2\big)$ in the expansion have been kept. Being somewhat unwieldy we now look to simplify this expression. The first term of the right hand side of Eq. (2.4) is the rest mass of the electron, however, as we are interested in electrons with energy close to the Fermi energy, which is generally a fraction of the rest mass, we can safely ignore this term as it simply produces fast oscillations. Similarly, by absorbing the spin independent fifth term (Darwin term) into the one-body scalar potential term we find

$$i\hbar\frac{\partial\psi}{\partial t} = \left\{ \underbrace{\frac{1}{2m}\boldsymbol{\Pi}^2}_{\text{kinetic}} + \underbrace{\frac{e\hbar}{2m}\mathbf{B}\cdot\boldsymbol{\sigma}}_{\text{Zeeman}} + \underbrace{\frac{e\hbar}{8m^2c^2}[\boldsymbol{\Pi}\cdot(\boldsymbol{\sigma}\times\mathbf{E}) + (\boldsymbol{\sigma}\times\mathbf{E})\cdot\boldsymbol{\Pi}]}_{\text{spin-orbit}} - e\Phi \right\}\psi \quad . \tag{2.5}$$

This equation – known as the Pauli equation – describes well the relativistic corrections required to describe the wave function of a low-energy electron [5].

2.1.2 Pauli's equation in a gauge covariant form

A powerful technique in quantum mechanics is the use of symmetries – namely the various transformations which leave the system invariant. To study such transformations an important concept is the use of objects known as covariant derivatives D_μ, which are used to write equation of motion in the form

$$i\hbar D_0\psi = -\frac{\hbar^2}{2m}D_iD_i\psi \quad . \tag{2.6}$$

Under a gauge transformation – a local transformation of the system such that it is unchanged – of the form $\psi \to e^{i\chi(x)}\psi$ where χ is some function of a particular algebra corresponding to a symmetry group – such as $\chi(x) \in \mathbb{C}$ in the case of a $U(1)$ symmetry or $\chi(x) = \mathbf{f}(x)\cdot\boldsymbol{\sigma}$ for an $SU(2)$ symmetry, the gauge-covariant derivative must transform in a way such that Eq. (2.6) is unchanged.

Studying Eq. (2.5), we note that the kinetic term is quadratic in the canonical momentum whilst the spin-orbit term is linear in the canonical momentum. This allows us to 'complete the square' and bring all of the terms of the right hand side

into a single squared momentum term. We introduce the real-valued functions $a_\mu(x)$ and $\rho_\mu(x) = \rho_{\mu i}(x)\sigma_i$ by

$$a_0(x) = -\frac{e}{\hbar}\Phi(x) \quad , \quad a_i(x) = \frac{e}{\hbar}A_i(x) \tag{2.7}$$

$$\rho_{0i}(x) = \frac{e}{2m}B_i(x) \quad , \quad \rho_{li}(x) = \frac{e}{4mc^2}\epsilon_{lik}E_k(x) \quad . \tag{2.8}$$

In this manner we have absorbed the electromagnetic potentials into a single 4-vector a_μ, as is standard in electrodynamics; this is a manifestation of the $U(1)_{\text{em}}$ phase symmetry of the electron's wavefunction. Furthermore, we have also introduced a separate function ρ_μ which, as σ_i is the i^{th} generator of the $\mathfrak{su}(2)$ Lie algebra, accounts for local spin symmetry. The zero and 3-vector components of this field account for the Zeeman shift and the spin-orbit term respectively. For ease of notation, in the remainder of this thesis we work in the 4-vector notation where $x \equiv (t, \mathbf{x})$.

From these functions we can define the following covariant derivative

$$D_\mu = \frac{\partial}{\partial x^\mu} + ia_\mu(x) + i\rho_\mu(x) \quad . \tag{2.9}$$

With the aim of simplifying Eq. (2.5), we note that

$$\begin{aligned} D_iD_i &= \left(\frac{\partial}{\partial x^i} + ia_i(x) + i\rho_i(x)\right)\left(\frac{\partial}{\partial x^i} + ia_i(x) + i\rho_i(x)\right) \\ &= \left(\frac{i}{\hbar}\Pi_i + i\frac{e}{4mc^2}\epsilon_{ilk}E_k(x)\sigma_l\right)\left(\frac{i}{\hbar}\Pi_i + i\frac{e}{4mc^2}\epsilon_{imn}E_n(x)\sigma_m\right) \\ &= -\frac{1}{\hbar^2}\Pi_i\Pi_i - \frac{e}{4mc^2\hbar}(\Pi_i(\boldsymbol{\sigma}\times\mathbf{E})_i - (\boldsymbol{\sigma}\times\mathbf{E})_i\Pi_i) - \frac{e^2}{16m^2c^4}(\mathbf{E}\times\boldsymbol{\sigma})^2 \quad . \end{aligned}$$

Hence by comparing Eq. (2.5) and Eq. (2.10) we can now write Pauli's equation in the form

$$i\hbar D_0\psi = -\frac{\hbar^2}{2m}(D_iD_i - \rho_i\rho_i)\psi \quad . \tag{2.10}$$

The $\rho_i\rho_i$ term on the right hand side of Eq. (2.10) appears like a diamagnetic term – terms proportional to $\mathbf{A}^2$ – hence in the literature it is known as the dia-colour term [6]. As with the diamagnetic term, very often the contribution from this term is negligible and by dropping a term of order $\mathcal{O}\big((1/m)^3\big)$, we can write Pauli's equation in the compact form

$$i\hbar D_0\psi = -\frac{\hbar^2}{2m}D_iD_i\psi \quad . \tag{2.11}$$

This simplification of Pauli's is not just for aesthetics, but rather to elucidate the $U(1)_{\text{em}}\times SU(2)_{\text{spin}}$ gauge symmetry inherent to non-relativistic quantum mechanics. By writing Pauli's equation in a gauge covariant form, with the use of covariant derivatives, the equation's invariance to $U(1)_{\text{em}} \times SU(2)_{\text{spin}}$ gauge transformations is made clear. The relevant gauge transformations that the functions $a_\mu(x)$ and

$\rho_\mu(x)$ must have for this to be true are defined as

$$U(1)_{\text{em}}: \qquad a_\mu \to a_\mu + \partial_\mu \chi \quad , \tag{2.12}$$

$$\psi \to e^{-i\chi}\psi \quad , \tag{2.13}$$

and

$$SU(2)_{\text{spin}}: \qquad \rho_\mu \to s\rho_\mu s^{-1} + s(\partial_\mu s)^{-1} \quad , \tag{2.14}$$

$$\psi \to s\psi \quad , \tag{2.15}$$

where $\chi(x)$ is any real-valued function over $\mathbb{R}^4$ and $s(x)$ is any $\mathfrak{su}(2)$ valued function (any function of the form $f(x) = f_i(x)\sigma_i$) over the same spacetime[2]. Clearly then we must view the electromagnetic fields as the components of a $U(1)$ gauge field, but also view the Zeeman and spin-orbit terms as components of a $SU(2)$ gauge field![3].

The boon of such a formulation of non-relativistic quantum mechanics is that it allows one to provide a unified description of a number of phenomena: including the Aharonov-Casher effect, the Einstein-de Haas effect, spin currents, and, as will be described in Chapter 7, anomalous phase shifts in Josephson junctions – see Refs. [4, 6, 7].

2.1.3 Effective Hamiltonians for crystalline systems

In general, we are interested in the dynamics of many-body system comprising of $\mathcal{O}(10^{23})$ constituent particles with an array of complicated interactions and potentials – namely the behaviour of electrons moving in crystalline backgrounds. This task is formidable and as such we must make a number of approximation to make the problem tractable.

Firstly, in this work we are interested in electrons in semiconducting systems coupled to superconductors. In these systems it is reasonable to assume that the characteristic wavelength of the electrons – known as the Fermi wavelength – is significantly larger than the lattice spacing of the crystal such that the electrons cannot resolve the discrete lattice structure of their environment [4]. As such, one can model the electron as if it is moving in a non-trivial manifold with some specific torsion and curvature which accounts for the defects in the lattice [8]. In this thesis

[2]It is worth noting that in non-relativistic quantum mechanics, where physical space is given by $\mathbb{R}^3$ and time by $\mathbb{R}$, that spacetime is given by $\mathbb{R}\times\mathbb{R}^3$ as time does not mix with the spatial dimensions. This is in contrast to relativistic quantum mechanics where spacetime has a Minkowski structure.

[3]Note that the components of the $SU(2)$ gauge field are currently written as functions of the electromagnetic fields – experimentally observable quantities! This appears to be a contradiction as it is well known that we cannot measure gauge fields. However, it is of course as this is just written for a particular gauge and the $SU(2)$ gauge fields themselves are indeed not measurable. For example, if the vector potential was given as $\mathbf{A} = \begin{pmatrix} -\cos(z) & \sin(z) & 0 \end{pmatrix}$, then $\mathbf{B} = \boldsymbol{\nabla} \times \mathbf{A} = \mathbf{A}$. Although this would appear as if we are measuring the gauge field, it is simply that for a specific choice of gauge the gauge field is equivalent to the magnetic field which indeed is measurable. If we performed a $U(1)$ gauge transformation we would no longer have $\mathbf{B} = \mathbf{A}$.

we will assume our environment is free of defects and henceforth that the manifold the electron is defined over to be simply $\mathbb{R}^3$ – i.e. the electrons are assumed to be travelling in free space. However, to account for the change in the electron dynamics due to interactions with the lattice we substitute the electron rest mass with an effective mass m_e instead. Hence the equation of motion for a low-energy electron in a crystalline background becomes simply

$$i\hbar D_0\psi = -\frac{\hbar^2}{2m_e} D_i D_i \psi \quad . \tag{2.16}$$

where D_i is the same as before except with the substitution $m \to m_e$. Thus one can take into account the complex crystalline background to first order by simply modelling a free electron in space with an adjusted mass. These arguments can be made exact in the language of $\mathbf{k}\cdot\mathbf{p}$ theory [9].

Similarly, the gauge field introduced to account for spin symmetry ρ_μ in Section 2.1.1 was initialised to account for the spin-orbit and Zeeman interaction between a single spin and a nucleus. In real materials this behaviour can be exceedingly complex; hence ρ_μ must itself be generalised by the introduction of some fitting parameters α and g to account for the dynamics of a specific material. Indeed, if given some specific Zeeman and spin-orbit terms of the form

$$H_{\text{Zeeman}} = g\mu_B \mathbf{B}(x)\cdot\boldsymbol{\sigma} \quad , \quad H_{\text{spin-orbit}} = \alpha\boldsymbol{\Pi}\cdot(\boldsymbol{\sigma}\times\mathbf{E}(x)) \quad , \tag{2.17}$$

where g and α are some fitting parameters, and μ_B is the Bohr magneton, then we can write the gauge fields as

$$\rho_0(x) = \frac{g\mu_B}{\hbar}\mathbf{B}(x)\cdot\boldsymbol{\sigma} \quad , \quad \rho_i(x) = \frac{m\alpha}{\hbar}\boldsymbol{\sigma}\times\mathbf{E}(x) \quad , \tag{2.18}$$

where the coefficients α and g must be fitted to the material in question.

2.1.4 Second quantisation

Thus far we have identified the equation of motion of a single low-energy electron in an ideal crystalline background. However, we do not suppose that the electron density is small enough that we can assume only a single electron is present in our devices. Indeed, in a real material the full wavefunction would be a many-body wavefunction comprising a number of electrons. As a result we now need to identify the Hamiltonian describing the dynamics of a *system* of low-energy electrons.

To this end, we introduce the notion of an electron field and the corresponding 2-spinor Pauli field operators $\psi(x)$ and $\psi^\dagger(x)$ where

$$\psi(x) = \begin{pmatrix}\psi_\uparrow(x)\\ \psi_\downarrow(x)\end{pmatrix} \quad , \quad \psi^\dagger(x) = \begin{pmatrix}\psi_\uparrow^*(x) & \psi_\downarrow^*(x)\end{pmatrix} \quad . \tag{2.19}$$

For $\alpha \in \big(\uparrow, \downarrow\big)$, $\psi_\alpha(x)$ is the usual annihilation operator on the Fock space and $\psi^*_\alpha(x)$ is its adjoint, the creation operator. In this manner an electron is now viewed as an excitation of the electron field.

To account for the anti-commutativity of the individual electrons, the operators Eq. (2.19) satisfy the usual fermionic anti-commutation relations[4]

$$\{\psi_\alpha(x), \psi_\beta(y)\} = \big\{\psi^*_\alpha(x), \psi^*_\beta(y)\big\} = 0 \quad , \tag{2.20}$$

for $\alpha, \beta \in \big(\uparrow, \downarrow\big)$, and

$$\{\psi^*_\alpha(x), \psi_\beta(x)\} = \big\{\psi_\alpha(x), \psi^*_\beta(y)\big\} = \delta_{\alpha,\beta}\delta(x-y) \quad . \tag{2.21}$$

In some situations it will be simpler to work in a spin resolved formalism such that Eq. (2.20) and Eq. (2.21) are utilised, otherwise we can use the full spinorial commutators [5]

$$\big\{\psi(x) \circledS \psi^\top(y)\big\} = \big\{\psi^*(x) \circledS \psi^\dagger(y)\big\} = 0 \quad , \tag{2.22}$$

$$\big\{\psi(x) \circledS \psi^\dagger(x)\big\} = \delta(x-y) \quad , \tag{2.23}$$

where $\{A \circledS B\} \equiv A \otimes B + B^\top \otimes A^\top$.

In this field-theoretic viewpoint, we can now view Eq. (2.16) as the 'Schrodinger-like' equation of motion in a single particle picture, as described by some single particle Hamiltonian H_{sp}. After some rearranging we can extract the single particle Hamiltonian of Eq. (2.16) as

$$\begin{aligned} H_{\text{sp}} &= -\frac{\hbar^2}{2m_e}\mathbf{D}^2 + \hbar a_0 + \hbar\rho_0 \quad , \\ &= -\frac{\hbar^2}{2m_e}\mathbf{D}^2 - e\Phi + g\mu_B \mathbf{B}\cdot\boldsymbol{\sigma} \quad , \end{aligned} \tag{2.24}$$

such that Eq. (2.16) reads as

$$H_{\text{sp}}\psi = i\hbar\frac{\partial\psi}{\partial t} \quad . \tag{2.25}$$

It may seem spurious to be identifying the single-particle Hamiltonian when we are interested in many-particle systems, however, given some set of creation and annihilation operators $\big\{a_\mu, a^\dagger_\mu\big\}$ that span a many-body Fock space, one can cast a generic single particle operator Q_{sp} in this many-body system as [10]

$$Q = \sum_{\mu\,\nu} a^\dagger_\mu \,\langle\mu|Q_{\text{sp}}|\nu\rangle\, a_\nu \quad . \tag{2.26}$$

[4]Note that $\{A, B\} \equiv AB + BA$.

[5]Note that $\psi \otimes \psi^\top = \begin{pmatrix}\psi_\uparrow(x)\\ \psi_\downarrow(x)\end{pmatrix} \otimes \begin{pmatrix}\psi_\uparrow(x) & \psi_\downarrow(x)\end{pmatrix} = \begin{pmatrix}\psi_\uparrow(x)\psi_\uparrow(x) & \psi_\uparrow(x)\psi_\downarrow(x)\\ \psi_\downarrow(x)\psi_\uparrow(x) & \psi_\downarrow(x)\psi_\downarrow(x)\end{pmatrix}$.

Thus to write an operator in a many-body picture, we simply need its single particle representation. Hence we can now write the Hamiltonian for the many-body system as

$$\begin{aligned} H &= \int \mathrm{d}x\, \psi^\dagger(x) H_{\mathrm{sp}} \psi(x). \\ &= \int \mathrm{d}x\, \psi^\dagger(x) \left[-\frac{\hbar^2}{2m_e}\mathbf{D}^2 - e\Phi + g\mu_B \mathbf{B}\cdot\boldsymbol{\sigma} \right] \psi(x) \quad . \end{aligned} \tag{2.27}$$

2.1.5 Heisenberg's equation of motion

As we are interested in the dynamics of systems, with the main focus being on transport through mesoscopic structures, the time-dependence of quantum operators is an important property. One of the axioms of quantum mechanics that given some operator $\hat{Q}(t)$, its time evolution is given by [11]

$$\frac{\mathrm{d}\hat{Q}}{\mathrm{d}t} = \frac{1}{i\hbar}\left[\hat{Q}, H\right] \quad . \tag{2.28}$$

Known as Heisenberg's equation, it will be critical to much of the subsequent analysis as from this we can study the dynamics of the system. Hence as we have isolated the full many-body Hamiltonian for low-energy electrons moving in a crystalline background in Eq. (2.27), then using Heisenberg's equation of motion we can compute the dynamics of any operator in question.

2.2 Quantum statistical field theory

In the previous section we identified the Hamiltonian for the full many-body system which led to Heisenberg's equation. However, in a many-body system at non-zero temperatures we are interested in *averages* of operators which we can compare to experiments, where the ensemble we average over consists of all possible quantum configurations. The mechanism to do so is known as quantum statistical field theory.

In this section we will introduce these techniques and illustrate how they are utilised both in, and out of, equilibrium. Furthermore, we will introduce a central object of this thesis, known as the Green's function, which will greatly aid in calculations.

2.2.1 Density matrices

In classical statistical mechanics, to compute an observable we do not attempt to 'solve' the system considering every microscopic element; rather, we aim to compute statistical averages of observables. The only difference now is that the ensemble is an ensemble of every possible quantum state.

We introduce a quantity known as the density matrix, which, defined at some point in time, is given by

$$\rho = \sum_{\Phi} p_{\Phi} \left|\Phi\right\rangle \left\langle\Phi\right| \quad , \tag{2.29}$$

where the sum is over every state $|\Phi\rangle$ in the many-body system and p_Φ is a weight corresponding to each state accounting for the probability of the occurrence of that particular state [12]. We see that the density matrix acts as a weighted projection operator such that if given some operator $\hat{Q}$, the application of the density matrix projects $\hat{Q}$ onto each state of the system $|\Phi\rangle$ and weights it according to the probability of that state p_Φ. Indeed we define the average of $\hat{Q}$ (denoted by Q) as precisely this weighted projection [13]

$$Q = \left\langle \hat{Q} \right\rangle \equiv \sum_{\Phi} p_{\Phi} \left\langle \Phi | \hat{Q} | \Phi \right\rangle = \mathrm{Tr}\Big[\rho \hat{Q}\Big] \quad . \tag{2.30}$$

Eq. (2.29) is the generic expression for the density matrix and is true whether the system is in, or out of, equilibrium. However, given a system which is in thermal equilibrium at some temperature T and with a chemical potential μ, and whose dynamics are characterised by a time independent Hamiltonian H, we can write the density matrix in a grand canonical ensemble[6] as [14]

$$\rho = \frac{\exp\Big\{-\beta\Big(H - \mu\hat{N}\Big)\Big\}}{\mathrm{Tr}\Big[\exp\Big\{-\beta\Big(H - \mu\hat{N}\Big)\Big\}\Big]} \quad , \tag{2.31}$$

where $\beta = 1/(k_B T)$ and k_B the Boltzmann constant. We shall see later that being in thermal equilibrium at some fixed chemical potential, such that we can cast the density matrix into the form of Eq. (2.31) greatly simplifies calculations[7].

2.2.2 Introduction to Green's functions

As we are now working with a field theory, rather than studying individual wavefunctions, it is prudent to briefly discuss their central computational tool – the notion of correlations. In a quantum field, an n-point correlation function describes how n creation or annihilation operators at different points in spacetime are correlated with each other. Most physically is the 2-point correlation function – also known as the Green's function[8] – which describes how the creation of an electron at some

[6] A grand canonical ensemble is simply a system in thermal equilibrium where particle number is not necessarily conserved. As we are interested in transport where particles flow between two reservoirs (leads) this is a very natural ensemble to work with.

[7] For the remainder of this thesis, instead of writing $H - \mu\hat{N}$ as the time evolution operator in the grand-canonical ensemble, we will simply write H to clean up the notation. However, it should be remembered that we are always working in a grand-canonical ensemble and hence there will always be a $-\mu\hat{N}$ term implicit in H. When we do explicit calculations this will be evident.

[8] What's in a name? The standard progression for scientific naming goes possessive, adjectival, then (if one is lucky) uncapitalised adjectival (Abel's group → Abel group → abelian group). The

points in space and time is correlated with its destruction at another. Being explicit, the Green's function is defined as

$$G(x,x') = \frac{1}{i\hbar}\left\langle T\big\{\psi(x)\otimes\psi^\dagger(x')\big\}\right\rangle \quad , \tag{2.32}$$

where the time ordering symbol T indicates that the order of the operators must be interchanged depending on which operator is applied first in time. Namely

$$T\big\{\psi(t,\mathbf{x})\otimes\psi^\dagger(t',\mathbf{x}')\big\} \equiv \begin{cases} \psi(t,\mathbf{x})\otimes\psi^\dagger(t',\mathbf{x}') & , \quad t>t' \\ -\psi^*(t',\mathbf{x}')\otimes\psi^\top(t,\mathbf{x}) & , \quad t<t' \end{cases} \quad , \tag{2.33}$$

where the minus sign in the $t > t'$ case is due to the fermionic anti-commutation relations of Eq. (2.22). For clarity, we can expand out the time ordering of the Green's function in Eq. (2.32)

$$\begin{aligned} G(x,x') &= \theta(t-t')\frac{1}{i\hbar}\left\langle\psi(x)\otimes\psi^\dagger(x')\right\rangle - \theta(t'-t)\frac{1}{i\hbar}\left\langle\psi^*(x')\otimes\psi^\top(x)\right\rangle \\ &\equiv \theta(t-t')G^>(x,x') + \theta(t'-t)G^<(x,x') \quad , \end{aligned} \tag{2.34}$$

where $\theta(\tau)$ is the usual Heaviside step function and $G^<$ and $G^>$ denote the 'lesser' and 'greater' Green functions respectively – merely indicating whether the first temporal argument is lesser or greater than the second.

Although somewhat nondescript, the 2-point correlator is an exceedingly powerful tool. Consider the lesser Green's function $G^<(x,x') \equiv \frac{i}{\hbar}\left\langle\psi^*(x')\otimes\psi^\top(x)\right\rangle$ for instance, physically this tells one how correlated the creation of a field excitation at position $\mathbf{x}'$ and time t' is is with the destruction of a field excitation at $\mathbf{x}$ and time t in the past. Although this may appear abstract, it is the field-theoretic equivalent of asking 'what is the probability of my electron propagating from $(t,\mathbf{x})$ to $(t',\mathbf{x}')$?'.

In a field theory, full knowledge of the system is equivalent to knowing all n-point correlators [13]. Although this is an impossible task, fortunately single-particle observables, such as current and electron density, only require the computation of the 2-point correlation function which greatly reduces the required computation [14]. As an example, the local electron density operator is given by

$$\hat{n}(x) = \sum_{i\in(\uparrow,\downarrow)} \psi_i^\dagger(x)\psi_i(x) \quad . \tag{2.35}$$

Hence the averaged observed probability density is

$$n(x) = \langle\hat{n}(x)\rangle = \mathrm{Tr}\big[\left\langle\psi^*(x)\otimes\psi^\top(x)\right\rangle\big] \quad , \tag{2.36}$$

'Green's function' was indeed following this trend (Green's function → Green function) but for some reason bucked this trend in the mid 90's [15] and is now commonly known as the Green's function in the literature. We shall use this nomenclature.

where the trace is taken over the spin subspace. As a result, assuming the Green's functions of the system is known, then the electron density would be simply given by

$$n(x) = -i\hbar \,\mathrm{Tr}[G^{<}(x,x)] \quad . \tag{2.37}$$

The evaluation of these Green's functions will form a central part of this thesis.

2.2.3 Evaluating Green's functions in equilibrium systems

As described in Section 2.2.2, the evaluation of Green's functions are critical for computing single-body observables such as electron density and current – precisely the quantities we wish to study. However, as described in Section 2.2.1, to compute a statistical average we must utilise a density matrix, which in its most general form is given by

$$\rho = \sum_{\Phi} p_{\Phi} \left|\Phi\right\rangle \left\langle\Phi\right| \quad , \tag{2.38}$$

where the sum is over every quantum state $|\Phi\rangle$ in the many-body system and the p_Φ is a weight corresponding to the probability of the occurrence of each state [12]. However, it is not obvious how one can construct these states $|\Phi\rangle$ such that this projection is conceivable. Indeed to study a system we would begin by constructing a many-body Hamiltonian H, which would then be diagonalised to find the eigenstates used to construct the density matrix ρ. However, assuming the system is in equilibrium at some temperature T we can side-step these difficulties immediately as we can write the density matrix as

$$\rho = \frac{\exp\{-\beta H)\}}{\mathrm{Tr}[\exp\{-\beta H\}]} \quad , \tag{2.39}$$

where there is only a reference to the known Hamiltonian H. For example, consider the following 2-point correlator

$$G^{<}_{q,q'}(t,t') = \frac{i}{\hbar}\left\langle \psi^{*}_{q'}(t')\psi_q(t)\right\rangle \quad , \tag{2.40}$$

where ψ_k are spin-less fermionic operators obeying the standard fermionic anti-commutation relations Eq. (2.22). In Appendix A.1, we show that it can be computed by

$$G^{<}_{q,q'}(t,t') = \frac{i}{\hbar}\big(1+e^{\beta\xi_q}\big)^{-1}\delta_{q',q}e^{i\xi_{q'}(t'-t)/\hbar} = \frac{if(\xi_q)}{\hbar}\delta_{q,q'}e^{i\xi_q(t-t')/\hbar} \quad , \tag{2.41}$$

where $f(\xi_q)$ is the usual Fermi function for fermions evaluated at energy ξ_q. Clearly then no explicit average must be taken over as all of the 'statistical' content has been shifted to the application of the Fermi function. Indeed this can only be well-defined in an equilibrium system where the Fermi function itself is well-defined.

Before we continue onto non-equilibrium systems, we must introduce another concept, that of the causal (G^R) and anti-causal (G^A) Green's functions which are defined respectively as

$$\begin{aligned} G^R(x,x') &= \theta(t-t')(G^>(x,x') - G^<(x,x')) \quad , \\ G^A(x,x') &= -\theta(t'-t)(G^>(x,x') - G^<(x,x')) \quad . \end{aligned} \tag{2.42}$$

From these definitions we note the identity

$$G^R(x,x') - G^A(x,x') = G^>(x,x') - G^<(x,x') \quad , \tag{2.43}$$

which is of such importance that we define

$$A(x,x') \equiv i\big(G^R(x,x') - G^A(x,x')\big) = i(G^>(x,x') - G^<(x,x')) \quad , \tag{2.44}$$

as the spectral weight function [13]. The spectral weight function contains the information on the availability of each state such that its diagonal elements, $A(x,x)$, are proportional to the local density of states at the point x. Returning to the lesser Green's function in Eq. (2.40), the reason we introduce these quantities is that it simplifies the computation of the Green's functions. Indeed, after some work, which we leave for Appendix A.2, one can show that

$$-iG^<(x,x';E) = f(E)A(x,x';E) \quad . \tag{2.45}$$

We will make extensive use of this identity in later chapters when we explicitly compute Green's functions in interacting, but equilibrium, systems.

2.2.4 Computing Green's functions out of equilibrium

In this work we are interested in transport through superconducting systems which are not necessarily in thermal equilibrium. Thus far we have shown how to evaluate Green's functions in equilibrium systems, but so far the problem of non-equilibrium systems has not been considered. In Section 2.2.3 it was mentioned that in equilibrium one does not need to solve the 'projection problem' – explicitly projecting one's operator of interest over a set of seemingly incalculable many-body wavefunctions – but rather one can reframe the problem such that all of the statistics is shifted to the use of Fermi functions. However, this was only valid when the average was taken with respect to the free Hamiltonian as in Eq. (A.2). We now show how one solves the projection problem for non-equilibrium systems where one does not have the luxury of a Fermi function.

We begin by partitioning the Hamiltonian $\mathcal{H}(t)$ of the system into two parts: an equilibrium part H, consisting of both a free part H_0 and an interaction term H', and a perturbing term $\tilde{H}(t)$ which drives the system out of equilibrium

$$\mathcal{H}(t) = H + \tilde{H}(t) = H_0 + H' + \tilde{H}(t) \quad . \tag{2.46}$$

We now assume that for times less than some reference time $t < t_r$, the system is in equilibrium governed by the Hamiltonian H. Although the system is in equilibrium, the interaction term in the Hamiltonian means the density matrix is still constructed from highly-correlated many-body states $|\Phi\rangle$ (unlike in Eq. (2.41) where the lack of interactions meant the system had trivial correlations)

$$\rho(t_r) = \sum_{\Phi} p_{\Phi(t_r)} \left|\Phi(t_r)\right\rangle \left\langle\Phi(t_r)\right| \quad . \tag{2.47}$$

As the system is assumed to be in equilibrium for these times we can simplify this expression to write the density matrix as

$$\rho(t_r) = \frac{\exp\{-\beta H(t_r))\}}{\mathrm{Tr}[\exp\{-\beta H(t_r)\}]} \quad . \tag{2.48}$$

For $t > t_r$ we now turn on the non-equilibrium perturbation $\tilde{H}(t)$ such that the system evolves under the full Hamiltonian $\mathcal{H}(t)$. Turning on the perturbation so suddenly induces transient phenomena as the equilibrium states $|\Phi\rangle$ are quickly mixed. In this work we are not interested in the transient phenomena but rather the steady-state which is reached at asymptotic times; we set $t_r \to -\infty$ to work in this regime.

We now define the statistical average to be with respect to the equilibrium density matrix of Eq. (2.47) hence we can write the Green's function as

$$G(x, x') = \frac{1}{i\hbar} \frac{\mathrm{Tr}\left[e^{-\beta H(t_r)} T\left\{\psi(t, \mathbf{x}) \otimes \psi^\dagger(t', \mathbf{x}')\right\}\right]}{\mathrm{Tr}[e^{-\beta H(t_r)}]} \quad . \tag{2.49}$$

As Eq. (2.49) is currently expressed in the Heisenberg picture – where the time evolution of the operators is governed by the complicated $\mathcal{H}$ – we look to rewrite the operators in the interaction picture – where the time evolution is governed by the simpler H_0. As is standard, we can express these Heisenberg picture operators in the interaction picture using $\mathcal{S}$ matrices [11]. Letting the pictures of the two representations coincide at $t = t_r$ we have

$$\psi(t, \mathbf{x}) \equiv \mathcal{S}(t_r, t) \psi_I(t_r, \mathbf{x}) \mathcal{S}(t, t_r) \quad , \tag{2.50}$$

where

$$\mathcal{S}(t, t') \equiv T \exp\left\{ \frac{1}{i\hbar} \int_{t'}^{t} \mathrm{d}\tau \, H_I'(\tau) + \tilde{H}_I(\tau) \right\} \quad , \tag{2.51}$$

and $\tilde{H}_I(t) = e^{-\frac{i}{\hbar} H_0 t} \tilde{H}_S(t) e^{\frac{i}{\hbar} H_0 t}$ and $H_I'(t) = e^{-\frac{i}{\hbar} H_0 t} H_S'(t) e^{\frac{i}{\hbar} H_0 t}$ are the perturbing and interacting term of the Hamiltonian formulated in the interaction picture respectively, whilst the subscript S denotes the operators in the Schrödinger picture [13].

Substituting these expressions into the Green's function of Eq. (2.49), we have that

$$G(x,x') = \frac{1}{i\hbar}\frac{\mathrm{Tr}\Big[e^{-\beta H(t_r)}T\Big\{\mathcal{S}(t_r,t)\psi_I(t,\mathbf{x})\mathcal{S}(t,t_r)\otimes\mathcal{S}(t_r,t')\psi_I^\dagger(t',\mathbf{x}')\mathcal{S}(t,t_r)\Big\}\Big]}{\mathrm{Tr}[e^{-\beta H(t_r)}]} \quad . \tag{2.52}$$

From Eq. (2.51), we note that the $\mathcal{S}$ matrices are themselves time ordered expressions. As a result we can unify the various $\mathcal{S}$ matrices by democratising the time variable to now lie on a contour $\tilde{\mathcal{C}}$ which runs from t_r to some final time t_f (such that $t,t' \in (t_r,t_f)$) then critically loops back on itself to t_r. This is known as the closed time contour and is illustrated in Fig. 2.1. By introducing contour ordering,

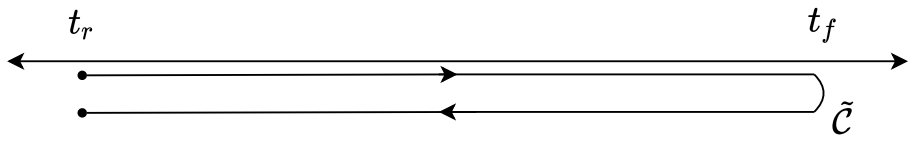

Figure 2.1: Closed time contour.

$T_{\tilde{\mathcal{C}}}$, where operators are ordered by the order their time argument appears on the contour $\tilde{\mathcal{C}}$ as it is traversed from start to finish, and defining

$$\mathcal{S}_{\tilde{\mathcal{C}}} = \exp\Big\{-\frac{i}{\hbar}\int_{\tilde{\mathcal{C}}}\mathrm{d}\tau\,\Big(H_I'(\tau)+\tilde{H}_I(\tau)\Big)\Big\} \quad , \tag{2.53}$$

we can write Eq. (2.52) as

$$G(x,x') = \frac{1}{i\hbar}\frac{\mathrm{Tr}\Big[e^{-\beta H(t_r)}T_{\tilde{\mathcal{C}}}\Big\{\mathcal{S}_{\tilde{\mathcal{C}}}\psi_I(t,\mathbf{x})\otimes\psi_I^\dagger(t',\mathbf{x}')\Big\}\Big]}{\mathrm{Tr}[e^{-\beta H(t_r)}]} \quad . \tag{2.54}$$

We now return to the projection problem – the presence of highly correlated electron states in the density matrix of Eq. (2.54). Indeed to be solvable, such that we can use Wick's theorem, we must average with respect to the free Hamiltonian as in Section 2.2.3 [1]. To do this we can construct the equilibrium density matrix of Eq. (2.48) by evolving the free density matrix in imaginary time using another $\mathcal{S}$ matrix [16]

$$e^{-\beta H(t_r)} = e^{-\beta H_0}e^{-\frac{i}{\hbar}\int_{t_r-i\beta}^{t_r}\mathrm{d}\tau H_I'(\tau)} \quad . \tag{2.55}$$

By extending the closed-time contour of Fig. 2.1 to include this extra expedition into the imaginary axis we have defined what is known as the Kadanoff-Baym contour – which we illustrate in Fig. 2.2 [17]

Indeed by defining

$$\mathcal{S}_{\mathcal{C}} = \exp\Big\{-\frac{i}{\hbar}\int_{\mathcal{C}}\mathrm{d}\tau\,\Big(H_I'(\tau)+\lim_{\eta\to 0}\Theta_{\mathcal{C}}(i\eta-\tau)\tilde{H}_I(\tau)\Big)\Big\} \quad , \tag{2.56}$$

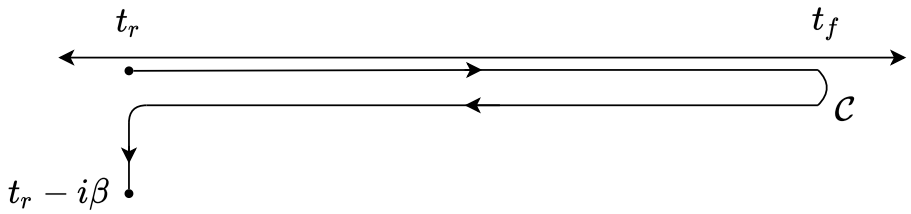

Figure 2.2: Kadanoff-Baym contour.

where $\Theta_{\mathcal{C}}$ is the generalised step function[9], then the Green's function of Eq. (2.54) can be written as

$$\begin{aligned} G(x,x') &= \frac{1}{i\hbar}\frac{\mathrm{Tr}\Big[e^{-\beta H_0}T_{\mathcal{C}}\Big\{\mathcal{S}_{\mathcal{C}}\psi_I(t,\mathbf{x})\otimes\psi_I^\dagger(t',\mathbf{x}')\Big\}\Big]}{\mathrm{Tr}[e^{-\beta H_0}\mathcal{S}_{\mathcal{C}}]} \\ &\equiv \frac{1}{i\hbar}\Big\langle T_{\mathcal{C}}\Big\{\mathcal{S}_{\mathcal{C}}\psi_I(t,\mathbf{x})\otimes\psi_I^\dagger(t',\mathbf{x}')\Big\}\Big\rangle_{H_0} \quad . \end{aligned} \tag{2.57}$$

Note the excess contour in the denominator will cancel with itself as $\mathcal{S}_{\mathcal{C}}(t_r,t_r)=1$. We have now written the Green's function of a non-equilibrium system in terms of both a quadratic density matrix – allowing for the use of Wick's theorem – and a single contour ordered $\mathcal{S}$ matrix – which allows for a perturbative expansion [1]. As we are averaging with respect to the free Hamiltonian we are no longer projecting onto highly correlated electron states, however the cost is we now have to integrate over a complex-valued contour time.

2.2.5 Initial correlations and Wick's theorem

In order to define statistical averages in non-equilibrium systems without reference to highly correlated electron states we had to allow for the time variables to lie on a complex-valued temporal contour. Although we claimed this is solvable it is somewhat opaque and we illustrate here the mechanisms by which it is done – namely the application of Wick's theorem and the ignoring of initial correlations.

The final expression for the contour ordered Green's functions over the Kadanoff-Baym contour was given by

$$\begin{aligned} G(x,x') &= \frac{1}{i\hbar}\frac{\mathrm{Tr}\Big[e^{-\beta H_0}T_{\mathcal{C}}\Big\{\mathcal{S}_{\mathcal{C}}\psi_I(t,\mathbf{x})\otimes\psi_I^\dagger(t',\mathbf{x}')\Big\}\Big]}{\mathrm{Tr}[e^{-\beta H_0}\mathcal{S}_{\mathcal{C}}]} \\ &\equiv \frac{1}{i\hbar}\Big\langle T_{\mathcal{C}}\Big\{\mathcal{S}_{\mathcal{C}}\psi_I(t,\mathbf{x})\otimes\psi_I^\dagger(t',\mathbf{x}')\Big\}\Big\rangle_{H_0} \quad , \end{aligned} \tag{2.58}$$

[9] We define the generalised step function as $\Theta_{\mathcal{C}}(t-t') = \int_{\mathcal{C}}^{t} \mathrm{d}\tau\, \delta_{\mathcal{C}}(\tau - t')$ where $\delta_{\mathcal{C}}$ is the generalised delta function and is defined such that $\int_{\mathcal{C}} \mathrm{d}\tau\, \delta_{\mathcal{C}}(\tau - t) = 1$ for $t \in \mathcal{C}$.

where $\mathcal{S}_\mathcal{C}$ is given by Eq. (2.56). As $\mathcal{S}_\mathcal{C}$ is an exponential quantity we can asymptotically expand to produce terms of the form

$$\left\langle T_\mathcal{C}\left\{\psi_I(t,\mathbf{x})\psi_I^\dagger(t',\mathbf{x}')\prod_i^n \psi_I(x_{2i})\psi_i^\dagger(x_{2i-1})\right\}\right\rangle_{H_0} \quad . \tag{2.59}$$

Although we do not prove it here, we can simplify Eq. (2.59) using a theorem known as Wick's theorem where we can convert averages of chains of time ordered operators into products of averages of only pairs [13]

$$\left\langle \prod_i^n \psi_I(x_{2i})\psi_I^\dagger(x_{2i-1})\right\rangle_{H_0} = \sum_{\sigma\in\mathcal{S}_{2n}}\prod_{j=1}^n \frac{\mathrm{sgn}(\sigma)}{2^n n!} g_{2j-1\,,\,2j} \quad , \tag{2.60}$$

where $g_{i,j} \equiv \left\langle T_\mathcal{C}\left\{\psi_I^\dagger(x_{\sigma(i)})\psi_I(x_{\sigma(j)})\right\}\right\rangle_{H_0}$ and the coefficient in front of $g_{i,j}$ accounts for both the sign flipping of different contractions as fermionic operators are interchanged, and the number of permutations of $\mathcal{S}_{2n}$ that give equivalent terms in the Wick series. The $g_{i,j}$ are the building blocks of the non-equilibrium Green's function formalism and are known as the free Green's functions. An exact example of them were given in Eq. (A.7) for an example free Hamiltonian. Hence, for any perturbation $\tilde{H}(t)$, one can expand out the $\mathcal{S}$ matrix, then decompose each term of the expansion into various free Green's functions using Wicks' theorem Eq. (2.60). As these free Green's functions are solvable then we can re-sum them to compute the total Green's function.

In Section 2.2.4 we began by defining the density matrix at t_r from a basis of highly-correlated electron states. For $t > t_r$ we then sharply turned on the non-equilibrium perturbation $\tilde{H}(t)$ which, as a result, will quickly mix the equilibrium states. Although the states will be heavily mixed due to the non-equilibrium term, there will always be a memory of these initial correlations in the system for times $t > t_r$. In this work, we made use of the Kadanoff-Baym contour, which by writing the interacting density matrix as the free density matrix rotated in imaginary time

$$e^{-\beta H(t_r)} = e^{-\beta H_0} e^{-\frac{i}{\hbar}\int_{t_r-i\beta}^{t_r} \mathrm{d}\tau H_I'(\tau)} \quad , \tag{2.61}$$

not only allowed for Wick's theorem to be utilised, but also shifted the effects of the initial correlations onto *only* the imaginary part of the contour [18]. Furthermore, as we are interested in steady-state transport which is reached at asymptotic times we set $t_r \to -\infty$ which, as a result, sent the imaginary part of the contour – starting from t_r and propagating downwards to $t_r + i\beta$ – infinitely far into the past. To deal with these initial correlations – which live only on the complex part of the contour infinitely far in the past – we note that Wick's theorem produces convolutions of free Green's functions of the form

$$\left\langle \psi^\dagger(t)\psi(t')\right\rangle \rightsquigarrow \int_\mathcal{C} \mathrm{d}\tau_1 \cdots \int_\mathcal{C} \mathrm{d}\tau_n\, g(t,\tau_1)g(\tau_1,\tau_2)\cdots g(\tau_n,t') \quad , \tag{2.62}$$

where we can see every expansion will contain one term with one temporal argument fixed at $t \gg t_r$. As the creation of an electron is not correlated with the annihilation of an electron after asymptotically long periods of time then $g(\tau_i, \tau_j) \to 0$ as $|\tau_j - \tau_i| \to \infty$ [13, 16]. Thus anytime any of the contour variables τ_i lie on the imaginary part of the contour at $\tau_i \to -\infty$, *all* of the other temporal variables must also lie on this part of the contour such that the integral doesn't vanish. However, as at least one free Green's function must have a temporal variable at $t \gg t_r$, then this condition can never be satisfied; as a result any contribution from the imaginary part of the contour vanishes. Therefore we can simply ignore this portion of the contour as it will not make any contribution to the integral of Eq. (2.62). As a result we can simplify the contour such that it traverses from t_r to t_f and back without leaving the real axis, see Fig. 2.5b. This contour is named the Schwinger-Keldysh contour and will be used throughout the rest of this thesis.

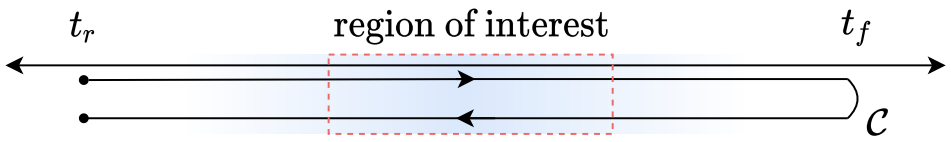

Figure 2.3: Schwinger-Keldysh contour with the temporal region of interest indicated in the dashed red box. The faded blue region illustrates the decay of the correlation functions when one time argument, t, is tied to the region of interest and the other is varied. As long as $t_r \ll t$, then the correlation function decays appropriately that the imaginary contour in Fig. 2.2 can be ignored. Physically a propagator with one of its arguments on the imaginary time appendix is damped on the time scale of the scattering time of the system.

2.2.6 Analytic continuation

To formulate statistical averages in non-equilibrium systems we had to introduce a temporal contour; out-of-equilibrium one cannot easily relate states in the infinite future with those in the infinite past which necessitates allowing time to run backwards. Unfortunately the temporal variable is no longer a simple real number but rather belongs to a complex contour. To compute experimental observables we are interested in real-time valued operators, hence we must somehow extract real-time valued observables from these contour ordered expressions. We now derive expressions that allow us to analytically continue expressions written with respect to this contour ordered time into real-time expressions.

To begin, to simplify the following we impose that the reference time and final time of the contour are set to $-\infty$ and $+\infty$ respectively. Consider now the general contour ordered function

$$C(t_1, t_2) = \int_{\mathcal{C}} \mathrm{d}\tau \, A(t_1, \tau) B(\tau, t_2) \quad , \tag{2.63}$$

where $\mathcal{C}$ denotes the Schwinger-Keldysh contour illustrated below for completeness. For simplicity we have suppressed all other degrees of freedom (spatial, spin, etc). We can parametrise the two branches of the Schwinger-Keldysh contour using real

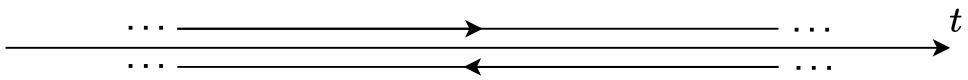

Figure 2.4: Schwinger-Keldysh contour extended to positive and negative infinity.

times by

$$\int_{\mathcal{C}} \mathrm{d}\tau \, [\cdots] = \int_{-\infty}^{\infty} \mathrm{d}t \, [\cdots] + \int_{\infty}^{-\infty} \mathrm{d}t \, [\cdots] \quad , \tag{2.64}$$

where we have denoted real time variables by the latin t and the contour valued times by τ. Assuming that $t_1 < t_2$, such that we are evaluating $C^<(t_1, t_2)$, we can consider the four possible positions τ can have on the contour relative to both the two branches and both t_1 and t_2 as illustrated in Fig. 2.5.

Using these possible orderings we can deconstruct Eq. (2.63) into four real time integrals

$$\begin{aligned} C^<(t_1, t_2) = &\int_{-\infty}^{t_1} \mathrm{d}t \, A^>(t_1, \tau) B^<(\tau, t_2) + \int_{t_1}^{t_2} \mathrm{d}t \, A^<(t_1, \tau) B^<(\tau, t_2) \\ &+ \int_{t_2}^{\infty} \mathrm{d}t \, A^<(t_1, \tau) B^>(\tau, t_2) + \int_{\infty}^{-\infty} \mathrm{d}t \, A^<(t_1, \tau) B^>(\tau, t_2) \quad , \end{aligned} \tag{2.65}$$

where the $>$ and $<$ symbols indicates whether the first is greater, or lesser, than the second respectively. Rearranging the integrals and adding a factor of zero, this can be rewritten as

$$\begin{aligned} C^<(t_1, t_2) = &\int_{-\infty}^{\infty} \theta(t_1 - t) \, \mathrm{d}\tau \, (A^>(t_1, \tau) - A^<(t_1, \tau)) B^<(\tau, t_2) \\ &+ \int_{-\infty}^{\infty} \theta(t_2 - t) \, \mathrm{d}\tau \, A^<(t_1, \tau) (B^<(\tau, t_2) - B^>(\tau, t_2)) \quad . \end{aligned} \tag{2.66}$$

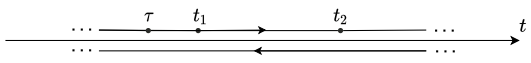

(a) τ appears before both t_1 and t_2.

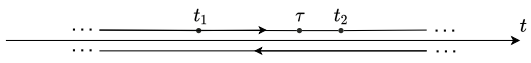

(b) τ appears before t_2 but after t_1.

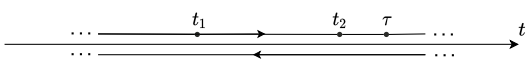

(c) τ appears after both t_1 and t_2 but is on the upper branch.

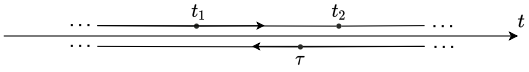

(d) τ appears after both t_1 and t_2 but is on the lower branch.

Figure 2.5: Various possible time orderings of the variables t_1, t_2, and τ on the Schwinger-Keldysh contour.

Hence by using the definitions of the causal Green's functions in Eq. (2.42), we have

$$C^{<}(t_1,t_2) = \int_{-\infty}^{\infty} \mathrm{d}t\, A^R(t_1,t)B^{<}(t,t_2) + A^{<}(t_1,t)B^A(t,t_2) \quad . \tag{2.67}$$

Thus by starting from the Schwinger-Keldysh contour, and making careful choices as to the time ordering of operators, we can write $C^{<}$ as an integral over purely real times as required. Other analytic continuations are possible, say if one wanted to compute $C^{>}$ or C^R instead; these are compiled in Table 2.1 below.

Table 2.1: Collation of different continuations. We implicitly imply convolutions over all adjacent terms under an integral.

Contour integral	Real-time integral
$C = \int_{\mathcal{C}} AB$	$C^{</>} = \int_t \left(A^R B^{</>} + A^{</>} B^A\right)$
	$C^{R/A} = \int_t A^{R/A} B^{R/A}$
$D = \int_{\mathcal{C}} ABC$	$D^{</>} = \int_t \left(A^R B^R C^{</>} + A^R B^{</>} C^A + A^{</>} B^A C^A\right)$
	$D^{R/A} = \int_t A^{R/A} B^{R/A} C^{R/A}$

Chapter 3

Dynamics in superconducting systems

The effective attraction between electrons near the Fermi surface, due to electron-phonon interaction, must lead to bound pairs of electrons, regardless of how weak the attraction may be. Since formation of pairs is energetically favorable, turning on the interaction causes the ground state of the system to be 'rebuilt'.

—A.A. Abrikosov *et al*, *Methods of Quantum Field Theory in Statistical Physics*

Chapter Summary

The central aim of this thesis is to study transport in Josephson junctions – devices consisting of two coupled superconductors. In the previous chapter Chapter 2 the mechanisms behind transport were introduced, however we have not yet introduced the superconducting theory yet. In this chapter we discuss the theoretical footing upon which superconductivity is placed. To begin, we introduce the mean-field Bardeen, Cooper, and Schrieffer (BCS) Hamiltonian which, by means of inducing instabilities in the background electron field, gives rise to bulk superconductivity.

By making use of the BCS Hamiltonian we derive equations of motion for electrons in superconductors. From these equations we then construct equations of motion for Green's function within superconductors – the eponymous Nambu-Gorkov equation. Finally, we will introduce the Hamiltonian for the Josephson junction and using this derive expressions for the current and density of states through the device.

3.1 Superconductivity

3.1.1 BCS Hamiltonian

Superconductivity has a rich experimental history, with a number of diverse physical properties uncovered since the initial observation of resistivity free supercooled mercury in 1911 by Onnes. Proving to be a theoretical enigma, the first complete microscopic theory was proposed some 50 years later by Bardeen, Cooper, and Schrieffer (BCS) in 1957. Their insight was that at low temperatures there exists an attractive pairwise interaction between electrons of opposite spins around the Fermi surface. These 'paired' electrons are known as Cooper pairs. Although the physical mechanism of this pairing is induced by the exchange of phonons in the lattice[1] for a simple model of s-wave pairing a point-like interaction of the form

$$U(x, x') = -g\delta(x - x') \quad , \tag{3.1}$$

where $g > 0$, is sufficient [19]. Although one can implement a realistic phonon model where the interaction is induced via electron coupling to a phonon bath as per [20], the simple BCS point interaction of Eq. (3.1) captures the relevant physics as we shall see. See Fig. 3.1 for an illustration of the BCS interaction in the language of Feynman diagrams [2].

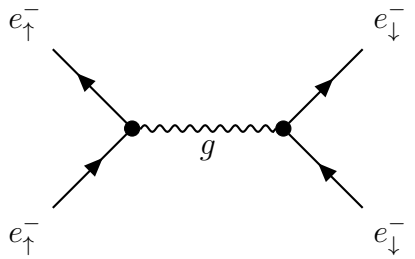

Figure 3.1: Feynman diagram for the BCS interaction wherein two electrons of opposite spin are scattered by some attractive potential g.

From Fig. 3.1, we can read off the spin explicit form of the interaction which we write as

$$H_{\text{BCS}} = -g \int \mathrm{d}x \left(\psi^*_\downarrow(x)\psi^*_\uparrow(x)\psi_\uparrow(x)\psi_\downarrow(x) + \psi^*_\uparrow(x)\psi^*_\downarrow(x)\psi_\downarrow(x)\psi_\uparrow(x) \right) \quad . \tag{3.2}$$

[1] Heuristically, the time for an electron to traverse an ion in the lattice is $\sim \hbar E_F^{-1}$. This slightly distorts the lattice which takes $\sim \omega_D^{-1}$ (ω_D being the Debye frequency) to relax to its equilibrium position. As $\omega_D^{-1} \gg \hbar E_F^{-1}$ then the displaced ion can induce another electron to traverse the ion before itself relaxes - hence the apparent attractive interaction. [10]

[2] Note we have illustrated the point-like interaction via a wavy line. This is as we are working in a many-body system and hence assume there are a number of distinct particles present. As a result the wavy interaction indicates that the attraction can be between two different particles.

This expression can be somewhat cumbersome, hence by introducing the transpose spinor as

$$\psi^*(x) = \begin{pmatrix} \psi^*_\uparrow(x) \\ \psi^*_\downarrow(x) \end{pmatrix} \quad , \quad \psi^\top(x) = \begin{pmatrix} \psi_\uparrow(x) & \psi_\downarrow(x) \end{pmatrix} \quad , \tag{3.3}$$

we can write the BCS interaction term in the Hamiltonian as [21]

$$H_{\text{BCS}} = -\frac{g}{2} \int \mathrm{d}x \left[\psi^\top(x)\,(i\sigma_2)\,\psi(x)\right]^\dagger \left[\psi^\top(x)\,(i\sigma_2)\,\psi(x)\right] \quad . \tag{3.4}$$

We will work with either Eq. (3.4) or Eq. (3.2) depending on whichever is more convenient at the time.

3.1.2 Mean-field theory

Naïvely, with the BCS interaction of Eq. (3.4) one can treat it perturbatively using the techniques outlined in Section 2.2. However, in doing so one finds that the Cooper pairs attract each other with an interaction strength which quickly becomes unbounded; such that the act of perturbing the electronic Fermi sea under a BCS interaction breaks down (see Appendix A.3 for an account of this instability). We now look to reformulate our reference state – which was previously a sea of interacting electrons – to that of a sea of condensed Cooper pairs.

The condensing of electrons into Cooper pairs leads to products of operators of the form $\psi^*_\uparrow(x)\psi^*_\downarrow(x)$ acquiring a non-zero expectation value; the system is stable under the addition of a Cooper pair. To this end we perform a mean-field decoupling in the Cooper channel to write the BCS interaction as [10][3]

$$H_{\text{BCS}} = -\frac{1}{2} \int \mathrm{d}x \left(\Delta^*(x) \left[\psi^\top(x)\,(i\sigma_2)\,\psi(x)\right] + \left[\psi^\top(x)\,(i\sigma_2)\,\psi(x)\right]^\dagger \Delta(x) \right) \quad , \tag{3.5}$$

where

$$\Delta(x) \equiv g \left\langle \psi^\top(x)\,(i\sigma_2)\,\psi(x) \right\rangle = g \left\langle \psi_\uparrow \psi_\downarrow \right\rangle - g \left\langle \psi_\downarrow \psi_\uparrow \right\rangle \quad , \tag{3.6}$$

is known as the gap parameter. One can view Eq. (3.5) as saying that we can replace the quantum operators by a stable 'averaged' value plus small deviations around this stable average [10]. In Eq. (3.5) we have omitted a term of order $|\Delta|^2$; this term corresponds to the background energy of the mean-field Cooper pair field and can simply be absorbed into the chemical potential [19]. We briefly note that parametrising the gap parameter by its magnitude and phase by $\Delta(x) =$

[3] Mean-field theory is only valid when the quantum fluctuations around the mean-field are irrelevant. The free energy of a fluctuation is of magnitude $k_B T$ and must act over a volume ξ_0^3 where ξ_0 is the coherence length - thus $F_{\text{fluc}} \sim k_B T/\xi_0^3$. Hence at low temperatures, and for highly correlated quantum effects, the disorder induced by quantum fluctuations is negligible and a mean-field theory is valid.

$|\Delta| \exp[i\phi(x)]$, then we see that under a fluctuation of the magnitude of Δ:

$$\Delta(x) \to |\Delta + \delta(x)| e^{i\phi(x)} \quad , \tag{3.7}$$

that the omitted term will transform as

$$|\Delta(x)|^2 \to |\Delta|^2 + 2|\Delta||\delta(x)| + |\delta(x)|^2 \quad , \tag{3.8}$$

where the second term, assuming a non-negligible value for Δ, will contribute significantly to the Hamiltonian. As a result, we regard the magnitude of Δ as a massive mode – such that fluctuations are energetically costly. Regardless, by decoupling the interaction in this manner we see that it is now quadratic in the field variables. For example, expanding out the spin structure of the first term of the right hand side of Eq. (3.5), we have terms of the form

$$H_{\text{BCS}} \sim \int \mathrm{d}x \, \Delta^*(x) \psi_\uparrow(x) \psi_\downarrow(x) \quad . \tag{3.9}$$

Although $\Delta(x)$ is merely a number corresponding to some expectation value, if we view it as the mean-field configuration of some bosonic field $\langle \Delta(x) \rangle$, then we can consider Eq. (3.9) to be the interaction vertex of two electrons annihilating to produce a Cooper pair – as shown in Fig. 3.2a. However, this process is exactly equivalent to a single-particle scattering process where an electron scatters with a Cooper pair into an outgoing hole [20] as depicted in Fig. 3.2b.[4]

(a) Scattering of two electrons into a Cooper pair.

(b) Scattering of an electron into a hole via production of a Cooper pair.

Figure 3.2: Equivalent Feynman diagrams corresponding to Eq. (3.11).

This equivalence in pictures is so important that we introduce the 4-component Nambu spinors

$$\Psi(x) = \begin{pmatrix} \psi(x) \\ \psi^*(x) \end{pmatrix} \quad , \quad \Psi^\dagger(x) = \begin{pmatrix} \psi^\dagger(x) & \psi^\top(x) \end{pmatrix} \quad , \tag{3.10}$$

[4] We have denoted the hole by an outgoing dashed line but it could also be drawn with an incoming full line - exactly the same as for the electron. This is as a hole moving backwards in spacetime is equivalent to an electron moving forwards (equivalent to how anti-particles are drawn in Feynman diagrams).

where the first component denotes the 'electron' sector whilst the second component denotes the 'hole' sector. This allows us to place electrons and holes on the same footing such that we can view $\Delta_0(x)$ as a scattering potential which couples the two components of the Nambu spinor – allowing us to rewrite Eq. (3.5) as

$$H_{\text{BCS}} = \int \mathrm{d}x\, \Psi^{\top}(x) \begin{pmatrix} 0 & \Delta(i\sigma_y) \\ \Delta^*(i\sigma_y)^{\dagger} & 0 \end{pmatrix} \Psi^*(x) \quad . \tag{3.11}$$

3.1.3 Excitation spectrum for bulk superconductors

To better understand the behaviour of the mean-field BCS interaction of Eq. (3.11), it is worthwhile to compute the low-energy excitation spectrum for a bulk superconductor; it is precisely these excitations that will determine the low-energy behaviour of the superconductor.

Ignoring spin-dependent interactions, by combining the BCS interaction with the generic many-body Hamiltonian of Eq. (2.27), we can write the full interacting Hamiltonian for a superconductor in momentum space as [10]

$$H = \sum_{\mathbf{k}} \xi_{\mathbf{k}} \psi^{\dagger}_{\mathbf{k}\uparrow} \psi_{\mathbf{k}\uparrow} + \xi_{\mathbf{k}} \psi^{\dagger}_{\mathbf{k}\downarrow} \psi_{\mathbf{k}\downarrow} - \Delta_0^* \psi_{-\mathbf{k}\downarrow} \psi_{\mathbf{k}\uparrow} - \Delta_0 \psi^{\dagger}_{\mathbf{k}\uparrow} \psi^{\dagger}_{-\mathbf{k}\downarrow} \quad , \tag{3.12}$$

where $\xi_{\mathbf{k}} \equiv \mathbf{k}^2/2m_e - \mu$. As in Section 3.1.2, we look to introduce particle-hole spinors to write the Hamiltonian in a bilinear form. To this end, we introduce the two-component[5] Nambu spinors in momentum space as

$$\Psi_{\mathbf{k}} = \begin{pmatrix} \psi_{\mathbf{k}\uparrow} \\ \psi^*_{-\mathbf{k}\downarrow} \end{pmatrix} \quad , \quad \Psi^{\dagger}(x) = \begin{pmatrix} \psi^*_{\mathbf{k}\uparrow} & \psi_{-\mathbf{k}\downarrow} \end{pmatrix} \quad , \tag{3.13}$$

such that we can write the Hamiltonian of Eq. (3.12) as

$$H = \sum_{\mathbf{k}} \Psi^{\dagger}_{\mathbf{k}} \begin{pmatrix} \xi_{\mathbf{k}} & -\Delta \\ -\Delta^* & -\xi_{\mathbf{k}} \end{pmatrix} \Psi_{\mathbf{k}} \quad . \tag{3.14}$$

The off-diagonal Δ terms couple the electron and hole fields, hence we now look to rotate our fields in the particle-hole space to diagonalise the single-particle Hamiltonian of Eq. (3.14). We introduce the operator γ which annihilates a linear superposition of electrons and holes by

$$\gamma_{\mathbf{k}} \equiv \begin{pmatrix} \gamma_{\mathbf{k}\uparrow} \\ \gamma^*_{-\mathbf{k}\downarrow} \end{pmatrix} = \begin{pmatrix} \cos\theta_{\mathbf{k}} & \sin\theta_{\mathbf{k}} \\ \sin\theta_{\mathbf{k}} & -\cos\theta_{\mathbf{k}} \end{pmatrix} \begin{pmatrix} \psi_{\mathbf{k}\uparrow} \\ \psi^*_{-\mathbf{k}\downarrow} \end{pmatrix} \quad . \tag{3.15}$$

[5]Here we are only considering two-component particle-hole spinors as we are currently neglecting the extra spin degree of freedom; with no applied magnetic fields the spin structure is trivial. This is in contrast to Section 3.1.2 where we were still considering a system with a non-trivial spin structure.

Now letting

$$\cos(2\theta_{\mathbf{k}}) = \frac{\xi_{\mathbf{k}}}{\sqrt{\Delta^2 + \xi_{\mathbf{k}}^2}} \quad , \quad \sin(2\theta_{\mathbf{k}}) = \frac{-\Delta}{\sqrt{\Delta^2 + \xi_{\mathbf{k}}^2}} \quad , \tag{3.16}$$

the Hamiltonian takes the diagonal form

$$H = \sum_{\mathbf{k}} \sqrt{\Delta^2 + \xi_{\mathbf{k}}^2} \gamma_{\mathbf{k}}^{\dagger} \tau_z \gamma_{\mathbf{k}} \quad , \tag{3.17}$$

where the $\gamma_{\mathbf{k}}^{\dagger}$ and $\gamma_{\mathbf{k}}$ operators create and annihilate linear superpositions of both electrons and holes. These excitations are known as Bogoliubov quasi-particles and correspond to the formation, or breaking, of a Cooper pair within the superconductor [10,22]. Due to the presence of the third Pauli matrix τ_z, the quasi-particle spectrum has negative and positive branches given by $\epsilon_{\mathbf{k}}^{\pm} = \pm\sqrt{\Delta^2 + \xi_{\mathbf{k}}^2}$. We illustrate these in Fig. 3.3. Critically the positive energy branch of the spectrum corresponds to the low energy excitations of a superconductor [22].

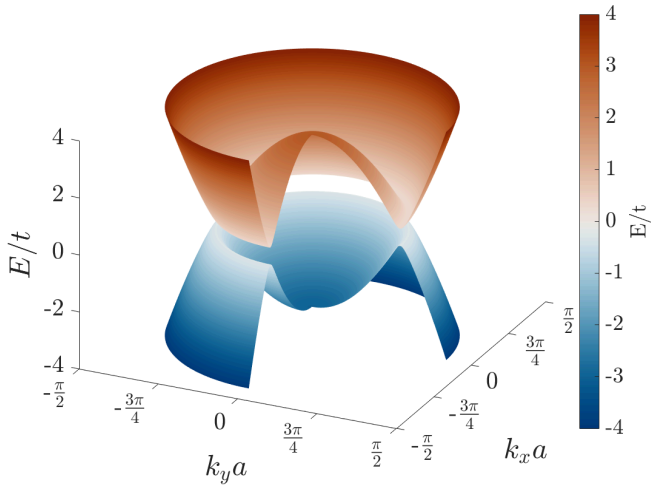

Figure 3.3: Dispersion relation for the Bogoliubov quasi-particles from a bulk 2D superconductor. The energies are normalised to some energy scale t, whilst the wavenumbers are multiplied by some lattice spacing a.

The most immediate observations is the gapped nature of the excitations, as to create an excitation one must break a Cooper pair which has a corresponding energy cost of Δ. The second is that near the Fermi wavenumber $\mathbf{k}_F$ – the point in the dispersion relation which minimises the excitation energy – the spectrum becomes nearly linear. Denoting the velocity of excitations at the Fermi wavenumber by v_F, the linearised spectrum $\epsilon_{\mathbf{k}} \sim v_F|\mathbf{k}_F - \mathbf{k}|$ has two branches: electron-like excitations with group velocity $v_{\mathbf{k}}^{+} = v_F\hat{\mathbf{k}}$ and hole-like excitations with velocity $v_{\mathbf{k}}^{-} = -v_F\hat{\mathbf{k}}$ [22]. This is clarified in Fig. 3.4 where the excitation spectrum for a one-dimensional superconductor has been overlaid over a that of a non-superconducting

one-dimensional material. Around the Fermi momentum the two branches are clear – one with $\partial_{\mathbf{k}}\epsilon_k > 0$ and the other with $\partial_{\mathbf{k}}\epsilon_k < 0$.

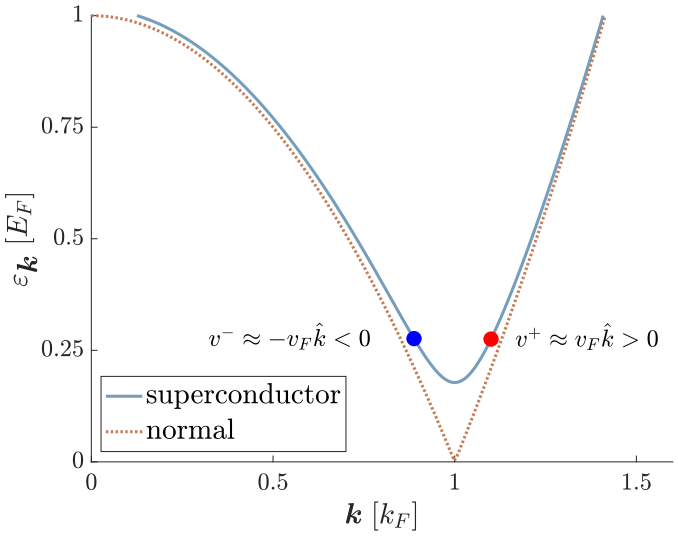

Figure 3.4: Excitation spectrum for a 1D superconductor overlaid over the dispersion relation for a normal material. Around the Fermi momentum the two branches have been distinguished by the direction of their velocity; one being electron-like with $v_{\mathbf{k}} > 0$, and the other hole-like with $v_{\mathbf{k}} < 0$.

3.2 Nambu-Gorkov equation

To evaluate electron transport, we must first identify the Hamiltonian of the system, then by making use of Hamilton's equation in Eq. (2.28) we can find the dynamics of the operator in question. As detailed in the previous chapter, a key quantity of interest for transport problems is that of the Green's function. However, we saw in the previous section that to incorporate superconductivity into the Hamiltonian we had to double the available degrees of freedom by expanding the electronic basis to include both electrons and holes. We now derive the equation of motion for Green's functions in this enlarged basis including the effects of superconductivity.

In the enlarged Nambu×spin basis, the Green's functions can be written as

$$\mathcal{G}(x,x') = \begin{pmatrix} G(x,x') & F(x,x') \\ \overline{F}(x,x') & \overline{G}(x,x') \end{pmatrix} = \frac{1}{i\hbar}\left\langle T\left\{\Psi(x) \otimes_{\text{Nambu}} \Psi^\dagger(x')\right\}\right\rangle \quad , \tag{3.18}$$

where

$$G(x,x') = \frac{1}{i\hbar}\left\langle T\left\{\psi(x)\otimes\psi^\dagger(x')\right\}\right\rangle \qquad F(x,x') = \frac{1}{i\hbar}\left\langle T\left\{\psi(x)\otimes\psi^\top(x')\right\}\right\rangle \tag{3.19}$$
$$\overline{F}(x,x') = \frac{1}{i\hbar}\left\langle T\left\{\psi^*(x)\otimes\psi^\dagger(x')\right\}\right\rangle \qquad \overline{G}(x,x') = \frac{1}{i\hbar}\left\langle T\left\{\psi^*(x)\otimes\psi^\top(x')\right\}\right\rangle \quad .$$

Respectively, each term describes: the Green's functions for electrons scattering to electrons (G), electrons scattering to holes (F), holes scattering to electrons ($\overline{F}$), and finally holes scattering into holes ($\overline{G}$). We now look to compute the equation of motion for this propagator – the Nambu-Gorkov equation.

3.2.1 Equation of motion for $\mathcal{G}$

To find an equation of motion for $\mathcal{G}$, we must first find equations of motion for the constituent spinors ψ. To this end we write out the fully spin resolved BCS Hamiltonian as

$$H = \int \mathrm{d}x' \, \psi^\dagger(x') H_{\mathrm{sp}}(x') \psi^\top(x') - \Delta^*(x') \psi_\uparrow(x') \psi_\downarrow(x') - \psi^*_\uparrow(x') \psi^*_\downarrow(x') \Delta(x') \quad , \tag{3.20}$$

where H_{sp} denotes the components of the single particle Hamiltonian described in Eq. (2.24). Using Heisenberg's equation of motion and Appendix A.4 we have that

$$\begin{aligned} \frac{\partial \psi(x)}{\partial t} &= \frac{i}{\hbar} e^{-\frac{i}{\hbar}Ht} [H, \psi(\mathbf{x})] e^{\frac{i}{\hbar}Ht} \\ &= \frac{i}{\hbar} e^{-\frac{i}{\hbar}Ht} \Big\{ -H_{\mathrm{sp}}(\mathbf{x}) \psi(\mathbf{x}) - (i\sigma_y)^\dagger \psi^\dagger(\mathbf{x}) \Delta_0(\mathbf{x}) \Big\} e^{\frac{i}{\hbar}Ht} \quad . \end{aligned} \tag{3.21}$$

As H commutes with H_{sp} at all but a finite number of times, and inserting $e^{-\frac{i}{\hbar}Ht} e^{\frac{i}{\hbar}Ht}$ between products of operators we find that

$$i\hbar \frac{\partial \psi(x)}{\partial t} = H_{\mathrm{sp}}(x) \psi(x) + \Delta_0(x) (i\sigma_y)^\dagger \psi^*(x) \quad . \tag{3.22}$$

A similar computation[6] gives

$$-i\hbar \frac{\partial \psi^*(x)}{\partial t} = H^*_{\mathrm{sp}}(x) \psi^*(x) - \Delta^*_0(x) (i\sigma_y) \psi(x) \quad . \tag{3.23}$$

Returning to Eq. (3.18), we now compute the various matrix elements of $\mathcal{G}(x, x')$. As an example, we focus on the element

$$\mathcal{G}_{1,1}(x, x') \equiv G(x, x') = \frac{1}{i\hbar} \left\langle T\big\{ \psi(x) \otimes \psi^\dagger(x') \big\} \right\rangle \quad . \tag{3.24}$$

Expanding out the time ordering as per Eq. (2.34), we have

$$\mathcal{G}_{1,1}(x, x') = \frac{1}{i\hbar} \big[\theta(t - t') \left\langle \psi(x) \otimes \psi^\dagger(x') \right\rangle - \theta(t' - t) \left\langle \psi^\dagger(x') \otimes \psi(x) \right\rangle \big] \quad . \tag{3.25}$$

[6]The H^*_{sp} appears as for this equation of motion it is convenient to integrate the non-interacting part of the BCS Hamiltonian by parts beforehand which introduces a hermitian conjugate.

Before we take the derivative of this expression with respect to time, we note that in the the Heisenberg picture, which Eq. (3.25) is currently expressed in, that $\partial_t \rho(t_r) = 0$ [17]. Hence

$$\partial_t\big(\mathrm{Tr}\big[\rho(t_r)\partial_t\big(T\big\{\psi(x)\otimes\psi^\dagger(x')\big\}\big)\big]\big) = \big\langle\partial_t\big(T\big\{\psi(x)\otimes\psi^\dagger(x')\big\}\big)\big\rangle \quad , \tag{3.26}$$

such that we can simply move the temporal derivative into the expectation value. As a result, taking the time derivative of Eq. (3.25) results in[7]

$$\begin{aligned} i\hbar\partial_t G(x,x') &= \partial_t\big(\theta(t-t')\left\langle\psi(x)\otimes\psi^\dagger(x')\right\rangle - \theta(t'-t)\left\langle\psi^\dagger(x')\otimes\psi(x)\right\rangle\big) &(3.27)\\ &= \delta(t-t')\big\{\psi(x)\overset{\otimes}{,}\psi^\dagger(x')\big\} + \big\langle T\big\{\partial_t\psi(x)\otimes\psi^\dagger(x')\big\}\big\rangle \quad . &(3.28)\end{aligned}$$

Substituting in the equation of motion for the electron spinor in Eq. (3.22), we have that

$$\begin{aligned} i\hbar\partial_t G(x,x') = \delta(x-x') &+ \frac{H_{\mathrm{sp}}}{i\hbar}\left\langle T\big\{\psi(x)\otimes\psi^\dagger(x')\big\}\right\rangle \\ &+ \frac{\Delta(x)(i\sigma_y)^\dagger}{i\hbar}\left\langle T\big\{\psi^*(x)\otimes\psi^\dagger(x')\big\}\right\rangle \quad . \end{aligned} \tag{3.29}$$

Letting Δ absorb the spin-structure and recognising the final term of Eq. (3.29) as $\mathcal{G}_{2,1}(x,x')$, we can write

$$(i\hbar\partial_t - H_{\mathrm{sp}}(x))G(x,x') - \Delta(x)\overline{F}(x,x') = \delta(x-x') \quad . \tag{3.30}$$

This can be repeated for each of the other components of $\mathcal{G}(x,x')$, which can be written as the following matrix equation

$$\begin{pmatrix} i\hbar\partial_t - H_{\mathrm{sp}}(x) & -\Delta(x) \\ -\Delta^\dagger(x) & i\hbar\partial_t + H^*_{\mathrm{sp}}(x)\end{pmatrix}\begin{pmatrix} G(x,x') & F(x,x') \\ \overline{F}(x,x') & \overline{G}(x,x')\end{pmatrix} = \delta(x-x') \quad . \tag{3.31}$$

This equation of motion defines the Nambu-Gorkov equation; the solutions of which provides the full Green's function for the equilibrium system.

3.2.2 Steady-state Nambu-Gorkov equation

The Nambu-Gorkov equation given in Eq. (3.31) is a function of two positions and two times as it relates how electrons and holes are correlated at two different points in spacetime. This is necessary for time-dependent systems, where each point in time is distinguishable from another. In this work we are interested in steady-state systems where there is no time-dependence; the critical parameter is the *difference* between the two times t and t', rather than their explicit values. As a result we can simplify the Nambu-Gorkov equation by Fourier transforming with respect to $\Delta t \equiv t' - t$.

[7] Note that in Eq. (3.27) we have made use of the spinorial anti-commutating relations defined in Eq. (2.22).

Doing so results in the following equation

$$\begin{pmatrix} E - H_{\text{sp}}(\mathbf{x}) & -\Delta(\mathbf{x}) \\ -\Delta^{\dagger}(\mathbf{x}) & E + H^{*}_{\text{sp}}(\mathbf{x}) \end{pmatrix} \begin{pmatrix} G(E,\mathbf{x},\mathbf{x}') & F(E,\mathbf{x},\mathbf{x}') \\ \overline{F}(E,\mathbf{x},\mathbf{x}') & \overline{G}(E,\mathbf{x},\mathbf{x}') \end{pmatrix} = \delta(\mathbf{x}-\mathbf{x}') \quad . \tag{3.32}$$

Physically the solutions of this equation relate how electrons and holes of some energy E are correlated at two different points in space.

3.3 Dynamics within a Josephson junction

By considering only bulk superconductors and equilibrium systems we have kept the discussion in this chapter to a relatively high level. However, in this thesis we are interested in the dynamics of a particular system – namely, Josephson junctions. As a result, it is appropriate to explore how one applies the general techniques of the proceeding two chapters to the specific case of Josephson junctions.

3.3.1 Hamiltonian for a Josephson junction

To numerically compute the dynamics of a Josephson junction we must first identify the corresponding Hamiltonian. As the leads of the device are assumed to be semi-infinite, we begin by partitioning the system into three distinct regions: left lead, central region, and right lead. As a result, we can partition the full Hamiltonian H as

$$H = H_L + H_{LC} + H_C + H_{CR} + H_R \quad , \tag{3.33}$$

where H_L, H_C, and H_R describe the dynamics of the the isolated left, centre, and right regions respectively and $H_{LC/CR}$ contains the information on the the coupling between regions. This is illustrated graphically for a discrete system in Fig. 3.5.

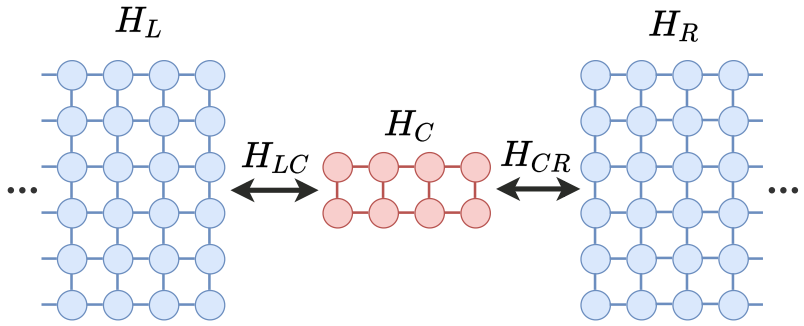

Figure 3.5: Standard partitioning of the Josephson junction to decouple the superconducting leads with the nanowire.

From Eq. (2.27) we can write the Hamiltonian for the central region – which we currently assume to be non-superconducting – as

$$H_C = \sum_{\mathbf{i}} \psi^{\dagger}_{\mathbf{i}}(t') \left[-\frac{\hbar^2}{2m_e}\mathbf{D}^2 - e\Phi + g\mu_B \mathbf{B}\cdot\boldsymbol{\sigma} - \mu \right] \psi_{\mathbf{i}}(t') \quad , \tag{3.34}$$

where $\sum_{\mathbf{i}}$ denotes that we are summing over every lattice site in the central region. Similarly, using Eq. (3.20) can write the Hamiltonians for the superconducting leads as

$$\begin{aligned} H_{L/R} = \sum_{\boldsymbol{\alpha/\beta}} \psi^{\dagger}_{\boldsymbol{\alpha/\beta}}(t') \left[-\frac{\hbar^2}{2m_e}\mathbf{D}^2 - e\Phi + g\mathbf{B}\cdot\boldsymbol{\sigma} - \mu \right] \psi_{\boldsymbol{\alpha/\beta}}(t') \\ + \psi^{\dagger}_{\boldsymbol{\alpha/\beta}}(t')\Delta_{\boldsymbol{\alpha/\beta}}\psi^{*}_{\boldsymbol{\alpha/\beta}}(t') + \psi^{\top}_{\boldsymbol{\alpha/\beta}}(t')\Delta^{\dagger}_{\boldsymbol{\alpha/\beta}}\psi_{\boldsymbol{\alpha/\beta}}(t') \quad , \end{aligned} \tag{3.35}$$

where $\boldsymbol{\alpha} \in L$, $\boldsymbol{\beta} \in R$ denotes every lattice site in the left and right leads respectively. To couple the regions of the Hamiltonian we introduce a parameter $V_{\boldsymbol{\alpha/\beta},\mathbf{i}}$ which parametrises the interaction between the sites in the left/right leads with those of the central region. Note that usage of Latin indices to denote lattice sites in the central region and Greek for site in the leads will be a convention used throughout this work. As a result, we can write the coupling terms as

$$H_{LC/CR} = \sum_{\boldsymbol{\alpha/i/\beta}} \psi^{\dagger}_{\boldsymbol{\alpha/\beta}}(t')V_{\boldsymbol{\alpha/\beta},\mathbf{i}}\psi_{\mathbf{i}}(t') + \psi^{\dagger}_{\mathbf{i}}(t')V_{\mathbf{i},\boldsymbol{\alpha/\beta}}\psi_{\boldsymbol{\alpha/\beta}}(t') \quad . \tag{3.36}$$

To extend this coupling Hamiltonian into the particle-hole space we introduce the generalised coupling strength $\mathcal{V}_{\boldsymbol{\lambda},\mathbf{i}} = \mathrm{diag}\big(V_{\boldsymbol{\lambda},\mathbf{i}}\ ,\ -V^{*}_{\boldsymbol{\lambda},\mathbf{i}}\big)$. Now in the usual Nambu basis Eq. (3.10), the coupling terms are expressed as

$$H_{LC/CR} = \sum_{\boldsymbol{\alpha/i/\beta}} \Psi^{\dagger}_{\boldsymbol{\alpha/\beta}}(t')\mathcal{V}_{\boldsymbol{\alpha/\beta},\mathbf{i}}\Psi_{\mathbf{i}}(t') + \Psi^{\dagger}_{\mathbf{i}}(t')\mathcal{V}_{\mathbf{i},\boldsymbol{\alpha/\beta}}\Psi_{\boldsymbol{\alpha/\beta}}(t') \quad . \tag{3.37}$$

3.3.2 Green's function for Josephson junctions

To determine the dynamics of the system, we first partition the Hamiltonian into a free term H_0 and a perturbation H'

$$H = H_0 + H' \quad , \tag{3.38}$$

where $H_0 = H_L + H_C + H_R$ and $H' = H_{RC} + H_{CL}$. Namely, we have decoupled the three regions from each other and assumed each is independently at equilibrium. With the free and perturbing Hamiltonian, we can now express all operators in the interaction picture as in Section 2.2.4. Furthermore, to handle systems out of equilibrium we must let the times lie on a generalised Schwinger-Keldysh contour, $\mathcal{C}$, illustrated again in Fig. 3.6.

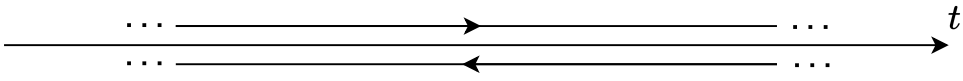

Figure 3.6: Schwinger-Keldysh contour.

To begin we will consider the Nambu-Gorkov Green's function in the interaction picture between a point $\boldsymbol{\lambda}$ in the left lead and a point $\mathbf{i}$ in the central region:

$$\mathcal{G}(\mathbf{i},\tau_1;\boldsymbol{\lambda},\tau_2) \equiv \frac{1}{i\hbar}\left\langle T_{\mathcal{C}}\Big\{\mathcal{S}_{\mathcal{C}}\Psi_{\mathbf{i}}(\tau_1)\otimes\Psi^{\dagger}_{\boldsymbol{\lambda}}(\tau_2)\Big\}\right\rangle \quad , \tag{3.39}$$

where τ_1 and τ_2 are contour times lying on the Schwinger Keldysh contour, $T_{\mathcal{C}}$ is the contour ordering operator, and

$$\mathcal{S}_{\mathcal{C}} = \exp\left\{\frac{1}{i\hbar}\int_{\mathcal{C}} \mathrm{d}\tau\, H_{LC}(\tau) + H_{CR}(\tau)\right\} \quad , \tag{3.40}$$

is the usual time evolution operator. For notational simplicity, we have omitted the subscript I on operators to denote that the time dependence is governed by the free Hamiltonian. A benefit of treating the leads as perturbations is that now the free Green's functions $\mathcal{G}^0$ – Green's functions with no $\mathcal{S}_{\mathcal{C}}$ matrix present – between sites in different regions are identically zero: for $\boldsymbol{\alpha}\in L$, $\boldsymbol{\beta}\in R$, and $\mathbf{i}\in C$ we have that

$$\begin{aligned}\mathcal{G}^0(\boldsymbol{\alpha},\tau_1;\mathbf{i},\tau_2) &\equiv \left\langle T_{\mathcal{C}}\Big\{\Psi_{\boldsymbol{\alpha}}(\tau_1)\otimes\Psi^{\dagger}_{\mathbf{i}}(\tau_2)\Big\}\right\rangle = 0\\ \mathcal{G}^0(\boldsymbol{\alpha},\tau_1;\boldsymbol{\beta},\tau_2) &\equiv \left\langle T_{\mathcal{C}}\Big\{\Psi_{\boldsymbol{\alpha}}(\tau_1)\otimes\Psi^{\dagger}_{\boldsymbol{\beta}}(\tau_2)\Big\}\right\rangle = 0 \quad .\end{aligned} \tag{3.41}$$

This is merely the statement that in the absence of coupling between regions an electron cannot propagate from say the left lead to the central region. As we have an explicit form for the coupling Hamiltonian in Eq. (3.37), we can asymptotically expand $\mathcal{S}_{\mathcal{C}}$ such that we can write Eq. (3.39) as

$$\begin{aligned}\mathcal{G}(\mathbf{i},\tau_1;\boldsymbol{\lambda},\tau_2) = \frac{1}{i\hbar}\Bigg\langle T_{\mathcal{C}}\Bigg\{\Psi_{\mathbf{i}}(\tau_1)\otimes\sum_{n=0}^{\infty}\frac{1}{(i\hbar)^{n+1}(n+1)!}\Bigg[\int_{\mathcal{C}}\mathrm{d}\tau\sum_{\boldsymbol{\alpha}/\mathbf{j}/\boldsymbol{\beta}}\Psi^{\dagger}_{\boldsymbol{\alpha}/\boldsymbol{\beta}}(\tau)\mathcal{V}^{\dagger}_{\mathbf{j},\boldsymbol{\alpha}/\boldsymbol{\beta}}\Psi_{\mathbf{j}}(\tau)\\ + \Psi^{\dagger}_{\mathbf{j}}(\tau)\mathcal{V}_{\mathbf{j},\boldsymbol{\alpha}/\boldsymbol{\beta}}\Psi_{\boldsymbol{\alpha}/\boldsymbol{\beta}}(\tau)\Bigg]^{n+1}\otimes\Psi^{\dagger}_{\boldsymbol{\lambda}}(\tau_2)\Bigg\}\Bigg\rangle \quad ,\end{aligned} \tag{3.42}$$

where as usual $\boldsymbol{\alpha}/\boldsymbol{\beta}\in L/R$. Note in Eq. (3.42) we have ignored the first term in the expansion as it is equivalent to the free propagator between a lattice site in the left lead and one in the device which from Eq. (3.41) is identically zero. We now need to utilise Wick's theorem of Section 2.2.5 to generate every permutation of free Green's functions. However, before we do so, we note that the left lead creation operator $\Psi^{\dagger}_{\boldsymbol{\lambda}}(\tau_2)$ at the very end of the expression *must* be contracted with one of the $\Psi_{\boldsymbol{\alpha}}(\tau)$ operators in the expanded interaction as *all other Wick contractions are identically zero* as per Eq. (3.41). As there are $n+1$ possible $\Psi_{\boldsymbol{\alpha}}(\tau)$ terms that can be contracted with, we can pull out that contraction alongside a factor of $n+1$ to

write

$$\mathcal{G}(\mathbf{i},\tau_1;\boldsymbol{\lambda},\tau_2) = \int_{\mathcal{C}} \mathrm{d}\tau \sum_{\boldsymbol{\alpha}/\mathbf{j}} \frac{1}{i\hbar} \Bigg\langle T_{\mathcal{C}} \Bigg\{ \Psi_{\mathbf{i}}(\tau_1) \otimes \underbrace{\sum_{n=0}^{\infty} \frac{1}{(i\hbar)^n n!} \Bigg[\int_{\mathcal{C}} \mathrm{d}\tau' \sum_{\boldsymbol{\alpha}'/\mathbf{j}'/\boldsymbol{\beta}} \Psi^{\dagger}_{\boldsymbol{\alpha}'/\boldsymbol{\beta}}(\tau') \mathcal{V}^{\dagger}_{\mathbf{j}',\boldsymbol{\alpha}'/\boldsymbol{\beta}} \Psi_{\mathbf{j}'}(\tau') + \Psi^{\dagger}_{\mathbf{j}'}(\tau') \mathcal{V}_{\mathbf{j}',\boldsymbol{\alpha}'/\boldsymbol{\beta}} \Psi_{\boldsymbol{\alpha}'/\boldsymbol{\beta}}(\tau') \Bigg]^n}_{\mathcal{S}_{\mathcal{C}}} \otimes \Psi^{\dagger}_{\mathbf{j}}(\tau) \Bigg\} \Bigg\rangle \mathcal{V}_{\mathbf{j},\boldsymbol{\alpha}} \frac{1}{i\hbar} \Big\langle T_{\mathcal{C}} \Big\{ \Psi_{\boldsymbol{\alpha}}(\tau) \otimes \Psi^{\dagger}_{\boldsymbol{\lambda}}(\tau_2) \Big\} \Big\rangle \quad . \tag{3.43}$$

By pulling out this factor, we see that we have recovered exactly the expanded $\mathcal{S}_{\mathcal{C}}$ which we can regroup to write

$$\begin{aligned} \mathcal{G}(\mathbf{i},\tau_1;\boldsymbol{\lambda},\tau_2) &= \int_{\mathcal{C}} \mathrm{d}\tau \sum_{\boldsymbol{\alpha}/\mathbf{j}} \frac{1}{i\hbar} \Bigg\langle T_{\mathcal{C}} \Bigg\{ \mathcal{S}_{\mathcal{C}} \Psi_{\mathbf{i}}(\tau_1) \otimes \Psi^{\dagger}_{\mathbf{j}}(\tau) \Bigg\} \Bigg\rangle \mathcal{V}_{\mathbf{j},\boldsymbol{\alpha}} \frac{1}{i\hbar} \Big\langle T_{\mathcal{C}} \Big\{ \Psi_{\boldsymbol{\alpha}}(\tau) \otimes \Psi^{\dagger}_{\boldsymbol{\lambda}}(\tau_2) \Big\} \Big\rangle \quad , \\ &= \int_{\mathcal{C}} \mathrm{d}\tau \sum_{\boldsymbol{\alpha}/\mathbf{j}} \mathcal{G}(\mathbf{i},\tau_1;\boldsymbol{\lambda},\tau) \mathcal{V}_{\mathbf{j},\boldsymbol{\alpha}} \mathcal{G}^0(\boldsymbol{\alpha},\tau;\boldsymbol{\lambda},\tau_2) \quad . \end{aligned} \tag{3.44}$$

Letting $\mathcal{G}(\mathbf{x},\tau_1;\boldsymbol{y},\tau_2)$ denote the (x,y) element of some matrix $\mathcal{G}_{X,Y}$ where $\mathbf{x}$ is a lattice site in X and $\mathbf{y}$ is a lattice site in Y, we can rewrite Eq. (3.44) in matrix form as

$$\mathcal{G}_{C,L}(\tau_1,\tau_2) = \int_{\mathcal{C}} \mathrm{d}\tau\, \mathcal{G}_{C,C}(\tau_1,\tau) \mathcal{V}_{C,L} \mathcal{G}^0_{L,L}(\tau,\tau_2) \quad . \tag{3.45}$$

As the free Green function $\mathcal{G}^0_{L,L}$ is defined over the disconnected left lead – which was assumed to be in equilibrium – we can compute this quantity using the standard Nambu-Gorkov equation. We are now left with the need to find an expression of the perturbed centre Green function $\mathcal{G}_{C,C}$.

As in Eq. (3.39), the matrix elements of the Green function for two lattice sites in the central region is given by

$$\mathcal{G}(\mathbf{i},\tau_1;\mathbf{j},\tau_2) = \frac{1}{i\hbar} \Big\langle T_{\mathcal{C}} \Big\{ \mathcal{S}_{\mathcal{C}} \Psi_{\mathbf{i}}(\tau_1) \otimes \Psi^{\dagger}_{\mathbf{j}}(\tau_2) \Big\} \Big\rangle \quad , \tag{3.46}$$

Exactly as before, by expanding out the $\mathcal{S}_{\mathcal{C}}$ matrix and ignoring all terms in the Wick series which are identically zero, we find that

$$\mathcal{G}(\mathbf{i},\tau_1;\mathbf{j},\tau_2) = \mathcal{G}^0(\mathbf{i},\tau_1;\mathbf{j},\tau_2) + \sum_{\mathbf{mn}} \int_{\mathcal{C}} \mathrm{d}\tau\, \mathrm{d}\tau'\, \mathcal{G}^0(\mathbf{i},\tau_1;\mathbf{m},\tau) \Sigma(\mathbf{m},\tau;\mathbf{n},\tau') \mathcal{G}(\mathbf{n},\tau';\mathbf{j},\tau_2) \quad . \tag{3.47}$$

where we introduce the the self-energy Σ by

$$\begin{aligned}\Sigma(\mathbf{m},\tau;\mathbf{n},\tau') &\equiv \Sigma_{\text{left}}(\mathbf{m},\tau;\mathbf{n},\tau') + \Sigma_{\text{right}}(\mathbf{m},\tau;\mathbf{n},\tau') \quad , \\ &\equiv \sum_{\boldsymbol{\alpha}} \mathcal{V}^{\dagger}_{\boldsymbol{\alpha},\mathbf{m}} \mathcal{G}^{0}_{\boldsymbol{\alpha}}(\tau,\tau') \mathcal{V}_{\boldsymbol{\alpha},\mathbf{n}} + \sum_{\boldsymbol{\beta}} \mathcal{V}^{\dagger}_{\boldsymbol{\beta},\mathbf{m}} \mathcal{G}^{0}_{\boldsymbol{\beta}}(\tau,\tau') \mathcal{V}_{\boldsymbol{\beta},\mathbf{n}} \quad . \end{aligned} \tag{3.48}$$

Writing this in terms of matrices one has that

$$\mathcal{G}_{C,C}(\tau_1,\tau_2) = \mathcal{G}^{0}_{C,C}(\tau_1,\tau_2) + \int_{\mathcal{C}} \mathrm{d}\tau\, \mathrm{d}\tau'\, \mathcal{G}^{0}_{C,C}(\tau_1,\tau) \Sigma(\tau,\tau') \mathcal{G}_{C,C}(\tau',\tau_2) \quad . \tag{3.49}$$

Although these expressions are valid, they are currently written in terms of an abstract contour time, whereas we want to evaluate these Green functions at real times. Using the techniques of Section 2.2.6, we can write Eq. (3.45) and Eq. (3.49) as functions of real times using the analytical continuation procedure of Table 2.1. The net result is that

$$\begin{aligned}\mathcal{G}^{<}_{C,L}(t_1,t_2) &= \int \mathrm{d}t\, \mathcal{G}^{R}_{C,C}(t_1,t) \mathcal{V}_{C,L} \mathcal{G}^{0\,<}_{\ L,L}(t,t_2) + \mathcal{G}^{<}_{C,C}(t_1,t) \mathcal{V}_{C,L} \mathcal{G}^{0\,A}_{\ L,L}(t,t_2) \quad , \\ \mathcal{G}^{R}_{C,C}(t_1,t_2) &= \mathcal{G}^{0\,R}_{\ C,C}(t_1,t_2) + \int \mathrm{d}t\, \mathrm{d}t'\, \mathcal{G}^{0\,R}_{\ C,C}(t_1,t) \Sigma^{R}(t,t') \mathcal{G}^{R}_{C,C}(t',t_2) \quad . \end{aligned} \tag{3.50}$$

Furthermore, we assume that our system is in a stationary state such that no quantities depend on the absolute times, but rather the distance between times. As such we can Fourier transform Eq. (3.50) to compute all quantities in terms of energy E. As these expressions are convolutions in time, they lead to the following products in energy space

$$\begin{aligned}\mathcal{G}^{<}_{C,L}(E) &= \mathcal{G}^{R}_{C,C}(E) \mathcal{V}_{C,L} \mathcal{G}^{0\,<}_{\ L,L}(E) + \mathcal{G}^{<}_{C,C}(E) \mathcal{V}_{C,L} \mathcal{G}^{0\,A}_{\ L,L}(E) \quad , \\ \mathcal{G}^{R}_{C,C}(E) &= \mathcal{G}^{0\,R}_{\ C,C}(E) + \mathcal{G}^{0\,R}_{\ C,C}(E) \Sigma^{R}(E) \mathcal{G}^{R}_{C,C}(E) \quad , \\ &= \left(\mathcal{G}^{0\,R}_{\ C,C}(E)^{-1} - \Sigma^{R}(E) \right)^{-1} \quad , \\ \mathcal{G}^{<}_{C,C}(E) &= \mathcal{G}^{R}_{C,C}(E) \Sigma^{<}(E) \mathcal{G}^{A}_{C,C}(E) \quad , \end{aligned} \tag{3.51}$$

where the Fourier transformed self-energy looks like

$$\Sigma(E) = \mathcal{V}^{\dagger}_{L,C} \mathcal{G}^{0}_{L,L}(E) \mathcal{V}_{L,C} + \mathcal{V}^{\dagger}_{R,C} \mathcal{G}^{0}_{R,R}(E) \mathcal{V}_{R,C} \quad . \tag{3.52}$$

Hence we have now decomposed the problem into a set of coupled equations, where each equation only relies on the free Green's functions. Within each region we can compute the free Green's function using the steady-state Nambu-Gorkov equation of Eq. (3.32).

3.4 Observables of interest

As this thesis concerns the transport through Josephson junctions we must derive the equations to produce precisely the quantities of interest. Indeed the primary quantity of interest is the supercurrent through the device as a function of the phase difference. Similarly, as will be shown in Section 6.1.2, the current itself is carried by bound states located within the normal region, hence we also look to how one computes the spectrum of bound states within a device.

3.4.1 Density of states

As will be shown in Section 6.1.2, for energies below the superconducting gap Δ, the supercurrent through a Josephson junction is entirely carried by Andreev bound states (ABS) – counter-propagating electrons and holes – located within the normal region [23]. We now wish to derive an expression for these bound states as a function of the free Green's functions which are computable using the Nambu-Gorkov equation.

To begin, we recall from Section 2.2.3 that the diagonal elements of the spectral weight function correspond to the local density of states at each point in our system. As a result, we can express the total density of states as the sum over the local density of states:

$$D(E) = \mathrm{Tr}[A(x, x'; E)] \quad . \tag{3.53}$$

Working in particle-hole space, we can generalise the spectral function to be [13]

$$A(x, x') \equiv i\big(\mathcal{G}^R(x, x') - \mathcal{G}^A(x, x')\big) \quad , \tag{3.54}$$

such that Eq. (3.53) computes the density of states in Nambu space as well.

3.4.2 Supercurrent

The central object of interest in this work is the supercurrent through a Josephson junction. We must now derive the equation for the supercurrent as a function of the computable Green's functions.

In this work we are only interested in steady-state transport which simplifies the problem greatly as then no charge piles up in the central region [24, 25]. As a result we can symmetrise the total charge current through the device such that the charge from the left lead through the central region and into the right lead can be given by

$$I(t) = \frac{1}{2}(I_{LC}(t) - I_{RC}(t)) \quad , \tag{3.55}$$

where I_{LC} and I_{RC} are currents *from* the left and right leads *into* the central region respectively. Consider the current from the left lead to the central region, I_{LC}, which we define as the change in the average number of charges in the left lead multiplied

by the charge per electron [24]

$$I_{LC}(t) \equiv -e \left\langle \frac{\partial \hat{n}^{\text{left}}}{\partial t'}(t) \right\rangle \quad , \tag{3.56}$$

where the number operator $\hat{n}^{\text{left}}(t)$ determines the number of charges in the left lead at some time, which we define in particle-hole space as [13]

$$\hat{n}^{\text{left}}(t) = \frac{1}{2} \sum_{\boldsymbol{\lambda} \in L} \tau_z \Psi^{\dagger}_{\boldsymbol{\lambda}}(t) \Psi_{\boldsymbol{\lambda}}(t) \quad , \tag{3.57}$$

where we included τ_z as the holes carry an opposite charge to the electrons. The factor of half is so not to double count the hole contribution; we arbitrarily doubled our degrees of freedom to include holes. We leave the explicit computation of Eq. (3.56), and in turn Eq. (3.55), to Appendix A.6. However, the final result is that the current through the junction can be given by

$$I = \frac{e}{2} \int \mathrm{d}E \, \mathrm{Re}\big\{ \mathrm{Tr}\big[\tau_z \mathcal{G}^{<}_{C,L}(E) \mathcal{V}_{L,C} - \tau_z \mathcal{G}^{<}_{C,R}(E) \mathcal{V}_{L,C} \big] \big\} \quad , \tag{3.58}$$

In this manner we have managed to express the steady-state current as a function of the full Green's functions.

Chapter 4

Lattice field theory

The problem of Bloch electrons in magnetic fields is a very peculiar problem, because it is one of the very few places in physics where the difference between rational numbers and irrational numbers makes itself felt... Now the crucial question is,"How physical is this spectrum?"

—D. Hofstadter, *Energy levels and wave functions of Bloch electrons in rational and irrational magnetic fields*

Chapter Summary

The previous chapters introduced a number of theoretical techniques for studying out-of-equilibrium superconducting systems. They culminated in the steady state Nambu-Gorkov equation of Eq. (3.32) whose solution provides the two point propagator, or Green's functions, of the system. However, for a generic single-particle Hamiltonian no analytic solution of the Nambu-Gorkov equation is possible [14]. Hence, before we can apply these techniques to problems, as an intermediate we must first discuss how these equations are solved numerically.

In this chapter we begin by introducing the tight-binding formalism which allows one to convert the Nambu-Gorkov equation into a matrix equation which can the be solved numerically. To verify our discretisation procedure we will produce the bandstructure of electrons in a two-dimensional lattice under an external magnetic field, this produces fractals known in the literature. Finally, we will include the effects of spin-orbit coupling to produce fractals not present in the literature.

4.1 Tight-binding formulation

In steady-state, the Nambu-Gorkov equation of Eq. (3.32) resolves to a matrix equation, however, as currently written the equation is a function of continuous variables and hence difficult to solve numerically. As a result we now look to discretising the system onto a lattice such that it can be solved numerically.

A generic Hamiltonian for a non-relativistic, and non-superconducting system has the form

$$H = \int \mathrm{d}\mathbf{x}\, \psi^\dagger(x) \left[-\frac{\hbar^2}{2m_e}\mathbf{D}^2 - e\Phi + g\mu_B \mathbf{B}\cdot\boldsymbol{\sigma} - \mu \right] \psi(x) \quad , \tag{4.1}$$

where $\mathbf{D}$ is the $SU(2) \times U(1)$ gauge covariant derivative given by

$$D_k = \frac{\partial}{\partial x^k} + i a_k(x) + i\rho_k(x) \quad , \tag{4.2}$$

and the individual gauge fields a_k and ρ_k depend on the system being modelled. To discretise Eq. (4.1), we first begin by defining the Hamiltonian on a $n_x \times n_y \times n_z$ site regular lattice with constant lattice spacing a, where we denote a lattice site by $\mathbf{x} \equiv (x, y, z)$. In this manner rather than creating a field excitation at any point $\psi^\dagger(x)$, we can only do so at the discrete lattice sites $\psi^\dagger_{\mathbf{x}}$. Critically, the anti-commutation relations for the discretised operators become

$$\left\{ \psi(x) \overset{\otimes}{,} \psi^\top(y) \right\} \to \left\{ \psi_{\mathbf{x}} \overset{\otimes}{,} \psi^\top_{\mathbf{y}} \right\} = 0 \quad , \tag{4.3}$$

$$\left\{ \psi(x) \overset{\otimes}{,} \psi^\dagger(y) \right\} \to \left\{ \psi_{\mathbf{x}} \overset{\otimes}{,} \psi^\dagger_{\mathbf{y}} \right\} = \delta_{\mathbf{x},\mathbf{y}} \quad , \tag{4.4}$$

As a result, we can cast Eq. (4.1) into the form

$$H = \sum_{\mathbf{x}} \psi^\dagger_{\mathbf{x}} \left[-\frac{\hbar^2}{2m_e}\mathbf{D}^2 - e\Phi + g\mu_B \mathbf{B}\cdot\boldsymbol{\sigma} - \mu \right]_{\mathbf{x},\mathbf{x}} \psi_{\mathbf{x}} \quad , \tag{4.5}$$

where the sum is now over every lattice site.

4.1.1 Discretising single particle Hamiltonian

To simplify the discussion, if initially one ignores the spin and electromagnetic fields, then the single particle Hamiltonian to be discretised resolves to

$$H_{\mathrm{sp}} = -\frac{\hbar^2}{2m_e}\nabla^2 \quad , \tag{4.6}$$

To see how $[\nabla^2]$ is to be discretised, we consider some generic 1D scalar function $f(x)$ where $x \in \mathbb{R}$. Now using a finite difference method the discretised 1D Laplacian

with some lattice spacing a acting on $f(x)$ can be given as [26]

$$\nabla^2 f(x) \approx \frac{f(x-a) + f(x+a) - 2f(x)}{a^2} \quad . \tag{4.7}$$

Hence discretising $f(x)$ itself on the same one dimensional lattice by making the substitution $f(x) \to f_x$ we can write the discrete laplacian as the following matrix equation

$$\nabla^2 f(x) \approx \frac{1}{a^2}\begin{bmatrix}1 & -2 & 1\end{bmatrix}\begin{bmatrix}f_{x-1}\\ f_x \\ f_{x+1}\end{bmatrix} \quad . \tag{4.8}$$

Hence the laplacian at some point factors in the value of the function at that point and all nearest neighbours. We can generalise this result for higher dimensions to write the Hamiltonian for a single particle with no electromagnetic fields and spin degeneracy as

$$\sum_{\mathbf{x}} \psi^\dagger_{\mathbf{x}} \left[-\frac{\hbar^2}{2m_e}\nabla^2\right]\psi_{\mathbf{x}} = \sum_{\mathbf{x}} \psi^\dagger_{\mathbf{x}}\, \epsilon\, \psi_{\mathbf{x}} - \sum_{\langle \mathbf{x},\mathbf{y}\rangle} \left(\psi^\dagger_{\mathbf{y}}\, t\, \psi_{\mathbf{x}} + \psi^\dagger_{\mathbf{x}}\, t\, \psi_{\mathbf{y}}\right) \quad , \tag{4.9}$$

where $\sum_{\langle \mathbf{x},\mathbf{y}\rangle}$ denotes summing over all nearest neighbouring sites and $t = \frac{\hbar^2}{2m_e a^2}$ and $\epsilon = \frac{\hbar^2}{m_e a^2}$. As per Eq. (4.8), we can formulate Eq. (4.10) as a matrix equation

$$\sum_{\mathbf{x}} \psi^\dagger_{\mathbf{x}} \left[-\frac{\hbar^2}{2m_e}\nabla^2\right]\psi_{\mathbf{x}} \equiv \psi^\dagger \left[H_{\text{s.p.}}\right]\psi \quad , \tag{4.10}$$

by making the identifications

$$\psi^\dagger = \begin{bmatrix}\psi^*_{(1,1,1)} & \psi^*_{(1,1,2)} & \cdots\end{bmatrix} \quad \text{and} \quad \left[H_{\text{s.p.}}\right] = \begin{bmatrix}\ddots & & & & \\ & \epsilon & -t & 0 & \\ & -t & \epsilon & -t & \\ & 0 & -t & \epsilon & \\ & & & & \ddots\end{bmatrix} \quad , \tag{4.11}$$

where ψ now denotes a vector of the field operators at every point in the lattice ($\psi^*_{(i,j,k)}$ creates an excitation at the (i,j,k) lattice site), and h_{ij} is the laplacian in matrix form.

4.1.2 Hubbard model

In the previous section we discretised the single particle Hamiltonian using a formal finite difference method, with the end result being the production of an 'on-site' term ϵ which coupled fields at a single lattice site, and 'hopping' terms t which coupled nearest neighbours site. These values were constant throughout the lattice and defined such that $\epsilon = 2t$. However, we can generalise this picture to let ϵ and

t be functions of the lattice themselves such that they can take different values depending on where they are in the lattice.

Indeed, this generalisation of the on-site and hopping terms is an equivalent picture to the dynamics of particles, namely that of a toy model consisting of lattice sites which the particles can hop between. At a vertex, the particle feels some potential $\epsilon_{\mathbf{x}}$, known as the on-site potential, and between nearest neighbour sites $\mathbf{x}$ and $\mathbf{y}$ there is some hopping parameter $t_{\mathbf{x},\mathbf{y}}$ which induces the hopping and describes the kinetic energy of the system. These parameters can then be tuned to match the material being modelled. This model is known as the Hubbard model and has had great success in modelling a number of condensed matter systems [27]. Making these substitutions, we can write the discretised single-particle Hamiltonian Eq. (4.12) as

$$\sum_{\mathbf{x}} \psi^\dagger_{\mathbf{x}} \left[-\frac{\hbar^2}{2m_e} \nabla^2 \right] \psi_{\mathbf{x}} \to \sum_{\mathbf{x}} \psi^\dagger_{\mathbf{x}}\, \epsilon_{\mathbf{x}}\, \psi_{\mathbf{x}} - \sum_{\langle \mathbf{x},\mathbf{y} \rangle} \left(\psi^\dagger_{\mathbf{y}}\, t_{\mathbf{x},\mathbf{y}}\, \psi_{\mathbf{x}} + \psi^\dagger_{\mathbf{x}}\, t^\dagger_{\mathbf{x},\mathbf{y}}\, \psi_{\mathbf{y}} \right) \quad . \tag{4.12}$$

We note that given a hopping parameter from $\mathbf{x}$ to $\mathbf{y}$ of $t_{\mathbf{x},\mathbf{y}}$, then the hopping parameter going from $\mathbf{y}$ to $\mathbf{x}$ is given by $t^\dagger_{\mathbf{x},\mathbf{y}}$ such that our Hamiltonian remains hermitian.

4.1.3 Discretising on-site potentials

Thus far we have focused on the introduction of on-site potentials $\epsilon_{\mathbf{x}}$ and hopping parameters $t_{\mathbf{x},\mathbf{y}}$ to discretise the Laplacian. However, considering the full Hamiltonian operator for a spin-$\frac{1}{2}$ electron moving in an electromagnetic field in Eq. (4.6) we note a number of on-site terms – terms that couple fields at the same lattice site – such as the Zeeman term $g\mu_B \mathbf{B} \cdot \boldsymbol{\sigma}$ and the electrostatic potential $e\Phi(x)$

$$H = \sum_{\mathbf{x}} \psi^\dagger_{\mathbf{x}} \left[-\frac{\hbar^2}{2m_e} \mathbf{D}^2 \underbrace{-e\Phi(x) + g\mu_B \mathbf{B}(x) \cdot \boldsymbol{\sigma} - \mu}_{\text{on-site terms}} \right] \psi_{\mathbf{x}} \quad , \tag{4.13}$$

where now $\psi^\dagger_{\mathbf{x}} \equiv \begin{pmatrix} \psi^*_{\uparrow_{\mathbf{x}}} & \psi^*_{\downarrow_{\mathbf{x}}} \end{pmatrix}$ denotes the discretised spinor. As the continuum on-site terms are functions over spacetime, we can discretise them simply by making the substitutions

$$\begin{aligned} \Phi(x) &\to \Phi_{\mathbf{x}} \\ \mathbf{B}(x) &\to \mathbf{B}_{\mathbf{x}} \end{aligned} \tag{4.14}$$

Similarly, from Eq. (3.5), the BCS interaction term with discretised spinors can be written as

$$H_{\text{BCS}} = \frac{1}{2} \sum_{\mathbf{x}} \psi^\top_{\mathbf{x}} \underbrace{[i\Delta^*(x)\sigma_2]}_{\text{on-site term}} \psi_{\mathbf{x}} - \psi^\dagger_{\mathbf{x}} \underbrace{[i\Delta(x)\sigma_2]}_{\text{on-site term}} \psi^*_{\mathbf{x}} \quad , \tag{4.15}$$

where we have highlighted that although the gap parameter couples electron and holes, it does so at the same lattice site. As a result, in particle hole space it too is

an on-site term and can be discretised accordingly

$$\Delta(x) \to \Delta_{\mathbf{x}} \tag{4.16}$$

As a result we can cast the full discretised on-site potential in particle-hole space as

$$\epsilon_{\mathbf{x}} \to \begin{pmatrix} \epsilon_{\mathbf{x}} - e\Phi_{\mathbf{x}} - g\mu_B \mathbf{B}_x \cdot \boldsymbol{\sigma} & i\Delta_{\mathbf{x}}\sigma_y \\ -i\Delta^*_{\mathbf{x}}\sigma_y & -(\epsilon_{\mathbf{x}} - e\Phi_{\mathbf{x}} - g\mu_B \mathbf{B}_x \cdot \boldsymbol{\sigma})^* \end{pmatrix} \tag{4.17}$$

4.1.4 Imposing gauge-invariance on the lattice

It is a reasonably straightforward process to discretise the on-site terms as they only couple spinors at a single lattice site with spinors at the same site. However, from Eq. (4.1) we have yet to discuss how to discretise the full covariant derivative $\mathbf{D}$. From the discretisation of the laplacian operator in Section 4.1.1, we saw that it produced 'hopping' terms which allowed the electron to jump between neighbouring lattice sites. However, in Section 2.1.3 we imposed that the continuum Hamiltonian have a $U(1) \times SU(2)$ gauge symmetry by introducing a number of gauge fields which the electron moves through. Hence by hopping between neighbouring lattice sites, the electron must acquire a phase factor proportional to the gauge fields it is moving through [21].

More formally, as under an $U(1) \times SU(2)$ gauge transformation of the form $g = \exp\{i\chi(x)\}$ the components of the continuum covariant derivative $\mathbf{D}_i$ transform as $\mathbf{D}_i \to g\mathbf{D}_i g^{-1}$ [21], then we must make an appropriate substitution to the hopping terms $t_{\mathbf{x}\,\mathbf{y}}$ such that the discrete single-particle Hamiltonian transforms in the same way. To facilitate this, we have to add what are known 'link variables' to the hopping terms to account for the difference between the gauge fields at those points [28]. Indeed the inclusion of link variables to account for transport through gauge fields is commonly used in all physics, albeit primarily in the context of high energy lattice field theory, but they are also utilised in condensed matter under the guise of the Peierl's substitution to account for the electromagnetic gauge field [29].

Consider an electron moving through a gauge potential $A^i(x)$ which hops from some point $\mathbf{x}$ to a neighbour at $\mathbf{y}$ along the hopping direction $\hat{d}$. We define the corresponding link variable as [28]

$$U(\mathbf{x}, \mathbf{y}) \equiv \exp\left\{ i \int_{\mathbf{x}}^{\mathbf{y}} A^i(x) dl_i \right\} \quad . \tag{4.18}$$

Then by making the substitution

$$t_{\mathbf{x},\mathbf{y}} \to t_{\mathbf{x},\mathbf{y}} U(\mathbf{x}, \mathbf{y}) \equiv t_{\mathbf{x},\mathbf{y}} \exp\left\{ i \int_{\mathbf{x}}^{\mathbf{y}} A^i(x) dl_i \right\} \quad , \tag{4.19}$$

we will imbue the discrete Hamiltonian with the appropriate gauge invariance. Discretising the gauge link itself, we can approximate $A^i(x)$ by a series of step functions

of height $A^i_{\mathbf{x}}$ and as a result Eq. (4.19) resolves to the simple substitution

$$t_{\mathbf{x},\mathbf{y}} \to t_{\mathbf{x},\mathbf{y}} \exp\Big(iaA^i_{\mathbf{x}}\hat{d}_i\Big) \quad , \tag{4.20}$$

where we are hopping in direction $\hat{d}$.

As an example, consider a 1D electron system aligned along the x-axis consisting of only two unit cells, which we label by i and j with spacing a, and with no applied external fields. Naïvely discretising the single-particle Hamiltonian we have

$$\sum_{\mathbf{x}} \psi^\dagger_{\mathbf{x}}\left[-\frac{\hbar^2}{2m_e}\mathbf{D}^2\right]\psi_{\mathbf{x}} \to \begin{pmatrix}\psi_i^\dagger & \psi_j^\dagger\end{pmatrix}\begin{pmatrix}\epsilon_i & -t\\ -t & \epsilon_j\end{pmatrix}\begin{pmatrix}\psi_i\\ \psi_j\end{pmatrix} \quad . \tag{4.21}$$

Now to impose $SU(2)$ gauge symmetry on the discrete Hamiltonian, with some $SU(2)$ gauge field $\rho^i(x)$, we include the gauge link variable of Eq. (4.20) by making the substitution

$$-\frac{\hbar^2}{2m_e}\mathbf{D}^2 \to \begin{pmatrix}\epsilon_i & -t\exp\Big\{i\int_i^j \rho^1(x)dx\Big\}\\ -t\exp\Big\{-i\int_i^j \rho^1(x)dx\Big\} & \epsilon_j\end{pmatrix} \quad . \tag{4.22}$$

Under an $SU(2)$ gauge transformation $s(x) = \exp\{i\chi(x)\}$, we note to first order in the commutators that ρ^1 transforms as (Eq. (2.14))

$$\rho^1 \to \rho^1 - \partial_x\chi(x) + i\big[\chi, \rho^1\big] \quad . \tag{4.23}$$

Hence by making the approximation

$$\int_i^j \rho^1 - \partial_x\chi + i\big[\chi,\rho^1\big]\,\mathrm{d}x \sim a\rho^1_i - \chi_j + \chi_i + \frac{ia}{2}\big[\chi_i,\rho^1_i\big] + \frac{ia}{2}\big[\chi_j,\rho^1_i\big] \quad , \tag{4.24}$$

and making use of the Baker-Campbell-Hausdorff formula which states that to first order in the commutators for any X and Y then $e^Xe^Y = e^{X+Y+\frac{1}{2}[X,Y]}$, we can decompose the link variable to write

$$\begin{aligned}-\frac{\hbar^2}{2m_e}\mathbf{D}^2 &\to \begin{pmatrix}e^{i\chi_i} & 0\\ 0 & e^{i\chi_j}\end{pmatrix}\begin{pmatrix}\epsilon_i & -te^{ia\rho^1_i}\\ -te^{-ia\rho^1_i} & \epsilon_j\end{pmatrix}\begin{pmatrix}e^{-i\chi_i} & 0\\ 0 & e^{-i\chi_j}\end{pmatrix}\\ &= s\left[-\frac{\hbar^2}{2m_e}\mathbf{D}^2\right]s^{-1} \quad .\end{aligned} \tag{4.25}$$

which is the appropriate transformation for the covariant derivative. Hence for practical calculations given some gauge potential $A_i(x)$ we simply make the substitution $t_{\mathbf{x},\mathbf{y}} \to t_{\mathbf{x},\mathbf{y}} \exp\Big(iaA^i(\mathbf{x})\hat{d}_i\Big)$ to imbue the discrete Hamiltonian with the appropriate gauge symmetry.

4.1.5 Discretising Rashba spin-orbit coupling

Although we have discretised a generic spin-orbit field in Section 4.1.4, in the Josephson junction literature there is a distinguished spin-orbit interaction known as Rashba spin-orbit coupling. As it will be used used extensively throughout the rest of the thesis, it is worth discussing in some detail here. Furthermore, we will derive the standard tight-binding formulation of the discretised Rashba spin-orbit term used in literature.

From expanding out Dirac's equation, the generic spin-orbit term was of the form Eq. (2.17)

$$H_{\text{spin-orbit}} = -\frac{\alpha}{\hbar}\Pi \cdot (\boldsymbol{\sigma} \times \mathbf{E}(x)) \quad , \tag{4.26}$$

where Π is the canonical momentum, $\mathbf{E}$ the external electric field, and α the variable which parametrises the strength of the interaction. However, in the specific case of the electric field being induced by a lack of inversion symmetry in say the z-axis due to some external confinement – such as due to crystalline interfaces – then we can express Eq. (4.26) as [30]

$$H_{\text{spin-orbit}} = -\frac{\alpha_R}{\hbar}\Pi \cdot (\boldsymbol{\sigma} \times \hat{z}) \quad , \tag{4.27}$$

which is known as Rashba spin-orbit coupling. The coefficient α_R characterises the strength of the interaction and is determined by both the material and the external electric fields [31].

From Eq. (2.18), we know that the $SU(2)$ gauge potential for the Rashba spin-orbit interaction will be expressed as

$$\rho_i = -\frac{m_e \alpha_R}{\hbar^2}(\boldsymbol{\sigma} \times \hat{z})_i \quad . \tag{4.28}$$

As a result, to formulate the Rashba spin-orbit in a tight-binding representation, we simply write the hopping from adjacent lattice sites in the $\hat{d}^{\,\text{th}}$ direction as

$$t_{\mathbf{x},\mathbf{y}} \to t_{\mathbf{x},\mathbf{y}} \exp\Big\{ i\rho_i(\mathbf{x})\hat{d}^i \Big\} \quad . \tag{4.29}$$

Although Eq. (4.29) will give the correct physics, it is somewhat unusual in the literature. To resolve this, we note that using some triple product identities and substituting in Eq. (4.28) that Eq. (4.29) can be written as

$$t_{\mathbf{x},\mathbf{y}} \to t_{\mathbf{x},\mathbf{y}} \exp\left\{ \frac{iam_e\alpha_R}{\hbar^2}\hat{z} \cdot \left(\boldsymbol{\sigma} \times \hat{d}\right) \right\} \quad . \tag{4.30}$$

Taylor expanding this to first order gives the conventional formulation in the literature [32]

$$\begin{aligned} t_{\mathbf{x},\mathbf{y}} &\to t_{\mathbf{x},\mathbf{y}}\left(1 + \frac{iam_e\alpha_R}{\hbar^2}\hat{z}\cdot\left(\boldsymbol{\sigma}\times\hat{d}\right)\right) \\ &= t_{\mathbf{x},\mathbf{y}} + \frac{i\alpha_R}{2a}\hat{z}\cdot\left(\boldsymbol{\sigma}\times\hat{d}\right) \end{aligned} \tag{4.31}$$

where we have used that $t = \frac{\hbar^2}{2m_e a^2}$.

4.1.6 Continuum parameters on the lattice

In electronic systems there are a number of continuum parameters which are used to characterise and understand systems such as energy dispersion relations, the Fermi wavevector, and the Fermi velocity. In a continuum model these are all derived from the continuum single-particle Hamiltonian. We now look to cast these parameters as functions of the discretised single-particle Hamiltonian.

To begin, we will consider a simple system consisting of a spin-less 1D chain of lattice sites with constant on-site energy ϵ and hopping t; From Eq. (4.11) the corresponding single-particle Hamiltonian can be given as:

$$\left[H_{\text{s.p.}}\right] = \begin{bmatrix} \ddots & & & & \\ & \epsilon-\mu & -t & 0 & \\ & -t & \epsilon-\mu & -t & \\ & 0 & -t & \epsilon-\mu & \\ & & & & \ddots \end{bmatrix} \quad , \tag{4.32}$$

A very useful quantity is the energy dispersion relation which provides the energy spectrum as a function of the wavevector k. Within this single-particle Hamiltonian, by multiplying out the discrete Schrödinger equation $H_{\text{s.p.}}\Psi = E\Psi$, we obtain equations of the form

$$-t\Psi_{-1} + (\epsilon-\mu)\Psi_0 - t\Psi_1 = E\Psi_0 \quad . \tag{4.33}$$

Using the discrete form of the translation operator $\Psi_i = e^{ika}\Psi_{i-1}$, we can write Eq. (4.33) as [27]

$$\left(\epsilon - \mu - te^{ika} - te^{-ika}\right)\Psi_0 = E\Psi_0 \quad , \tag{4.34}$$

which produces the discrete dispersion relation

$$E(k) = \epsilon - 2t\cos(ka) - \mu \quad . \tag{4.35}$$

We now look to computing the Fermi wavevector k_F – the wavevector at the Fermi energy – and the Fermi velocity v_F – the curvature of the dispersion relation at the Fermi wavevector. We first note that as we are generally working at temperatures corresponding to a thermal energy much less than the energy scale of the system,

$k_B T \ll t$, then the Fermi energy μ_F is equivalent to the chemical potential μ. Additionally, as we have included the chemical potential in the dispersion relation Eq. (4.35), then we are measuring the energy relative to the chemical potential itself. As a result, the Fermi wavevector must satisfy

$$E(k_F) = \epsilon - 2t\cos(k_F a) - \mu = 0 \quad , \tag{4.36}$$

which corresponds to

$$k_F a = \arccos\left(\frac{\epsilon - \mu}{2t}\right) \quad . \tag{4.37}$$

As am immediate result, we can identify the Fermi wavelength of the electrons – the length scale associated to the electron's matter wave – as

$$\lambda_F \equiv 2\pi k_F^{-1} = \frac{2\pi a}{\arccos\left(\frac{\epsilon-\mu}{2t}\right)} \quad . \tag{4.38}$$

Similarly, the Fermi velocity v_F can be given as [27]:

$$v_F \equiv \frac{1}{\hbar}\frac{\partial E}{\partial k}\bigg|_{k=k_F} = \frac{2ta}{\hbar}\sin(k_F a) = \frac{a}{\hbar}\sqrt{4t^2 - (\epsilon-\mu)^2} \quad . \tag{4.39}$$

4.2 Hofstadter's butterfly

Thus far we have described how to discretise a single-particle Hamiltonian such that it retains any gauge symmetries. To ground the conversation, we will now consider the bandstructure for a simple two-dimensional lattice possessing a $U(1) \times SU(2)$ gauge symmetry. This analysis was popularised by the work of Hofstadter who studied the energy spectrum of a two-dimensional lattice under an applied magnetic field. Under the magnetic field the discretised Hamiltonian will gain a $U(1)$ gauge link which, as first noted by Hofstadter, will lead to complex fractal behaviour in the band structure which we now look to reproduce [29]. We will then extend this by considering the effects of a Rashba spin-orbit interaction.

The device in question consists of a two-dimensional lattice with side length L and lattice spacing a – as illustrated below in Fig. 4.1. A magnetic field of the form $\mathbf{B} = B\hat{z}$ is applied such that the flux through each unit cell of the lattice is $\Phi = a^2 B$. Working in the Landau gauge, the vector potential can then be written as

$$\mathbf{A} = Bx\hat{y} \equiv Ban_x\hat{y} \quad , \tag{4.40}$$

where n_x denotes the discrete lattice site number in x. Similarly, as the device is confined in the z-axis, we will assume that the material feels a Rashba spin-orbit term of the form

$$H_{\text{spin-orbit}} = -\alpha_R \Pi \cdot (\boldsymbol{\sigma} \times \hat{z}) \quad . \tag{4.41}$$

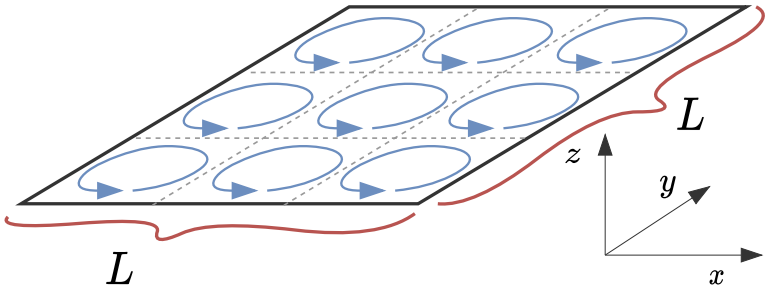

Figure 4.1: Diagram of a simple two-dimensional lattice. A magnetic field is applied in the z direction such that each unit-cell has a flux of $\Phi = a^2 B$ passing through it.

4.2.1 $U(1)$ butterfly

To compute the bandstructure of Fig. 4.1, we must first identify the single-particle Hamiltonian. To simplify the discussion we only imbue the Hamiltonian with a $U(1)$ symmetry, ignoring for now the Rashba spin-orbit interaction. Similarly, we will ignore any on-site potentials.

From Eq. (4.12) the discretised Hamiltonian for a 2-dimensional lattice with no on-site terms can be written as

$$H = -\sum_{\langle \mathbf{x},\mathbf{y} \rangle} \left(\psi^\dagger_{\mathbf{y}}\, t_{\mathbf{x},\mathbf{y}}\, \psi_{\mathbf{x}} + \psi^\dagger_{\mathbf{x}}\, t^\dagger_{\mathbf{x},\mathbf{y}}\, \psi_{\mathbf{y}} \right) \quad . \tag{4.42}$$

To imbue this discrete Hamiltonian with the $U(1)$ gauge symmetry we must add the appropriate phase factors in the hopping terms. With the vector potential given by Eq. (4.40), then using Eq. (2.7) we can show that the electromagnetic gauge potential is given by

$$\mathbf{a} = \frac{2\pi e a n_x}{h} B \hat{y} \quad , \tag{4.43}$$

where h is the non-reduced Planck's constant. Strictly we should include a Zeeman potential in Eq. (4.42), however, assuming the lattice spacing a in Eq. (4.43) is far greater than the g factor for the Zeeman interaction then for small magnetic fields the Zeeman shift can be ignored relative to the phase gained[1]. As the only non-zero component is along the y-axis, then as stated in Eq. (4.20), to impose $U(1)$ gauge invariance on the lattice we simply make the substitutions

$$\begin{aligned} t_{(n_x,n_y),(n_x+1,n_y)} &\to t_{(n_x,n_y),(n_x+1,n_y)} \\ t_{(n_x,n_y),(n_x,n_y+1)} &\to t_{(n_x,n_y),(n_x,n_y+1)} \exp\left\{ \frac{2\pi i e a^2 n_x}{h} B \right\} \quad . \end{aligned} \tag{4.44}$$

[1] This is the reason that experimental observations of the Hofstadter butterfly lagged the theoretical developments, as it required the use of Moiré lattices with their enlarged lattice spacing.

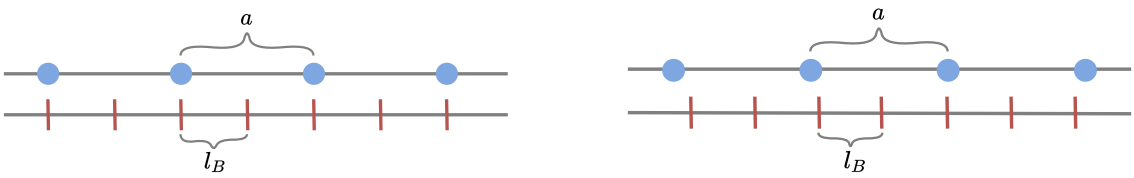

(a) $a/l_B \in \mathbb{Z}$. **(b)** $a/l_B \notin \mathbb{Z}$.

Figure 4.2: Illustrating the behaviour of the two lattices with spacing a and l_B respectively. If the two length scales are commensurate and 'fit' together then the hopping parameters gain a trivial phase. If the two lattices are not commensurate then one will observe complex fractal like behaviour in the band structure.

From Eq. (4.44), we note the appearance of the length scale a, but also a magnetic field length scale l_B given by [33]

$$l_B = \sqrt{\frac{h}{eB}} \quad . \tag{4.45}$$

As a result, the phase – which is necessarily unit-less – can be written as

$$t_{(n_x,n_y),(n_x,n_y+1)} \to t_{(n_x,n_y),(n_x,n_y+1)} \exp\left[2\pi i n_x \left(\frac{a}{l_B}\right)^2\right] \quad . \tag{4.46}$$

In this manner the competition between the two length scales is clear – if their ratio is integer valued the phase picked up is trivial, whilst if the ratio is fractional the phase will be non-trivial. This competition between length scales is illustrated in Fig. 4.2 where two lattices of spacing a and l_B have been drawn.

To study the consequences of this lattice mismatch, we begin by constructing the Hamiltonian for the system with side length $L = 56a$. To see the effects varying the ratio a/l_B has on the bandstructure, we can tune the magnetic field through the lattice such that a/l_B varies from 0 to 1. Now by applying Eq. (4.11) and the hopping parameters of Eq. (4.44) we can construct the discretised single-particle Hamiltonian. By numerically diagonalising this matrix we will then compute the set of energy eigenvalues as a function of the ratio a/l_B. Doing exactly this the results are plotted in Fig. 4.3 – note we plot the original fractal pattern by Hofstadter in the insert for comparison.

The result, shown in Fig. 4.3, is a highly symmetric fractal like behaviour with the appearance of a number of energy bands. This was first observed by Hofstadter in Ref [29], which we plot in the insert, who likened the self repeating bands to that of a butterfly. For a discussion on the physics of the electrons within the bands which manifest we refer to Ref [34]. However, as this behaviour is experimentally observable, we note that the link variables added to the discrete Hamiltonian are necessary to include correctly the physics of electrons in magnetic fields. Note the 'discreteness' of Hofstadter's results is he used an iterative process to construct his

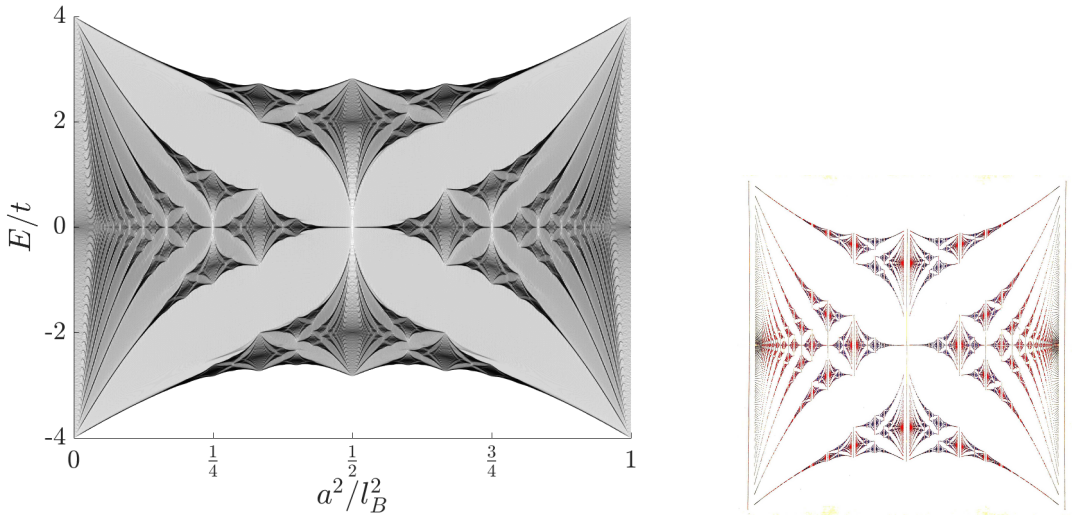

(a) **(b)**

Figure 4.3: Energy eigenvalues of a 56×56 two-dimensional lattice as the magnetic flux perpendicular to the lattice is varied. By letting the ratio of the squared characteristic lengths a^2/l_B^2 ranch from 0 to 1 a distinct fractal like pattern appears in the allowed energies. This was first identified by Hofstadter in [29]. Note the energies have been normalised by the hopping parameter t. **a**) Original work of this thesis. **b**) Gplot - By Douglas Hofstadter, CC BY-SA 3.0, https://commons.wikimedia.org/w/index.php?curid=5044529. For copyright purposes we note that the image was rotated by 90 degrees to align with out axis.

butterfly, whilst we are computing the eigenvalues of a discrete system; they would converge if we computed the eigenvalues of an infinite system.

4.2.2 $SU(2)$ butterfly

In Section 4.2.1 we simplified the discussion by imbuing the single-particle Hamiltonian with only a $U(1)$ symmetry. In doing so we produced a well known fractal known as Hofstadter's butterfly. However, there has been less work considering the appearance of fractal-like behaviour in band structures of two-dimensional lattices with the inclusion of $SU(2)$ link variables. The most comprehensive work seems to be Ref [35] where they studied the fractals that emerge from a *generic* spin-orbit interaction. In this section, rather than reproducing their results, we include a Rashba spin-orbit term to the discrete Hamiltonian of Section 4.2.1 and see how it modulates the conventional Hofstadter butterfly.

Assuming a Rashba spin-orbit term of the form

$$H_{\text{spin-orbit}} = -\alpha_R \Pi \cdot (\boldsymbol{\sigma} \times \hat{z}) \quad , \tag{4.47}$$

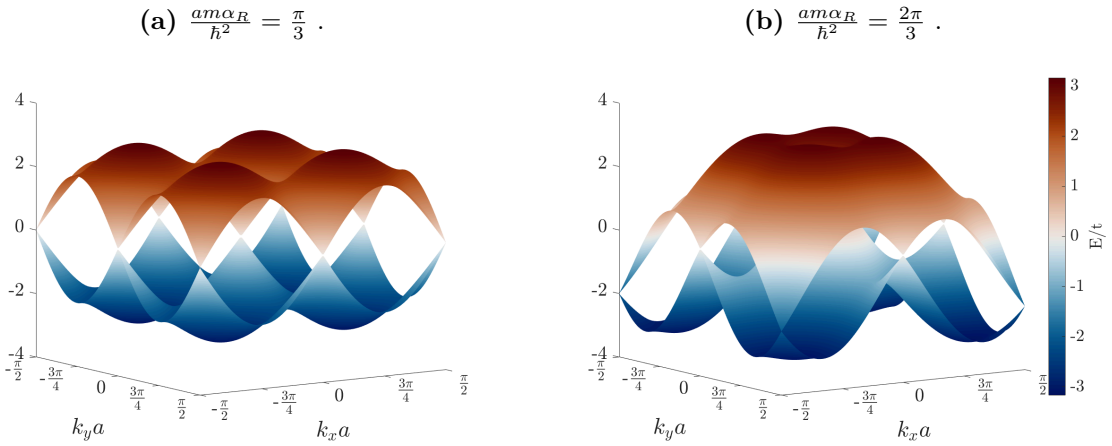

Figure 4.4: Bandstructure of a two-dimensional grid including the effects of Rashba spin orbit coupling. The Rashba strength α_R has been tuned such that the exponential in Eq. (4.49) varies from $\pi/3$ to $2\pi/3$.

where α_R is the coupling strength which parametrises the strength of the interaction, we can use Eq. (2.7) to show that the $SU(2)$ gauge potential is given by

$$\rho_i = -\frac{m_e \alpha_R}{\hbar^2}(\boldsymbol{\sigma} \times \hat{z})_i \quad . \tag{4.48}$$

Now as per Eq. (4.29), to imbue discrete Hamiltonian with a $SU(2)$ symmetry we simply make the substitutions

$$\begin{aligned} t_{(n_x,n_y),(n_x+1,n_y)} &\to t_{(n_x,n_y),(n_x+1,n_y)} \exp\left[-\frac{iam_e\alpha_R}{\hbar^2}\sigma_y\right] \\ t_{(n_x,n_y),(n_x,n_y+1)} &\to t_{(n_x,n_y),(n_x,n_y+1)} \exp\left[\frac{iam_e\alpha_R}{\hbar^2}\sigma_x\right] \quad . \end{aligned} \tag{4.49}$$

Although these appear similar to the phases gained in the $U(1)$ case, albeit now with a spin-dependence, a key difference is that these phases are a global – having no position dependence – phase shift. As a result, rather than producing a fractal like bandstructure, the Hamiltonian is instead analytically diagonalisable [31]. To illustrate this we plot the band structure of a bulk 2D material with some different values of the $SU(2)$ phase in Fig. 4.4. Visibly, the spinful nature of the splitting is evident as we see two different surfaces separated by a gap; this corresponds to the two different spin bands in the material. Although the band structures have interesting features, such as the appearance of Dirac cones[2], it does not display any fractal behaviour.

In the case of the $U(1)$ fractal, each spin was degenerate hence both spin up and down electrons gained the same $U(1)$ phase. However, due to the presence of the

[2]Regions where the bandstructure is approximately linear in momentum such that two opposing cones appear.

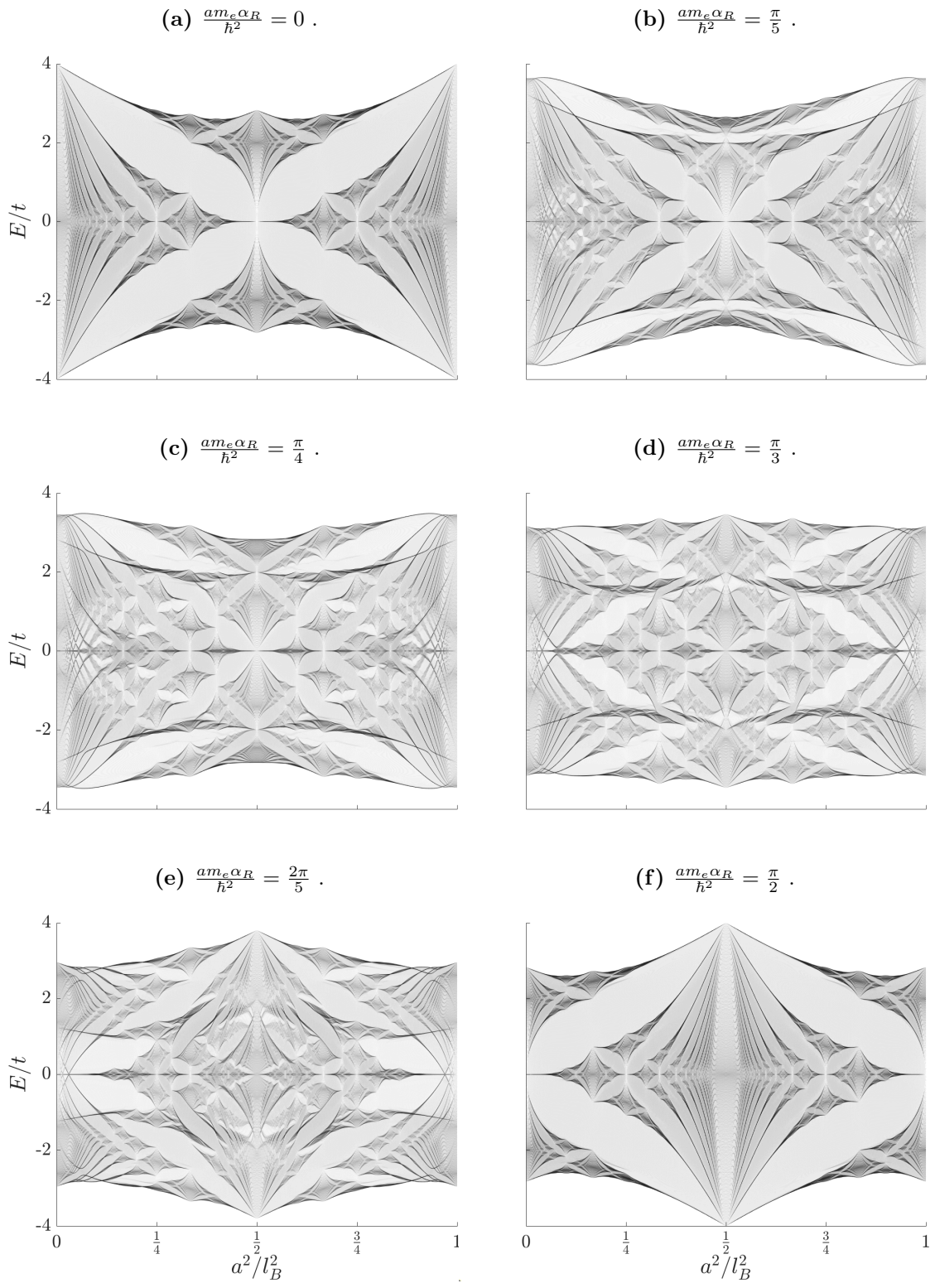

Figure 4.5: Energy eigenvalues of a 56×56 two-dimensional lattice as the magnetic flux perpendicular to the lattice is varied. In each plot a Rashba field strength, $\frac{am_e\alpha_R}{\hbar^2}$, of 0, $\pi/5$, $\pi/4$, $\pi/3$, $2\pi/5$, and $\pi/2$ is applied respectively.

off-diagonal σ_x and σ_y matrices in Eq. (4.49), we see that the $SU(2)$ phases couple the spin up electrons with the spin down electrons and vice-versa. As a result, if we include Rashba spin orbit coupling within the $U(1)$ butterfly, we expect to see some perturbation to the standard Hofstadter butterfly; as the electron hops it simultaneously gains a $U(1)$ phase, and is scattered into its spin partner. To study this, we consider the system as in Section 4.2.1, namely a 2D lattice with spacing a and length $L = 56a$. By tuning the magnetic field through the lattice we can make a/l_B vary from 0 to 1. However, we now include the effects $SU(2)$ phase factor to see how it affects the bandstructure. For a range of $SU(2)$ phases, we plot the resulting band structures in Fig. 4.5.

Visually the fractal nature of the band structure is apparent. Furthermore, by varying the $SU(2)$ phase from 0 to $\pi/2$, we note that the bandstructure is modulated from the standard $U(1)$ butterfly to the same fractal but shifted along the x-axis by exactly a half-period such that the 'trivial' behaviour is reached when the the crystal lattice (with spacing a) and the magnetic lattice (with spacing l_B) are precisely out of phase. To date there seems to have been no experimental realisation of these effects. An interesting question is indeed whether this fractal can manifest in a physical device; a potential candidate would be graphene superlattices with their controllable lattice spacing and variable Rashba spin-orbit coupling [36].

Chapter 5

Tridiagonal block matrix inversion

> *In principle the most efficient method to evaluate the transmission matrix is to calculate the transfer matrix in a real-space representation and then invert the transfer matrix. However, the transfer matrix blows up exponentially so that the matrix inversion necessary to obtain* [the transmission] *rapidly becomes singular.*
>
> —Fisher and Lee, *Relation between conductivity and transmission matrix*

Chapter Summary

Thus far in this work we have introduced the theoretical tools required to derive and solve the steady state Nambu-Gorkov equation. Furthermore, in Section 4.1 it was discussed how to discretise continuum equations such they can be solved numerically. Although this process is formally solvable, if we consider a modest 3D device consisting of 32 lattice sites in each direction, and a basis consisting of both spin and particle/hole subspaces, then it would take 512GB to store the full Green's function at a single point in energy. This alone is difficult to store, yet the inversion required to produce this mass of data is clearly difficult, and impossibly time-consuming.

To solve this numerical problem, we must first truncate the full inverse Green's function into a number of distinct block components. Then by some algorithm we must reconstruct the inverse of the full Green's function from these block components. The standard approach in the literature is an algorithm known as the Recursive Green's Function (RGF). We will briefly discuss it here before introducing a new algorithm, which we call the Truncated Transfer Matrix (TMM) method. The TTM generalises the RGF approach, allowing one to choose between numerical stability and computational speed. We will conclude this section with some discussion on the mutual benefits of the two approaches.

5.1 Block tridiagonlisation

We now consider a discretised system consisting of n individual layers, with each layer having a $n_x \times n_y$ cross section; the total number of lattice sites is thus $n_x \times n_y \times n$. To manage the memory requirements of storing and computing Green's functions, we must first partition the single-particle Hamiltonian into distinct block components. From the discussion in Section 4.1.1, the next nearest neighbour decomposition of the laplacian implies that we can partition the discretised Hamiltonian as a tridiagonal block matrix; the diagonal blocks corresponding to the single-particle Hamiltonian describing a single layer, whilst the off-diagonal matrices describe the nearest neighbour coupling between adjacent layers. We visualise this for a three layer system in Fig. 5.1. In this manner we have expressed the the Nambu-Gorkov

$$H \equiv \begin{pmatrix} H_{1,1} & H_{1,2} & 0 \\ H_{2,1} & H_{2,2} & H_{2,3} \\ 0 & H_{3,2} & H_{3,3} \end{pmatrix} \quad \Longleftrightarrow$$

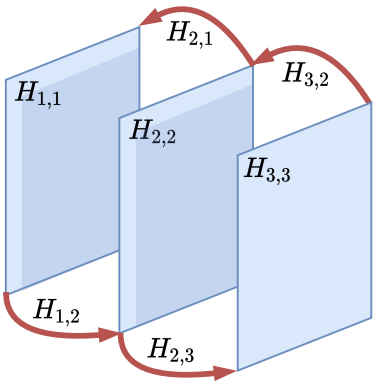

Figure 5.1: Diagrammatic mapping between the block tridiagonal matrix and the physical origin of each block matrix.

equation, Eq. (3.32), as a tridiagonal block matrix inversion problem; the benefit of which is that there is significant literature on this problem [37].

We can generalise the inverse Greens function matrix with some arbitrary block tridiagonal matrices as

$$\mathcal{G}^{-1} = \begin{pmatrix} A_1 & B_1 & 0 & 0 & \cdots & 0 & 0 \\ C_1 & A_2 & B_2 & 0 & \cdots & 0 & 0 \\ 0 & C_2 & A_3 & B_3 & \cdots & 0 & 0 \\ 0 & 0 & C_3 & A_4 & \cdots & 0 & 0 \\ \vdots & \vdots & \vdots & \vdots & \ddots & \vdots & \vdots \\ 0 & 0 & 0 & 0 & \cdots & A_{n-1} & B_{n-1} \\ 0 & 0 & 0 & 0 & \cdots & C_{n-1} & A_n \end{pmatrix}, \tag{5.1}$$

where A_i is some complex (d_i, d_i) dimensional matrix, B_i is a complex (d_i, d_{i+1}) matrix, and C_i is a complex (d_{i+}, d_i) matrix. For a hermitian Hamiltonian then $C_i \equiv B_i^\dagger$, however we do not assume so here for the purpose of generality. For notational ease, we also block partition $\mathcal{G}$ into the same form such that $\mathcal{G}_{i,j}$ has dimensions (d_i, d_j) and is located at the (i, j) block index of Eq. (5.1).

From the introduction of this chapter, we noted that in general it is not feasible to compute the entire Green's function whereby one would need to compute $\mathcal{G}_{i,j}$ for every i and j. Rather we look for some iterative algorithm which works with the block elements A_i, B_i, and C_i – rather than the entire matrix $\mathcal{G}^{-1}$ – to produce only the required $\mathcal{G}_{i,j}$ of interest. The remainder of this chapter will outline a number of algorithms to do so.

5.2 Recursive Green's function approach

In the physics literature, the standard approach to invert a block tridiagonal matrix is known as the Recursive Green's function (RGF) approach. As there are a number of comprehensive sources detailing these algorithm we will only briefly outline the required computations – see Ref [38] for more details. Although in principle one can compute any block element of the full $\mathcal{G}$ matrix using the RGF algorithm, for brevity we will only consider the left-most block components $\{\mathcal{G}_{i,1}\}$, and the diagonal blocks $\{\mathcal{G}_{i,i}\}$; as will be seen later in the thesis these are the most commonly required block components of the full inverse.

Within the RGF algorithm, one computes a set of intermediary matrices g_i from which one can construct the block components of $\mathcal{G}$. For a device with n layers, we are required to compute the entire set $\{g_i\}$ where $i = 1 \dots n$. To begin, we start from the bottom-right block of $\mathcal{G}^{-1}$, denoted by A_n, and compute the inverse

$$g_n = {A_n}^{-1} \quad . \tag{5.2}$$

We then iteratively sweep backwards from the n^{th} layer to the 1^{st} layer to produce the rest of the set by

$$\begin{aligned} g_{n-1} &= \left(A_{n-1} - B_{n-1} g_n C_{n-1}\right)^{-1} \quad , \\ &\vdots \\ g_i &= \left(A_i - B_i g_{i+1} C_i\right)^{-1} \quad , \\ &\vdots \\ g_1 &= \left(A_1 - B_1 g_2 C_1\right)^{-1} \quad . \end{aligned} \tag{5.3}$$

Using these $\{g_i\}$ matrices as building blocks, one can iteratively compute any block component of the matrix $\mathcal{G}$. For example, to compute the leftmost blocks of $\mathcal{G}$ we

use the iteration

$$\begin{aligned}
\mathcal{G}_{1,1} &= g_1 \quad , \\
\mathcal{G}_{2,1} &= -g_2 C_1 \mathcal{G}_{1,1} \quad , \\
&\vdots \\
\mathcal{G}_{i,1} &= -g_i C_{i-1} \mathcal{G}_{i-1,1} \quad , \\
&\vdots \\
\mathcal{G}_{n,1} &= -g_n C_{n-1} \mathcal{G}_{n-1,1} \quad .
\end{aligned}$$

Whilst for the diagonal blocks we use that

$$\begin{aligned}
\mathcal{G}_{2,2} &= g_2 + g_2 C_1 \mathcal{G}_{1,1} B_1 g_2 \quad , \\
&\vdots \\
\mathcal{G}_{i,i} &= g_i + g_i C_{i-1} \mathcal{G}_{i-1,i-1} B_{i-1} g_i \quad , \\
&\vdots \\
\mathcal{G}_{n.n} &= g_n + g_n C_{n-1} \mathcal{G}_{n-1,n-1} B_{n-1} g_n \quad .
\end{aligned}$$

5.2.1 Discussion on RGF

Being used in many numerical software packages the RGF algorithm is now somewhat ubiquitous to the non-equilibrium Green's function field [38,39]. The main benefits being the simplicity of the algorithm and apparent numerical robustness [37]. However, it does have a number of frustrating drawbacks: At every step in the generation of the g_i matrices one must invert a full matrix which can become a costly numerical operation. Additionally, to compute block elements of $\mathcal{G}$ one has to use an iterative procedure; if only a single block of $\mathcal{G}$ is required this is highly inefficient.

We now briefly discuss a physical motivation for the RGF algorithm. Returning to the language of physics, the matrix g_n, being the inverse of A_n – the single particle Hamiltonian for that isolated layer – is then the Green's function for the final layer if it was decoupled from the rest of the device. Furthermore, the iterative process utilised to produce the matrices g_i can be seen as equivalent to considering the i^{th} layer of the device and coupling a self energy term Σ that accounts for all layers to the right of it by

$$g_i = (A_i - B_i g_{i+1} C_i)^{-1} \equiv (A_i - \Sigma_i)^{-1} \quad . \tag{5.4}$$

This is the same mechanism as in Eq. (3.48) when we derived the self-energy terms to account for the effects of the leads on the device, the difference being now the self-energy is to couple adjacent layers. As a result, it is no surprise that g_1 is equal to $\mathcal{G}_{1,1}$, as it is defined as the Green's function for the first layer *including* the effects of all layers to the right – namely, including the effects of the rest of the device! We demonstrate this process diagrammatically in Fig. 5.2. These arguments can be made formal using a Dyson expansion as in Ref [40] and as briefly shown in Eq. (3.48).

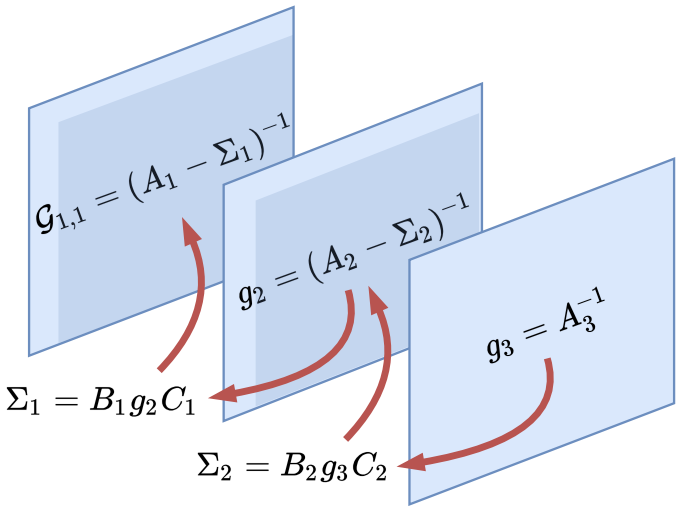

Figure 5.2: Diagram of the RGF algorithm for a three layer device. Starting from the right hand side we first initialise g_3. By then constructing self energies from this isolated layer, we couple the third layer to the second. By computing g_2 we find the surface Green's function for the last two layers. We can then couple this surface Green's function to the last layer via another self energy. The final inversion computes the surface Green's function considering every layer, precisely $\mathcal{G}_{1,1}$.

5.3 Transfer matrix approach

In the mathematical tridiagonal matrix literature the RGF algorithm, in a somewhat abstract form, was introduced in Ref [41] by Concus *et al.* as a method of stabilising an older algorithm from Asplund in Ref [42]. Asplund's algorithm was then generalised to tridiagonal block matrices by Bevilacqua in Ref [43]; a form applicable to our system. There does not appear to be a standard name for this approach in the literature, hence we have named it the 'transfer matrix approach' due to its connection with the transfer matrix method in physics; we detail this relationship in the discussion section Section 5.3.1.

To compute block elements of $\mathcal{G}$ we begin by initialising four matrix sequences $\{T_i\}$ and $\{\check{T}_i\}$, and $\{S_i\}$ and $\{\check{S}_i\}$ – each set consisting of n matrices, corresponding to the n layers of the device – with the elements

$$T_n = I \qquad T_{n-1} = -C_{n-1}^{-1} A_n \tag{5.5}$$
$$\check{T}_1 = I \qquad \check{T}_2 = -A_1 C_1^{-1} \tag{5.6}$$
$$S_1 = I \qquad S_2 = -B_1^{-1} A_1 \tag{5.7}$$
$$\check{S}_n = I \qquad \check{S}_{n-1} = -A_n B_{n-1}^{-1} \quad . \tag{5.8}$$

We can then iterate through the rest of the sequence using

$$T_i = -C_i^{-1}(A_{i+1}T_{i+1} + B_{i+1}T_{i+2}) \tag{5.9}$$
$$\check{T}_i = -\big(\check{T}_{i-1}A_{i-1} + \check{T}_{i-2}B_{i-2}\big)C_{i-1}^{-1} \tag{5.10}$$
$$S_i = -B_{i-1}^{-1}(A_{i-1}S_{i-1} + C_{i-2}S_{i-2}) \tag{5.11}$$
$$\check{S}_i = -\big(\check{S}_{i+1}A_{i+1} + \check{S}_{i+2}C_{i+1}\big)B_i^{-1} \quad . \tag{5.12}$$

Finally, we compute the matrices

$$\tilde{\Theta} = -(A_1T_1 + B_1T_2)^{-1} \tag{5.13}$$
$$\tilde{\Sigma} = -(A_nS_n + B_{n-1}S_{n-1})^{-1} \quad . \tag{5.14}$$

The $(i,j)^{\text{th}}$ block component of the full $\mathcal{G}$ matrix can be easily computed by [43]

$$\mathcal{G}_{i,j} = \begin{cases} T_i\tilde{\Theta}\check{T}_j \ , \ \text{for } i \geq j \\ S_i\tilde{\Sigma}\check{S}_j \ , \ \text{for } i \leq j \end{cases} \quad . \tag{5.15}$$

5.3.1 Discussion

The main drawbacks of the RGF algorithm was its frequent full matrix inversion and the necessarily iterative approach to computing blocks of $\mathcal{G}$. Visibly the transfer matrix approach solves both of these problems as only two matrix inversions are required – the production of $\tilde{\Theta}$ and $\tilde{\Sigma}$ – and each block of $\mathcal{G}$ can be computed independently. The drawback to this method is that it is highly numerically unstable, so much so that it is unusable for most applications [44]. We will identify the origin of these numerical instabilities in Section 5.4, however, for some brief physical insight, we note that from Eq. (5.15)

$$\mathcal{G}_{n,1} = \tilde{\Theta} \equiv -(A_1T_1 + B_1T_2)^{-1} \quad . \tag{5.16}$$

Physically $\mathcal{G}_{n,1}$ corresponds to correlations between one end of the device with the other; for certain energies it is reasonable that $|\mathcal{G}_{n,1}| \sim 0$ as electrons simply cannot propagate through the device. As a result, the matrix inversion required to compute $\tilde{\Theta}$ becomes unstable as we are attempting to compute a rank deficient matrix using a matrix inverse [45]. Additionally, due to the frequent inverses of the off-diagonal block matrices, then if the dimensions of the layers differ – such that the off-diagonal matrices are not always square – then the method breaks down. This is in contrast to the RGF approach which is robust against changing layer dimensions.

We now discuss the nomenclature of the transfer matrix approach. Returning to a physical picture, the inverse Green's function $\mathcal{G}^{-1} \equiv (E - H_{\text{sp}})$ must satisfy the single-particle equation [13]

$$\mathcal{G}^{-1}\Psi = 0 \quad , \tag{5.17}$$

where $\Psi^\top \equiv \begin{pmatrix}\Psi_1 & \Psi_2 & \cdots & \Psi_n\end{pmatrix}$ is the single-particle wavefunction partitioned into the value of the wavefunction at each layer. Using Eq. (5.1) we see that Eq. (5.17) produces a set of coupled equations which can be represented as

$$\begin{pmatrix}\Psi_{i-1}\\ \Psi_i\end{pmatrix} = \underbrace{\begin{pmatrix}-C_{i-1}^{-1}A_i & -C_{i-1}^{-1}B_i\\ 1 & 0\end{pmatrix}}_{\text{transfer matrix}} \begin{pmatrix}\Psi_i\\ \Psi_{i+1}\end{pmatrix} \quad , \tag{5.18}$$

where we have identified the conventional transfer matrix relating the wavefunction at different layers. From comparing the structure of these equation with Eq. (5.9), we see the resulting series of coupled equations have identical form – hence the name 'transfer matrix approach' as we are essentially solving for the transfer matrix. In Fig. 5.3 we diagrammatically illustrate the transfer matrix approach and how it iteratively computes each new layer

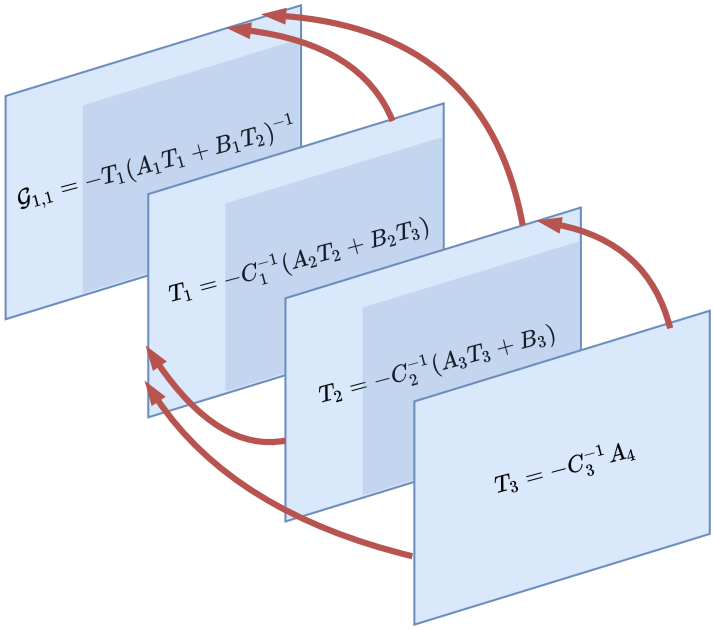

Figure 5.3: Diagram of the transfer matrix approach. Starting from the final layer – in this case A_4 – one iterates down the device, folding in new layers as one does so to produce a set $\{T_i\}$. In the final layer, after a single matrix inversion one computes the top-left block of $\mathcal{G}$.

In the physics literature, transfer matrices in general have seen much success applied to scattering matrix problems [46, 47]. However, the first to relate the transfer matrix to block components of the Green function – as seen here – is in the seminal work of Fisher and Lee (Ref [48]) who in their eponymous relation relate the scattering formalism to the Green's function method. As with the mathematical literature, they comment that this process is numerically unstable for most practical applications due to the numerical errors induced by inverting the transfer matrix.

5.4 Truncated transfer matrix approach

Thus far we have introduced two tridiagonal matrix inversion algorithms: the RGF approach which is stable but mildly inefficient, and the transfer matrix approach which is efficient but wildly unstable. However, it is possible to generalise both approaches as limiting cases of a more general matrix inversion algorithm which we denotes as the 'truncated transfer matrix' (TTM) approach. The idea is that given some layered device, we can partition the device into a discrete set of regions such that each region has few enough layers that one can utilise the transfer matrix approach within that domain. Then, analogous to the RGF method, we can stitch the regions together with appropriate self-energy terms which solve any numerical instabilities with the use of some self-energy terms. We illustrate this algorithm in Fig. 5.4.

To begin, given a system with n layers, we divide it into p partitions of k layers, and a final partition partition containing the remainder r layers. For simplicity we assume that k evenly divides n such that $n = pk$; as a result $r = 0$. We label the partitions such that the first layer is contained within the first partition, whilst the last layer is contained within the p^{th} partition. Initially, we simply compute the first k matrices of the transfer matrix approach:

$$\begin{aligned}
T_n &= I \\
T_{n-1} &= -C_{n-1}^{-1} A_n \\
&\vdots \\
T_{n-k+1} &= -C_{n-k+1}^{-1}(A_{n-k+2}T_{n-k+2} + B_{n-k+2}T_{n-k+3}) \\
\check{T}_1 &= I \\
\check{T}_2 &= -A_1 C_1^{-1} \\
&\vdots \\
\check{T}_k &= -\big(\check{T}_{k-1}A_{k-1} + \check{T}_{k-2}B_{k-2}\big)C_{k-1}^{-1} \quad .
\end{aligned} \tag{5.19}$$

For brevity we have neglected the S and $\check{S}$ matrices. Having reached the edges of the initial partitions, instead of computing the next matrices in the transfer matrix series we compute their inverses directly

$$\big[T_{n-k}\big]^{-1} = -(A_{n-k+1}T_{n-k+1} + B_{n-k+1}T_{n-k+2})^{-1}C_{n-k} \tag{5.20}$$

$$\big[\check{T}_{k+1}\big]^{-1} = -C_k\big(\check{T}_k A_k + \check{T}_{k-1}B_{k-1}\big)^{-1} \quad . \tag{5.21}$$

We now aim to stitch the first and last partitions to their neighbouring partitions. In the RGF approach we made the substitution $A_i \to A_i - B_i g_{i+1} C_i$ to couple all layers to the right of the i^{th} layer with the i^{th} layer. It is possible to show that $g_{i+1} = T_i {T_{i-1}}^{-1} C_{i-1}^{-1}$ [49], and hence to couple the neighbouring partitions we make

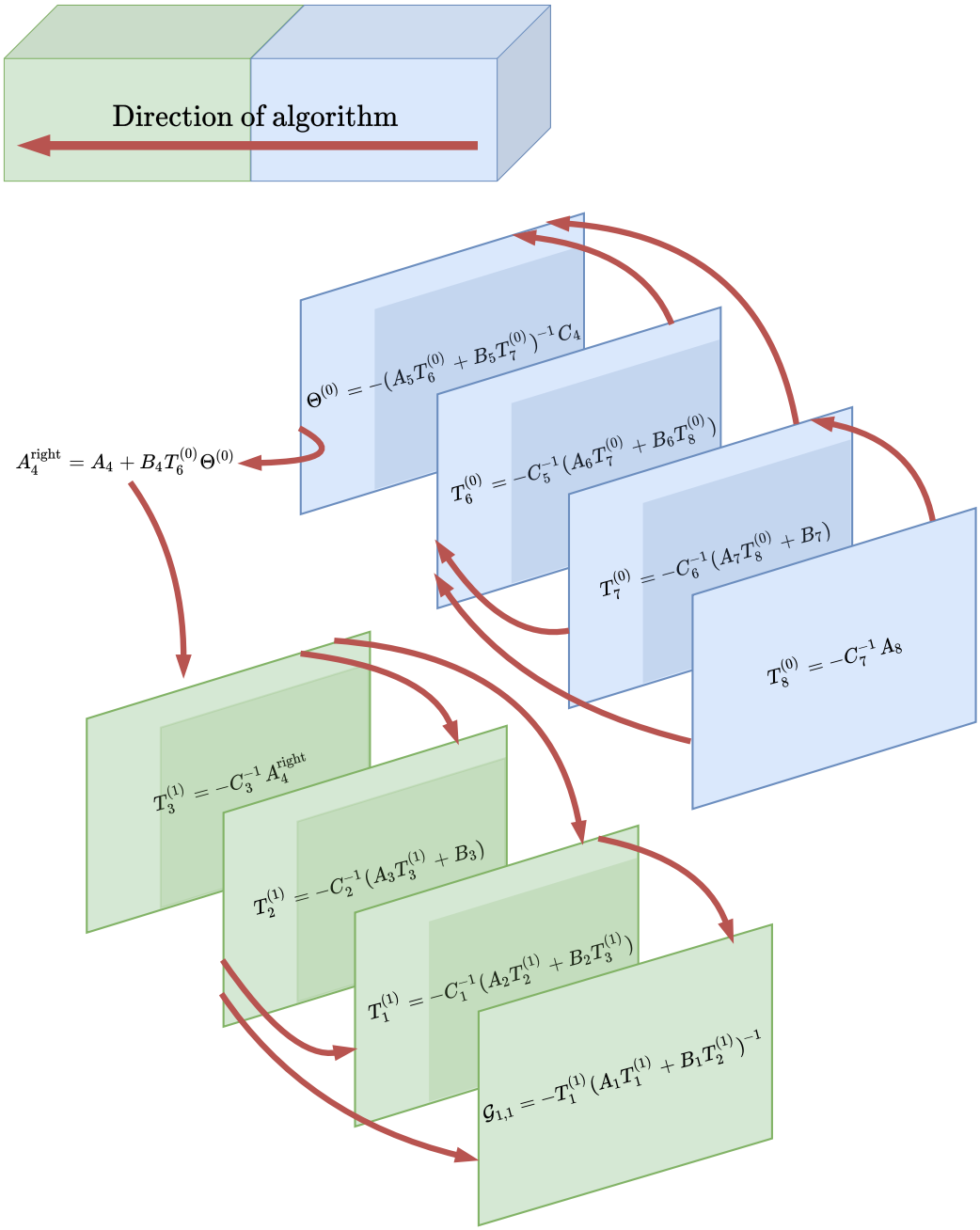

Figure 5.4: Diagram of the truncated transfer matrix approach with the device partitioned into two regions, each with four layers. Starting from the right-most edge of the device, the algorithm propagates through the first partition utilising the standard transfer matrix approach. At the intersection of the two regions, it renormalises the first layer of the second region by introducing a self-energy term – exactly as in the RGF method.

the substitution

$$A_{n-k} \to A_{n-k}^{\text{right}} \equiv A_{n-k} + B_{n-k}T_{n-k+1}[T_{n-k}]^{-1} \quad , \tag{5.22}$$

where the superscript 'right' on A_{n-k} keeps track of the fact that the layer has been renormalised to include the effects of all layers to the right. One can do the same for A_{n-pk+1} to include the effects of all the layers to its left by

$$A_{k+1} \to A_{k+1}^{\text{left}} \equiv A_{k+1} + \left[\check{T}_{k+1}\right]^{-1}\check{T}_k B_k \quad . \tag{5.23}$$

Critically we can now simply restart the transfer matrix approach in the neighbouring partitions with the renormalised A matrices, namely

$$T_{n-k} \equiv I \qquad T_{n-k-1} = -C_{n-k-1}^{-1}A_{n-k}^{\text{right}} \tag{5.24}$$

$$\check{T}_{k+1} \equiv I \qquad \check{T}_{k+2} = -A_{k+1}^{\text{left}}C_{k+1}^{-1} \quad , \tag{5.25}$$

where now the superscript index has increased as we have renormalised the quantities. This process can be iterated for the remaining layers, progressively working through the device and at the boundary between partitions renormalising every quantity.

From these matrices we can then compute blocks of $\mathcal{G}$. For $lk + i \geq mk + j$, we show in Appendix B.1 that the blocks are given by

$$\mathcal{G}_{lk+i,mk+j} = T_{lk+i}\mathcal{G}_{lk+1,mk+1}\check{T}_{mk+j} \quad , \tag{5.26}$$

where

$$\mathcal{G}_{lk+1,mk+1} = [T_{lk}]^{-1}\mathcal{G}_{(l-1)k+1,mk+1} \quad , \tag{5.27}$$

where

$$\mathcal{G}_{1,mk+1} = -\left[A_{mk+1}^{\text{left}}T_{mk+1} + B_{mk+1}T_{mk+2}\right]^{-1} \quad . \tag{5.28}$$

5.4.1 Discussion

In the RGF approach one had to compute n matrix inversion – one for every layer – whilst in the TTM approach, due to the p partitions, only $2p$ matrix inversions are necessary. Hence for small p this can constitute a considerable increase in time due to the poor scaling for matrix inversion. On the other hand, in the naïve transfer matrix approach all n layers will be progressively multiplied which led to numerical instabilities, however, in the TTM approach only k layers are iteratively multiplied before a matrix inversion is performed to stabilise the result. As a result, there is an inherent trade-off between computational speed and numerical stability; we want to maximise k such that we require as few as possible matrix inversions, however, if k is too large the numerical errors dominate the results. In the remainder of this section we will study the error increasing k will introduce.

Finally, we can recognise that the TTM method generalises both the transfer matrix approach and the RGF algorithm. For $k = 1$, such that each partition consists of a single layer, then we recover the usual RGF algorithm. Due to the number of inversions this method is slow but stable. Similarly, for $k = n$, such that the device consists of a single partition consisting of every layer, then we have only a two matrix inversions to compute but the numerical errors diverge. The TTM allows one to work somewhere in the middle, where a trade-off between numerical precision and speed can be made if required.

5.4.2 Error analysis of the TTM approach

Within the truncated transfer matrix (TTM) approach the number of layers per partition k is a free variable. Letting $k = 1$ we are equivalent to the stable RGF method, whilst if $k = n$ we are in the unstable transfer matrix approach. As a result, to make best use of the algorithm ideally one can *a priori* estimate the uncertainty that a certain length of partition will introduce. Although the specific numerical error is a difficult problem – depending strongly on the specific matrix on hand – we now derive a rough metric to estimate the maximum possible value k can obtain given a certain error threshold.

We consider an idealised n layer device where $C_i = B_i = C$ and $A_i = A$ for every layer; each layer itself being an $L \times L$ dimensional matrix. Letting $-C^{-1}A \equiv 2X$, then we see that the first k T matrices are computed by

$$\begin{aligned} T_n &= I \\ T_{n-1} &= 2X \\ &\vdots \\ T_{n-k} &= 2XT_{n-k+1} - T_{n-k+2} \quad . \end{aligned} \tag{5.29}$$

We now wish to estimate the numerical error introduced by inverting T_{n-k}. In error analysis there is a useful rule of thumb for the relative error ϵ of a matrix inversion as a function of the eigenvalues: Given an $N \times N$ matrix with eigenvalues $\{\lambda_i\}$, the relative error of the inversion is approximately [50]

$$\epsilon \sim L\epsilon_M \frac{\max(\{\lambda_i\})}{\min(\{\lambda_i\})} \quad , \tag{5.30}$$

where ϵ_M is the relative error induced by the floating point arithmetic. We introduce the quantity $\xi \equiv |\max(\{\lambda_i\}) - \min(\{\lambda_i\})|$ denoting the spread of the eigenvalues. The question is now how to estimate the maximum and minimum eigenvalues of T_{n-k}. From Eq. (5.29), although these are matrix valued expressions, we see they are identical to the recurrence relation defining the second Chebyshev polynomials

$U_n(x)$, with [37]

$$\begin{aligned} U_0(x) &= 1 \\ U_1(x) &= 2x \\ &\vdots \\ U_n(x) &= 2xU_{n-1}(x) - U_{n-2}(x) \quad , \end{aligned} \tag{5.31}$$

We illustrate the behaviour of these polynomials in Fig. 5.5. The reason we draw

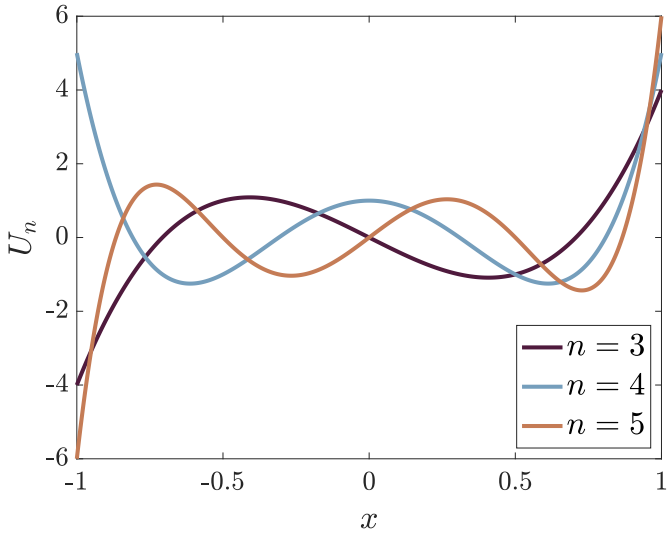

Figure 5.5: Graph of a subset of the Chebyshev polynomials of the second kind U_n.

this parallel is given the eigenvectors $\{\lambda_i\}$ of $2X$, we note that the eigenvalues of T_{n-k} can be evaluated using the Chebyshev polynomials

$$\text{eig}(T_{n-k}) = U_k(\{\lambda_i\}) \quad . \tag{5.32}$$

As a result, we can rewrite Eq. (5.30) – the estimate error of inverting T_{n-k} – as

$$\epsilon \sim N\epsilon_M \frac{\max(U_k(\{\lambda_i\}))}{\min(U_k(\{\lambda_i\}))} \quad . \tag{5.33}$$

We now look to estimating this ratio for some set of eigenvalues $\{\lambda_i\}$. To do so, we note that for $|x| < 1$, U_k is bounded, whilst for $x > 1$ it grows exponentially, hence we can obtain a rough bound to the ratio by letting $\min(U_k(\{\lambda_i\}))$ be near the right most zero of the function, whilst $\max(U_k(\{\lambda_i\})) \sim \max(U_k(\{\xi\}))$ – namely as far right as possible whilst having at least one eigenvalue near the the right most zero. Assuming the distance between a zero of the polynomial and an eigenvalue is proportional to the density of eigenvalues, then $\min(U_n(\{\lambda_i\})) \sim 1/L$. Similarly, as

shown in Appendix B.2, we can approximate

$$\max(U_n(\{\lambda_i\})) \sim \frac{w^{k+1}}{w - w^{-1}} \quad , \tag{5.34}$$

where $w = \exp\left[\cosh^{-1}(\xi)\right]$. As a result, the total estimate of the error is of the order

$$\epsilon \sim L^2 \epsilon_M \frac{w^{k+1}}{w - w^{-1}} \quad . \tag{5.35}$$

Rearranging Eq. (5.35), for some chosen error ϵ we can extract an estimate for the maximum number of layers k per partition

$$k(\epsilon) < \frac{1}{\ln(w)} \ln\left(\frac{\epsilon(w - w^{-1})}{L^2 \epsilon_M}\right) - 1 \quad . \tag{5.36}$$

Letting $\epsilon \sim 10^{-5}$, and $\xi = 4t$ we can place an estimate on k such that the error introduced by inverting T_{n-k} is on the order of 10^{-5} as a function of the size of the block matrices L

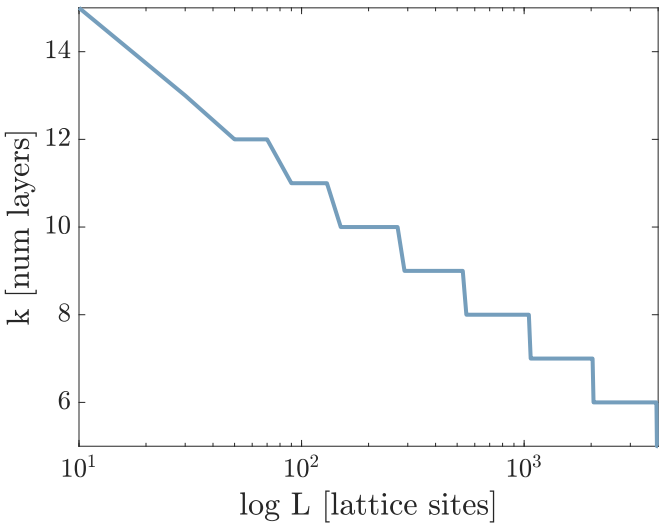

Figure 5.6: Maximum number of layers per partition such that the error introduced by the TTM method is on the order of 10^{-5}.

5.5 Comparison of different algorithms

Having now introduced a new technique for tri-diagonal block matrix inversion, we wish to compare it the existing literature. To this end, we consider a prototypical quantum transport problem – the conductance of a square tight-binding system – and compare both the results and the time required for each algorithm.

5.5.1 Conductance as a function of Green's functions

The conductance $G(E) \equiv 1/R$, where R is the resistance, of a device returns the ease at which current can pass through it as a function of the incident electron energy. As the conductance is a common measurement in solid-state systems, then its simulation is a standard result. Although we do not derive it here for brevity, the conductance can be expressed as a function of the Green's functions of the device [27]. As a result, by constructing the Hamiltonian for the system and solving the corresponding Gorkov[1] equation.

To this end we begin by considering a 2D lattice constructed of some central region connected on two opposite edges by semi-infinite leads. The system is as depicted in Fig. 5.7. To solve the system we first separate the Hamiltonian for

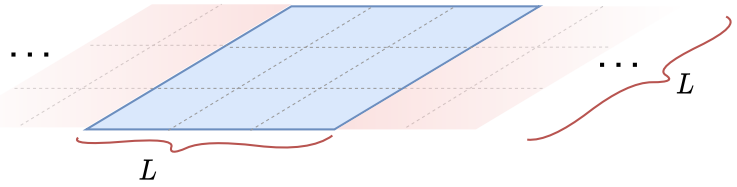

Figure 5.7: Diagram of square tight-binding system with leads attached to two opposite ends. We compute the conductance of the lattice square.

the leads from that the Hamiltonian of the central region and treat them as a perturbation to the device. Although this will be treated formally in Chapter 6 when we study Josephson junctions, we can view this as equivalent to the RGF procedure of identifying a self energy term Σ to couple the layers of the lead to the layers of the central region. Now assuming that the leads are homogenous and in thermal equilibrium, such that each layer and the hopping between layers is identical, we can use highly efficient algorithms to find said self energies [51, 52].

Before we continue we must briefly introduce a new concept. If we looked at the central region isolated form the leads, due to its relatively small size – say a few hundred lattice sites – we expect the density of states to be a set of delta functions; indicating that there are sharp resonances at certain energies with long lifetimes. This is distinct from the device when coupled to the leads, where in the density of states we expect peaks with some considerable spectral width as the lifetime of the resonances are strongly reduced; electrons like to leak from the device into the leads [27]. For a simple 1D wire this is illustrated in Fig. 5.8. The quantity which provides this broadening of the density of states is known as the level-width function $\Gamma_{\text{left/right}}(E)$, and is given by [27]

$$\Gamma_{\text{left/right}}(E) = \left(\Sigma^{\dagger}_{\text{left/right}}(E) - \Sigma_{\text{left/right}}(E)\right) \quad , \tag{5.37}$$

[1] Although the derivation of the Nambu-Gorkov equation had superconducting systems in mind, if $\Delta = 0$, then we can block partition the electron and hole components exactly. As a result we can simply solve for $\mathcal{G}_{1,1}$ – the electron correlator – independently; this is known as simply Gorkov's equation.

where the left/right subscript indicates the broadening due to the left or right lead respectively. Now given the Green's function of the device $\mathcal{G}$, partitioned in the

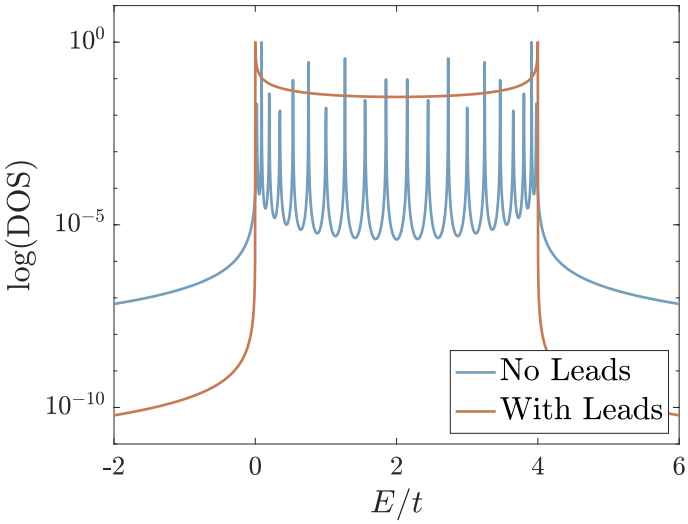

Figure 5.8: Log plot of the density of states (DOS) for an ideal 1D chain of 20 lattice sites. When no leads are attached we see sharp resonances in the DOS corresponding to long-lived resonances which are sharply peaked in energy; these correspond to the eigenmodes of the 1D chain. When the chain is coupled to the semi-infinite leads – which act as electronic reservoirs – we see that the eigenmodes broaden considerably to produce a smeared peak in the DOS. This corresponds to a greater availability of states with a reduced lifetime as resonances can now decay into the leads.

same blocks as the Hamiltonian Eq. (5.1), we can compute the conductance as

$$\begin{aligned} G(E) &= \mathrm{Tr}\left[\mathcal{G}^R_{L,1}(E)\Gamma_{\text{left}}(E)\mathcal{G}^A_{1,L}(E)\Gamma_{\text{right}}(E)\right] \\ &\equiv \mathrm{Tr}\left[\mathcal{G}^R_{L,1}(E)\Gamma_{\text{left}}(E)\mathcal{G}^{R\,\dagger}_{L,1}(E)\Gamma_{\text{right}}(E)\right] \quad , \end{aligned} \tag{5.38}$$

where the trace is now over all space.

5.5.2 Benchmarking different algorithms

We now wish to compute the conductance of an $L \times L$ grid connected to two leads. According to Eq. (5.38), this amounts to computing the bottom-left block of the causal Green's function $\mathcal{G}^R_{L,1}$. To compute this matrix element, we will use both the recursive Green's function (RGF) approach of Section 5.2 and the truncated transfer matrix (TTM) approach of Section 5.4. Additionally, for a different perspective we will compare all results with the modern open-source standard in numerical transport problems Kwant. Rather than solving a 'Green's function problem' Kwant solves the 'scattering problem', which is akin to describing how waves from the leads will scatter when incident upon the device [39]. It should be noted that Kwant is written in Python whilst we used a Matlab implementation for the RGF and TTM methods, and that no attempt was made to optimise the Kwant code. As a result

only a qualitative comparison can be made between the Kwant results and the Green's function approaches.

To compute the conductance, we consider an $L \times L$ square device with a single orbital at each lattice site. On two opposite edges, semi-infinite leads of width L are connected – see Fig. 5.7. By constructing the single-particle Hamiltonian for the system we can use the RGF and TTM algorithm to compute the matrix element $\mathcal{G}^R_{L,1}$. Using the Green's function we can solve Eq. (5.38) to find the conductance through the device. As a brief example, for a device with dimensions $L = 20$ we plot the computed conductance in Fig. 5.9. From Fig. 5.9, we note the sharp

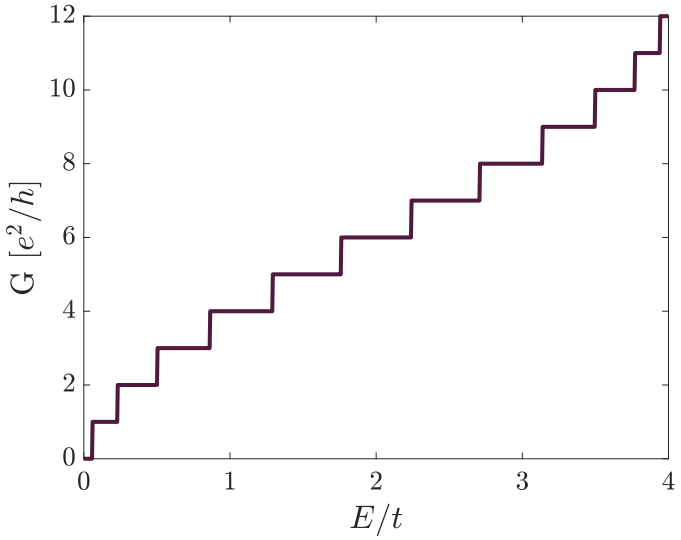

Figure 5.9: Conductance of a 20×20 lattice connected to two semi-infinite leads using the RGF approach. We note that both Kwant and the TTM method gave equivalent plots to the eye hence only one line is plotted here.

quantisation of the conductance. Due to the small width of the device, only a discrete number of modes exist which electrons from the leads can tunnel through, hence the quantisation.

We now let the dimensions of the 2D lattice vary, and compute the conductance using the RGF approach, the TTM approach with 4, 6, and then 12 layers per partition, and finally using Kwant. We also fix the energy such that the conductance is proportional to L. In Fig. 5.10 we plot the time required for the different methods to compute the conductance. To provide a fairer comparison we do not include the time required for constructing the systems of equations within the respective algorithms, only including the computation time. From a complexity analysis one can compute that Kwant will scale at $\mathcal{O}(L^3)$, whilst both RGF and the TTM will scale at $\mathcal{O}(L^4)$ [39]. As a result we can plot the continuation of the data to determine the long term temporal behaviour of the algorithms.

The first notable observation is that the TTM approach is similar in time to the standard RGF but shifted downwards by approximately an order of magnitude. This is to be expected as with $k = 6$ the TTM involves six fewer matrix inversions than

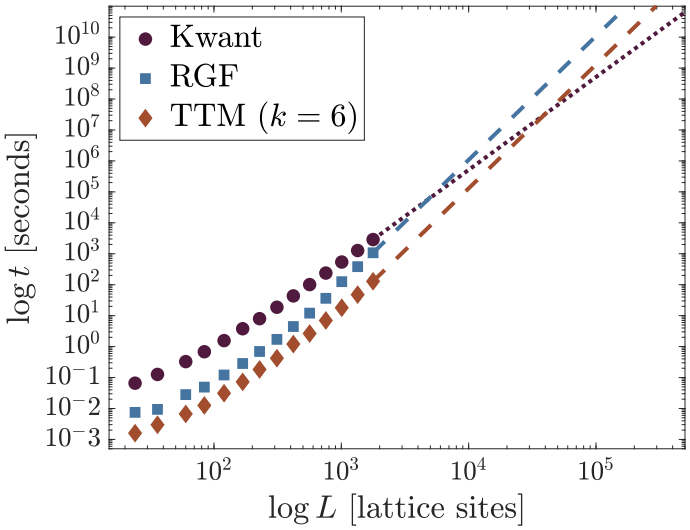

Figure 5.10: Time required to compute the conductance of a simple $L \times L$ device at a single point in energy using all three methods. By using the time complexity of each algorithm we can continue the plots to the large L limit.

the RGF. Furthermore, although we used only a naive implementation of Kwant we see that it becomes faster than the RGF approach at around $L \sim 3000$ layers, with a computation time of approximately an hour. This is in contrast to the TTM approach which, although scales in time the same as the RGF, it becomes slower to Kwant at around $L \sim 30,000$ layers at a computation time of approximately three years. As they have the same time complexity, the TTM approach will always be faster than the RGF in the long L limit.

Additionally, a central question with the TTM approach was how many layers to include in a partition such that numerical instabilities do not overrun the calculation. To study this we compared the conductance as computed from the TTM method for a range of k layers per partition to that computed from the RGF algorithm. For a comparison we simply computed the absolute difference between the two computations

$$\epsilon \equiv |G_{\text{TTM}} - G_{\text{RGF}}| \quad . \tag{5.39}$$

Although the RGF approach will itself have some numerical error associated to it, as it is the standard method in the literature it is reasonable to benchmark the TTM approach to it. For three different numbers of layers per partition, we plot the computed error ϵ in Fig. 5.11. In Eq. (5.36) we derived an expression estimating the maximum number of layers per partition k such that the inversion is stable. Indeed in Fig. 5.6 we plotted k as a function of L such that the error introduced would be on the order $\epsilon \sim 10^{-5}$. In that plot it indicated that the TTM approach is stable when $k < 6$ for devices up to $L \sim 10^3$, however, it shows that after a few hundred lattice sites the $k = 12$ cases quickly becomes unstable. These results are paralleled by Fig. 5.11, indicating that Eq. (5.36) is a reasonable metric for inversion stability.

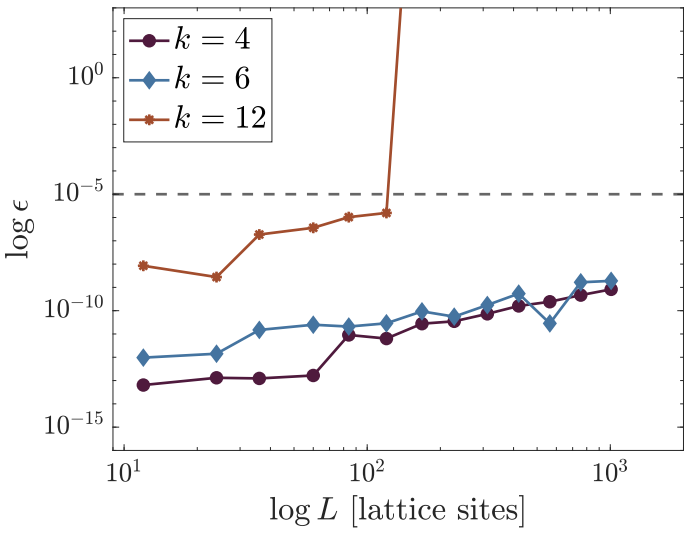

Figure 5.11: Absolute difference between the conductance computed from the RGF and the TTM algorithm for various layers per partition. The dashed grey line indicates an arbitrary threshold error of 10^{-5}.

Chapter 6

Josephson junctions with no spin-orbit coupling

States defined as eigenfuctions of the Bogoliubov quasi-particle number operator contain phase-coherent superpositions of states with the same total number of electrons, but different numbers in the two regions. However, if the regions are independent these states must be capable of superposition with arbitrary phases. On switching the transfer term the particular phases chosen will affect the predicted tunnelling current.

—B. Josephson, *Possible new effects in superconducting tunneling*

Chapter Summary

The overarching purpose of this thesis is to study transport in coupled superconducting systems: devices known as Josephson junctions. In this chapter we will introduce the Josephson current and the mechanism as to which the current is carried through the device. We will then fully outline the numerical procedure required to compute the Josephson current. Beginning with an idealised device, we will compare the numerical results of our calculations with analytic scattering theory to verify our simulations. We will then probe superconducting constrictions to study the implementation of self-consistency within our model by looking for depairing current as indicated by existing theory. Finally, we will study the π-phase flip observed in junctions under an external magnetic field by comparing our results to previous numerical work. To simplify the present results we will ignore any spin-orbit coupling.

6.1 Dynamics within a Josephson junction

In the early sixties it was observed that in the absence of a potential bias, current can flow through junctions formed by two superconductors separated by a gap. Known as Josephson junctions, these devices have found incredible use in a diverse number of applications; most famously as the building blocks for superconducting quantum interference devices (SQUIDs) [53]. Although Josephson junctions can appear in a diverse range of physical architectures, we shall focus on the specific case of nanowire Josephson junctions: two superconductors separated by a thin wire of width W and length L. A crude diagram is shown in Fig. 6.1.

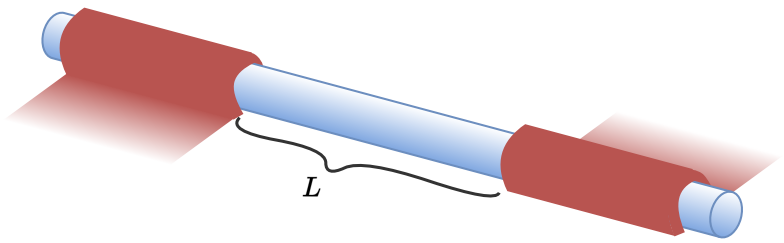

Figure 6.1: Illustration of the prototypical nanowire Josephson junction studied in this chapter. In red we see the two superconducting leads which extend to positive and negative infinity, whilst in blue we see a depiction of the long thin nanowire separating the two bulk superconductors.

6.1.1 Josephson current

We begin our study of Josephson junctions by outlining the characteristic behaviour – namely, the phase dependent flow of supercurrent. For a system of two superconductors separated by some gap, the wavefunctions of the two superconductors – assuming a weak enough gap between them – will interfere. Assuming the superconductors have macroscopic wavefunctions with phases denoted by ϕ_1 and ϕ_2 respectively, then the dynamic parameter characterising the interference is the *gauge invariant phase difference* φ defined by [54]

$$\varphi \equiv \int_1^2 (\boldsymbol{\nabla}\phi - \mathbf{A}) \cdot \hat{l}\, \mathrm{d}s \equiv \int_1^2 \tilde{\mathbf{A}} \cdot \hat{l}\, \mathrm{d}s \quad , \tag{6.1}$$

where $\hat{l}$ is the unit-vector parallel to the gap separating the two superconductors, and $\tilde{\mathbf{A}}$ is the potential energy per unit element of current. Using this potential energy, we can write the energy F of the device as [55]

$$F = \int \tilde{\mathbf{A}} \cdot \mathbf{j}\, \mathrm{d}V \quad , \tag{6.2}$$

where $\mathbf{j}$ is the current density. Taking a functional derivative we can write the current density, using Eq. (6.2), as

$$\mathbf{j} = \frac{\delta F}{\delta \tilde{\mathbf{A}}} \quad . \tag{6.3}$$

As the free energy F is characterised by φ, which is simply a phase factor, then $F(\varphi)$ is necessarily a periodic function in the phase difference and can be written as a Fourier series. However, such that the free energy is at a minimum when $\varphi = 0$ – as this is the case inside a bulk homogenous superconductor[1] – we can approximate the free energy to first order by

$$F(\varphi) = -b\cos(\varphi) \quad , \tag{6.4}$$

where b is some Fourier coefficient. Hence solving Eq. (6.3), we find that

$$\mathbf{j} = \frac{\delta F}{\delta \varphi}\frac{\delta \varphi}{\delta \tilde{\mathbf{A}}} = b\sin(\varphi)\,\hat{l} \quad , \tag{6.5}$$

where the current is flowing along $\hat{l}$ and through the junction. This electrical current with sinusoidal dependence on the bulk phase difference was first determined by Josephson in Ref [2] and is commonly known as the Josephson current. Although Eq. (6.5) relies upon a number of approximations, the fundamental idea is that the energy of the system is dependent on the interference between the two superconductors, which itself is dependent on the gauge invariant vector potential $\tilde{\mathbf{A}}$. Hence varying the energy with respect to the vector potential – which is akin to varying the phase between the superconductors – leads to a change in the junction's energy which results in the flow of current. We now look to a description of the nature of this current and the physical mechanism by which it is carried.

6.1.2 Andreev bound states

In a clean heterostructure formed by a non-superconducting material sandwiched between two superconductors, it is not clear *a priori* what the physical mechanism is such that current – the flow of charges carriers, be them electrons or holes – can move across the device. To understand the nature of the current we consider an electron in the normal region with some energy E incident upon one of the superconductors. As described in Fig. 3.4, the excitation spectrum of a superconductor around the Fermi wavevector $\mathbf{k}_F$ has two distinct branches: electron-like excitations with positive velocity, and hole-like excitations with negative velocity. Hence when incident upon the superconductor some of the electron's wave will transmit through as an electron-like excitation, whilst the rest will reflected back. By assuming a perfectly clean interface there is no mechanism by which the electron will be reflected

[1] For systems that break time-reversal symmetry or spatial inversion symmetry this condition is not necessarily true as we will see later in the thesis.

back as another electron, however, the electron-hole pairing potential Δ within the superconductor allows for the scattering of electrons into holes through the production of a Cooper pair – the Feynman diagram for this process illustrated in Fig. 3.2. As a result, within this ideal clean interface, the reflected component of the of the incident electron wave will always be a hole-like excitation.

To understand the nature of the reflected hole, we note that the change in the magnitude of the momentum δp during the reflection can be given by

$$\delta p \sim \frac{\partial p}{\partial t}\delta t \quad , \tag{6.6}$$

where $\partial_t p$ is the 'force' inducing the reflection, and δt denotes the characteristic time for the reflection process. Assuming a clean interface, this force must be proportional to the strength of the scattering potential Δ within the superconductor divided by the distance over which it is felt, hence $\partial_t p \sim \Delta/\xi$ [56]. Similarly, as the incoming electron has velocity characterised by v_F then the time for reflection is on the order $\delta t \sim \xi/v_F$. As a result the change in momentum can be given by

$$\delta p \sim \frac{\partial p}{\partial t}\delta t \sim \frac{\Delta}{\xi}\frac{\xi}{v_F} = p_F\frac{\Delta}{p_F v_F} \equiv p_F\frac{\Delta}{\mu_F} \quad , \tag{6.7}$$

where we have substituted in the definition of the Fermi energy μ_F. However, as first noted by Andreev, a good approximation for many systems is that $\Delta \ll \mu_F$ such that superconductivity lives in a thin shell around the Fermi surface, hence from Eq. (6.7) one can has that $\delta p \sim 0$ [57]. Furthermore, as the velocity must change direction in this process, then in this approximation – now known as the 'Andreev approximation' – the incident electron *must be* retro-reflected as a hole such that the magnitude of the momentum is mostly unchanged after scattering. As a result, for an electron with energy $E > \Delta$, the incident electron can either be retro-reflected as a hole or be transmitted as an electron-like excitation in the superconductor; as the energy of the incident electron increases, the probability of the electron being transmitted also increases [58]. However, for $E < \Delta$, due to the gapped nature of the superconductor, there are no available states within the superconductor for the electron to transmit to, as a result the electron will be entirely retro-reflected as a hole! In Fig. 6.2 we use the results of Ref [58] to plot the probabilities for the incident electron to be either retro-reflected as a hole or transmitted as an electronic excitation within the superconductor.

Returning to the Josephson junction – where the normal material is sandwiched between the two superconductors – when electrons within the normal region with $E < \Delta$ are incident upon one of the superconductors they will be retro-reflected as a hole in nigh the opposite direction. This hole will then be incident on the other superconductor, where, as there are no accessible hole-like excitations in the superconductor, will itself be retro-reflected as an electron. This process of retro-reflection gives rise to electron-hole bound states localised within the normal region known as Andreev bound states (ABS) [22]. These ABS efficiently carry charge

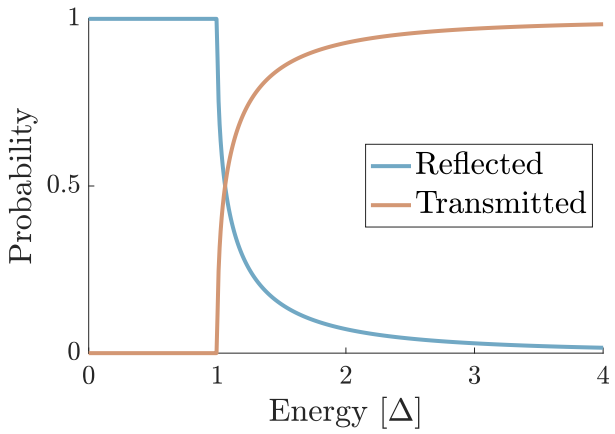

Figure 6.2: Transmission and reflection coefficients for a normal electron with energy E incident upon a superconductor with gap Δ computed using the formulas of Ref [58]. Note in the clean limit the electron is either reflected as a hole or is transmitted into an electron-like excitation within the superconductor.

.

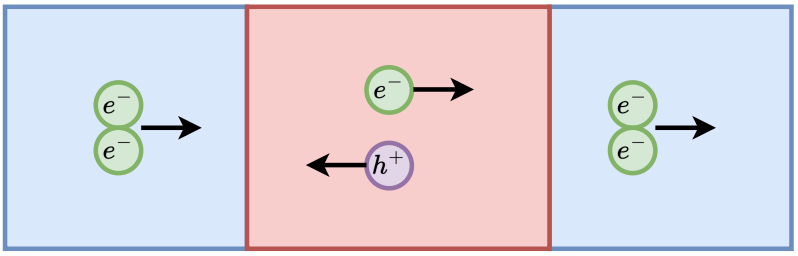

Figure 6.3: Illustration depicting how Andreev bound states (ABS) carry current between the two superconductors. The pair of counter-propagating electrons and holes within the normal region define the ABS.

of $2e$ across the junction, with this contribution to the total current known as the bound state current [23]. We illustrate this process in Fig. 6.3. Although we will predominantly focus on the bound state current, for $E > \Delta$ excitations can still be carried through the junction; either by some retro-reflection with finite lifetime or by direct tunnelling of excitations from one superconductor to the other [23]. This contribution is known as the continuum contribution; for $E > \Delta$ there is a continuum of states within the superconductors to tunnel from and to. From Fig. 6.2 we note that electrons with energies slightly above Δ will have a significant, but not unity, probability of being reflected as a hole. As a result, they will form what are known as a 'leaky' Andreev bound states: coherent counter-propagating electrons and holes but with a finite lifetime as they have some probability of decaying into the leads [59].

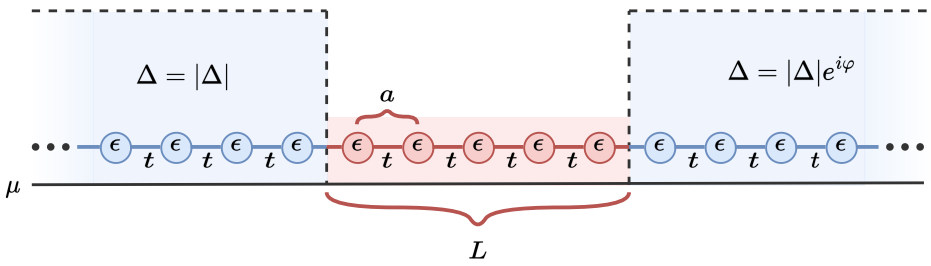

Figure 6.4: Numerical model a of one-dimensional Josephson junction. In the left and right superconductors there is a spatially constant order parameter, which is identically zero in the gap. The gauge has been chosen such that the order parameter to the left is real, whilst the right has phase φ such that the total phase difference between the superconductors is identically φ. For now we assume constant chemical potential μ alongside constant on-site energies ϵ, inter-lattice site distances a, and hopping parameters t. The length of the gap separating the two superconductors is denoted by L.

6.2 Simulating prototypical Josephson junctions

To illustrate the mechanisms of this thesis, we now simulate the dynamics of prototypical Josephson junctions – namely, a one-dimensional nanowire Josephson junction consisting of two semi-infinite superconducting leads connected to a central non-superconducting region of length L. We depict this basic device in Fig. 6.4. Although the behaviour of this device is well known, by studying it numerically we can validate our numerical results.

For simplicity we will ignore all external electromagnetic fields and assume that throughout the entire system all lattice variables, such as the chemical potential μ, the on-site energies ϵ, the inter-lattice site distance a, and the inter-site hopping t, are constant. Furthermore, we choose to work in a gauge such that the order parameter in the left lead is the real valued $\Delta_L = |\Delta|$, whilst in the right lead it possesses a phase $\Delta_R = |\Delta|e^{i\varphi}$ such that the phase difference across the junction is identically φ. Finally, with no scattering potentials in the device we are working in the so called 'clean' junction limit. To parametrise a cross over to the 'dirty' limit – devices possessing scattering sites – we add the somewhat contrived potential $U(x) = U_0 a\delta(\mathbf{x})$ to the centre of the device[2]. It should be noted that the clean/dirty comparison here concerns the ratio between the mean free path of the electron versus the length of the device, rather than the clean/dirty dichotomy for diffusive superconductors [60].

6.2.1 Exemplar numerical solver

In Chapter 3 we derived expressions for the bound states density and the current through a Josephson junction as a function of the free Green's functions. Furthermore, we also introduced the Nambu-Gorkov equation which, when solved, computes

[2] a is the unit-cell length and cancels the inverse length units of the delta function.

the free Green's functions in question. However, to numerically solve this problem we must convert it to one a computer may understand through a process of discretisation – the contents of Chapter 4. In this section, we put the pieces together to illustrate the entire workflow to compute the dynamics of a Josephson junction.

6.2.1.1 Tuning the model

To begin, one must first define the regime (short junction limit, dirty limit, ...) the device is working in. Conventionally, these limits are defined using continuum variables, however, in our lattice model we can only tune the lattice parameters $\{\epsilon, t, \mu, \Delta, U_0\}$. We now discuss the relevant quantities to be considered to define the characteristic behaviour of the device.

In Eq. (4.38) we computed the wavelength of the electron as a function of the lattice parameters to be

$$\lambda_F \equiv \frac{2\pi}{k_F} = \frac{2\pi a}{\arccos\left(\frac{\epsilon-\mu}{2t}\right)} \quad . \tag{6.8}$$

Hence, for the system to model a confined electron, we require that $\lambda_F > a$ which places a constraint on ϵ, μ, and t.

Additionally, for superconductors an important macroscopic parameter is the coherence length ξ of the Cooper pairs, which can be given by [10]

$$\xi_0 \equiv \frac{\hbar v_F}{\Delta \pi} \quad . \tag{6.9}$$

As before, in Eq. (4.39) we derived an expression for the Fermi velocity v_F for our lattice system, hence the coherence length as a function of the lattice parameters can be given by

$$\xi_0 = \frac{a\sqrt{4t^2 - (\epsilon-\mu)^2}}{\pi\Delta} \quad . \tag{6.10}$$

Furthermore, an important property of devices is their transparency – namely, the transmission through the structure. In the 1D model being considered here, the transmission probability T_r through the structure can be given by [27]

$$T_r = \left(1 + \left(\frac{U_0}{\hbar v_F}\right)^2\right)^{-1} \quad , \tag{6.11}$$

where we note that for $U_0 = 0$ then $T_r = 1$ and for $U_0 \to \infty$ then $T_r \to 0$ as expected.

Finally, as we are interested in comparing to analytic scattering theory results, which are only valid in the Andreev regime, we must know if we are working in this limit. As this only requires that $\mu \gg \Delta$, then it is a relatively straight-forward constraint to apply.

6.2.1.2 Discretised system

Using the results of Section 3.3.1, we can partition the Hamiltonian as

$$H = H_L + H_{LC} + H_C + H_{CR} + H_R \quad , \tag{6.12}$$

where H_L, H_C, and H_R contain the dynamics within the left, central, and right regions of Fig. 6.4 respectively, whilst H_{LC} and H_{RC} contain the dynamics of the coupling. Using the results of Chapter 4, the discretised Hamiltonian for the central region can be given as

$$H_C = \sum_{i=-L/2}^{L/2} \psi_i^\dagger(t')[\epsilon - U_0\delta_{i,0} - \mu]\psi_i(t') - t\sum_{\langle i,j\rangle}^{L} \Big(\psi_i^\dagger(t')\psi_j(t') + \psi_j^\dagger(t')\psi_i(t')\Big) \quad . \tag{6.13}$$

Similarly, using Eq. (3.20) we can write the discretised Hamiltonians for the superconducting leads as

$$\begin{aligned} H_{L/R} = &\sum_{\alpha\in L/R} \big(\psi_\alpha^\dagger(t')[\epsilon-\mu]\psi_\alpha(t') + \psi_\alpha^\dagger(t')\Delta_\alpha\psi_\alpha^*(t') + \psi_\alpha^\top(t')\Delta_\alpha^\dagger\psi_\alpha(t')\ \big) \\ &- t\sum_{\langle\alpha,\beta\rangle\in L/R} \Big(\psi_\alpha^\dagger\psi_\beta(t') + \psi_\beta^\dagger\psi_\alpha(t')\Big) \quad , \end{aligned} \tag{6.14}$$

where $\alpha \in L$ corresponds to all sites with $\alpha < -L/2$ and $\alpha \in R$ corresponds to all sites with $\alpha > L/2$. Akin to the hopping terms introduced in Chapter 4, to couple the different regions of the Hamiltonian we introduce a parameter $V_{L/R}$ which parametrises the interaction between the lattice sites in the left/right leads with those of the central region by

$$H_{LC/CR} = \psi_{L/R}^\dagger(t')V_{L/R}\psi_i(t') + \psi_i^\dagger(t')V_{L/R}^*\psi_{L/R}(t') \quad . \tag{6.15}$$

where L denotes the final site of the left lead at $j = -L/2$, whilst R denotes the first on the right lead at $j = L/2$.

6.2.1.3 Computing observables

We now look to computing some observables of interest, to do se we must first compute the various Green's functions for the system. To begin, we must compute the self-energy contribution from the left and right leads $\Sigma_{L/R}$; from Eq. (3.52) these are given by the formulas

$$\Sigma_L(E) = \mathcal{V}_L^\dagger\mathcal{G}_{0,0}^0(E)\mathcal{V}_L \qquad \text{and} \qquad \Sigma_R(E) = \mathcal{V}_R^\dagger\mathcal{G}_{L+1,L+1}^0(E)\mathcal{V}_R \tag{6.16}$$

where $\mathcal{G}_{0,0}^0$ and $\mathcal{G}_{L+1,L+1}^0$ denote the free Green's functions at the ends of the two leads – known as the surface Green's functions of the isolated leads. As these are components of the Green's functions for the equilibrium leads isolated from the rest

of the system, then using the results of Chapter 4 we can find these block matrix elements by solving the Nambu-Gorkov equation. However, as the leads are assumed to be semi-infinite, then solving the Nambu-Gorkov equation would be tantamount to inverting an infinite matrix. However, we can work around this problem entirely by making use of an iterative algorithm which, although assumes a finite lead size, will converge to the correct result – see Ref [51] for an example of such an algorithm.

Given the self-energy terms $\left(\Sigma^R, \Sigma^<\right)$ from these iterative algorithms, we can then compute the relevant Green's functions of the system from Eq. (3.51):

$$\begin{aligned}
\mathcal{G}^R_{C,C}(E) &= \left(\mathcal{G}^{0R}_{C,C}(E)^{-1} - \Sigma^R(E)\right)^{-1} \quad , \\
\mathcal{G}^<_{C,C}(E) &= \mathcal{G}^R_{C,C}(E)\Sigma^<(E)\mathcal{G}^A_{C,C}(E) \quad , \\
\mathcal{G}^<_{C,L}(E) &= \mathcal{G}^R_{C,C}(E)\mathcal{V}_{C,L}\mathcal{G}^{0<}_{L,L}(E) + \mathcal{G}^<_{C,C}(E)\mathcal{V}_{C,L}\mathcal{G}^{0A}_{L,L}(E) \quad .
\end{aligned} \tag{6.17}$$

From these Green's functions for the device, we can compute the observables of interest – namely, the density of states $D(E)$ which is given by Eq. (3.53):

$$D(E) = \mathrm{Tr}\left[\mathcal{G}^R_{C,C} - \mathcal{G}^{R\dagger}_{C,C}\right] \quad , \tag{6.18}$$

and the steady-state current through the device using Eq. (3.58):

$$I = \frac{e}{2}\int \mathrm{d}E\, \mathrm{Re}\left\{\mathrm{Tr}\left[\tau_z\mathcal{G}^<_{C,L}(E)\mathcal{V}_{L,C} - \tau_z\mathcal{G}^<_{C,R}(E)\mathcal{V}_{L,C}\right]\right\} \quad . \tag{6.19}$$

6.2.2 Analytic theory

Although the non-equilibrium Green's function (NEGF) formalism is purely computational, we must introduce some theory to identify what to expect in the numerical results. As described in Section 6.1.2, the current through the junction will be carried by Andreev bound states (ABS) – counter-propagating electron-hole pairs. As these are constructed from electronic states of the nanowire, we must determine the behaviour of these states first.

The Hamiltonian for the pure nanowire is written as

$$H = \int \mathrm{d}\mathbf{x}\, \psi^\dagger(x)\left[-\frac{\hbar^2}{2m_e}\nabla^2 + U_0 a\delta(\mathbf{x}) - \mu\right]\psi(x) \quad , \tag{6.20}$$

By working within the Andreev approximation we know that $\mu \gg \Delta$, however, we also assume that $\mu \gg U_0$ such that the chemical potential is the dominant energy scale of the system. Within this continuum model with dispersion $E(k) = \frac{\hbar^2 k^2}{2m_e} - \mu$, the Fermi wavevector is given by

$$k_F = \frac{\sqrt{2m_e\mu}}{\hbar} \quad , \tag{6.21}$$

In Fig. 6.5 we plot the dispersion relation for this regime. We note that for a thin

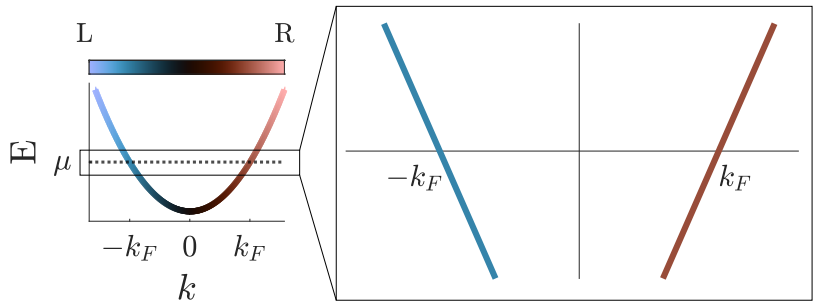

Figure 6.5: Dispersion relation of non-superconducting nanowire in momentum space. The colour-bar depicts the curvature of the dispersion relation, with a negative slope corresponding to left-moving states, whilst a positive slope corresponds to right-moving states. By zooming in on the dispersion over a small energy range around the Fermi level – exactly where superconductivity lives – we see the presence of two isolated states with different handedness.

shell around the Fermi level – which, as the chemical potential is the dominant energy scale, is precisely where the dynamics of the system reside – the states can be linearised into a set of spin degenerate left-moving and right-moving states. To do so, we expand the field $\psi(x)$ around the Fermi wavevector by a linear combination of right moving $\psi_R(x)$ and left moving $\psi_L(x)$ components:

$$\psi(x) = e^{-ik_F x}\psi_L(x) + e^{ik_F x}\psi_R(x) \quad , \tag{6.22}$$

where we assume that $\psi_L(x)$ and $\psi_R(x)$ vary on length scales much greater than k_F^{-1} [61]. Under this substitution the laplacian produces the term

$$\begin{aligned} \nabla^2\psi(x) \to\ & e^{-ik_F x}\left[-k_F^2 - 2ik_F\nabla + \nabla^2\right]\psi_L(x) \\ & + e^{ik_F x}\left[-k_F^2 + 2ik_F\nabla + \nabla^2\right]\psi_R(x) \quad . \end{aligned} \tag{6.23}$$

Now by ignoring quickly oscillating terms proportional to $e^{\pm 2ik_F x}$, and expanding out the kinetic term of Hamiltonian Eq. (6.20) to order $\mathcal{O}(k_F)$, we can rewrite the Hamiltonian for the bare nanowire as

$$\begin{aligned} H = & \int \mathrm{d}\mathbf{x}\, \psi_L^\dagger(x)[i\hbar v_F\partial_x + U_0\delta(\mathbf{x})]\psi_L(x) \\ & + \int \mathrm{d}\mathbf{x}\, \psi_R^\dagger(x)[-i\hbar v_F\partial_x + U_0\delta(\mathbf{x})]\psi_R(x) \\ & + U_0\Big(\psi_L^\dagger(0)\psi_R(0) + \psi_R^\dagger(0)\psi_L(0)\Big) \quad , \end{aligned} \tag{6.24}$$

where $v_F \equiv \frac{\hbar k_F}{m_e}$ in the continuum model. The delta function scattering within the wire now couples the right and left moving states at the site of the scattering. As a result, for no scattering potential, $U_0 = 0$, the left-moving and right-moving states are completely decoupled whilst in the presence of the scattering they mix to form standing waves within the nanowire.

As mentioned previously, within the Andreev approximation it is possible to derive analytic results using scattering theory. We do not derive these results here (see Refs [23, 53, 59, 60] for a more substantial review), but rather simply state the governing behaviour. To begin, the number of ABS within the device increases as the length of the central region increases [62]. As a result, for a short junction there are only two possible ABS, which we label by $E_{L/R}$ [59]. The subscript L and R denote whether the ABS is constructed from a left-moving electron and a right-moving hole, or a right-moving electron with a left-moving hole.

Assuming a transmission for the junction of T_r, the energy of the two ABS can be given by [59]

$$E_{L/R}(\varphi) = \pm\Delta\sqrt{1 - T_r \sin^2(\varphi/2)} \quad . \tag{6.25}$$

Additionally, assuming that we are working at zero temperature the current carried by each of those states is given by [59]

$$I_{L/R} = \mp\frac{e\pi}{\hbar} T_r \sin(\varphi/2) \frac{\cos(\varphi/2)}{\sqrt{1 - T_r \sin^2(\varphi/2)}} \quad . \tag{6.26}$$

6.2.3 Short clean junctions

We now simulate the dynamics of the 1D nanowire junction depicted in Fig. 6.4. To begin, we consider so called 'short' junctions, where the length L of the device is much shorter than the superconducting coherence length ξ.

To impose the short junction limit, we first set $\Delta/t = 10^{-3}$ such that from Eq. (6.10) the coherence length is on the order $\xi/a \sim 10^3$. As a result, by setting the length of the device $L/a = 30$, we are certainly in the correct regime. Similarly, to enforce the Andreev approximation such that the analytic scattering theory is valid, we set $\mu/t = 1.8$ such that $\Delta \ll \mu$. Additionally, as we are utilising a 1D lattice model, we require that the width W of the constriction is smaller Fermi wavelength λ_F such that the physical wire is indeed one-dimensional from the perspective of the electron. From Eq. (6.8), by setting the on-site potential to $\epsilon/t = 2$, we are comfortably working in this 1D regime as $\lambda_F = 4a$. Finally, to work in the clean limit we set $U_0 = 0$ such that we have perfect transmission through the device.

6.2.3.1 Numerical results

Following the discussion within Section 6.2.1, with the aforementioned parameters we can discretise our system and solve the relevant Green's functions. As we are interested in the current carried by the Andreev bound states, we only consider the energy range[3] $E \in [-\Delta, \Delta]$. We also sweep across the phase difference φ across the junction, varying from 0 to 2π. From solving Eq. (6.18), we can compute the density of states $D(\varphi, E)$ of the system which we plot the logarithm of in Fig. 6.6. The first

[3]It should be noted that as we are always working in a grand canonical ensemble all energies are measured relative to μ.

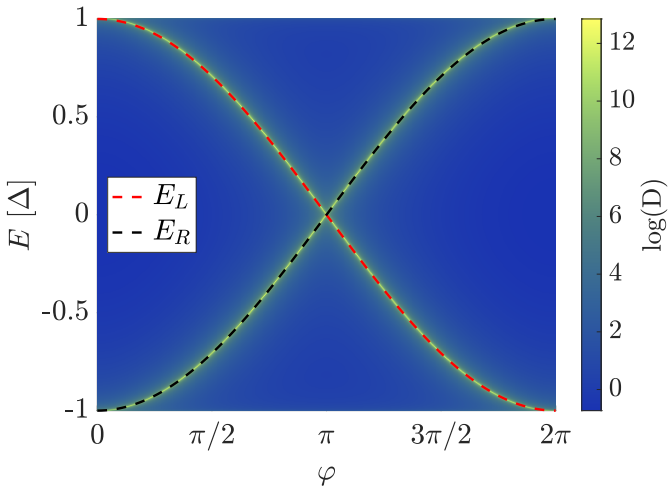

Figure 6.6: Heatmap of the log of the total density of states $D(\varphi, E)$ as a function the phase difference φ and energy E. Note that the logarithm is taken as the resonances are so sharp a log plot is needed to resolve them. Overlaid are the analytical expressions for the ABS dispersion relation resolved using Eq. (6.25).

noticeable feature of this plot is the sharp peaks in the logarithm of the density of states. Indeed the peaks are so sharp that if we plotted simply the density of states and not the logarithm, they would not be resolvable. If the Andreev regime was exact, these states would have infinite lifetime and hence would appear as delta functions in the density of states, however, in this discrete model this is never the case and there is always some inherent numerical broadening. However, the sharpness of these peaks indicates we are working close to the theoretical ideal regime.

Similarly, by solving Eq. (6.19), we can compute the current across this device as carried by the states of Fig. 6.6. By working in the zero temperature limit, so we can compare with the analytic results of Eq. (6.26), we plot the numerical results in Fig. 6.7. Again, we see excellent agreement with the analytic expressions. The most interesting aspect of this plot is the sudden change in the current at $\varphi = \pi$. This is merely an artefact of working at zero temperature, as then the Fermi function of Eq. (2.45) imposes a sharp cut-off such that only states below the Fermi level are accessible. As a result, reading off Fig. 6.6, for $\varphi < \pi$ only the state E_R is available, and hence a current of $I_R = \frac{e\pi}{\hbar}\sin(\varphi/2)$ is carried, however, for $\varphi > \pi$ the available state is E_L which carries a current of $I_L = -\frac{e\pi}{\hbar}\sin(\varphi/2)$. By increasing the temperature, we broaden the Fermi function allowing both E_L and E_R to be occupied which mixes the left-moving and right-moving current recovering the familiar sine wave for the Josephson current – we plot the current through the device for a range of temperatures in Fig. 6.8.

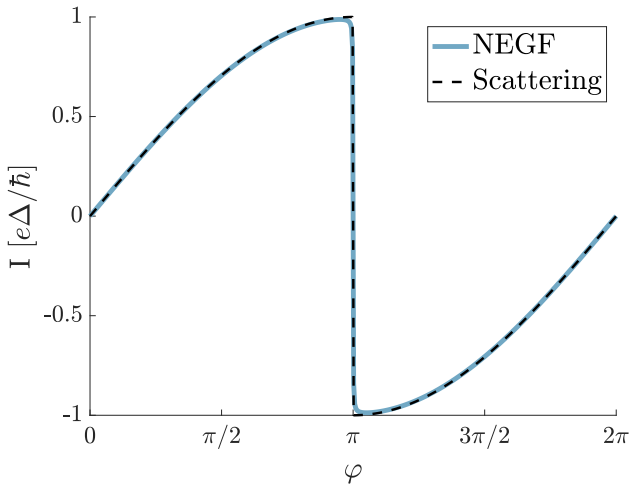

Figure 6.7: Supercurrent through ideal 1D Josephson junction at zero temperature. The abrupt change at $\varphi = \pi$ is due to being at zero temperature, as only states with negative energy are accessible; from Fig. 6.6 we note that at $\varphi = \pi$ the accessible state flips from E_R to E_L.

6.2.4 Short dirty junctions

In the previous section we assumed that the device had perfect transmission – the 'clean' limit. We now wish to include the effects of disorder within the nanowire. To still compare with analytic results, we add disorder in a somewhat contrived way by adding the potential $U(x) = U_0\delta(\mathbf{x})$ to the device. In this way we can easily control the transmission through the device using Eq. (6.11).

We repeat the method of Section 6.2.3 to evaluate numerically both the density of states and the current through the dirty structure. To understand the effects of changing the transmission, we tune the scattering potential U_0 such that the transmission takes the values

$$T_r \in \{1, 0.99, 0.75, 0.5\} \quad . \tag{6.27}$$

We plot the resulting set of Andreev bound states in Fig. 6.9. Note unlike in Fig. 6.6, we have numerically isolated the peaks of the density of states and simply plotted those as a line plot. Furthermore, in the filled markers, we have overlaid the analytic ABS spectrums from the scattering theory.

The most noticeable feature of Fig. 6.9 is that at $\varphi = \pi$ a gap opens in the spectrum; this is due to the impurity coupling left-moving and right-moving states such that an avoided crossing forms where E_L and E_R were previously degenerate. Furthermore, as the strength of the scattering site increases, and hence the transmission reduces, we see the gap widens as the left and right moving states are progressively more coupled. The close fit between the numerical formulas derived from scattering theory of Eq. (6.25) and our numerical results is an excellent validation.

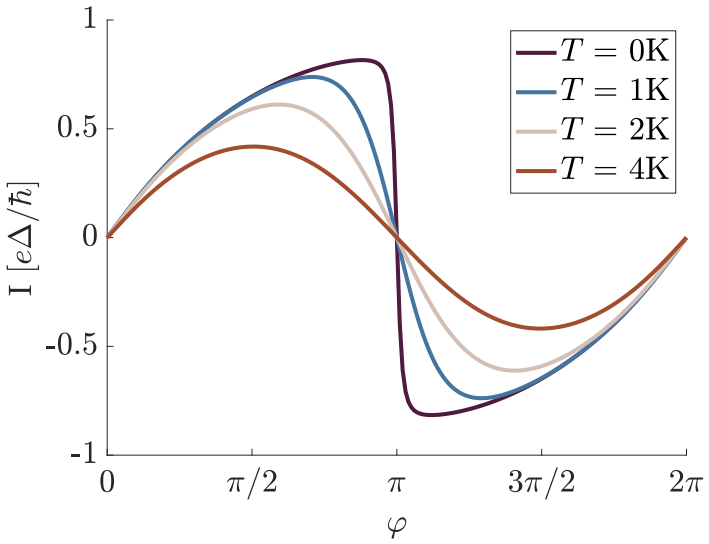

Figure 6.8: Supercurrent through a short one-dimensional Josephson junction at a range of temperatures. The current for all of these plots is carried by the ABS of Fig. 6.6. By increasing the temperature we recover the familiar sine wave.

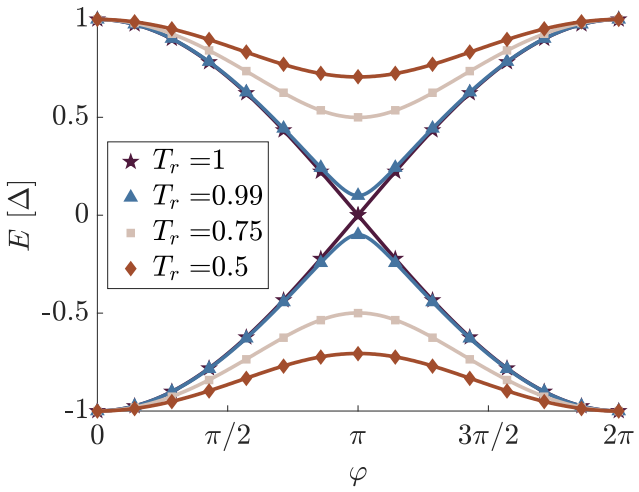

Figure 6.9: Overlay of all of the ABS spectrums for a range of transmissions through the device. The coloured lines are the peaks of the numerical spectrum, whilst the markers are the result of the closed form scattering results.

.

Again working in the zero temperature limit, we plot the resulting supercurrent carried by the bound states of Fig. 6.9 in Fig. 6.10. To compare with the analytic theory, we plot the numerical results in the unbroken lines, then overlay the results of Eq. (6.26) with the discrete markers. The first observation is again the close match between the analytic results and our computational results. Furthermore, we observe that Fig. 6.10 looks very similar to Fig. 6.8; in both cases we are observing

a cross-over between a discontinuous current carrying $\sin(\varphi/2)$ and a continuous current carrying $\sin(\varphi)$ – even though in one we are sweeping transmission and in the other temperature. In the finite temperature case current could flow through both the left-moving and right-moving states, whilst in the reduced transmission case the left-moving and right-moving states *themselves* are coupled. As a result, in both cases current is carried by a superposition of the two and the results appear similar. As a result, we observe a smooth sinusoidal current as these coupled states form standing waves in the device which cannot carry current [59].

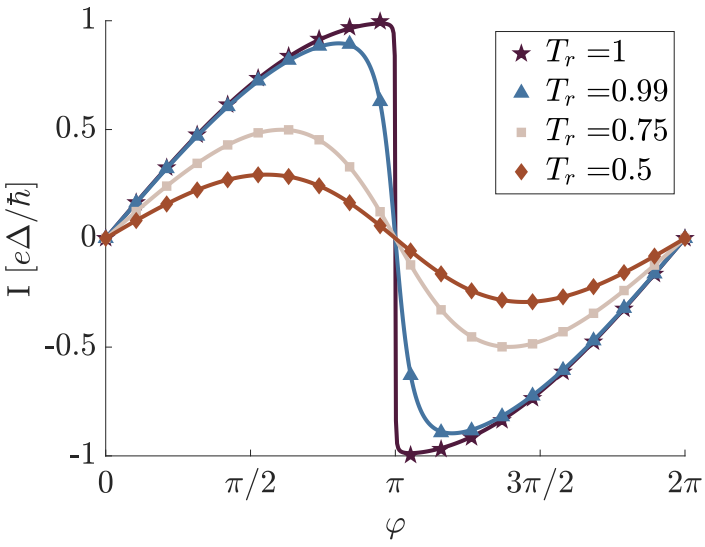

Figure 6.10: Supercurrent at zero Kelvin through a short, dirty, one-dimensional Josephson junction with a range of transmissions.

6.3 Self-consistent order parameter

In Section 3.1.2 we performed a mean-field decoupling and introduced a gap parameter Δ which described the background field of Cooper pairs. Although we motivated it by introducing a bosonic Cooper pair field where the gap parameter was the expectation value of that field $\langle\Delta(x)\rangle$, it is worth remembering that at their core the Cooper pairs are simply paired electrons. Hence it is very reasonable to question the relationship between Δ and the Green's function $\mathcal{G}$ – which itself is a function of Δ. Indeed, for given some Green's function $\mathcal{G}$, the gap parameter can be computed via the relation derived in Appendix A.5:

$$\Delta(\mathbf{x}) = ig \int \mathrm{d}E \, \mathrm{Tr}[(i\sigma_2)F^<(E,\mathbf{x},\mathbf{x})] \quad , \tag{6.28}$$

where $F^<(E)$ is the $(1,2)$ block component of $\mathcal{G}^<$, and g is the electron-phonon coupling coefficient. As a result, there is a cyclicity to the order parameter in the

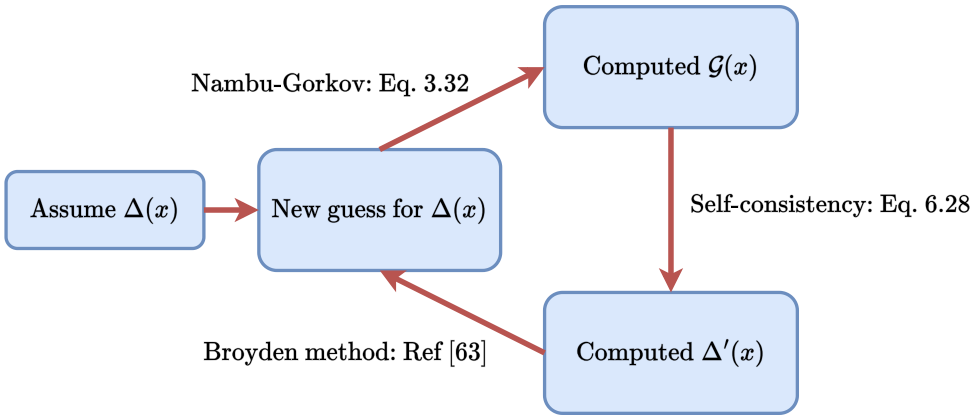

Figure 6.11: Flowchart outlining the self-consistent procedure to compute the order parameter within the device. By supplying an initial guess for the order parameter – usually a homogenous solution – one can iteratively solve the Nambu-Gorkov equation of Eq. (3.32), the self-consistency relation of Eq. (6.28), then utilise some algorithm to produce a new guess considering all of the information at hand – as in Ref [63]. When the value of Δ is invariant under a loop to some chosen precision the solution has converged.

numerical model: one must assume a given order parameter such that one can numerically solve the Nambu-Gorkov equation, but then by solving Eq. (6.28) one finds a new 'guess' for the order parameter which can be used to recompute the Green's function *ad nauseam*.

Although this may appear somewhat involved, the numerical recipe is relatively straightforward: For a given Josephson junction, we first pick bulk values of the order parameter in the three region $(\Delta_L, \Delta_C, \Delta_R)$ such that the junction is working in the expected regime. We now tune the coupling constant g such that Δ is invariant after solving Eq. (6.28). To do so we construct bulk lattices with periodic boundary conditions and tune g within each region such that the self-consistent order parameter approaches the required bulk value. Now that the bulk order parameters have been chosen – which supply the initial conditions – and the coupling constant has been tuned for a bulk model, we can self-consistently solve for the order parameter in the real device using Eq. (6.28) in conjunction with the Nambu-Gorkov equation. This is plotted graphically in Fig. 6.11

Unfortunately, this self-consistent procedure can struggle with convergence. The difficulty is that after assuming the bulk solutions for the initial 'guess' for the order parameter Δ^0, then by solving Eq. (6.28) we are left with a new order parameter $\Delta^{0\prime}$ which factors in the previous guess Δ^0. The questions is how to best choose the next guess Δ^1 such that the process will eventually converge? Anecdotally, we found best success using a Broyden-like algorithm to make the next guess for the order parameter – see Ref [63] for a full description of these methods. In Ref [64], the order parameter is self-consistently solved and they too remark that they had to use a Broyden-like algorithm to solve convergence issues.

6.3.1 Superconducting constrictions

To validate our implementation of self-consistency, we must search for solutions to to order-parameter which cannot be explicitly computed *a priori*, then let the system find the solution itself. To do so, we consider superconducting constriction: Josephson junctions formed entirely of superconductors, where a superconducting constriction (S') is sandwiched between two bulk superconducting leads (S) – in a device known as a S-S'-S Josephson junction. An example 2D S-S'-S device is illustrated in Fig. 6.12. Often when Josephson junction are discussed it is implicit that

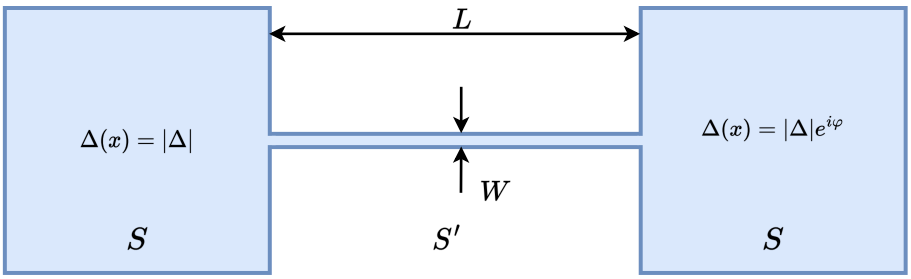

Figure 6.12: Diagram of a simple 2D superconducting constriction. The material is assumed to be homogenous throughout the device, the only difference being that the width W of the constriction is significantly smaller than the width of the superconducting leads on either side.

the gap between the two superconducting reservoirs is some non-superconducting material. However, a more general formalism is that it simply be a 'weak-link' – namely any material where the critical current is less than in the bulk superconducting electrodes [60]. Tautologically this is true for a non-superconducting region separating the two superconductors, but curiously, if one has a superconducting nanowire or filament which, due to its sharp constriction, has a reduced critical current then this too can constitute a weak-link.

In Section 6.1.1 we discussed how in a short S-N-S junction the current is predominantly transported through Andreev bound states formed within the normal region. However, in a superconducting constriction the condensate itself can carry the current as it does not necessarily vanish in the constriction as in a S-N-S junction. To study current flow in superconductors, we consider a bulk superconductor possessing an order parameter of the form $\Delta(\mathbf{x}) = |\Delta|e^{i\chi(\mathbf{x})}$, where as per Eq. (3.8) the magnitude is assumed to be constant. As $\Delta(x)$ describes the charged condensate within a superconductor, the current through the system is proportional to usual quantum-mechanical expression for current density [19]

$$\mathbf{j}(x) = -\frac{ie\hbar}{2m_e}(\Delta^*(x)\boldsymbol{\nabla}[\Delta(x)] - \boldsymbol{\nabla}[\Delta^*(x)]\Delta(x)) = \frac{e\hbar}{m_e}|\Delta|^2\boldsymbol{\nabla}\chi(x) \quad . \tag{6.29}$$

As the magnitude $|\Delta|^2$ describes the *density* of the charged condensate, then by comparing with the usual expression for current density $\mathbf{j} = \rho e\mathbf{v}$, we can identify $\mathbf{p} \equiv \hbar\boldsymbol{\nabla}\chi(x)$ as the momentum per Cooper pair [19]. Hence the local current density

in the superconducting constriction is proportional to the gradient of the phase at that point in space.

Returning to the superconducting constriction, if we assume that left lead's order parameter is given by $\Delta_L = |\Delta|$ and the right lead's by $\Delta_R = |\Delta|e^{i\varphi}$, such that there is a phase difference between the bulk leads of φ. The lowest energy current carrying solution is a linear drop of the phase along the constriction [65]

$$\Delta(x) = |\Delta|e^{i\varphi x/L} \quad , \tag{6.30}$$

such that the current flow is along the entire constriction – we denote this by the linear solution. However, as noted in Ref [66], there is another solution for the condensate along the constriction where the phase drop appears as a step function

$$\Delta(x) = |\Delta|e^{i\Theta(x-L/2)} \quad , \tag{6.31}$$

As a result, the current flow is localised to only a small region of the wire – this is known as, for reasons that will be explained later, the solitonic solution.

6.3.1.1 Initial guess for order parameter in each solution

As we are utilising a self-consistent procedure to compute the two different current solutions, we must supply appropriate initial guesses such that the self-consistent procedure converges to the different solutions. To construct such guesses, we must consider the nature of the solutions themselves.

For simplicity, we assume that the constriction has length L and set $\varphi = 0$ such that there is no phase difference between the bulk leads. As a result, the linear solution can be given by the constant solution $\Delta_{\text{linear}}(x) = |\Delta|$. However, as φ is a phase variable then the order parameter in the constrictions has an entire family of solutions given by

$$\Delta_k(x) = |\Delta|e^{i2k\pi x/L} \quad . \tag{6.32}$$

Although for $k > 0$ these states are energetically unfavourable due to the higher current density, they satisfy the required boundary condition that $\arg(\Delta(L)) - \arg(\Delta(0)) = 0$; the difference between the solutions is that they each wind around the x-axis k times. We do not prove it here, but this winding number is a topologically protected quantity such that for small deformations in the order parameter, this winding number is unchanged[4]. This inherently gives rise to topological defects – also known as topological solitons – which are solutions to the order parameter separating the topologically distinct winding solutions. We can illustrate the free energy as a function of the condensate phase χ in Fig. 6.13.

Langer and Ambegaokar in Ref [66] determined analytic results for the solitonic solution across an ideal one-dimensional constriction. Using their results, we plot

[4]More correctly, we can view our problem onto considering maps of the form $f : [0, 1] \to S^1 \mid f(0) = f(1) = 0$. The fundamental group π_1 of this mapping is then given simply by $\mathbb{Z}$ – where the integer corresponds to the number of winds [67].

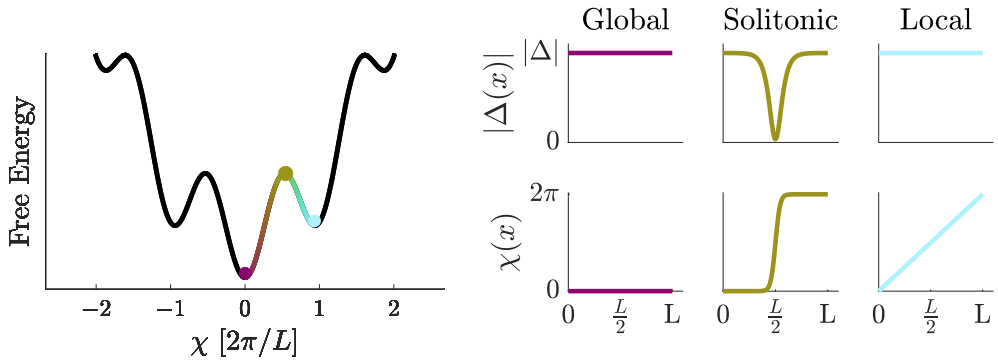

Figure 6.13: Illustrative diagram of the free energy surface of the superconducting filament. The global minima occurs at $\chi = 0$, as indicated by the purple dot, there is also a local minima occurring at $\chi = (2\pi)/L$, indicated by the blue dot. We have drawn a path traversing from the global minima to the nearest local minima; in doing so we have passed through a meta-stable saddle point solution – illustrated by the brown dot. The value of the order parameter within the constriction decomposed into its magnitude $|\Delta|$ and phase χ at each of the points of interest: the global minima, the saddle point, and the local minima.

the magnitude and phase of the order parameter at each of the three points marked in Fig. 6.13 – namely, the global minima, the solitonic solution, and a local minima. The most striking observation of Fig. 6.13 is the jump in condensate phase corresponds to the diminishment of the order parameter within the solitonic solution. Due to the highly localised current flow, the energy density is large enough to break the Cooper pairs resulting in a localised reduction of $|\Delta|$ in an effect known as the depairing current [60]. Regardless, for an initial guess for the order parameter in the solitonic solution we can approximate the jump in phase by a simple step function, and the drop in magnitude by a simple triangle-wave. The initial guesses for the linear solutions are much simpler due to the constant gradient in the phase and the constant magnitude of the order parameter.

6.3.1.2 Tuning the numerical model

We now explicitly consider the device depicted in Fig. 6.12 – namely, a pair of large semi-infinite superconducting leads connected by a long 1D superconducting constriction. As in Ref [64], we set $\epsilon = \mu = 0$ throughout the system such that dynamics for a bare electron at some energy E is equivalent that of a hole at the same energy. Additionally, such that a step function order parameter is not a reasonable approximation, we must work in a long junction limit such that $L \gg \xi$ [60]. To do this end, we set $\Delta/t = 0.1$ such that $\xi \sim 10$, and let $L = 80$. Finally, such that the leads act as effective reservoirs of phase we set their width to be 25 lattice sites such that the order parameter converges to the required bulk value.

Additionally, we arbitrarily set the bulk phase difference across the junction to be $\varphi = 1.05\pi$ such that the left lead has order parameter $\Delta = |\Delta|$ and the right has $\Delta = |\Delta|e^{1.05\pi}$. Letting the constriction lie along the x-axis, to converge to the 'linear' solution we choose as an initial guess for the order parameter as

$$\Delta_{\text{linear}}(x) = |\Delta| \exp\left[i\frac{1.05\pi x}{L}\right] \quad . \tag{6.33}$$

To converge to the 'solitonic' solution, the initial guess for the order parameter within the constriction is

$$\Delta_{\text{solitonic}}(x) = |\Delta| \min\left(\left|\frac{2x}{L} - 1\right|, 1\right) \exp\left[i1.05\pi\theta\left(x - \frac{L}{2}\right)\right] \quad , \tag{6.34}$$

where $\theta(x)$ is the usual unit step function. With these two initial guesses, we can now undergo the procedure outlined in Section 6.3 to determine the self-consistent solutions for the order parameter. In doing so, after $\sim 10^2$ iterations we reach numerical convergence and find two different solutions for the order parameter; we plot the results for the resulting magnitude and phase in Figs. 6.14 and 6.15 respectively. Note to test robustness of the converged solutions we perturbed the initial guesses and they still converged to the same solution up to numerical precision.

Visually, the two converged solutions have characteristics highly reminiscent of their idealised initial guesses. This is particularly visible in Fig. 6.14 where the magnitude of the order parameter across the constriction oscillates around the constant bulk value, whilst in the solitonic solution the magnitude decays to nearly zero at the centre of the constriction. Similarly, for the phase of the order parameter across the constriction in Fig. 6.15, we note that the phase linearly varies from 0 to 1.05π whilst in the solitonic solution the phase oscillates around a step function. As these converged solution are stable under perturbations of the initial guesses, and qualitatively agree with the existing literature (see Refs [64, 68]) then this validates the self-consistent procedure.

Considering Fig. 6.14 we note the appearance of ripples in the magnitude of the order parameter within the leads. These were first observed in Ref [69] and correspond to constructive interference along semi-classical ballistic trajectories; in the absence of scattering sites waves originating from the leads will scatter against the constriction and produce interference patterns. Furthermore, in all plots we note spatial oscillations with a wavelength of $2a$, the smallest resolvable oscillations. These oscillations are seen in Refs [68] and [64], and are attributed to Friedel oscillations which would indeed have a wavelength of $\lambda_F/2 = 2a$ – exactly as observed here. Indeed, the period and decay of the oscillations in the magnitude of the order parameter across the constriction in the linear solution appears identical to Friedel oscillations observed in Ref [70] within the context of linear drops in the chemical potential of disordered chains; this gives weight to the argument that the condensate scatters when incident upon the constriction [71]. Contrastingly, within the solitonic solution, the decay of the oscillations does not seem to be localised around

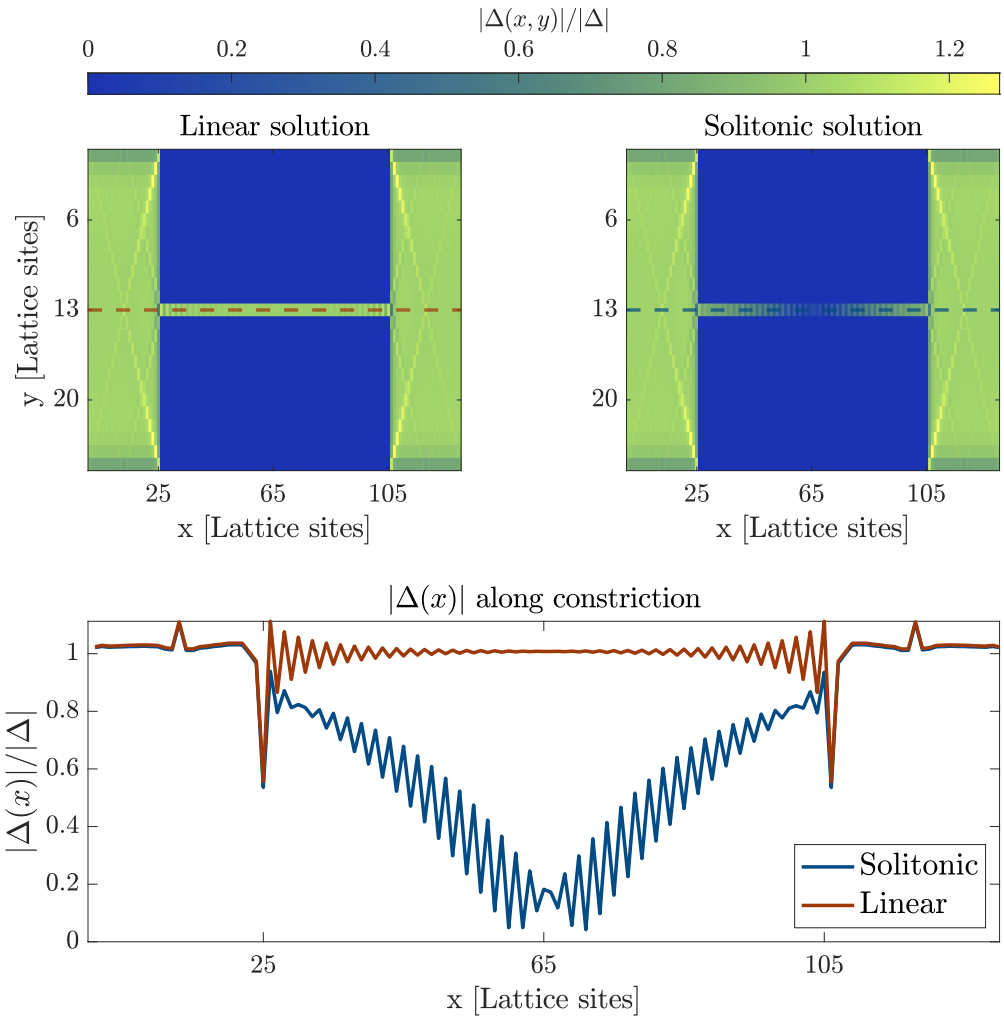

Figure 6.14: Magnitude of the converged self-consistent order parameter within the superconducting constriction. The top two colour-plots plot the magnitude of the order parameter over the entire device for both the linear and the solitonic solutions normalised by the bulk order magnitude. In the lower line-plot we plot the magnitude across just the centreline – through the constriction – for both solutions. In this figure we can see that in both solutions the magnitude of the order parameter converges to the bulk value as expected. Similar results were obtained in Ref [64].

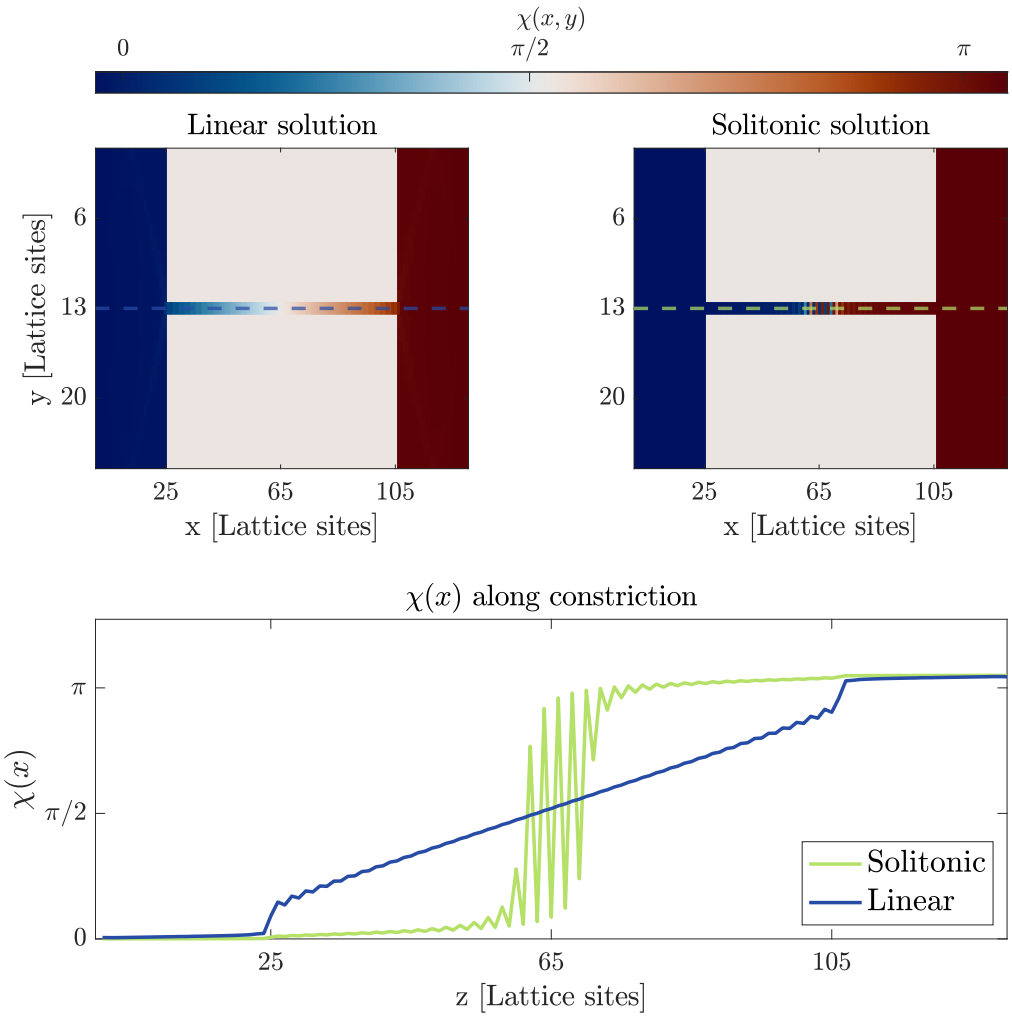

Figure 6.15: Phase of the converged self-consistent order parameter within the superconducting constriction. The top two colour-plots plot the complex phase χ of the order parameter over the entire device for both the linear and the solitonic solutions. In the lower line-plot we plot just the phase across the centreline – through the constriction – for both solutions. As with Fig. 6.14, although the two solutions exhibit very different behaviour we see that the phase χ approaches the correct bulk values as required. Similar results were obtained in Ref [64].

the constriction, but rather at the centre of the device; furthermore this decay does not appear to be exponential as expected within a Friedel model. As a result, it is difficult to prescribe a physical origin to the oscillations observed in the solitonic solution.

6.4 Simulating junctions under an external magnetic field

Thus far in the work we have retained spin-degeneracy in our simulations by ignoring any spin-dependent fields. We now consider the case of a superconducting-normal-superconducting Josephson junction – a normal material sandwiched between two superconductors – where an external magnetic field is applied to the normal region.

6.4.1 Dynamics of a junction in a magnetic field

In Section 6.2.1 we computed the bound state density and current through clean and dirty Josephson junctions in the absence of magnetic fields. In those cases the current was carried entirely by two Andreev bound states (ABS) which were labelled by either right moving or left moving states. However, when we include spin into our system, we must now understand how this extra degree of freedom effects the resulting ABS.

To this end, we write the Hamiltonian for the pure nanowire under an external magnetic field along the z-axis – ignoring for now any superconductivity – as

$$H = \int \mathrm{d}\mathbf{x}\, \psi^\dagger(x)\left[-\frac{\hbar^2}{2m_e}\nabla^2 + U_0 a\delta(\mathbf{x}) - g\mu_B B\sigma_z - \mu\right]\psi(x) \quad , \tag{6.35}$$

We also assume that the dominant energy scale is set by the chemical potential $\mu \gg \Delta, U_0, g\mu_B B$, such that we can still linearise the normal-state dispersion relation around the Fermi wavevectors k_F. This is illustrated in Fig. 6.16. Note the fact that $\mu \gg \Delta$ implies we are still working in the Andreev approximation regime. Repeating the procedure outlined in Section 6.2.2, to order $\mathcal{O}(k_F)$, we can rewrite the Hamiltonian for the bare nanowire as

$$\begin{aligned} H = &\int \mathrm{d}\mathbf{x}\, \psi_L^\dagger(x)[i\hbar v_F\partial_x + U_0\delta(\mathbf{x}) - g\mu_B B\sigma_z]\psi_L(x) \\ &+ \int \mathrm{d}\mathbf{x}\, \psi_R^\dagger(x)[-i\hbar v_F\partial_x + U_0\delta(\mathbf{x}) - g\mu_B B\sigma_z]\psi_R(x) \\ &+ U_0\Big(\psi_L^\dagger(0)\psi_R(0) + \psi_R^\dagger(0)\psi_L(0)\Big) \quad . \end{aligned} \tag{6.36}$$

Motivated by Fig. 6.16, we now introduce the interior spinor by

$$\psi_{\mathrm{in}} = \begin{pmatrix} \psi_{R\downarrow} \\ \psi_{L\downarrow} \end{pmatrix} \quad , \tag{6.37}$$

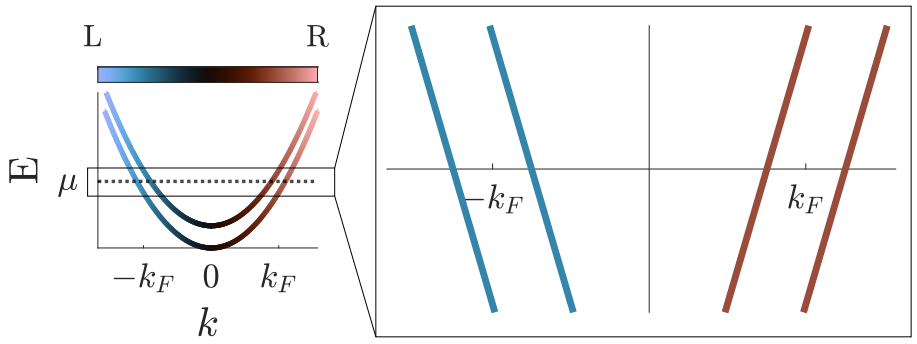

Figure 6.16: Dispersion relation of nanowire under an external magnetic field. The colour-bar depicts the curvature of the dispersion relation: a negative slope corresponds to left-moving states, whilst a positive slope corresponds to right-moving states. By zooming in on the dispersion over a small energy range around the Fermi level we see the presence of an inner mode and an outer mode, each consisting of a right-moving and left-moving state. Essentially the spin-degenerate states of Fig. 6.5 have been split by the external magnetic field.

and the exterior spinor by

$$\psi_{\text{ext}} = \begin{pmatrix} \psi_{R\uparrow} \\ \psi_{L\uparrow} \end{pmatrix} \quad , \tag{6.38}$$

such that we can split the Hamiltonian into two decoupled Hamiltonians: $H = H_{\text{in}} + H_{\text{ext}}$, where

$$H_{\text{in}} = \int \mathrm{d}\mathbf{x}\, \psi^{\dagger}_{\text{in}}(x)[-i\hbar v_F \partial_x \tau_z + U_0(I + \tau_x)\delta(\mathbf{x}) - g\mu_B B]\psi_{\text{in}}(x) \quad , \tag{6.39}$$

and

$$H_{\text{ext}} = \int \mathrm{d}\mathbf{x}\, \psi^{\dagger}_{\text{ext}}(x)[i\hbar v_F \partial_x \tau_z + U_0(I + \tau_x)\delta(\mathbf{x}) + g\mu_B B]\psi_{\text{ext}}(x) \quad . \tag{6.40}$$

The main difference between Eq. (6.36) and Eqs. (6.39) and (6.40) is that we have decoupled the Hamiltonian from a pair of coupled left-moving and right-moving spinors into a pair of decoupled inner and exterior spinors. However, the scattering potential U_0 now mixes the left-moving and right-moving components of each spinor, but not the spinor's themselves; the scattering potential cannot perform spin-flips.

Denoting the inner and outer bands by energies of the inner and outer bands by $E_{\pm}$ respectively, the continuum dispersion relation is thusly modified as

$$E_{\pm} = \frac{\hbar^2 k^2}{2m_e} - \mu \pm g\mu_B B \quad . \tag{6.41}$$

Similarly, the respective Fermi wavevector k_F for each band is given by

$$\begin{aligned} k_F^{\pm} &= \sqrt{\frac{2m_e\mu}{\hbar^2} \mp \frac{2m_e g\mu_B B}{\hbar^2}} \\ &= \sqrt{k_F^2 \mp \frac{2m_e g\mu_B B}{\hbar^2}} \\ &\sim k_F \mp \frac{m_e g\mu_B B}{\hbar^2 k_F} = k_F \mp \frac{g\mu_B B}{\hbar v_F} \quad , \end{aligned} \tag{6.42}$$

where the last approximation assumes that $g\mu_B B \ll \frac{\hbar^2 k_F}{2m_e}$. As a result, we introduce a phase parameter θ_B to parametrise the strength of the magnetic field by

$$\theta_B \equiv \frac{2g\mu_B BL}{\hbar v_F} \quad . \tag{6.43}$$

From Eq. (6.42), we can determine that θ_B corresponds to the phase the electrons and holes will pick up as they perform a round-trip of length $2L$ in the normal region whilst under an external magnetic field [72].

6.4.2 Simulating clean junctions under an external magnetic field

We now simulate the dynamics of the one-dimensional junction under an external magnetic field. We utilise the same lattice parameters as in Section 6.2.3. With regard to the magnetic field, we tune the strength of the field B such that θ_B in Eq. (6.43) varies from 0 to π. In Fig. 6.17 we plot the bound state density within the nanowire for a range of θ_B.

Compared to the density of states shown in Fig. 6.6, we now see four bound states instead of two. This is as we no longer have spin degeneracy and are now observing both spin-up and spin-down *and* right-moving and left-moving states. Additionally, we see in Fig. 6.17 that as θ_B increases, the two bands move up and down relative to each other; this is simply the two spin-bands being Zeeman shifted. However, when $\theta_B = \pi$ the bands coalesce and are degenerate again. To understand this phenomena, we return to the description of ABS in Section 6.1.2: For energies $|E| > \Delta$ Andreev bound states of finite lifetime are present as they can tunnel into the superconductor. However, although the Zeeman shift pushes previously bound states out of the gap, it also necessarily cycles states from below the gap *inside*. As a result, the total number of bound states within the gap remains unchanged. When $\theta_B = \pi$, an Andreev state below the Fermi level has now been brought up in energy such that it is degenerate with the initial state, which itself has been pushed up in energy such that it has finite lifetime and no longer bound.

In Fig. 6.18 we plot the current for each of the applied external magnetic fields at zero temperature. The most startling result is the appearance of a π phase shift in the current-phase relationship when $\theta_B = \pi$. Indeed this effect was first

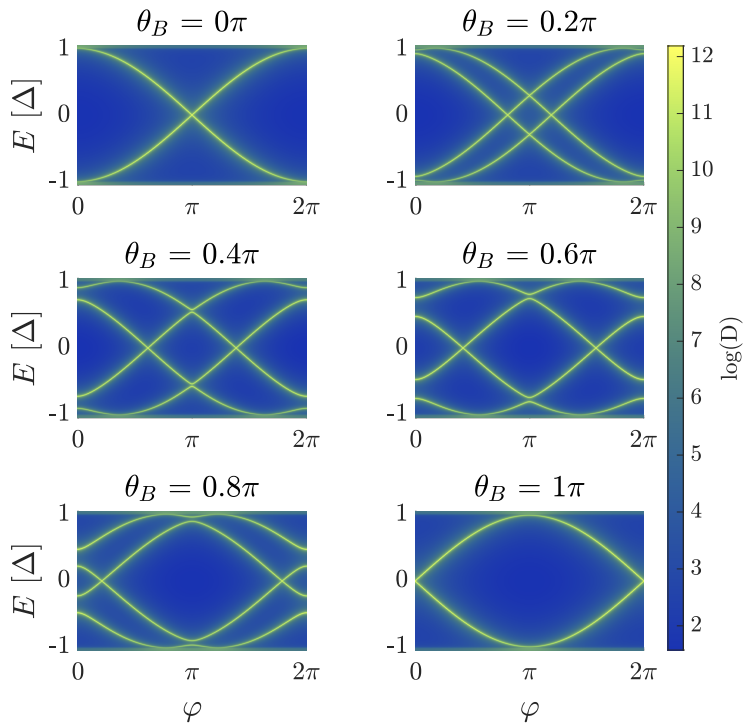

Figure 6.17: Heatmap of the log of the total density of states $D(\varphi, E)$ as a function the phase difference φ and energy E for a range of magnetic field strengths parametrised by θ_B from Eq. (6.43). Similar results were observed in Ref [72].

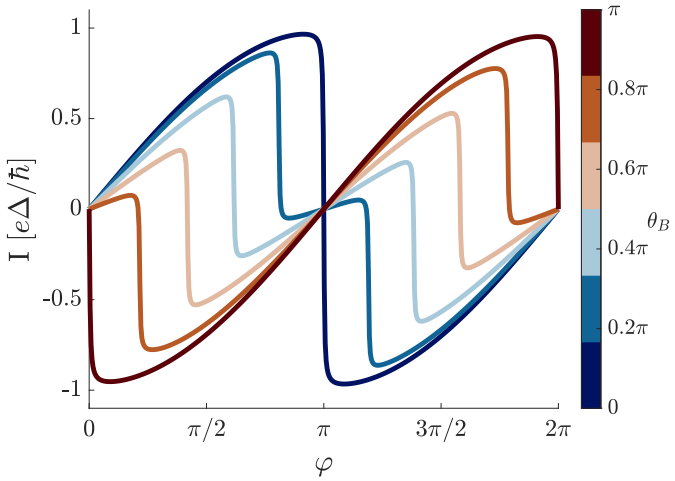

Figure 6.18: Supercurrent through a one-dimensional clean Josephson junction under an external magnetic field at zero temperature. The different plots overlaid correspond to a different external magnetic field strength B which is parametrised through the angle θ_B. Similar results were observed in Ref [72].

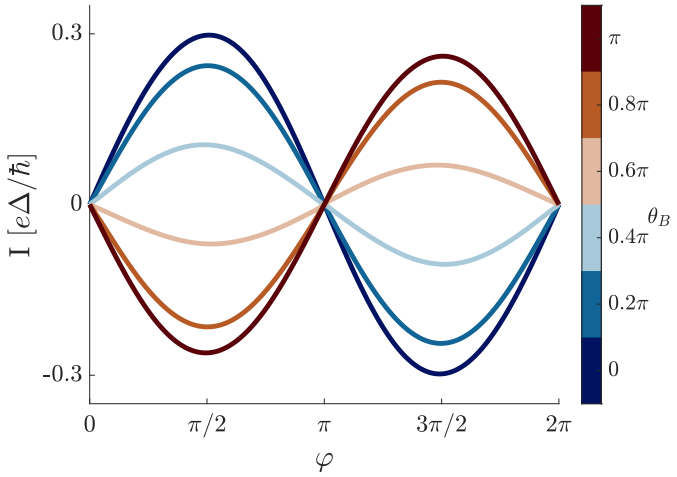

Figure 6.19: Supercurrent through a one-dimensional clean Josephson junction under an external magnetic field at a temperature of $T = \Delta(2k_B)^{-1}$. The different plots overlaid correspond to a different external magnetic field strength B which is parametrised through the angle θ_B.

clearly predicted in Ref [73] and observed experimentally in Refs [74, 75]. The appearance of this result can be inferred from Fig. 6.17 alone: as we are working at zero temperature only states with energies below the Fermi level are occupied; initially for $\varphi < \pi$ this is a right-moving state carrying positive current, whilst for $\varphi > \pi$ this is a left-moving state carrying negative current. However, under the external magnetic field the states move relative to each other such that when $\theta_B = \pi$, for $\varphi < \pi$ now the *left-moving* state is below the Fermi-level, whilst for $\varphi > \pi$ the *right-moving* state is below the Fermi-level. As a result, we see a 'flip', or π-phase shift in the Josephson current as the direction of the current carrying states has flipped. Note that the discontinuities of the current are due to working at zero temperature; at finite temperature the Fermi function broadens the Fermi level such that states both above and below the Fermi level can be occupied. In this regime, current can be carried by both the left-moving and right-moving states resulting in a smoothing of the discontinuities. We plot the results for finite temperatures in Fig. 6.19.

In Fig. 6.19 we now observe the smooth sine wave and the pronounced π phase flip as expected from conventional theory [72]. To probe the nature of these phase flips, we can parametrise the current phase relation by $I = I_C(B)\sin(\varphi + \varphi_0(B))$, where φ_0 is the phase shift induced by the external magnetic field, and I_C is the modified critical current. By sweeping the magnetic field strength, we can extract critical current and phase shifts which we plot in Fig. 6.20

In Fig. 6.20 we can observe oscillations in the critical current which were first predicted by Buzdin in Ref [73]. These oscillations in the critical current correspond

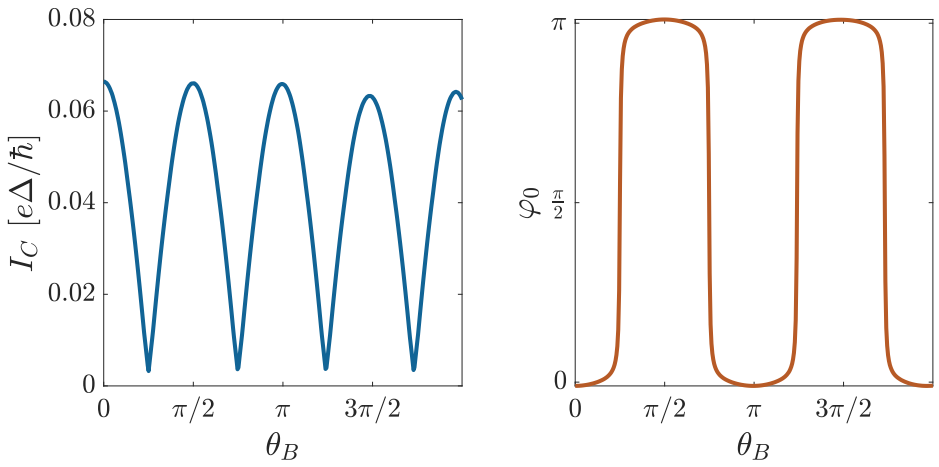

Figure 6.20: The critical current and phase shift induced by the external magnetic field. On the left the critical current drops when the phase shift experiences a π flip as the current must pass through zero to experience a π-phase flip – with more precision we should see the critical current drop to zero at points of transition. Similar results were observed in Ref [72].

to the π-flips within the phase, as the current must necessarily go through zero to flip. It is only due to numerical imprecision that we do not see the critical current vanishing when the phase flips. We also observe that the phase shift φ_0 flip-flops between 0 and π as we sweep through the external magnetic field strength. Note that the rounded transitions as we jump in phase is simply due to numerical imprecisions in parametrising the phase shift φ_0 at small critical currents.

6.4.3 Simulating dirty junctions under an external magnetic field

In Section 6.4.2 we observed that the magnetic field splits the Andreev bound states according to their spin, but did not couple the left-moving states with the right-moving. However, in Eqs. (6.39) and (6.40) we noted that the inclusion of the scattering potential will indeed couple the left-moving and right-moving components of each spin-band.

We now repeat the simulation of Section 6.4.2 with the same lattice parameters except with the inclusion of a scattering potential within the nanowire. We also fix the external magnetic field such that $\theta_B = 0.4\pi$ and instead vary the scattering potential such that the transmission coefficient varies from 1 to 0.5. We plot the resulting bound state densities in Fig. 6.21.

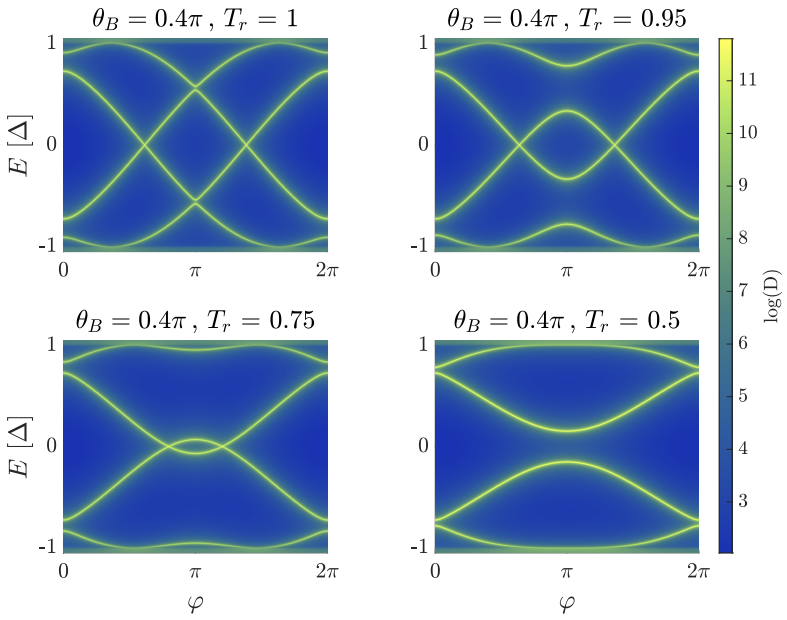

Figure 6.21: Heatmap of the log of the total density of states $D(\varphi, E)$ of a Josephson junction under an external magnetic field as a function the phase difference φ and energy E and for a range of transmission coefficients. For each plot the magnetic field is tuned such that $\theta_B = 0.4\pi$

From Fig. 6.21 we note that as the transmission decreases – and hence the coupling between the left and right moving states increases – we see an avoided crossing opening at $\varphi = \pi$ as the scattering potential is now coupling these states. This avoided crossing increases as the scattering potential increases due to the increased mixing of left-moving and right-moving states. Furthermore, we note that some of the crossings appear to remain degenerate; these are crossings of left-moving and right-moving states with *different* spin as the impurity is a spin-independent scatterer and cannot perform spin-flips. A final feature of note is that when the scattering potential is large enough, a gap forms within the ABS spectrum. To observe the effects of this gapped spectrum, we plot the current through the device for the varying transmissions in Fig. 6.22 – again working at zero temperature for clarity.

The prominent trend in the current-phase relations is that as the transmission coefficient decreases, the maximum current is reduced and the shape of the current is 'smoothed'. Indeed there is a competition between the external magnetic field which splits the two spin bands, and the scattering potential which opens an avoided crossing in the spectrum. However, for a large enough scattering strength we necessarily open a gap in the spectrum leading to only a single current carrying state being occupied at zero temperature. As a result, we transition from a B-field dominated device characterised by discontinuities in the current, to a scattering dominated regime with a smooth current as only a single mixed state is occupied

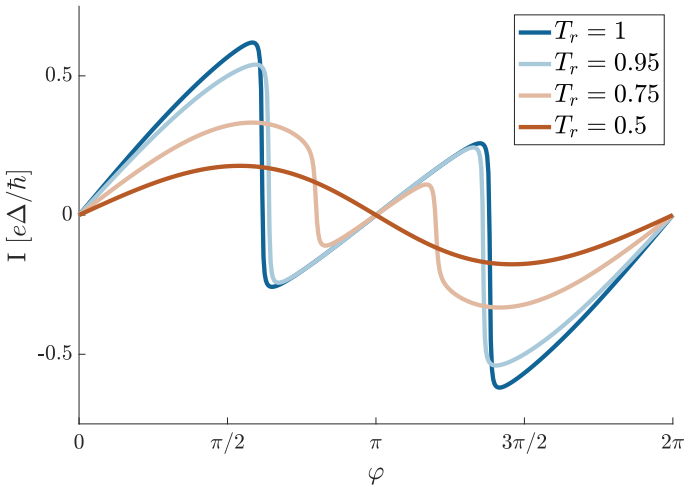

Figure 6.22: The zero-temperature supercurrent corresponding to Fig. 6.21 overlaid on the same axis. For each current, the colour indicate the transmission through that particular junction. An external magnetic field is applied in all of the plots such that $\theta_B = 0.4\pi$.

for any phase difference φ. At finite temperatures these effects are washed out and we simply see a sine wave which decays in amplitude as the scattering is increased.

Chapter 7

Anomalous Josephson current

The critical current between an ordinary and extraordinary superconductor is strongly dependent on the angle between the surface of the sample and the crystal axes... The minimum energy of the contact does not always correspond to the point $\varphi = 0$.

—V.B. Geshkenbein and A.I. Larkin, *The Josephson effect in superconductors with heavy fermions*

Chapter Summary

The purpose of this thesis is to outline the $SU(2)$ gauge covariant description of transport in non-equilibrium systems, and apply it to transport through Josephson junctions. Although we have mostly ignored spin to better clarify the preceding discussion, we now study the effects of spin dependent interactions on the transport; for brevity we will focus on transport through Josephson junctions possessing Rashba spin-orbit coupling under an external magnetic field. In this situation rather than observing a simple Josephson effect, we will observe anomalous current – the flow of current even at zero phase bias in the junction.

To study this, we will consider four separate physical systems: junctions with transverse sub-band mixing due to spin-orbit coupling, junctions with a spin-flipping term in the Hamiltonian, junctions containing disorder, and finally 'topological' junctions where the proximitised leads contain the effects of spin-orbit coupling which quantitatively changes the induced superconducting correlations. In each case we will study the appearance of the anomalous effect, and in the case of the junctions with disorder we will model experimental data probing the anomalous Josephson effect.

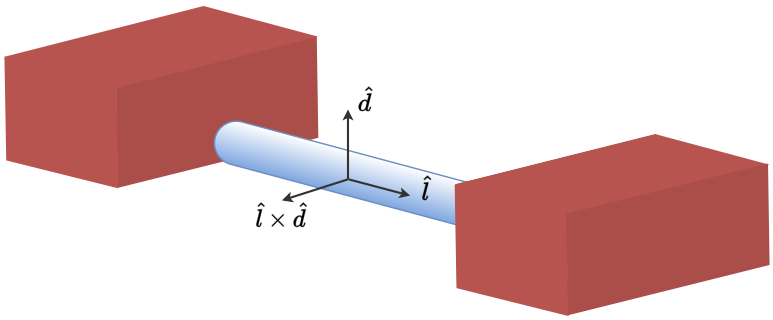

Figure 7.1: Nanowire Josephson junction where the red regions indicate the bulk superconducting leads, whilst the blue region depicts the nanowire. The axis is chosen such that $\hat{l}$ is the axis of transport, and $\hat{d}$ is normal to the substrate and hence the direction of the Rashba spin-orbit interaction.

7.1 Anomalous Josephson current

Given two superconductors with a phase difference of φ separated by a weak-link, the usual Josephson effect states that a current proportional to $\sin(\varphi)$ will flow. In Section 6.4.2 we found that under an external magnetic field, the Josephson current could undergo a so-called π-flip and be proportional to $\sin(\varphi + \pi)$. However, as noted by Buzdin in Ref [76], if both time-reversal and spatial-inversion symmetry are broken within the junction then an arbitrary phase shift $\varphi_0 \in (0, \pi)$ can be induced such that

$$I(\varphi) \propto \sin(\varphi + \varphi_0) \quad . \tag{7.1}$$

This effect, known as the anomalous Josephson effect, has recently been experimentally measured in various different Josephson junction architectures [77, 78].

7.1.1 Origin of anomalous Josephson current

Before we study numerically the anomalous Josephson effect, we must derive the origin of the effect. We begin by considering a semiconducting nanowire on some substrate which two superconducting leads have been deposited onto. The axis is orientated such that the l-axis is parallel to the nanowire, and the d-axis is parallel to the normal of the substrate plane – see Fig. 7.1 for an illustration. As a result, the interfacial electric field between the nanowire and the substrate then points in the d-axis such that single particle Hamiltonian can be given by [31]

$$H_{\text{s.p.}} = -\frac{\hbar^2}{2m_e}\nabla^2 - i\alpha\nabla \cdot \left(\boldsymbol{\sigma} \times \hat{d}\right) - \mu \quad . \tag{7.2}$$

For this device, the eigenvectors of Eq. (7.2) are given by $|\Psi\rangle = e^{ik\hat{l}\cdot\mathbf{r}}|\chi\rangle$, where

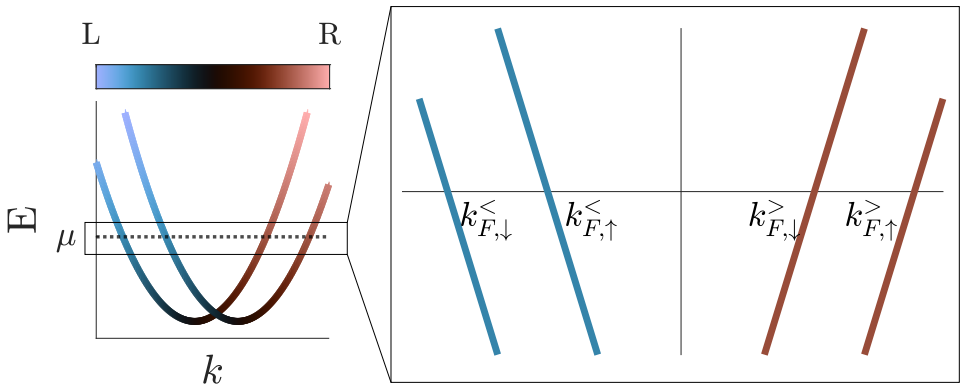

Figure 7.2: Dispersion relation for a one-dimensional nanowire with spin-orbit coupling and setting $B = 0$. The colour-bar depicts the curvature of the dispersion relation: a negative slope corresponds to left-moving states, whilst a positive slope corresponds to right-moving states. By looking at a small region around the Fermi level – generally $\mu \pm \Delta$ as this is the region where superconducting effects play a role – we note the presence of four separate bands: a pair of spin-up and spin-down left moving states, and a pair of right-moving spin-up and spin-down states. The point along the x-axis at which each state crosses the Fermi level defines the Fermi wavevector for each state.

$|\chi\rangle \equiv a\,|\uparrow\rangle + b\,|\downarrow\rangle$ for some coefficients a and b, such that

$$H_{\text{s.p.}}\,|\Psi\rangle = \left[\frac{\hbar^2 k^2}{2m_e} + \alpha k \boldsymbol{\sigma}\cdot\left(\hat{d}\times\hat{l}\right) - \mu\right]|\Psi\rangle = E\,|\Psi\rangle \quad . \tag{7.3}$$

Rotating the spin-basis such that it is parallel to $\hat{l}\times\hat{d}$, we plot the dispersion relation of Eq. (7.3) in Fig. 7.2. The key observation is that by linearising the system around the Fermi level – exactly as done in Section 6.4.1 – we obtain four different states depending on the spin, and direction of travel, of the electron state; the Fermi wavevectors of these states are denoted by $k_{F,\uparrow/\downarrow}^{</>}$ where $<$ denotes left-moving, whilst $>$ right-moving.

As described in Section 6.1.2, the supercurrent through this device will be predominantly carried by Andreev bound states (ABS): bound states consisting of a counter-propagating electron and hole pair with different spins. As these states are constructed from the available electronic states, in the spin-orbit coupled nanowire they can either be constructed from the outer states – those with larger wavevector – of Fig. 7.2, or the inner states – those with smaller wavevector; this separation of inner and outer states was first introduced in Section 6.4 within the context of the π-flip. Furthermore, assuming we are working in the Andreev approximation such that $\Delta \gg \mu_F$, then from Eq. (6.7) an Andreev bound state constructed from, say, the outer states will not scatter into the inner states. For an 'outer' ABS, the total

phase shift of the electron and hole as they traverse the normal region of length L – more simply the net phase they pick up as they cross the gap – is given by [72]

$$\phi_{\text{out}} \equiv L(k^{>}_{F,\uparrow} + k^{<}_{F,\downarrow}) \ , \tag{7.4}$$

whilst for an 'inner' bound state it is given by

$$\phi_{\text{in}} \equiv L(k^{<}_{F,\uparrow} + k^{>}_{F,\downarrow}) \ . \tag{7.5}$$

Letting γ be some constant proportional to the *ratio* of the density of states of the outer ABS relative to the inner ABS then we can introduce another phase parameter

$$\phi \equiv \gamma\phi_{\text{out}} + (1-\gamma)\phi_{\text{in}} \ , \tag{7.6}$$

which acts to measure the *net* phase picked up across the junction. This quantity – expressed in a slightly different form – was first introduced by Krive *et al.* in Ref [79] and further expanded upon by Yokoyama *et al.* in Ref [72].

Regarding anomalous current through the junction, we note that the ground state, and hence the state with no current flow, occurs when the phase gained by traversing the junction is completely compensated by the phase offset of the bulk leads [80]. As a result, if $\phi \neq 0$ then this implies a phase asymmetry in the junction such that the ABS will carry a *net* phase shift across the gap. For zero phase difference between the two bulk superconducting leads, this net phase gain is not offset and, as a result, anomalous current will flow.

7.1.2 Conditions for observing anomalous current

As discussed in Section 7.1.1, to observe an anomalous current the Andreev bound states (ABS) must carry a net phase ϕ across the junction. Although there are many possible ways one can enforce this, we shall focus on two general schemes which are very common in the literature: systems exhibiting dispersion relation asymmetry, and systems with a spin-flipping field.

7.1.2.1 Systems with a spin-flipping term

The minimal model exhibiting anomalous Josephson effects due to a spin-flipping term in the Hamiltonian is illustrated in Fig. 7.3. It consists of a one-dimensional system with spin-orbit interaction, exactly as discussed in Section 7.1.1, however, we now add a magnetic field in the plane perpendicular to $\hat{d}$. As described in Section 7.1.1, the strong spin-orbit interaction polarises the spins along the $\hat{l} \times \hat{d}$ axis, hence the component of the magnetic field along the $\hat{l}$ axis acts to tilt the spins, and will induce spin-flips in the system. For a discrete model, we plot the numerical dispersion relation for a nanowire with the inclusion of the spin-flipping field in Fig. 7.4

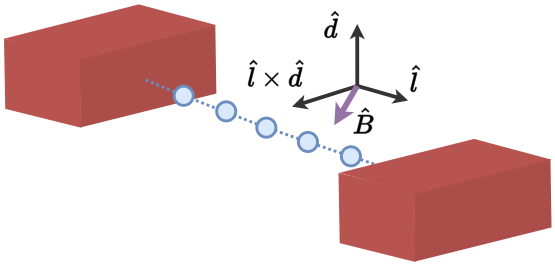

Figure 7.3: Schematic of the minimal model exhibiting anomalous current due to a spin-flipping term. The 1D nanowire wire is aligned along the $\hat{l}$ direction, whilst the Rashba spin-orbit interaction points along the perpendicular $\hat{d}$ direction. The magnetic field has some component in both the $\hat{l}$ and the $\hat{l} \times \hat{d}$ axis.

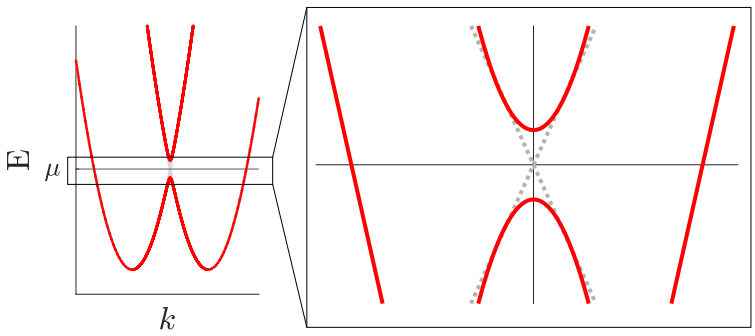

Figure 7.4: Dispersion relation corresponding to the device in Fig. 7.3. In grey we have plotted the dispersion relation where $B = 0$, exactly as plotted in Fig. 7.2. By linearising the states around the Fermi level, we can see that the inner spinors have been coupled by the inclusion of the magnetic field perpendicular to the spin-polarisation axis.

The consequence of the spin-flipping term, as visible in Fig. 7.4, is the opening of an avoided crossing in the dispersion relation between the inner states of opposite spin. By positioning the Fermi level within this gap, we reduce the density of states of the inner states, as left-moving spin-up electrons will now couple with right-moving spin-down electrons to form standing waves within the device [59]. Letting k_F and k_α correspond to the characteristic wavevectors of the Fermi level and the spin-orbit interaction respectively, then the component of the magnetic field aligned with the spins shifts the Fermi wavevectors such that [72]

$$\begin{aligned} k^{>}_{F,\uparrow} &= -k_F - k_\alpha + \frac{g\mu_B B}{\hbar v_F} & \qquad k^{<}_{F,\downarrow} &= k_F + k_\alpha + \frac{g\mu_B B}{\hbar v_F} \\ k^{<}_{F,\uparrow} &= -k_F + k_\alpha - \frac{g\mu_B B}{\hbar v_F} & \qquad k^{>}_{F,\downarrow} &= k_F - k_\alpha - \frac{g\mu_B B}{\hbar v_F} \end{aligned} \tag{7.7}$$

As a result, the phases picked up by the inner and outer ABS are given by $\phi_{\text{out}} = -\phi_{\text{in}} = \frac{2g\mu_B B}{\hbar v_F}$. Using Eq. (7.6), the net phase across the junction is given by

$$\phi = (2\gamma - 1)\frac{2g\mu_B B}{\hbar v_F} , \tag{7.8}$$

where γ is proportional to the ratio of the density of states of the inner and the outer states. Critically, the spin-flipping term modulates the density of the inner states such that $\gamma \neq \frac{1}{2}$. As a result $\phi \neq 0$, and a net phase is picked up as Andreev bound states traverse the normal region; this will lead to an anomalous Josephson current.

7.1.2.2 Systems with dispersion relation asymmetry

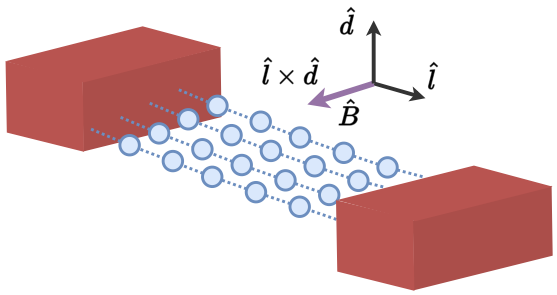

Figure 7.5: Schematic of the minimal model exhibiting anomalous current due to a dispersion relation asymmetry. Note that the nanowire is now a 2D lattice such that we have transverse sub-bands. The magnetic field now points completely in the $\hat{l} \times \hat{d}$ direction.

The minimal model exhibiting anomalous Josephson effects due to dispersion relation asymmetry is illustrated in Fig. 7.5. Note that the lattice corresponding to the nanowire must be two-dimensional, containing lattice sites along both the axis of transport $\hat{l}$, and along the spin-polarisation axis $\hat{l} \times \hat{d}$, and we have also applied a magnetic field along the $\hat{l} \times \hat{d}$ axis. Due to the confinement along the $\hat{l} \times \hat{d}$ axis, our system will possess transverse sub-bands states. Critically, the Rashba spin-orbit interaction will couple different sub-bands of opposite spin and produce asymmetry in the resulting bandstructure. As an example, we plot the band-structure for a system possessing two sub-bands in Fig. 7.6 – see Appendix C.2 for a description of this calculation.

Ignoring for now the external magnetic field, the sub-band coupling heavily modulates the inner states, whilst leaving the outer states mostly invariant – this can be clearly seen in the inset of Fig. 7.6. As a result, the Fermi velocity of the outer states $v_{F,\text{out}}$, which can be well approximated by the initial Fermi velocity v_F, can be distinguished from the Fermi velocity of the inner states $v_{F,\text{in}}$. When we include the effects of the magnetic field along the $\hat{l} \times \hat{d}$ direction, we can rewrite Eq. (7.7)

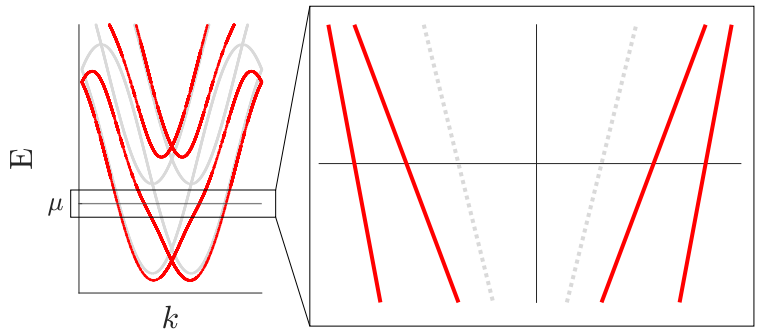

Figure 7.6: Dispersion relation corresponding to Fig. 7.5. On the full bandstructure on the left, the parabolas in grey correspond to the dispersion relation in the absence of spin-orbit coupling; we see that they consist of two sets of parabolas shifted in energy – these are the transverse subbands. The spin-orbit coupling mixes the subbands of different spin, however, by linearising the states around the Fermi level we only notice a shift in the wavevectors of the inner spinor.

as [72]

$$\begin{aligned} k^{>}_{F,\uparrow} &= -k_F - k_\alpha + \frac{g\mu_B B}{\hbar v_{F,\text{out}}} & k^{<}_{F,\downarrow} &= k_F + k_\alpha + \frac{g\mu_B B}{\hbar v_{F,\text{out}}} \\ k^{<}_{F,\uparrow} &= -k_F + k_\alpha - \frac{g\mu_B B}{\hbar v_{F,\text{in}}} & k^{>}_{F,\downarrow} &= k_F - k_\alpha - \frac{g\mu_B B}{\hbar v_{F,\text{in}}} \end{aligned} \tag{7.9}$$

such that $\phi = \frac{g\mu_B BL}{2\hbar}\left(v^{-1}_{F,\text{out}} - v^{-1}_{F,\text{in}}\right)$. Once again, as $\phi \neq 0$ we expect to observe anomalous current.

To conclude, to observe an anomalous Josephson effect within devices possessing some Rashba-spin orbit coupling we must apply an external magnetic field such that

$$\left(\hat{l} \times \hat{d}\right) \cdot \hat{B} \neq 0 \quad . \tag{7.10}$$

Although Eq. (7.10) is the oft-cited condition that must be met such that one will measure an anomalous Josephson effect (see Refs [6,76,78,81]) we note that although Eq. (7.10) *must* be met, it is not, by itself, sufficient. Indeed we must still introduce some asymmetry between the inner and outer states; either by mixing sub-bands to induce Fermi velocity asymmetry between the inner and outer states as in Fig. 7.6, or by coupling the inner states with a magnetic field with some component perpendicular to $\hat{l} \times \hat{d}$ as in Fig. 7.4. For a superconducting constriction the argument is outlined in Appendix C.3, however, the idea is the same in that we simply require a net phase pickup across the junction.

7.2 Simulating anomalous Josephson current

As described in Section 7.1.1, the origin of the anomalous Josephson effect – current flow at zero phase bias of the bulk superconductors – is due to the interplay between

spin-orbit coupling and an external magnetic field. We now look to simulating the effect numerically for the cases outlined in Section 7.1.2 – namely, systems with dispersion asymmetry and systems with a spin-flipping term. To clarify the current section, we will ignore the effects of any spin effects in the superconducting leads leaving this discussion for Section 7.4.

7.2.1 Discretised Hamiltonian for both systems

For the remainder of this section we will be considering the physical device pictured in Fig. 7.1; a semiconducting nanowire on some substrate which two superconducting leads have been deposited onto. We assume that the device is two-dimensional where the central region has length denoted by L and width by W. The axis is orientated such that the x-axis is parallel to the nanowire and the y-axis is normal to the substrate plane. As a result, the interfacial electric field between the nanowire and the substrate then points in the z-axis such that the Rashba spin-orbit term can be given by [31]

$$H_{\text{spin-orbit}} = \frac{\alpha_R}{\hbar}(\hat{z} \times \hat{\mathbf{p}}) \cdot \boldsymbol{\sigma} \quad . \tag{7.11}$$

As for the external magnetic field, we assume it is applied solely in the xz-plane and is parameterised by an angle θ. Considering these assumptions, we can use Section 3.3.1 to write the full Hamiltonian for the proximitised nanowire as

$$H = \int \mathrm{d}x \begin{pmatrix} \psi^\dagger(x) & \psi^\top(x) \end{pmatrix} \begin{pmatrix} H_{\text{nanowire}} & i\Delta S(x)\sigma_y \\ -i\Delta^* S(x)\sigma_y & -H^*_{\text{nanowire}} \end{pmatrix} \begin{pmatrix} \psi(x) \\ \psi^*(x) \end{pmatrix} \quad , \tag{7.12}$$

where

$$H_{\text{nanowire}} = \frac{\hat{\mathbf{p}}^2}{2m_e} + (1 - S(x))(i\alpha\hat{p}_x\sigma_z - i\alpha\hat{p}_z\sigma_x - g\mu_B\mathbf{B}\cdot\boldsymbol{\sigma}) - \mu \quad , \tag{7.13}$$

describes the single particle Hamiltonian for the isolated nanowire with Rashba spin-orbit coupling and an externally applied magnetic field, and

$$S(x) \equiv \Theta(-x - L/2) + \Theta(x - L/2) \quad , \tag{7.14}$$

acts as a generalised step-function to turn terms of the Hamiltonian off and on in different regions of the device – $\Theta(x)$ is the usual Heaviside step-function.

Concerning the discretised Hamiltonian, as in Section 6.2.1 we separate the device into three distinct regions: the left lead, the central region, and the right lead. In the left and right leads we assume a homogenous superconductivity with no external magnetic field or spin-orbit terms. This is in contrast to the central region which we assume to be non-superconducting and with some intrinsic spin-orbit coupling. As a result, for the left lead L, and the right lead R, we assume the same

Hamiltonian utilised in Section 6.2.1, namely:

$$\begin{aligned} H_{L/R} = &\sum_{\alpha\in L/R} \left(\psi_\alpha^\dagger(t')[\epsilon-\mu]\psi_\alpha(t') + \psi_\alpha^\dagger(t')\Delta_\alpha\psi_\alpha^*(t') + \psi_\alpha^\top(t')\Delta_\alpha^\dagger\psi_\alpha(t')\ \right) \\ &- t\sum_{\langle\alpha,\beta\rangle\in L/R}\Big(\psi_\alpha^\dagger\psi_\beta(t') + \psi_\beta^\dagger\psi_\alpha(t')\Big) \quad , \end{aligned} \tag{7.15}$$

where $\alpha \in L/R$ sums over all lattice sites in the respective lead and $\langle\cdots\rangle$ implies summing over nearest neighbours in each lead. For the central region, we set $\Delta = 0$ such that the material is non-superconducting, and include the term

$$H_{\mathbf{B}} = \sum_{\mathbf{x}\in C}\psi_{\mathbf{x}}^\dagger g\mu_B\mathbf{B}(x)\cdot\boldsymbol{\sigma}\psi_{\mathbf{x}} \quad , \tag{7.16}$$

where $\mathbf{x} \in C$ denotes summing over all sites in the central region, to include the effects of the magnetic field. We recall the useful phase parameter θ_B introduced in Section 6.4 to parametrise the phase shift induced by the external magnetic field:

$$\theta_B \equiv \frac{2g\mu_B BL}{\hbar v_F} \quad , \tag{7.17}$$

in general we will refer to θ_B rather than the explicit value for $\mathbf{B}$. Using Section 4.1.5 to include the effect of the Rashba spin-orbit coupling, we add spin dependent phase shifts to the hopping parameters as per

$$\begin{aligned} t_{(n_x,n_z),(n_x+1,n_z)} &\to t_{(n_x,n_z),(n_x+1,n_z)}\exp\left[-\frac{iam_e\alpha_R}{\hbar^2}\sigma_z\right] \\ t_{(n_x,n_z),(n_x,n_z+1)} &\to t_{(n_x,n_z),(n_x,n_z+1)}\exp\left[\frac{iam_e\alpha_R}{\hbar^2}\sigma_x\right] \quad . \end{aligned} \tag{7.18}$$

7.2.2 Model with dispersion relation asymmetry

As described in Section 7.1.1, to induce an anomalous Josephson effect we must include some asymmetry within the system. One possibility outlined was the inclusion of Fermi velocity asymmetry between the inner and outer spinors – a model for this is depicted in Fig. 7.5, where the transverse sub-bands couple with the spin-orbit coupling to induce Fermi velocity asymmetry. To this end, in this section we set $n_z = 8$ such that our simulation is two-dimensional, yet set $\lambda_F = 16a$ such that the device has the same physics as a one-dimensional wire[1]. Finally, unless otherwise stated we set the temperature to be $T = 150$mK.

[1] As outlined in Section 6.2.3, as long as the Fermi wavelength λ_F is greater than the width of the device, then from the electron's perspective the device is quasi-1D regardless of the number of lattice sites in the z-axis

Given a two-dimensional device in the xz-plane with a spin-orbit vector pointing in the $\hat{y}$-axis, we can write the single-particle Hamiltonian as

$$H_{\text{s.p.}} = \frac{\mathbf{p}^2}{2m_e} + i\alpha p_x \sigma_z - i\alpha p_z \sigma_x - \mu \quad . \tag{7.19}$$

Here we see how the spin-orbit terms – those linear in momentum – couple the x and z components of the electron's momentum through its spin. As a result, assuming that $n_z \ll n_x$ such that the direction of transport is along the x-axis, then the dispersion relation for the x-component of the momentum will have coupled sub-bands – we plot an example for two transverse bands in Fig. 7.6. See Appendix C.2 for a more in-depth analysis of the effect of this sub-band mixing.

To observe an anomalous current we must satisfy the condition of Eq. (7.10) that

$$(\hat{x} \times \hat{y}) \cdot \hat{B} \neq 0 \quad . \tag{7.20}$$

As a result, we set $\mathbf{B} = B\hat{z}$ such that the magnetic field is identically aligned with the vector perpendicular to both the axis of transport x and the spin-orbit direction $\hat{y}$. Using the lattice parameters outlined in Section 7.2.1, we sweep the strength of the externally applied magnetic field by varying θ_B from 0 to $5\pi/4$. To begin, we compute the density of states of the two-dimensional device using the procedures outlined in Section 6.2.1. We plot the results in Fig. 7.7.

In Fig. 7.7 we can see the familiar band-splitting due to the Zeeman field which was explained in Section 6.4, however, we now see that the bands are not just being shifted vertically in energy, but also horizontally as a function of the phase difference φ across the junction. To explore the consequences of this shift in the bound state density, we plot the current-phase relation in Fig. 7.8.

The striking feature of this plot is that as the magnetic field increases, we see phase shifts in the resulting Josephson current – rather than observing zero current at $\varphi = 0$ we observe zero current at $\varphi = -\varphi_0$. This is the predicted anomalous Josephson current predicted to exist in this device due to the sub-band mixing and the external magnetic field. As discussed in Section 7.1.1, we can parametrise the anomalous Josephson current as

$$I(\varphi) = I_C(B)\sin(\varphi + \varphi_0(B)) \quad , \tag{7.21}$$

where φ_0 is the phase shift and I_C is the change in critical current. By sweeping θ_B from 0 to 2π we can extract the critical current I_C and the phase shift φ_0 which we plot in Fig. 7.9.

This analysis was first done for systems exhibiting Fermi velocity asymmetry due to sub-band asymmetry in Ref [72] where they observed the same oscillations in the critical current and the jumps in the phase shift φ_0 as in Fig. 7.9. To validate that the induced phase shift is due to Eq. (7.10) in combination with the sub-band mixing, we set $\mathbf{B} = B\hat{x}$ whilst maintaining sub-band mixing and observed no anomalous

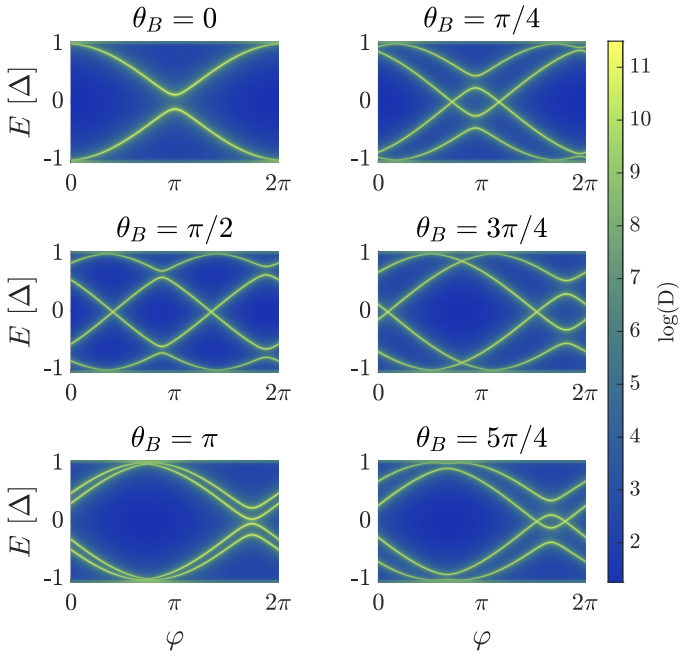

Figure 7.7: Heatmap of the logarithm of the total density of states $D(\varphi, E)$ as a function the phase difference φ and energy E for a two-dimensional device with Rashba spin-orbit coupling. A magnetic field is applied in the z-axis – the axis of spin-polarisation induced by the spin-orbit coupling – such that the induced phase shift varies from 0 to $5\pi/4$. Similar results were observed in Ref [72].

physics. Setting $\mathbf{B} = B\hat{y}$ but removing the term $i\alpha p_z \sigma_x$ from the Hamiltonian, also resulted in no anomalous current.

7.2.3 Model with a spin-flipping term

In Section 7.2.2 we introduced Fermi velocity asymmetry through sub-bands coupling which allowed for the observation of an anomalous Josephson effect. However, in Section 7.1.2 we noted that one could also observe the same physics by considering a one-dimensional system with a component of the magnetic field *perpendicular* to the spin-polarisation axis. This is depicted in Fig. 7.3.

To study this, we consider the same lattice model as outlined in Section 7.2.1, except we now set $n_z = 1$ such that the device is purely one-dimensional and there is no possibility of sub-band coupling. Furthermore, we generalise the magnetic field such that it is given by

$$\mathbf{B} = \begin{pmatrix} B_x & 0 & B_z \end{pmatrix} = B\begin{pmatrix} \cos(\theta) & 0 & \sin(\theta) \end{pmatrix} \quad . \tag{7.22}$$

In this manner we still meet the condition of Eq. (7.10) necessary to observe the anomalous Josephson effect; the B_z term is aligned with the spin-orbit polarisation and acts to drive the anomalous current, whilst the B_x component tilts the spin direction and opens an avoided crossing in the spectrum as depicted in Fig. 7.4. We

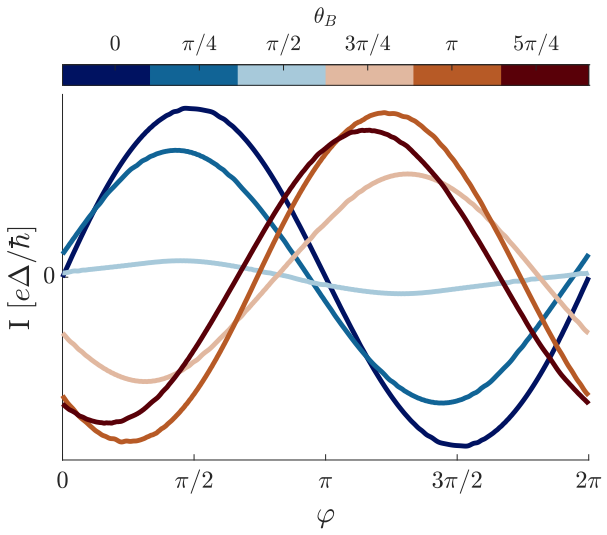

Figure 7.8: Current phase relation for a two-dimensional device with Rashba spin-orbit coupling at $T = 150$mK. A magnetic field is applied in the z-axis – the axis of spin-polarisation induced by the spin-orbit coupling – such that the induced phase shift varies from 0 to $5\pi/4$. The corresponding bound states which carry the current are shown in Fig. 7.7. Similar results were observed in Ref [72].

still use the parameter θ_B to parametrise the magnetic field strength, however, we now define it such that it considers only the magnetic field along the $\hat{z}$-axis:

$$\theta_{B_z} \equiv \frac{2g\mu_B B_z L}{\hbar v_F} \quad . \tag{7.23}$$

To tune the Fermi level such that it is placed between the avoided crossing induced by the spin-tilting B_x field, we swept the value for the Fermi level till we saw the most pronounced Josephson effect; this ending up being when $\mu = \epsilon_\alpha$. By setting $g\mu_B B_z = 10\Delta$ and varying θ_{B_z} from 0 to $5\pi/4$, we plot the resulting density of states in Fig. 7.10.

In Fig. 7.10 the ABS have been split into distinct inner and outer bands, each consisting of two bound states themselves. Furthermore, by changing the magnetic field strength the two bands do not cross. Although, under the external magnetic field the two bound states of the inner band do move up and down relative to each other – reminiscent of Fig. 6.17 – we note that the outer band seems to be shifted horizontally in phase, albeit in a somewhat asymmetric fashion. To probe the consequences of this, working at $T = 150$mK we plot the resulting supercurrent in Fig. 7.11.

Within Fig. 7.11 the anomalous Josephson effect is apparent as we see the sinusoid shifting to the left in phase. As in Section 7.2.2, we can parametrise the shifted sine wave using Eq. (7.21). In doing so we plot the extracted critical current and phase shift φ_0 in Fig. 7.12

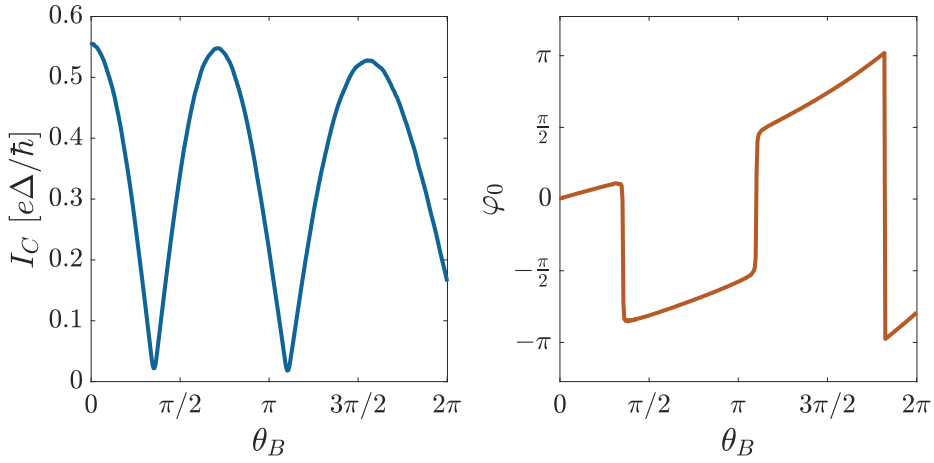

Figure 7.9: Extracted values for the critical current I_C and anomalous phase shift φ_0 as we vary the magnetic field applied along the z-axis to a two-dimensional Josephson junction with Rashba spin-orbit coupling. The sub-band mixing induced by the spin-orbit coupling combined with the magnetic field aligned with the spins drives the anomalous current.

Although there are quantitative differences between Fig. 7.12 and Fig. 7.9, they do share qualitative features – namely, a critical current and phase shift which oscillates with the external magnetic field.

7.3 Modelling an experimental device

Thus far we have validated our results by comparing to a range of different theoretical results from a range of groups using different computational techniques. However, although we have reproduced many of the 'classic' Josephson junction results, such as the sinusoidal Josephson relation of Fig. 6.8, or the π phase flip of Fig. 6.19, many of which have been found experimentally by different groups, we have not yet modelled experimental data using our numerical model. To this end, we will consider a recent experiment performed by Strambini *et al.* (see Ref [78] for the published results) where they observe a Josephson junction 'battery' which converts an external magnetic field passing through a material possessing some Rashba spin-orbit coupling into a phase bias across the superconducting leads.

7.3.1 Review of experiment

In the actual experiment, they made use of a superconducting quantum interference device (SQUID) to measure the phase shift in the Josephson junction, however, for brevity we will outline only the salient features of the device relative to this thesis.

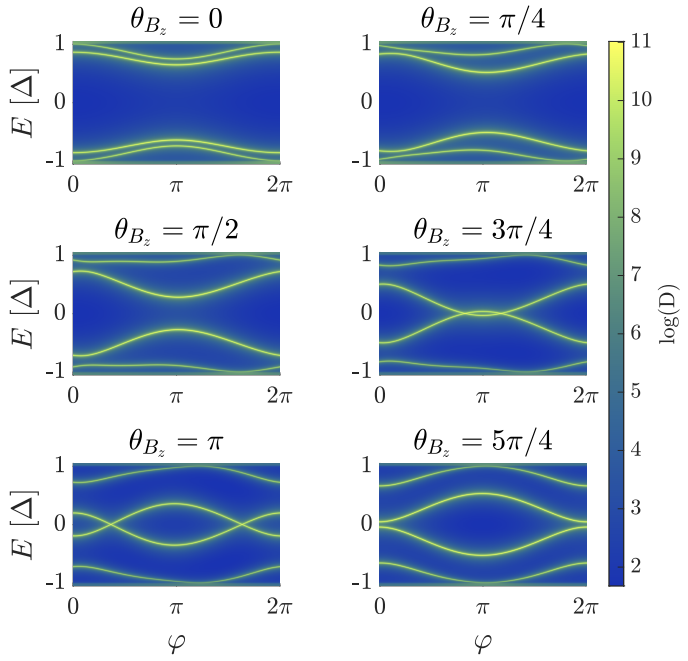

Figure 7.10: Heatmap of the log of the total density of states $D(\varphi, E)$ through a one-dimensional Josephson junction as a function the phase difference φ and energy E. We apply a magnetic field of strength $g\mu_B B_x = 10\Delta$ in the x-axis and tune the magnetic field strength in the z-axis such that θ_{B_z} varies from 0 to $5\pi/4$. We also set $\mu = \epsilon_\alpha$ to best observe the anomalous Josephson effect.

To this end, the device in question can be well modelled by Fig. 7.13: two trivial aluminium superconducting leads separating a InAs nanowire possessing some Rashba spin-orbit coupling with an external magnetic field applied. In the experiment the nanowire penetrates several coherence lengths into the superconductor thus a sharp transition between the superconducting leads and the normal region is not realistic, but rather we must include an 'intermediate' region where the nanowire experiences a proximity induced pairing potential. This intermediate region sandwiches a normal region, which as usual, possesses no order parameter. The values of the different terms of the Hamiltonian are illustrated in Fig. 7.13. Furthermore, to better match the diffusive device, we add a Gaussian potential at each lattice site to include the effects of disorder. We found that the presence of this disorder, which breaks the homogeneity of the device, was critical to modelling the data.

In the experiment they applied a magnetic field perpendicular to the axis of transport and the normal vector of the substrate – the axis of the Rashba spin-orbit coupling – hence the experiment satisfies the condition Eq. (7.10) necessary for the appearance of an anomalous Josephson effect. Furthermore, as this is a real device with many transverse sub-bands which would be coupled by the spin-orbit coupling, we expect to observe an anomalous current as described in Section 7.2.2.

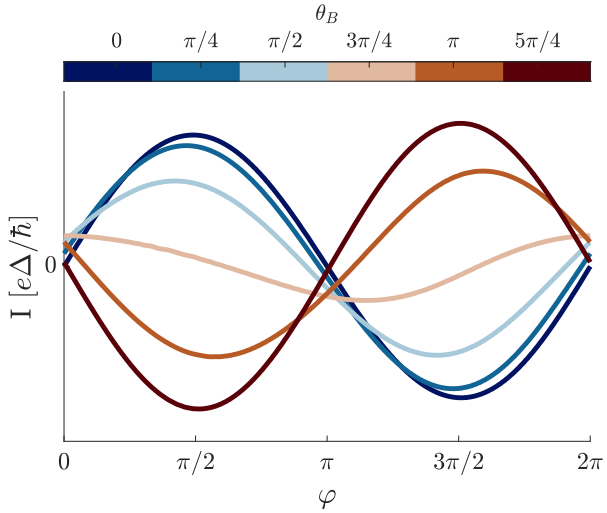

Figure 7.11: Current phase relation for a one-dimensional Josephson junction possessing Rashba spin-orbit coupling under an external magnetic field. We apply a magnetic field of strength $g\mu_B B_x = 10\Delta$ in the x-axis and tune the magnetic field strength in the z-axis such that θ_{B_z} varies from 0 to $5\pi/4$. We also set $T = 150$mK, and let $\mu = \epsilon_\alpha$ to best observe the anomalous Josephson effect.

7.3.2 Numerical results

To tune the numerical model to the physical system, we first set the effective mass to $m_e = 0.023m$, the bulk superconducting gap in the aluminium leads to $|\Delta_{\text{Al}}| = 340\mu$eV, and the proximitised superconducting gap in the InAs nanowire as $|\Delta_{\text{InAs}}| = 200\mu$eV [82]. For the nanowire, we set the g factor to 4, and the Rashba spin-orbit strength to $\alpha = 8 \times 10^{-11}$eV m, which we will discuss later. Additionally, we set the chemical potential μ and the lattice spacing a such that the Fermi velocity is given by $v_F \sim 10^6 \text{ms}^{-1}$. Additionally, we set the average strength of the Gaussian impurities such that the resulting mean free path is given by $l_e \sim 100$nm (refer to Ref [83] for a detailed account of these computations). These parameters then give a coherence length of $\xi = 200$nm. Finally, we set the physical dimensions of the normal region of the device to have a width of 20nm and a length of 40nm. By doing so the lattice model is two-dimensional and, as a result of the confinement, will produce transverse sub-bands. As a result, with the inclusion of a magnetic field, from Section 7.2.2 we expect to observe an anomalous current due to the dispersion relation asymmetry induced by the confined sub-bands. We also set the temperature to $T = 50$mK to match the experimental setup.

To measure the phase shift, we begin by aligning the nanowire in the x-axis and applying the spin-orbit vector in the y-axis such that hopping the zx-plane accrues a phase shift as described in Section 7.2.2. To induce a phase shift we then apply a magnetic field in the y-axis. By parametrising the resulting current phase relation by $I \propto \sin(\varphi - \varphi_0)$, we can extract the phase shift φ_0 produced.

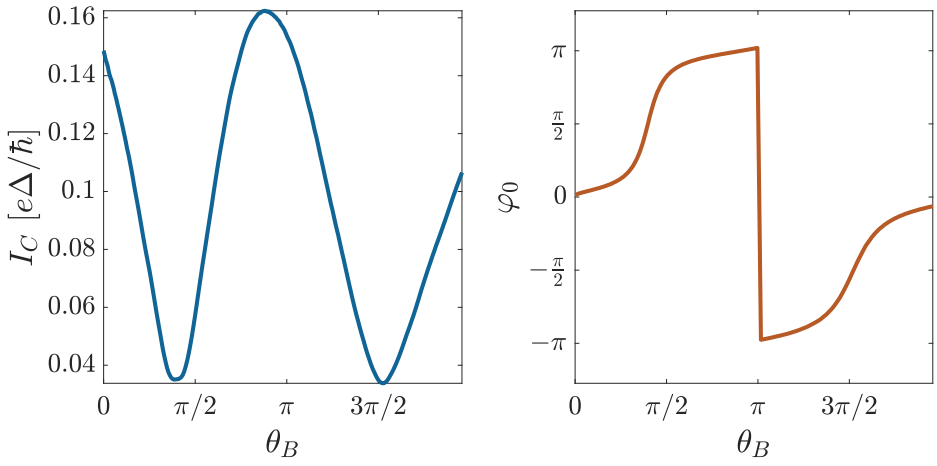

Figure 7.12: Extracted values for the critical current I_C and anomalous phase shift φ_0 as we vary the magnetic field applied along the z-axis to a one-dimensional Josephson junction with Rashba spin-orbit coupling. We have also applied a magnetic with with strength 10Δ in the x-axis to couple the inner spinors.

Without knowing the explicit impurity distribution of the device, we must average the resulting phase shift over a range of chosen impurities. To do so, we first select an impurity distribution then compute the phase shift φ_0 in the resulting Josephson current. We then redraw from the impurity distribution and repeat the process such that we have an ensemble of different phase shifts. Finally, to match with the experiment we consider the *extrinsic phase shift* of the device defined as $\varphi_{\text{ex}} \equiv 2\varphi_0$; this is an artifact of the experimental device involving a SQUID which possesses two Josephson junctions.

In Fig. 7.14 we plot, in dark blue, the mean extrinsic phase shift at different magnetic field strengths whilst around this line, in light blue, we plot one standard deviation. In the orange markers we overlay the experimental data taken from Ref [78]. Overall, the behaviour of the numerical model closely matches the experimental results. The most striking features is the linear regime for $-15\text{mT} \lesssim B \lesssim 15\text{mT}$, followed by a sharp transition to a saturated regime for magnetic fields outside of this. The fact that the computational model also observes these features allows us to potentially understand why they are present in the data – we leave this for future work. We should comment that increasing the magnetic field further decreases, and eventually destroys the phase shift. This is in contrast to the ideal theory present in Ref [78] where the phase shift approaches a non-zero asymptote.

Although we see a good fit to the data, we must discuss the physical parameters used to fit it – namely, some of the parameters chosen do not agree entirely with that

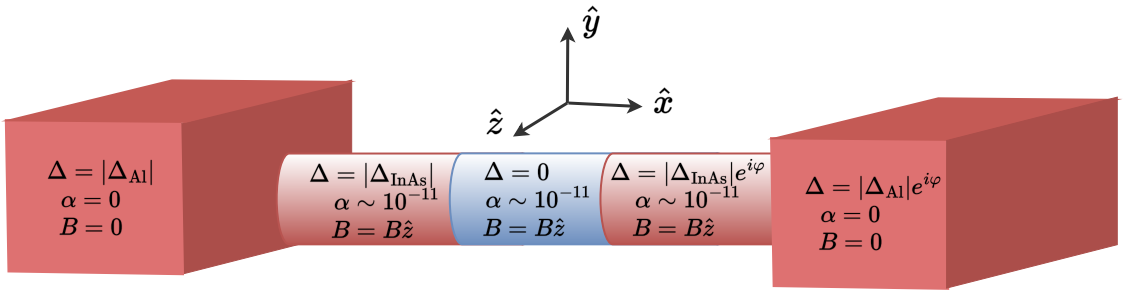

Figure 7.13: Diagram of the device being modelled to recreate the experimental data of Ref [78]. Physically, the device consists of two aluminium leads separated by an indium arsenide nanowire. A magnetic field is applied along the z-axis. The two bulk leads consist of bulk s-wave superconductors, however, connected to them is a region of proximitised nanowire. As a result, this region contains a superconducting gap, Zeeman term, and spin-orbit coupling. In the centre of the device is a region of un-proximitised nanowire.

of the experiments. For instance, we set the g factor to 4 and the Rashba spin-orbit strength to 8×10^{-11}eV$\cdot$m, whilst we would expect these values to be closer to 12 and 3×10^{-11}eV $\cdot$ m respectively for an InAs nanowire. Similarly, in the supplementary section of Ref [78] they measure the mean free path to be 30nm and estimate the coherence length to be closer to 100nm, which is a factor of approximately $2-3$ smaller than our parameters. Additionally, their nanowires have a radius closer to 90nm and have an un-proximitised length of around 100nm, again a factor of approximately $2-3$ greater than our parameters. Furthermore, in our simulations the behaviour of the junction as a function of the parameters does not seem to be particularly smooth – small changes in the chosen parameters lead to large shifts in the behaviour of the junction. As a result, we had to carefully tune each parameter till we saw the phase saturation at approximately $\phi_{\mathrm{ex}} = \pm\pi/2$. Anecdotally it seems the disorder strength, together with the length of the device, plays the critical role in determining this; we leave this analysis for a later work.

7.4 Topological Josephson junctions

In Section 7.2 we numerically explored the anomalous Josephson current in devices where the leads were assumed to be bulk superconductors with no spin-splitting or spin-orbit terms present. However, in devices where the normal region is only covered by a thin layer of superconducting material the magnetic field can penetrate the device easily. Similarly, if the superconductor is deposited over parts of the nanowire larger than the coherence length of the condensate, we must also include spin-orbit effects in the leads. As the bulk leads supply the superconducting correlations

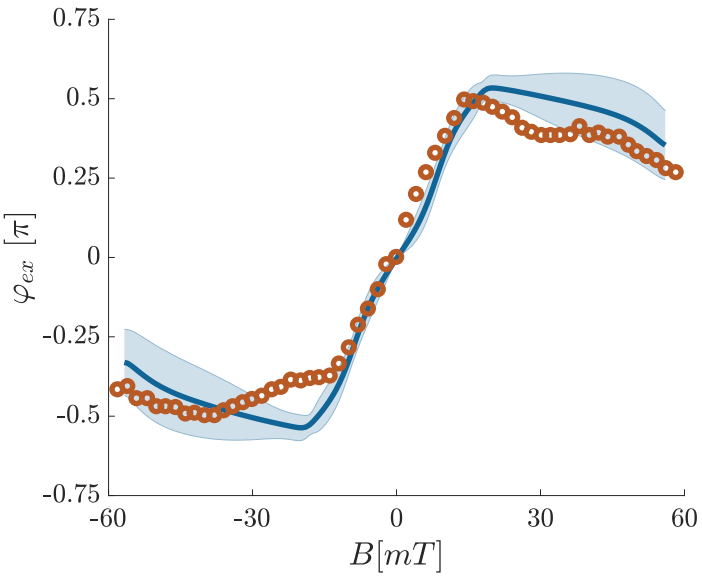

Figure 7.14: Extrinsic phase shift for a system described by Fig. 7.13 as a function of the external magnetic field. The thick blue line corresponds to an average phase shift for an ensemble of impurity strengths, whilst the light blue region surrounding it plots one standard deviation from the mean. The orange markers overlaid are the experimental data taken from Ref [78].

which drive the Josephson effect, then the physics of the leads strongly determines the resulting dynamics. As a result, by including spin effects in the leads, the correlations will be qualitatively different to bulk s-wave leads (see Ref [84] for more reasoning on this). In this section we explore how these correlations modify the anomalous Josephson effect, and in turn how we can use anomalous current to detect topological transitions.

7.4.1 Hamiltonian for the system

For the remainder of this chapter we will be considering the device pictured in Fig. 7.15; a semiconducting nanowire on some substrate upon which two thin superconducting leads have been deposited. The axis is orientated such that the x-axis is parallel to the nanowire and the y-axis is parallel to the normal of the substrate plane. As a result, we can utilise the Hamiltonian of Section 7.2.1 as the physics of the two systems are identical. However, to allow for the spin-orbit coupling and Zeeman splitting to be present in the leads we must modify Eq. (7.13) to read as

$$H_{\text{nanowire}} = \frac{\hat{\mathbf{p}}^2}{2m_e} + i\alpha\hat{p}_x\sigma_z - i\alpha\hat{p}_z\sigma_x - g\mu_B\mathbf{B}\cdot\boldsymbol{\sigma} - \mu \quad , \tag{7.24}$$

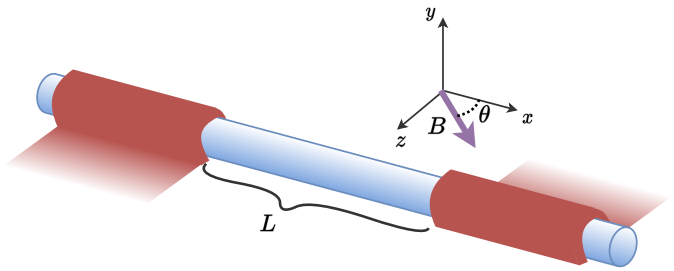

Figure 7.15: Illustration of the device considered in Section 7.4. The superconducting leads in red are only a thin layer relative to the London penetration depth such that an external magnetic field penetrates them completely. Furthermore, rather than treating the leads as bulk superconductors, we rather treat the portions of the nanowire which are proximitised by the deposited superconductor as the bulk leads; this assumes the the superconducting coherence length is much smaller than the proximitised regions such that they do indeed act as reservoirs for the condensate.

where we have removed the generalised step-function. We also introduce a parameter which parametrises the strength of the spin-orbit interaction ϵ_α by

$$\epsilon_\alpha \equiv \frac{m_e \alpha^2}{2\hbar^2} \quad , \tag{7.25}$$

we can also parametrise the spin-orbit interaction by the wavevector

$$k_\alpha \equiv \sqrt{\frac{2m_e\epsilon_\alpha}{\hbar^2}} = \frac{m_e\alpha}{\hbar^2} \quad . \tag{7.26}$$

Finally, to simplify the problem, we set the chemical potential to zero and assume that

$$\epsilon_\alpha \gg g\mu_B B \ , \ \Delta \tag{7.27}$$

such that the dominant energy contribution is due to the spin-orbit coupling.

7.4.2 Topology in superconducting quantum wires

An emerging field in condensed matter is that of 'topological materials' with the application of algebraic topology for the purpose of classifying physical phenomena. Topology, tautologically, is the study of topological spaces; for physicists the main application is in the study and classification of smooth manifolds. A central question in topology is if given two manifolds, is it possible to continuously deform one manifold into the other, then reverse the deformation to return to the original manifold? If this is possible, the manifolds are said to be homeomorphic and share the same topological properties [67]. To ground the conversation, our object of interest are gapped Hamiltonians – systems with a finite energy difference between the ground and first excited states. In a gapped system the ground state is 'protected' from higher states by the presence of the gap; in contrast to un-gapped systems where a system initially prepared in the ground state can be easily excited to another state

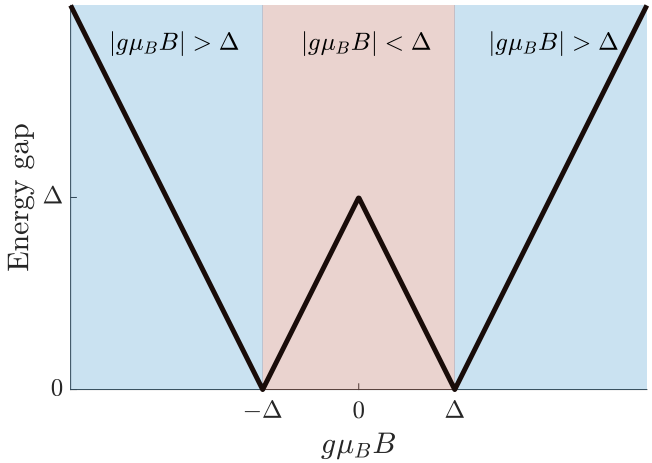

Figure 7.16: Energy gap of a one-dimensional superconducting system with the dominant energy scale being the spin-orbit interaction as the external magnetic field is tuned. The gap is defined as the difference between the positive and negative branches of the quasiparticle spectrum. We have shaded the regions depending on the sign of $g\mu_B|B| - \Delta$, where we note that the regions also define the closing and opening of the gap.

by a perturbation. Indeed, given two gapped Hamiltonians we want to know if it is possible to deform one into the other without destroying the gap; do the two Hamiltonians have the same topology?

In the context of the proximitised nanowires with Hamiltonians given by Eq. (7.12) we note that by setting $\mu = B = 0$, then due to the superconducting gap – which for now we will assume to be present throughout the entire nanowire – the trivial excitation spectrum will be gapped due solely to the superconducting gap. However, by letting B vary, such that it solely parametrises the Hamiltonian, we want to know for what values of B is the energy gap preserved – i.e. what magnetic fields define changes in the topological phase. To this end, assuming the magnetic field is applied down the length of the nanowire $\mathbf{B} = B\hat{x}$, we can diagonalise the single-particle Hamiltonian of Eq. (7.12) to find the following single particle spectrum [85]

$$E(k)_{\pm}^2 = (g\mu_B B)^2 + \Delta^2 + \left(\frac{\hbar^2 k^2}{2m_e}\right)^2 + (\alpha k)^2 \pm \sqrt{(g\mu_B B\Delta)^2 + \left(\frac{\alpha\hbar^2 k^3}{2m_e\hbar}\right)^2 + \left(\frac{g\mu_B B\hbar^2 k^2}{2m_e}\right)^2} \quad . \tag{7.28}$$

We plot the energy gap as a function of the external magnetic field along the axis of the nanowire in Fig. 7.16. In this plot we can see that the gap closes at the critical value $g\mu_B|B| = \Delta$. Denoting the Hamiltonian at $B = 0$ as being in the trivial phase, we note for a Hamiltonian characterised by $g\mu_B|B| > \Delta$, we cannot deform the spectrum into the trivial Hamiltonian's without closing the energy gap. As a result we view Hamiltonians parametrised by $g\mu_B|B| > \Delta$ as being in the topological phase [3]. For a magnetic field in the plane of the nanowire parametrised by an angle

θ:

$$\mathbf{B} = B\big(\cos(\theta) \quad 0 \quad \sin(\theta)\big) \quad , \tag{7.29}$$

the conditions for the nanowire to be in the topological phase (assuming $\mu = 0$), which we do not prove here, is given by [3, 86]

$$g\mu_B|B| > \Delta \quad \text{and} \quad g\mu_B|B|\sin(\theta) < \Delta \quad . \tag{7.30}$$

7.4.3 Dynamics within spin-orbit coupled nanowires

We now study the nature of the low-energy states within the nanowire, as it is these electronic states which will construct the current carrying Andreev bound states (ABS).

From the assumptions outlined in Section 7.4.1, we can write the Hamiltonian for the bare, un-proximitised nanowire as

$$H_{\text{nanowire}} = \int \mathrm{d}x\, \psi^\dagger(x)\left(-\frac{\hbar^2\mathbf{D}^2}{2m_e} - \hbar\rho_0 - \epsilon_\alpha\right)\psi(x) \quad , \tag{7.31}$$

where the $SU(2)$ gauge fields are given by

$$\rho_\mu = \big(\tfrac{g\mu_B B}{\hbar}(\cos(\theta)\sigma_x + \sin(\theta)\sigma_z) \quad k_\alpha\sigma_z \quad 0 \quad 0\big) \quad , \tag{7.32}$$

and the spin-orbit energy shift, which now appears as a chemical potential, of the form

$$\epsilon_\alpha = \frac{m_e\alpha^2}{2\hbar^2} \quad . \tag{7.33}$$

To simplify Eq. (7.31), we apply an $SU(2)$ gauge transformation to transform to a rotating-spin basis $\psi(x) \to \tilde{\psi}(x) \equiv s(x)\psi(x)$ where

$$s(x) = e^{ik_\alpha x\sigma_z} \quad . \tag{7.34}$$

As the transformation of the components of ρ_μ are given by

$$\rho_\mu \to s\rho_\mu s^\dagger - is\partial_\mu s^\dagger \quad , \tag{7.35}$$

then the gauge field transforms as

$$\rho_\mu \to g\mu_B B\big(\cos(\theta)[\cos(2k_\alpha x)\sigma_x - \sin(2k_\alpha x)\sigma_y] + \sin(\theta)\sigma_z \quad 0 \quad 0 \quad 0\big) \quad , \tag{7.36}$$

where we made use of Appendix C.1. In this rotating-spin basis it appears that we have 'removed' the spin-orbit term, however, it has only been shifted into an effective magnetic field which rotates down the length of the nanowire.

As a result, we can write the bare un-proximitised nanowire Hamiltonian in the rotating-spin basis as

$$H_{\text{nanowire}} = \int \mathrm{d}x\, \tilde{\psi}^\dagger(x)\left(-\frac{\hbar^2\partial_x^2}{2m_e} - \tilde{\mathbf{B}}(x)\cdot\boldsymbol{\sigma} - \epsilon_\alpha\right)\tilde{\psi}(x) \quad , \tag{7.37}$$

where

$$\tilde{\mathbf{B}}(x) = g\mu_B B\big(\cos(\theta)\cos(2k_\alpha x) \quad \cos(\theta)\sin(2k_\alpha x) \quad \sin(\theta)\big) \quad . \tag{7.38}$$

Making use of the Nambu spinors in the rotated frame $\tilde{\Psi}^\dagger = \begin{pmatrix}\tilde{\psi}^\dagger & \tilde{\psi}^\top\end{pmatrix}$, we can now rewrite the full Hamiltonian for the proximitised[2] nanowire in the rotating-spin basis by

$$H = \int \mathrm{d}x\, \tilde{\Psi}^\dagger(x)\left[\left(-\frac{\hbar^2\partial^2}{2m_e} - \epsilon_\alpha - \tilde{B}_x\sigma_x - \tilde{B}_z\sigma_z\right)\tau_z - \tilde{B}_y\sigma_y - \Delta(x)\tau_y\otimes\sigma_y\right]\tilde{\Psi}(x) \quad . \tag{7.39}$$

7.4.3.1 Linearisation of states

In the linearisation process of Section 6.4.1 we projected the fermionic creation and annihilation operators around the left and right Fermi points $\pm k_F$. We repeat this projection, however, when the spin-orbit energy is the dominant contribution the left and right Fermi points are found at the spin-orbit wavevector $\pm k_\alpha$ – see Fig. 7.17 for justification. Indeed, we decompose the spin-rotated field $\tilde{\psi}(x)$ into a left-moving $\psi_L(x)$ and right-moving $\psi_R(x)$ component by

$$\tilde{\psi}(x) = e^{-ik_\alpha x}\psi_L(x) + e^{ik_\alpha x}\psi_R(x) \quad , \tag{7.40}$$

where we have projected onto the leading wavevector $\pm k_\alpha$. We further assume that $\psi_{L/R}$ vary over length scales much larger than k_α^{-1} such that $\psi_{L/R}$ account for small shifts in the wavevector around the Fermi points.

As in Section 6.4.1, we introduce the interior and exterior spinors by

$$\psi_{\text{in}} = \begin{pmatrix}\psi_{R\uparrow}\\ \psi_{L\downarrow}\end{pmatrix} \tag{7.41}$$

$$\psi_{\text{ext}} = \begin{pmatrix}\psi_{L\uparrow}\\ \psi_{R\downarrow}\end{pmatrix} \tag{7.42}$$

We can fully decouple Eq. (7.39) into two disjoint Hamiltonians

$$H = H_{\text{in}} + H_{\text{ext}} \ , \tag{7.43}$$

[2]Using Appendix C.1 one can show that the superconducting order parameter is unchanged in the rotating basis.

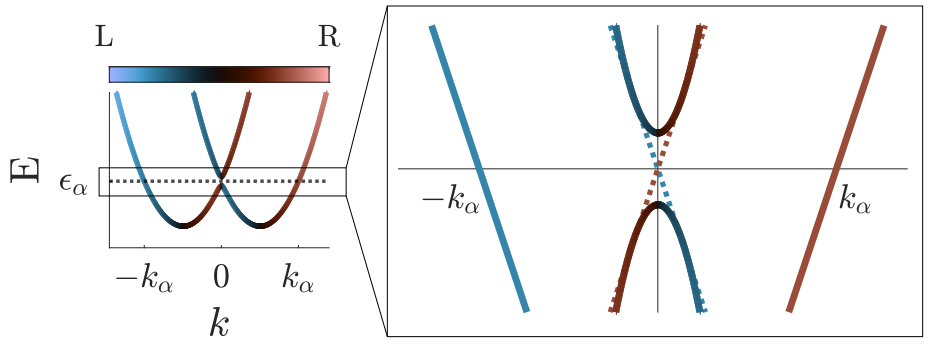

Figure 7.17: Dispersion relation of non-superconducting nanowire under an external magnetic field where the nanowire possesses some intrinsic spin-orbit coupling which provides the characteristic energy of the system. The colour-bar depicts the curvature of the dispersion relation: a negative slope corresponds to left-moving states, whilst a positive slope corresponds to right-moving states. By zooming in on the dispersion over a small energy range around the spin-orbit energy ϵ_α we see the presence of an inner mode and an outer mode. The outer modes consists of a right-moving and left-moving state, whilst the inner mode consists of a left/right moving pair which have been mixed by the external magnetic field.

where one describes the inner spinor

$$H_{\text{in}} = \int \mathrm{d}x \begin{pmatrix} \psi_{\text{in}}^\dagger & \psi_{\text{in}}^\top \end{pmatrix} \begin{pmatrix} h_{\text{in}} - g\mu_B B\cos(\theta)\sigma_x & \Delta i\sigma_y \\ -\Delta i\sigma_y & -h_{\text{in}}^* + g\mu_B B\cos(\theta)\sigma_x \end{pmatrix} \begin{pmatrix} \psi_{\text{in}} \\ \psi_{\text{in}}^* \end{pmatrix} \tag{7.44}$$

and the other the exterior

$$H_{\text{ext}} = \int \mathrm{d}x \begin{pmatrix} \psi_{\text{ext}}^\dagger & \psi_{\text{ext}}^\top \end{pmatrix} \begin{pmatrix} h_{\text{ext}} & \Delta i\sigma_y \\ -\Delta i\sigma_y & -h_{\text{ext}}^* \end{pmatrix} \begin{pmatrix} \psi_{\text{ext}} \\ \psi_{\text{ext}}^* \end{pmatrix} \tag{7.45}$$

where

$$h_{\text{in}} = -i\alpha\partial_x\sigma_z - g\mu_B B\sin(\theta)\sigma_z \quad , \tag{7.46}$$

and

$$h_{\text{ext}} = i\alpha\partial_x\sigma_z - g\mu_B B\sin(\theta)\sigma_z \quad . \tag{7.47}$$

Although the inner and outer Hamiltonians are highly similar – both possessing a magnetic field along the z-axis – the critical difference is the presence of the $g\mu_B B\cos(\theta)\sigma_x$ term which is present only in the inner Hamiltonian. As described in Section 7.1.1, this coupling of the inner states induced by the component of the magnetic field perpendicular with the spin-polarisation axis will induce anomalous current.

7.4.4 Probing the topological limit

We now consider the system outlined in Section 7.4.1 – namely, a one-dimensional nanowire with two thin superconducting leads coating the ends. As written in that

section, the nanowire possesses a Rashba spin-orbit term which defines the dominant energy scale of the system. We assume the same lattice parameters as in Section 6.4, however, to impose the spin-orbit term as the dominant energy contribution we tune the Rashba coefficient α_R such that ϵ_α from Eq. (7.25) takes the value $\epsilon_\alpha = 10t$. Furthermore, we set $\mu = 0$ to simplify the analysis.

To probe the topological junction, we first set $\theta = \pi/2$ such that the magnetic field is purely in the z-direction – namely, perpendicular to the nanowire and parallel to the spin-orbit spin polarisation direction. As a result, the condition of Eq. (7.10) is not satisfied and we do not expect to see an anomalous Josephson effect. For a range of magnetic field strengths we plot the resulting Andreev bound states (ABS) in Fig. 7.18.

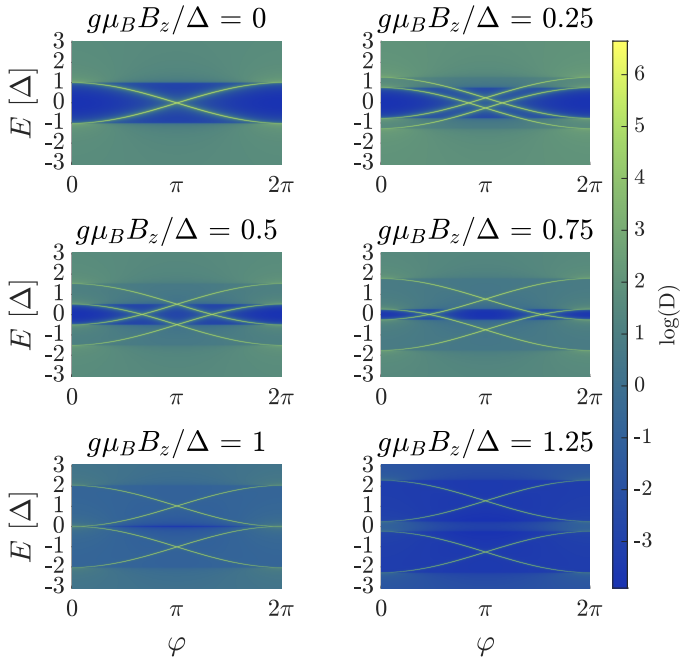

Figure 7.18: Heatmap of the log of the total density of states $D(\varphi, E)$ for a one-dimensional Josephson junction as a function the phase difference φ and energy E. A magnetic field is applied in the z-axis, parallel to the spin-polarisation axis supplied by the strong spin-orbit coupling.

From Fig. 7.18, as the external magnetic field parallel to the spin-polarisation axis is increased, the ABS split into two disjoint bands. The disjointed nature of the two bands is expected as for a magnetic field solely in this direction, we can map the Hamiltonians of Eqs. (7.44) and (7.45) onto the Hamiltonian of Section 6.4.1 by a simple basis rotation. Although, in that case, as the magnetic field increased it cycled bound states in and out of the region $E \in [-\Delta, \Delta]$ – namely, the magnetic field would push a state out of gap and into the continuum, whilst at the same time pulling a state out of the continuum and into the gap. However, in this case the magnetic field penetrates the proximitised nanowires themselves. As a result, the

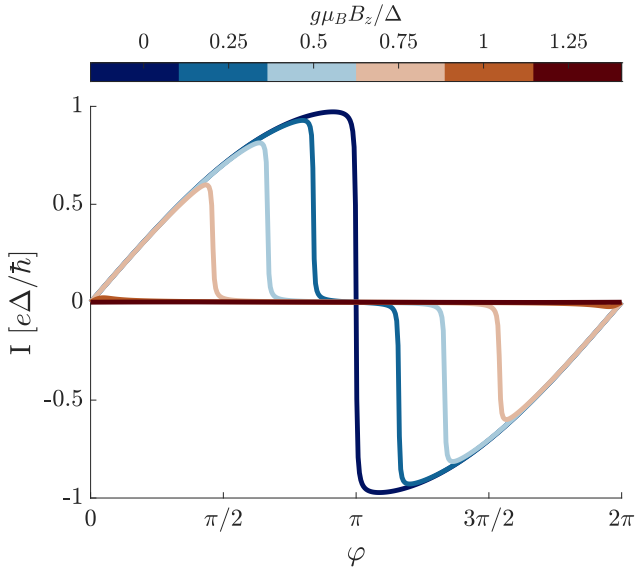

Figure 7.19: Current phase relations at zero temperature corresponding to the density of states of Fig. 7.18. The different plots overlaid correspond to a different external magnetic field strength B_z along the spin-polarisation axis.

gapped region *itself* shifts in energy according to $E \in [-\Delta \pm g\mu_B B_z, \Delta \pm g\mu_B B_z]$. Working at zero temperature, we plot the current corresponding to Fig. 7.18 in Fig. 7.19 where we observe that the supercurrent forms a plateau around $\varphi = 0$. In Fig. 7.18 we note that as the magnetic field increases, the left-moving and right-moving states of different spin bands cross; as they do so, the current carried by the left-moving and right-moving states of the lower spin-band cancel each other out to produce the observed plateau. In the extreme case of $g\mu_B B \geq \Delta$, the left-moving and right-moving states of only a single spin-band are accessible as only they have energy below the Fermi level, hence the current is completely cancelled. Furthermore we do not observe an anomalous Josephson current as expected.

We now apply the magnetic field such that it is applied parallel to the nanowire and perpendicular to the spin-polarisation axis by setting $\theta = 0$. Although we do satisfy Eq. (7.10), as there is no spin-tilting or sub-band mixing we do not expect to see any anomalous effects. As before, we plot the resulting Andreev bound state densities in Fig. 7.20.

In Fig. 7.20 we first note that one pair of bound states is entirely invariant to the change in the external magnetic field; these are the Andreev states formed by the exterior spinors as they do not feel the external magnetic field along the x-axis. However, we note that as the inner magnetic field increases in strength, curiously the gap of the inner modes *shrinks* rather than just being shifted as in Fig. 7.18. Indeed when the magnetic field has values of $g\mu_B B_x \geq \Delta$, the inner band disappears entirely! As described in Section 7.4.2, when $g\mu_B B_x > \Delta$ we are now longer in the

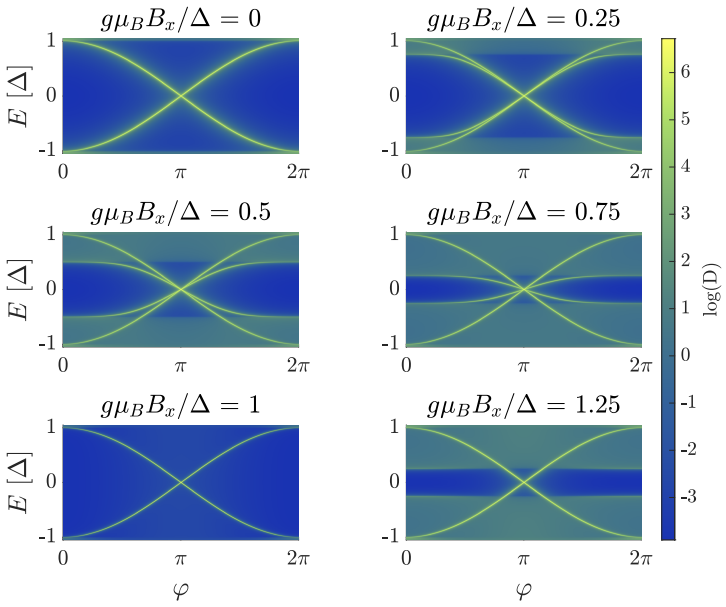

Figure 7.20: Heatmap of the log of the total density of states $D(\varphi, E)$ of a one-dimensional Josephson junction as a function the phase difference φ and energy E. The external magnetic field is parallel to the nanowire and perpendicular to the spin-polarisation axis supplied by the strong spin-orbit coupling.

trivial phase but rather in a topological phase. A sign of this topological phase transition is the disappearance of the inner Andreev states [87]. As further evidence to the vanishing of the inner mode, we plot the current, again working in the zero temperature limit, corresponding to Fig. 7.20 in Fig. 7.21. The first observation is that for no external magnetic field the maximum current has a value of $e\Delta/\hbar$ at $\varphi \sim \pi$. However, by increasing the field strength down the nanowire, although the shape of the current phase relation remains unchanged, the maximum current decreases steadily. We see that the maximum current through the device modulates from a maximum of $I_C = e\Delta/\hbar$ when $B = 0$ to a minimum of $I_C = 0.5e\Delta/\hbar$ when $g\mu_B B > \Delta$. As the inner bound state should vanish in the topological phase, one of the two current carrying states are no longer accessible. As each ABS can carry a maximum current of $0.5e\Delta/\hbar$, then as a result, the maximum critical current halves.

7.4.5 Anomalous current in topological junctions

We reproduce the numerical model outlined in Section 7.4.4 except we now let the magnetic field be directed in the xz-plane. As described in Section 7.2.3, if there is a component of the magnetic field in both the z and x-axis we should observe anomalous Josephson currents. To probe the relationship between anomalous current and the topological phase, we first set the external magnetic field to be of the form

$$\mathbf{B} = \frac{0.75\Delta}{g\mu_B}\begin{pmatrix}\cos(\theta) & 0 & \sin(\theta)\end{pmatrix} \quad . \tag{7.48}$$

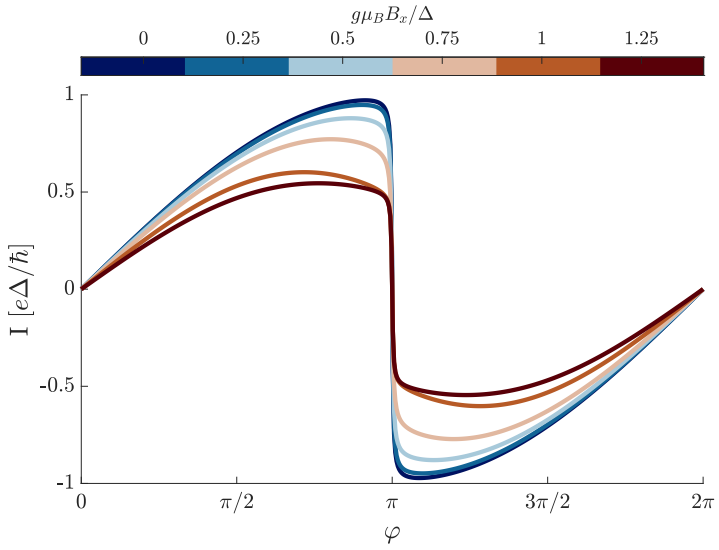

Figure 7.21: Current phase relations at zero temperature corresponding to the ABS of Fig. 7.20. The different plots overlaid correspond to a different external magnetic field strength B_x along the axis of the nanowire. We note that by increasing the magnetic field strength, the maximum supercurrent – the critical current – decreases as half of the current carrying states vanish.

such that we are in the trivial phase as $|\mathbf{B}| < |\Delta|$. We plot the corresponding bound state density for a range of angles θ in Fig. 7.22.

Although a relatively complex set of plots, we can recognise familiar cases from Section 7.4.4: when $\theta = 0$ the inner gap is reduced in strength and when $\theta = \pi/2$ the bands are uncoupled and Zeeman shifted in energy. For angles $\theta \in (0\ ,\ \pi/2)$ we see how the bound states transition between the two regimes; this mixing produces a number of crossings within the spectrum as the angle changes. Critically, we note that for all values of θ there are always four reasonably distinct bands, which is to be expected as we are in the trivial phase. To explore the ramifications of mixing the two different regimes, we plot the current phase relations in Fig. 7.23.

The most noticeable feature of Fig. 7.23 is the appearance of a plateau in the critical current that forms around $\varphi \sim \pi$. This can be understood from Fig. 7.22 whereby changing θ the occupation of the various bound states change as the states mix between the $\theta = 0$ and $\theta = \pi/2$ regimes. However, we do not see any appreciable anomalous Josephson current, although for $\varphi = \pi$ we do note that the current shifts slightly from $I = 0$. The reason being that the inner and outer states are both available to carry current hence from the results in Section 7.1 we do not see an appreciable anomalous current.

We now probe the topological regime by setting the external magnetic field to be of the form

$$\mathbf{B} = \frac{1.25\Delta}{g\mu_B}\big(\cos(\theta) \quad 0 \quad \sin(\theta)\big) \quad . \tag{7.49}$$

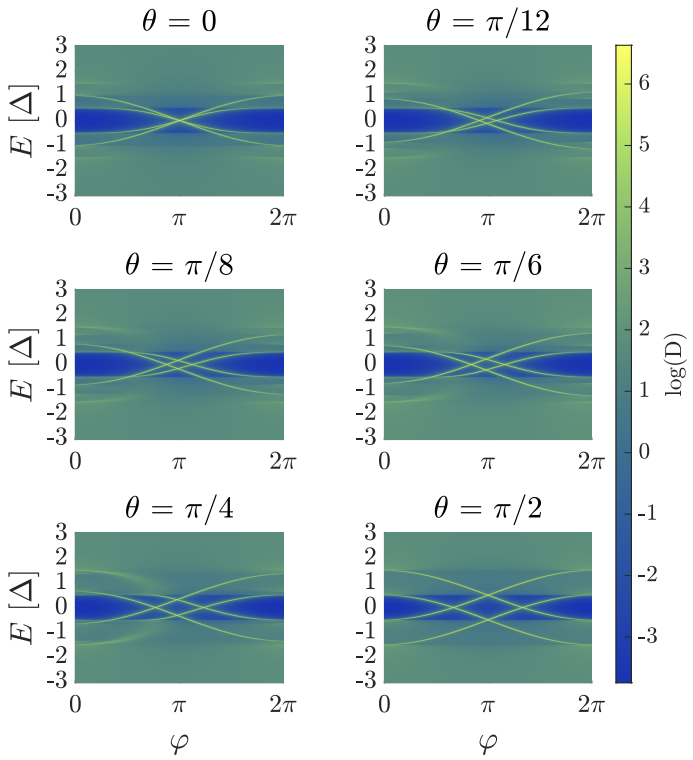

Figure 7.22: Heatmap of the log of the total density of states $D(\varphi, E)$ for a one-dimensional Josephson junction as a function the phase difference φ and energy E. The magnitude of the magnetic field is set to $B = \frac{0.75\Delta}{g\mu_B}$ such that we are in the trivial phase. In each plot we vary the angle within the xz-plane that the magnetic field points.

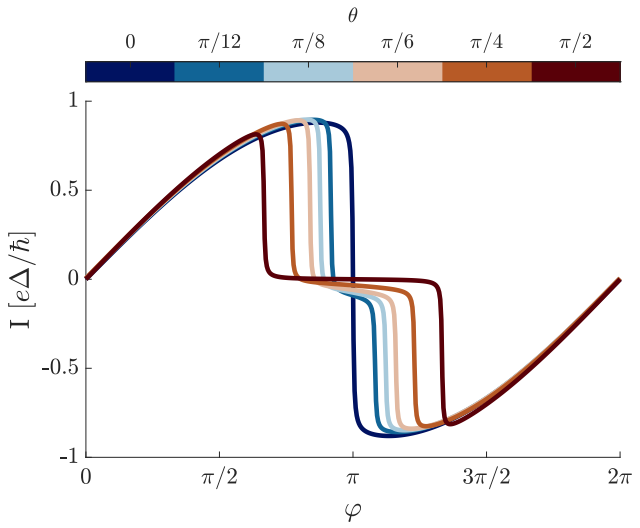

Figure 7.23: Current phase relations at zero temperature corresponding to Fig. 7.22. The magnitude of the magnetic field is set to $B = \frac{0.75\Delta}{g\mu_B}$ such that we are in the trivial phase. θ parametrises the direction of the magnetic field in the xz-plane.

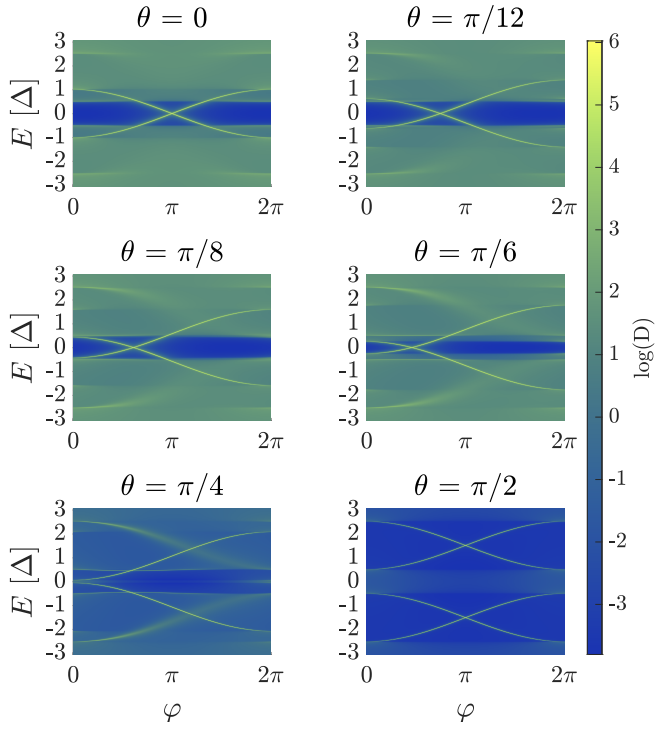

Figure 7.24: Heatmap of the log of the total density of states $D(\varphi, E)$ as a function the phase difference φ and energy E for a range of magnetic field angles. The magnitude of the magnetic field is set to $B = \frac{1.25\Delta}{g\mu_B}$ such that we are in the topological phase.

such that $|\mathbf{B}| > |\Delta|$ and we are in the topological phase. We plot the corresponding bound state density for a range of angles θ in Fig. 7.24. The $\theta = 0$ and the $\theta = \pi/2$ cases are to be expected, with the complete disappearance of the inner modes for $\theta = 0$ and the full Zeeman shift of the states when $\theta = \pi/2$. However, the striking difference between Fig. 7.24 and Fig. 7.22 is that by parametrising the crossover between $\theta = 0$ and the $\theta = \pi/2$ regimes in the topological phase, the *number* of bound states is no longer conserved. Indeed when $\theta = 0$ and we are in the topological phase, we begin with only two states, then when $\theta = \pi/2$ such that we are back in the trivial phase, we must return to four bound states. As a result, by changing θ we can modulate the amount of current which is carried by the inner and outer spinors available to form Andreev bound states. As described in Section 7.1, this asymmetry will lead to an anomalous current. We plot the resulting supercurrent for these bound states in Fig. 7.25 in both the zero-temperature limit and at $T = 0.15K$. In this figure see that when $\varphi = k\pi$ for $k \in \mathbb{Z}$, the supercurrent is *not* identically zero – namely, we are observing some anomalous Josephson effects.

The study of the anomalous Josephson effect in topological junction was first performed by Ref [86] where they observed a current phase relation identical to Fig. 7.25. As here, they note that the component of the magnetic field parallel to the spins 'drives' the effect, whilst the component parallel to the nanowire is necessary to break the symmetry of the inner and outer spinors. In their work they also derive the maximum anomalous current I_h capable of being induced by the magnetic field, which is defined as $I_h \equiv eg\mu_B B_z/\hbar$ – see Appendix C.3 for more discussion on this

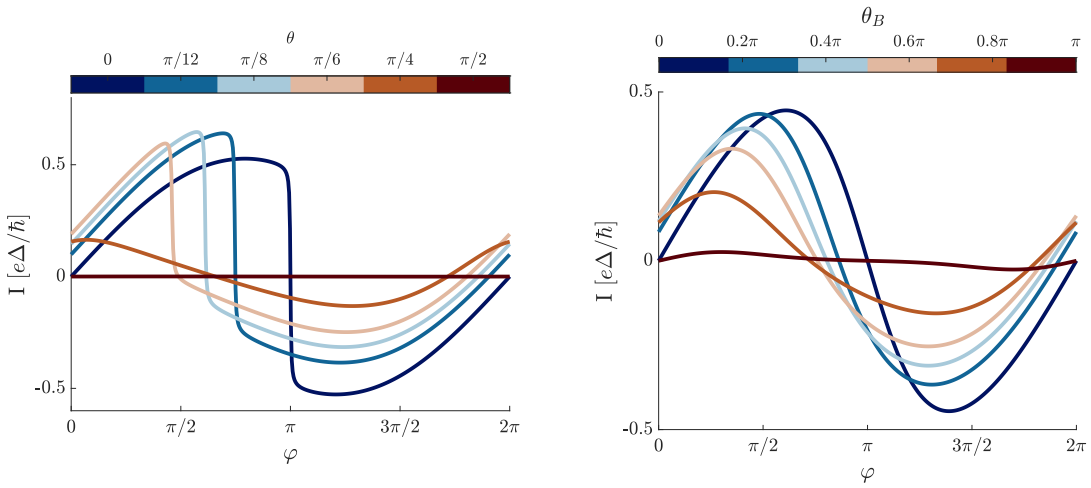

Figure 7.25: Current phase relations for a one-dimensional Josephson junction corresponding to Fig. 7.24. The magnitude of the magnetic field is set to $B = \frac{1.25\Delta}{g\mu_B}$ such that, using Eq. (7.30), for $\theta \lesssim 0.9\pi$ we are in the topological phase. On the left is the zero-temperature limit, whilst on the right the simulation is repeated at $T = 0.15K$. Similar results were observed in Ref [86].

point. Denoting the current at $\varphi = 0$ as the anomalous current I_{an}, we plot the magnitude of the anomalous current as a function of the magnetic field strength in Fig. 7.26 where we have included a dotted red to outline the theoretical boundary between the topological and the trivial phases. We normalise the anomalous current by the maximum current induced by the magnetic field I_h. The central feature of this plot is the appearance of a plateau of maximal anomalous current. We note that the plateau of anomalous current resides entirely in the topological phase and decays in the trivial regime – this is expected as the condition for anomalous current requires an asymmetry between the current carried by the inner and outer spinors, which is most true in the topological phase due to the vanishing of the inner set of Andreev bound states.

Although we have implemented a somewhat naïve model, most critically ignoring any g-factor anisotropy as one would expect of such nanowires [88], we consider the following experimental proposal depicted in Fig. 7.27.

It consists of a nanowire on some substrate with a thin superconducting layer deposited on the ends of the nanowire. Importantly, the bulk superconductor is simply connected topologically such that the bulk phase is constant across the superconductor. The substrate is then placed on a gate material such that we can tune both the chemical potential in the nanowire, but also the strength of the Rashba spin-orbit term. Placing such a device in a vector magnet allows an external magnetic field to be applied in the plane of the nanowire with variable angle θ and strength B. Indeed with an appropriate lead setup such that one could measure current flow through

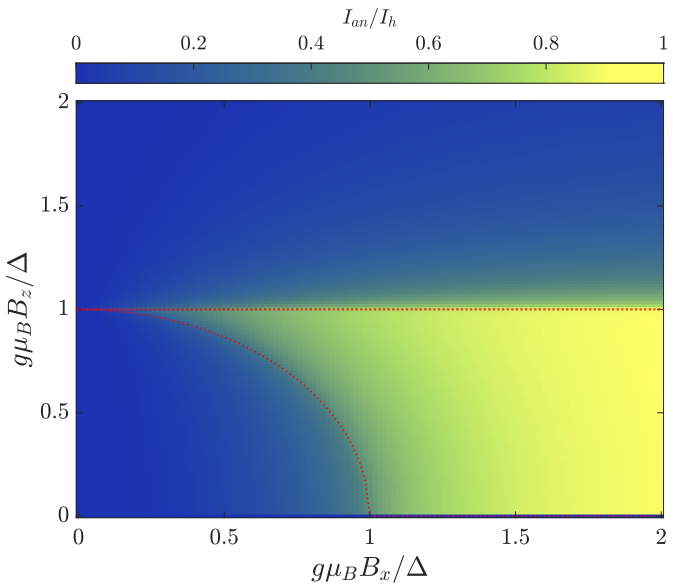

Figure 7.26: Heatmap of the anomalous current I_{an} normalised by the maximum anomalous current I_h of Eq. (C.20) as a function of the magnetic field parallel to the nanowire (x-axis) and the magnetic field parallel to the spins (z-axis). In the red dotted line we have outlined the boundaries between the topological and trivial phases.

the nanowire, we could use this device to test for topological phase transitions in the nanowire by looking for the plateau in current observed in Fig. 7.26.

Similarly, although we have styled the observation of the anomalous Josephson effect as an experimental technique to determine whether the nanowire is in the topological or trivial phase, it could instead be utilised for a number of technological applications. For example, with some leads to carry bias current in and out of the nanowire, the device would act as a superconducting diode with the anomalous current preferring a direction of current flow; the junction will have an asymmetric critical current – bias current in one direction will exceed the critical current and cause a voltage drop across the junction, whilst current in the other direction will remain supercurrent. Devices with a similar architecture, and much the same physics, have been recently proposed [89]. However, one should be wary of the amount of anomalous current expected, for an induced gap in the nanowire on the order of 10^{-1} meV [82], the maximum anomalous current will be on the order of 10 nA – some proposals have even predicted it to be on the order of 10 pA [90]. As a result, the experimental apparatus depicted in Fig. 7.27 may be unsuitable and a device embedded in a superconducting ring may be required such that a superconducting interference device (SQUID) can detect minuscule changes in the current – precisely as done in Ref [78].

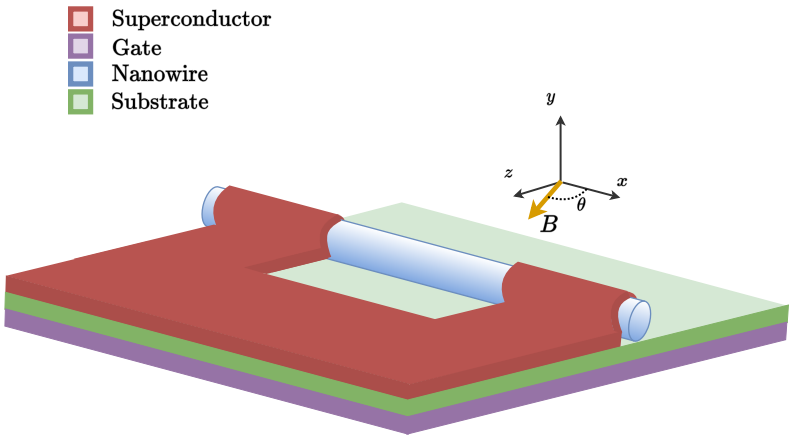

Figure 7.27: Experimental proposal leveraging the anomalous current produced in the topological Josephson junction. The device consists of a nanowire with some intrinsic spin-orbit term on a substrate layer placed on a gate material. A thin superconducting layer is then etched on the device such that it covers the ends of the nanowire and has no holes for flux to pass through – such that the bulk phase across the superconductor is constant. The device is then placed in a vector magnet such that a variable magnetic field can be applied in the plane of the substrate. With such a device we would expect to be able to probe the anomalous Josephson current – from which we can infer information on the topological phase of the nanowire.

Chapter 8

Conclusion

We have introduced, and in most cases, derived the formalism required to simulate transport in superconducting systems out-of-equilibrium. Furthermore, we explicitly did so with the inclusion of a generic $SU(2)$ gauge field which allows for the inclusion of spin-orbit coupling and the observation of the resulting spin-currents from a more theoretically grounded perspective, rather than with some ad-hoc substitution. As an example of these methods, we studied the interplay between Rashba spin-orbit coupling and an external magnetic field on the bandstructure of a two-dimensional lattice model. This led to the appearance of intricate fractals. These particular fractals, which do not seem to be present in the literature, could manifest in the experimental energy spectrum of Moiré lattices under external electric and magnetic fields (see Ref [36] for a similar use of Moiré lattices).

Similarly, after describing the standard matrix inversion algorithms utilised to solve the central equation of superconducting transport – namely the Nambu-Gorkov equation – we introduced a novel matrix inversion algorithm not found in the literature. The algorithm, which we denote by the truncated transfer matrix method, trades numerical stability with computational speed. Although difficult to derive analytical formulae describing the trade-off for arbitrary matrices, we found that within the context of transport, for minimal numerical error one can gain reasonable improvements in runtime. By using this new algorithm we can sweep over a denser range of parameter space in less time, greatly increasing efficiency.

We also made an in-depth numerical case study of nanowire Josephson junctions working in a number of regimes. For the case of no external magnetic fields, and in the absence of spin-orbit coupling, we compared our non-equilibrium Green's functions results with that of scattering theory. In doing so we found agreement up to numerical precision. We then extended these results to the study of superconducting constrictions where the current through the device is carried by a helical condensate. Making use of a self-consistent solver we observed the appearance of a solitonic solution as predicted to exist within these devices, which validates the robustness of the physics within the modelling. We then returned to superconducting-normal-superconducting junctions under an external magnetic field. Within this regime we saw the appearance of π phase flips in the device behaviour; where the dependence of the supercurrent on the phase difference across the function flips as a function of the

external magnetic field. The results we obtained agree with the existing literature, further validating the simulation tool.

In the last chapter we included the effects of spin-orbit coupling within the nanowire through the introduction of an $SU(2)$ gauge field. The interplay between spin-orbit coupling and an external magnetic field drives the so-called anomalous Josephson effect, where current flows in the absence of a phase bias. We introduced a condition that must be met to observe this physics, and explored the resulting anomalous currents for a range of devices. By introducing the language of topology within nanowires, we showed how in the topological phase an anomalous current can be produced. By sweeping parameter space we found the regions of external magnetic field which produced an anomalous current agree precisely with both the topological conditions and the existing literature – providing a metric to detect whether one is in a topological phase or not. We then concluded the discussion with a sketch of an experimental device which could probe these observed effects. Finally, we modelled some experimental data exhibiting anomalous Josephson physics. This data observed a linear phase shift at small magnetic fields, followed by a saturation at larger fields. Our modelling is capable of simulating the device behaviour over all magnetic field strengths, something the analytic theory in the paper cannot do; understanding the mechanism behind this is an ongoing project.

Finally, although we described the powerful $SU(2)$ transport formalism, we only leveraged it to analyse the fractals in lattice bandstructures and to simplify the discussion on anomalous currents. However, by studying the conserved currents of this gauge field – namely, the spin current densities within the system – there is a vast range of exciting theoretical possibilities, such as non-equilibrium spin-currents in superconducting systems, which have yet to be studied. As a result, although we demonstrated some capabilities of the $SU(2)$ non-equilibrium Green's function formalism, there is much exciting work to do on both the numerical and theoretical side. For example, within the context of transport through Josephson junctions, although previous modelling can also observe anomalous Josephson current, through the extra data available in the non-equilibrium Green's function approach – such as the density of states and the conductance – we can begin to describe *why* we observe the saturation in the phase shift at large magnetic fields. We leave this for a later work.

Appendix A

Chapters Two and Three

A.1 Example Green's function in equilibrium

As an example of the benefit of equilibrium systems we will compute the following 2-point correlator

$$G^{<}_{q,q'}(t,t') = \frac{i}{\hbar}\left\langle \psi^*_{q'}(t')\psi_q(t)\right\rangle \quad , \tag{A.1}$$

where ψ_k are spin-less fermionic operators obeying the standard fermionic anti-commutation relations Eq. (2.22). We assume that our equilibrium system consists of free spin-less fermions at temperature T and at chemical potential μ such that the Hamiltonian can be given by

$$H_0 = \sum_k (\epsilon_k - \mu)\psi^*_k\psi_k \equiv \sum_k \xi_k\psi^*_k\psi_k \quad , \tag{A.2}$$

where ϵ_k are the energies of the single-particle states. As everything is currently written in the Heisenberg representation, the time dependence of all operators is given by

$$\psi_q(t) = e^{iH_0t/\hbar}\psi_q e^{-iH_0t/\hbar} \quad . \tag{A.3}$$

Using the anti-commutation relations of the fermionic operators to note that

$$H_0\psi_q = \sum_k \xi_k\psi^*_k\psi_k\psi_q = \sum_k \xi_k\psi_q\psi^*_k\psi_k - \psi_q\xi_q = \psi_q(H_0 - \xi_q) \quad , \tag{A.4}$$

we can simplify Eq. (A.3) to write the time dependence as

$$\psi_q(t) = \psi_q e^{-i\xi_q t/\hbar} \quad . \tag{A.5}$$

Because of the simplicity of this expression, we can show that the anti-commutator of the *time-dependent* operators becomes

$$\left\{\psi^*_{q'}(t'), \psi_q(t)\right\} = \psi^*_{q'}(t')\psi_q(t) + \psi_q(t)\psi^*_{q'}(t') = \delta_{q',q}e^{i\xi_q(t'-t)/\hbar} \quad . \tag{A.6}$$

Taking the statistical average of this anti-commutator we find that

$$\begin{aligned}\delta_{q',q}e^{i\xi_{q'}(t'-t)} &= \mathrm{Tr}\left[e^{-\beta H_0}\psi^*_{q'}(t')\psi_q(t)\right] + \mathrm{Tr}\left[e^{-\beta H_0}\psi_q(t)\psi^*_{q'}(t')\right] \quad , \\ &= \left\langle\psi^*_{q'}(t')\psi_q(t)\right\rangle + \mathrm{Tr}\left[e^{-\beta\left(H_0-\xi_{q'}\right)}\psi^*_{q'}(t')\psi_q(t)\right] \quad , \\ &= \left(1+e^{\beta\xi_q}\right)\left\langle\psi^*_{q'}(t')\psi_q(t)\right\rangle \quad , \end{aligned} \tag{A.7}$$

where in the penultimate line we made use of the cyclic nature of the trace[1] combined with Eq. (A.4). Returning now to the original Green's function of Eq. (2.40), using Eq. (A.7), we can solve it as

$$G^<_{q,q'}(t,t') = \frac{i}{\hbar}\left(1+e^{\beta\xi_q}\right)^{-1}\delta_{q',q}e^{i\xi_{q'}(t'-t)/\hbar} = \frac{if(\xi_q)}{\hbar}\delta_{q,q'}e^{i\xi_q(t-t')/\hbar} \quad , \tag{A.8}$$

where $f(\xi_q)$ is the usual Fermi function for fermions evaluated at energy ξ_q.

A.2 Fluctuation-dissipation theorem

Assuming that our equilibrium system consists of interacting spin-less fermions at temperature T with some generic Hamiltonian H, the lesser Green's function can be given by

$$G^<_{q,q'}(t,t') = \frac{i}{\hbar\,\mathrm{Tr}[e^{-\beta H}]}\,\mathrm{Tr}\left[e^{-\beta H}\psi^*_{q'}(t')\psi_q(t)\right] \quad . \tag{A.9}$$

Using the cyclic properties of traces this can be written as

$$\begin{aligned} G^<_{q,q'}(t,t') &= \frac{i}{\hbar\,\mathrm{Tr}[e^{-\beta H}]}\,\mathrm{Tr}\left[e^{-\beta H}e^{\beta H}\psi_q(t)e^{-\beta H}\psi^*_{q'}(t')\right] \\ &= \frac{i}{\hbar}\left\langle\psi_q(t-i\beta)\psi^*_{q'}(t')\right\rangle \\ &= -G^>_{q,q'}(t-i\beta,t') \quad . \end{aligned} \tag{A.10}$$

Assuming that the Green's function only depends on the relative difference between the two times, rather than their specific values, by Fourier transforming Eq. (A.10) with respect to $\tau = t'-t$, we get the important identity

$$G^>_{q,q'}(E) = -e^{E\beta}G^<_{q,q'}(E) \quad . \tag{A.11}$$

Now using the definition of the spectral function in Eq. (2.43) we find that

$$-iG^<_{q,q'}(E) = f(E)A_{q,q'}(E) \quad , \tag{A.12}$$

where f is the usual Fermi function and A is the spectral weight function introduced in Eq. (2.44).

[1] As we are dealing with traces of operators, the validity of this trace is indeed not obvious. However, the $\exp\{-\beta H_0\}$ term bounds the expression such that the trace as an operation is well-defined – see [91] for a thorough discussion.

A.3 Cooper instability

Having introduced the BCS interaction of Eq. (3.2), we must explore its repercussions – with the appearance of the hallmarks of superconductivity, such as the repulsion of magnetic fields, certainly not obvious from the BCS interaction alone! To this end, we will explore the behaviour of these paired electrons – the Cooper pairs – under the weak BCS interaction.

More formally, as per Eq. (2.46), we separate the full Hamiltonian of the superconductor into $H = H_0 + H_{\text{BCS}}$, where H_0 describes the dynamics of an equilibrium electron system, and H_{BCS} is given by Eq. (3.2). Explicitly working in the interaction picture, we consider the correlation between the annihilation of two electrons at time $t = 0$ and position $\mathbf{r}$ followed by the creation of two electrons at some time t later and at position $\mathbf{r} + \mathbf{l}$

$$C(\mathbf{l}, t) = \frac{1}{i\hbar} \left\langle T\left\{\mathcal{S}\psi_\downarrow^*(\mathbf{r}+\mathbf{l}, t)\psi_\uparrow^*(\mathbf{r}+\mathbf{l}, t)\psi_\uparrow(\mathbf{r}, 0)\psi_\downarrow(\mathbf{r}, 0)\right\}\right\rangle \quad , \tag{A.13}$$

where $\mathcal{S} = T\exp\left\{\frac{1}{i\hbar}\int H'_{\text{BCS}}\right\}$ is the scattering matrix formulated in the interaction picture. This is formally a four point electron correlator, but can also be viewed as the usual Green's function for a Cooper pair. Expanding out the interaction term and utilising the generalised Wicks' theorem of Section 2.2.5, we can decompose the correlator C into a number of Feynman diagrams

$C(\mathbf{l}, t) \sim$ 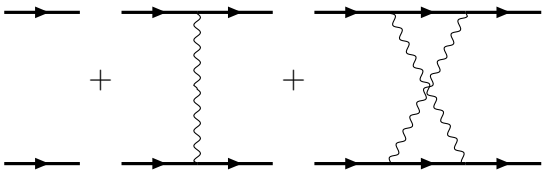 $+ \cdots$ (A.14)

To zeroth and first order in the asymptotic expansion, there are only two diagrams – precisely the first two shown in Eq. (A.14). However, every higher order term can be partitioned into two distinct partitions: those containing any crossed interactions and those without. To second order in the expansion there is only one of each – precisely the crossed and uncrossed diagrams – which are given graphically below

. (A.15)

Although it can be proven exactly, assuming that the electron density in the superconductor is large enough, we can safely ignore all diagrams that contain crossed interaction lines and factor in only the contributions from the uncrossed diagrams [10]. Heuristically, in a dense system the contribution from diagrams which minimise the mean distance between interaction sites dominate those which rely on the electrons travelling large distances before interacting. As the uncrossed diagrams minimise the mean distance between interactions compared to the crossed diagrams, we can

consider only these diagrams [10]. As a result we can write all contributing diagrams and sum them in an appropriate fashion as described below

$C(\mathbf{l},t) =$ 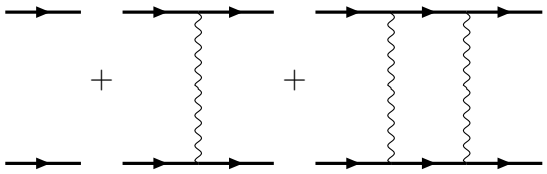 (A.16)

$=$ 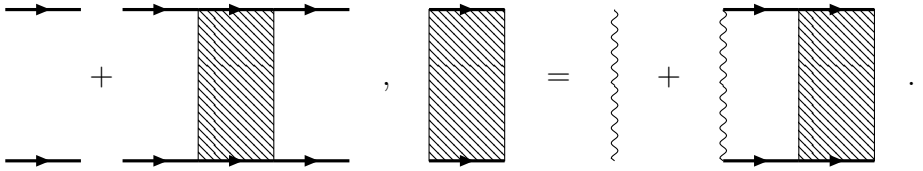

In this manner, we have expanded out the correlator, then re-summed it by identifying the most important family of interactions. As a result we have written the infinite number of diagrams as only two – the free propagation of the two Cooper pairs, plus the case where they interact once with some renormalised interaction strength. We now aim to evaluate the strength of this renormalised interaction.

We can write the final line of Eq. (A.16) as

$$C(\mathbf{l},t) = G^2(\mathbf{l},t) + \int \mathrm{d}x\,\mathrm{d}y\, G^2(\mathbf{x},t_x)\Gamma(\mathbf{y},t_y)G^2(\mathbf{l}-\mathbf{x}-\mathbf{y},t-t_x-t_y) \quad , \quad \text{(A.17)}$$

where $G(\mathbf{l},t)$ is the Green's function for an electron with no BCS interaction present and

$$\Gamma(\mathbf{y},t_y) = g\delta(y) + g\int \mathrm{d}w\, G^2(\mathbf{y}-\mathbf{w},t_y-t_w)\Gamma(\mathbf{w},t_w) \quad . \quad \text{(A.18)}$$

This Γ is known as the vertex strength and accounts for the renormalised interaction between the Cooper pairs [10]. We can now Fourier transform Eq. (A.18) to isolate Γ, which, making use of the convolution theorem, provides

$$\Gamma(\mathbf{q},\omega) \equiv g + g\sum_{\mathbf{p}}\int \mathrm{d}\omega'\, G(\mathbf{p},\omega')G(\mathbf{q}-\mathbf{p},\omega-\omega')\Gamma(\mathbf{q},\omega) \quad . \quad \text{(A.19)}$$

Rearranging we can isolate the interaction strength

$$\Gamma(\mathbf{q},\omega) = \frac{g}{1 - g\sum_{\mathbf{p}}\int \mathrm{d}\omega'\, G(\mathbf{p},\omega')G(\mathbf{q}-\mathbf{p},\omega-\omega')} \quad . \quad \text{(A.20)}$$

Making a further simplification that the interaction is entirely homogenous in space and time, then we only need to evaluate the term $\Gamma(\mathbf{0},0)$[2]. When $(\mathbf{q},\omega) = (\mathbf{0},0)$, the convolved Green's functions in the denominator of Eq. (A.20) can be written

[2]This is as $\Gamma(\mathbf{0},0) = \int \mathrm{d}x\,\Gamma(\mathbf{x},t_x)$ and hence corresponds to the 'total' interaction strength in space and time.

as [92]

$$\sum_{\mathbf{p}} \int \mathrm{d}\omega' \, G(\mathbf{p},\omega')G(-\mathbf{p},-\omega') = \sum_{\mathbf{p}} \int \mathrm{d}\omega' \, \frac{1-f(\xi_{\mathbf{p}})}{\omega' + i\eta - \xi_{\mathbf{p}}} \frac{f(\xi_{\mathbf{p}})}{-\omega' + i\eta - \xi_{\mathbf{p}}} \quad , \quad \text{(A.21)}$$

where f is the Fermi function and $\xi_{\mathbf{p}}$ is the energy level of that momentum state. As each momentum state consists of a simple pole, this can be computed as [93]

$$\begin{aligned} \sum_{\mathbf{p}} \int \mathrm{d}\omega' \, G(\mathbf{p},\omega')G(-\mathbf{p},-\omega') &= \sum_{\mathbf{p}} \frac{1-2f(\xi_{\mathbf{p}})}{2\xi_{\mathbf{p}}} \quad , \qquad \text{(A.22)} \\ &= \int_{-\infty}^{\infty} \mathrm{d}\epsilon \, \rho(\epsilon) \frac{1-2f(\epsilon)}{2\epsilon} \quad , \end{aligned}$$

where in the last line we have replaced a sum over momentums with an integral over energies by including the density of momentum states at each energy $\rho(\epsilon) = \sum_{\mathbf{p}} \delta(\epsilon - \xi_{\mathbf{p}})$. The final integral in Eq. (A.22) is divergent, however, as the interaction is limited to a shell of energies around the Fermi energy $\sim E_F \pm \hbar\omega_D$[3] and that the Fermi function f cuts off the singularity at energies below $k_B T$ then

$$\sum_{\mathbf{p}} \int \mathrm{d}\omega' \, G(\mathbf{p},\omega')G(-\mathbf{p},-\omega') = \rho(E_F) \int_{k_B T}^{\hbar\omega_D} \frac{\mathrm{d}\epsilon}{\epsilon} = \rho(E_F) \ln\left(\frac{\hbar\omega_D}{k_B T}\right) \quad . \quad \text{(A.23)}$$

As a result the 'total' interaction strength is given by

$$\int \mathrm{d}x \, \Gamma(\mathbf{x}, t_x) = \frac{g}{1 - g\rho(E_F) \ln\left(\frac{\hbar\omega_D}{k_B T}\right)} \quad . \quad \text{(A.24)}$$

Interestingly, we note that for temperatures close to a critical temperature $T_c \equiv \frac{\hbar\omega_D}{k_B} \exp[-g\rho(E_F)]$ the total interaction strength diverges and is no longer bounded. From the Feynman diagrams of Eq. (A.16), we managed to write the scattering of two Cooper pairs as a single attractive interaction with strength Γ. However, we now see that for certain temperatures the total strength of this interaction becomes unbounded and the attraction between Cooper pairs over any distance in space becomes infinite! Indeed this divergence in the propagator indicates that the process of perturbing the electronic Fermi sea under a BCS interaction breaks down – we can no longer view Cooper pairs as 'paired' electrons which travel in a background electronic sea [10]. Rather we must find a new mean-field which takes into account the strongly bound Cooper pairs.

[3] As the lattice takes on the order $\sim \omega_D^{-1}$ (ω_D being the Debye frequency) seconds to relax to its equilibrium position then the energy scale phonon induced superconductivity can act over is $\sim \hbar\omega_D$ [10].

A.4 Commutator trick

We first prove a useful commutator 'trick' that will be used extensively through this thesis. Given a Hamiltonian of the form

$$H \sim \int \mathrm{d}x' \prod_i^{n_A} A_i(x') \prod_i^{n_B} B_i(x') \prod_i^{n_C} C_i(x') \quad , \tag{A.25}$$

where we have omitted spacetime arguments for brevity. And some operator $X(x)$ such that for all k

$$\{C_k(x'), X(x)\} = 0 \quad \text{and} \quad \{A_k(x'), X(x)\} = \delta(x - x') \quad , \tag{A.26}$$

and for all but a finite number of spacetime point[4]

$$[B_k(x'), X(x)] = 0 \quad . \tag{A.27}$$

Then

$$\begin{aligned} HX(x) &= \int \mathrm{d}x' \prod_i^{n_A} A_i(x') \prod_i^{n_B} B_i(x') \prod_i^{n_C} C_i(x') X(x) \\ &= \sum_k^{n_A} (-1)^{n_C+n_A-k} \left[\prod_{i,i\neq k}^{n_A} A_i(x) \prod_i^{n_B} B_i(x) \prod_i^{n_C} C_i(x) \right] \\ &\quad + (-1)^{n_C+n_A} \int \mathrm{d}x' \, X(x) \prod_i^{n_A} A_i(x') \prod_i^{n_B} B_i(x') \prod_i^{n_C} C_i(x') \\ &= \sum_k^{n_A} (-1)^{n_C+n_A-k} \frac{\delta H}{\delta A_k(x)} + (-1)^{n_C+n_A} X(x) H \quad . \end{aligned} \tag{A.28}$$

In the second equality of Eq. (A.28), as there are only finite points in the integrand where B_k does not commute with X, then the measure of these extra terms in the integral is zero and can be discarded. Hence the commutator of this complicated Hamiltonian can be simply computed by

$$[H, X(x)] = \sum_k^{n_A} (-1)^{n_C+n_A-k} \frac{\delta H}{\delta A_k(x)} + (-1)^{n_C+n_A} X(x) H - X(x) H \quad , \tag{A.29}$$

and in the usual case when $n_C + n_A$ is even[5] then

$$[H, X(x)] = \sum_k^{n_A} (-1)^{n_C+n_A-k} \frac{\delta H}{\delta A_k(x)} \quad . \tag{A.30}$$

[4]Implicitly we assume that all points this commutator is finite.
[5]Generally either $n_A = n_C$ or $n_A = 0$ and $n_C = 2$.

If however X anti-commutes with C instead of A, we get the expression $[H, X(x)] = \sum_k^{n_C} (-1)^{n_C-k} \frac{\delta H}{\delta C_k(x)}$.

A.5 Self-Consistent Relation

We note that the order parameter is defined as

$$\Delta_0(\mathbf{x}) = g \left\langle \psi^\top(x) \left(i\sigma_2\right) \psi(x) \right\rangle \quad , \tag{A.31}$$

whilst the lesser electron/hole correlator is defined as

$$F^<(x, x') = \frac{i}{\hbar} \left\langle \psi(x) \otimes \psi^\top(x) \right\rangle \quad . \tag{A.32}$$

As a result, we can express one as a function of the other – defining a self-consistent relationship.

$$\begin{aligned} \Delta_0(\mathbf{x}) &= g \left\langle \psi^\top(x) \left(i\sigma_2\right) \psi(x) \right\rangle \\ &= -g \operatorname{Tr}\left[\left(i\sigma_2\right) \left\langle \psi(x) \otimes \psi^\top(x) \right\rangle \right] \\ &= ig\hbar \lim_{t \nearrow t'} \operatorname{Tr}[(i\sigma_2) F^<(x, x')] \\ &= ig \int \mathrm{d}E \operatorname{Tr}[(i\sigma_2) F^<(E, \mathbf{x}, \mathbf{x})] \quad . \end{aligned} \tag{A.33}$$

A.6 Current operator

As in Section 3.3.1, we first partition the system into three distinct regions: left lead, central region, and right lead. We assume exactly the same form of the Hamiltonian which can be partitioned as

$$H = H_L + H_{LC} + H_C + H_{CR} + H_R \quad , \tag{A.34}$$

where H_L, H_C, and H_R describe the dynamics of the the isolated left, centre, and right regions respectively and $H_{LC/CR}$ contains the information on the the coupling between regions. We refer to Section 3.3.1 for an explicit form for each of these Hamiltonians, however, as we will see the critical term for current flow is the coupling terms which we repeat here are given in Nambu space by

$$H_{LC/CR} = \sum_{\boldsymbol{\alpha}/\mathbf{i}/\boldsymbol{\beta}} \Psi^\dagger_{\boldsymbol{\alpha}/\boldsymbol{\beta}}(t') \mathcal{V}_{\boldsymbol{\alpha}/\boldsymbol{\beta},\mathbf{i}} \Psi_{\mathbf{i}}(t') + \Psi^\dagger_{\mathbf{i}}(t') \mathcal{V}^\dagger_{\boldsymbol{\alpha}/\boldsymbol{\beta},\mathbf{i}} \Psi_{\boldsymbol{\alpha}/\boldsymbol{\beta}}(t') \quad , \tag{A.35}$$

where $\boldsymbol{\alpha}$ denotes a lattice site in the left lead, $\boldsymbol{\beta}$ denotes a site in the right lead, and $\mathbf{i}$ denotes a site in the central region. The $\mathcal{V}_{\boldsymbol{\alpha}/\boldsymbol{\beta},\mathbf{i}}$ potential contain the coupling between those individual lattice sites.

To begin, we will solely consider the current from the left lead to the central region, I_{LC}, which we define as the change in the average number of charges in the

left lead multiplied by the charge per electron [24]

$$I_{LC}(t) \equiv -e \left\langle \frac{\partial \hat{n}^{\text{left}}}{\partial t'}(t) \right\rangle \quad , \tag{A.36}$$

where the number operator $\hat{n}^{\text{left}}(t)$ determines the number of charges in the left lead at some time, which we define in particle-hole space as [13]

$$\hat{n}^{\text{left}}(t) = \frac{1}{2} \sum_{\boldsymbol{\lambda} \in L} \tau_z \Psi^\dagger_{\boldsymbol{\lambda}}(t) \Psi_{\boldsymbol{\lambda}}(t) \quad , \tag{A.37}$$

where we included τ_z as the holes carry an opposite charge to the electrons. The factor of half is so not to double count the hole contribution; we arbitrarily doubled our degrees of freedom to include holes. As all operators are currently in the Heisenberg picture, then by utilising Heisenberg's equation of motion Eq. (2.28), we write Eq. (3.56) as

$$\begin{aligned} I_{LC}(t) &\equiv -e \left\langle \frac{\partial \hat{n}^{\text{left}}}{\partial t'}(t) \right\rangle \\ &= \frac{e}{2i\hbar} \left\langle \left[H, \hat{n}^{\text{left}}(t) \right] \right\rangle \\ &= \frac{e}{2i\hbar} \sum_{\boldsymbol{\lambda} \in L} \tau_z \left\langle \left[H, \Psi^\dagger_{\boldsymbol{\lambda}}(t) \Psi_{\boldsymbol{\lambda}}(t) \right] \right\rangle \\ &= \frac{e}{2i\hbar} \sum_{\boldsymbol{\lambda} \in L} \tau_z \Big(\left\langle \left[H, \Psi^\dagger_{\boldsymbol{\lambda}}(t) \right] \Psi_{\boldsymbol{\lambda}}(t) \right\rangle + \left\langle \Psi^\dagger_{\boldsymbol{\lambda}}(t) [H, \Psi_{\boldsymbol{\lambda}}(t)] \right\rangle \Big) \quad , \end{aligned} \tag{A.38}$$

where in the last equality we have broken the commutator into two terms. Expanding out the Hamiltonian using Eq. (A.34), we note that as $\Psi_{\boldsymbol{\lambda}}$ acts only on the left lead, then $\left[H_{C/CR/R}, \Psi^\dagger_{\boldsymbol{\lambda}} \right] = \left[H_{C/CR/R}, \Psi_{\boldsymbol{\lambda}} \right] = 0$ as H_C, H_{CR}, and H_R do not act on the left lead. However, as H_L and H_{LC} do indeed act on the left lead, more care must be taken in evaluating those contributions. Indeed, by making use of Eq. (A.29), we can show that

$$\left[H_L, \Psi^\dagger_{\boldsymbol{\lambda}}(t) \right] \Psi_{\boldsymbol{\lambda}}(t) = -\Psi^\dagger_{\boldsymbol{\lambda}}(t) [H_L, \Psi_{\boldsymbol{\lambda}}(t)] \quad , \tag{A.39}$$

and that

$$\begin{aligned} \left[H_{LC}, \Psi^\dagger_{\boldsymbol{\lambda}}(t) \right] \Psi_{\boldsymbol{\lambda}}(t) &= \Psi^\dagger_{\mathbf{i}}(t) \mathcal{V}^\dagger_{\boldsymbol{\lambda},\mathbf{i}} \Psi_{\boldsymbol{\lambda}}(t) \\ \Psi^\dagger_{\boldsymbol{\lambda}}(t) [H_{LC}, \Psi_{\boldsymbol{\lambda}}(t)] &= -\Psi^\dagger_{\boldsymbol{\lambda}}(t) \mathcal{V}_{\boldsymbol{\lambda},\mathbf{i}} \Psi_{\mathbf{i}}(t) \end{aligned} \tag{A.40}$$

Substituting these expressions into Eq. (A.38), we have that

$$\begin{aligned} I_{LC}(t) &= \frac{e}{2i\hbar}\sum_{\boldsymbol{\lambda}\in L}\tau_z\left\langle \Psi^\dagger_{\mathbf{i}}(t)\mathcal{V}^\dagger_{\boldsymbol{\lambda},\mathbf{i}}\Psi_{\boldsymbol{\lambda}}(t) - \Psi^\dagger_{\boldsymbol{\lambda}}(t)\mathcal{V}_{\boldsymbol{\lambda},\mathbf{i}}\Psi_{\mathbf{i}}\right\rangle \\ &= \frac{e}{2i\hbar}\sum_{\boldsymbol{\lambda}\in L}\mathrm{Tr}\Big[\tau_z\left\langle \Psi^*_{\mathbf{i}}(t)\otimes\Psi^\top_{\boldsymbol{\lambda}}(t)\right\rangle\mathcal{V}^\dagger_{\boldsymbol{\lambda},\mathbf{i}} - \tau_z\mathcal{V}_{\boldsymbol{\lambda},\mathbf{i}}\left\langle \psi^*_{\boldsymbol{\lambda}}(t)\otimes\psi^\top_{\mathbf{i}}(t)\right\rangle\Big] \\ &\equiv \frac{e}{2}\sum_{\boldsymbol{\lambda}\in L}\mathrm{Tr}\Big[\tau_z\mathcal{V}_{\boldsymbol{\lambda},\mathbf{i}}\mathcal{G}^<_{\mathbf{i},\boldsymbol{\lambda}}(t,t) - \tau_z\mathcal{G}^<_{\boldsymbol{\lambda},\mathbf{i}}(t,t)\mathcal{V}^\dagger_{\boldsymbol{\lambda},\mathbf{i}}\Big] \quad , \end{aligned} \tag{A.41}$$

where the trace is over the spin and particle-hole subspace. We can simplify this expression further by noting that $\mathcal{G}^<_{\boldsymbol{\lambda},\mathbf{i}} = -\mathcal{G}^{<\,\dagger}_{\mathbf{i},\boldsymbol{\lambda}}$ such that we can write the expression for the left lead current as [13]

$$\begin{aligned} I_{LC}(t) &= \frac{e}{2}\sum_{\boldsymbol{\lambda}\in L}\mathrm{Tr}\Big[\tau_z\mathcal{V}_{\boldsymbol{\lambda},\mathbf{i}}\mathcal{G}^<_{\mathbf{i},\boldsymbol{\lambda}}(t,t) + \tau_z\big(\mathcal{V}_{\boldsymbol{\lambda},\mathbf{i}}\mathcal{G}^<_{\mathbf{i},\boldsymbol{\lambda}}(t,t)\big)^\dagger\Big] \quad , \\ &= e\sum_{\boldsymbol{\lambda}\in L}\mathrm{Re}\big\{\mathrm{Tr}\big[\tau_z\mathcal{V}_{\boldsymbol{\lambda},\mathbf{i}}\mathcal{G}^<_{\mathbf{i},\boldsymbol{\lambda}}(t,t)\big]\big\} \quad , \end{aligned} \tag{A.42}$$

As in Section 3.3.2, letting $\mathcal{G}(\mathbf{x},\tau_1;\boldsymbol{y},\tau_2)$ denote the (x,y) element of some matrix $\mathcal{G}_{X,Y}$ where $\mathbf{x}$ is a lattice site in X and $\mathbf{y}$ is a lattice site in Y, we can rewrite the current as

$$I_{LC}(t) = e\,\mathrm{Re}\big\{\mathrm{Tr}\big[\tau_z\mathcal{G}^<_{C,L}(t,t)\mathcal{V}_{L,C}\big]\big\} \quad , \tag{A.43}$$

We can repeat this procedure to compute the current from the right lead to the central region

$$I_{RC}(t) = e\,\mathrm{Re}\big\{\mathrm{Tr}\big[\tau_z\mathcal{G}^<_{R,L}(t,t)\mathcal{V}_{R,C}\big]\big\} \quad . \tag{A.44}$$

As a result, returning to the current through the entire device in Eq. (3.55), the total current through the junction is given by

$$I(t) = \frac{e}{2}\,\mathrm{Re}\big\{\mathrm{Tr}\big[\tau_z\mathcal{G}^<_{C,L}(t,t)\mathcal{V}_{L,C} - \tau_z\mathcal{G}^<_{C,R}(t,t)\mathcal{V}_{L,C}\big]\big\} \quad , \tag{A.45}$$

As mentioned, we are interested in steady-state currents hence can express the right hand side of Eq. (A.45) as

$$I = \frac{e}{2}\int \mathrm{d}E\,\mathrm{Re}\big\{\mathrm{Tr}\big[\tau_z\mathcal{G}^<_{C,L}(E)\mathcal{V}_{L,C} - \tau_z\mathcal{G}^<_{C,R}(E)\mathcal{V}_{L,C}\big]\big\} \quad , \tag{A.46}$$

In this manner we have managed to express the steady-state current as a function of the full Green's functions.

Appendix B

Chapters Four and Five

B.1 Truncated Transfer Matrix Proof

To begin, given a system with n layers, we divide it into p partitions of k layers, and a final partition partition containing the remainder r layers. For simplicity we assume that k evenly divides n such that $n = pk$; as a result $r = 0$. We label the partitions such that the first layer is contained within the first partition, whilst the last layer is contained within the p^{th} partition. With the renormalisation procedures of the RGF approach in mind, we introduce a new superscript index on every quantity to keep track of how many times a quantity has been renormalised. For example, the initial T and S matrices of Eq. (5.5) would now be written as

$$T_n^{(0)} = I \qquad T_{n-1}^{(0)} = -C_{n-1}^{-1} A_n \tag{B.1}$$

$$\check{T}_1^{(0)} = I \qquad \check{T}_2^{(0)} = -A_1 C_1^{-1} \quad . \tag{B.2}$$

as no self-energy terms have been introduced thus far. For brevity we have neglected the S and $\check{S}$ matrices. Similarly, within this notation the g_{n-i+1} matrix of the RGF algorithm defined in Eq. (5.3) would now be written as $g_{n-i+1}^{(i)}$ as it is renormalised after every layer. Returning to the transfer matrix approach, we can now iteratively construct the first k matrices as usual. The final quantities within the first and last partitions are given by:

$$T_{n-k+1}^{(0)} = -C_{n-k+1}^{-1}\Big(A_{n-k+2} T_{n-k+2}^{(0)} + B_{n-k+2} T_{n-k+3}^{(0)}\Big) \tag{B.3}$$

$$\check{T}_k^{(0)} = -\Big(\check{T}_{k-1}^{(0)} A_{k-1} + \check{T}_{k-2}^{(0)} B_{k-2}\Big) C_{k-1}^{-1} \quad . \tag{B.4}$$

Having reached the edges of the initial partitions, instead of computing the next matrices in the transfer matrix series we compute their inverses directly

$$\Big[T_{n-k}^{(0)}\Big]^{-1} = -\Big(A_{n-k+1} T_{n-k+1}^{(0)} + B_{n-k+1} T_{n-k+2}^{(0)}\Big)^{-1} C_{n-k} \tag{B.5}$$

$$\Big[\check{T}_{k+1}^{(0)}\Big]^{-1} = -C_k\Big(\check{T}_k^{(0)} A_k + \check{T}_{k-1}^{(0)} B_{k-1}\Big)^{-1} \quad . \tag{B.6}$$

We now aim to stitch the first and last partitions to their neighbouring partitions. In the RGF approach we made the substitution $A_i \rightarrow A_i - B_i g_{i+1} C_i$ to couple all layers to the right of the i^{th} layer with the i^{th} layer. It is possible to show that $g_{i+1} = T_i^{(0)} {T_{i-1}^{(0)}}^{-1} C_{i-1}^{-1}$ [49], and hence to couple the neighbouring partitions we make the substitution

$$A_{n-k} \rightarrow A_{n-k}^{\text{right}} \equiv A_{n-k} + B_{n-k} T_{n-k+1}^{(0)} \left[T_{n-k}^{(0)} \right]^{-1} \quad , \tag{B.7}$$

where the superscript 'right' on A_{n-k} keeps track of the fact that the layer has been renormalised to include the effects of all layers to the right. One can do the same for A_{n-pk+1} to include the effects of all the layers to its left by

$$A_{k+1} \rightarrow A_{k+1}^{\text{left}} \equiv A_{k+1} + \left[\check{T}_{k+1}^{(0)} \right]^{-1} \check{T}_k^{(0)} B_k \quad . \tag{B.8}$$

Critically we can now simply restart the transfer matrix approach in the neighbouring partitions with the renormalised A matrices, namely

$$T_{n-k}^{(1)} = I \qquad T_{n-k-1}^{(1)} = -C_{n-k-1}^{-1} A_{n-k}^{\text{right}} \tag{B.9}$$

$$\check{T}_{k+1}^{(1)} = I \qquad \check{T}_{k+2}^{(1)} = -A_{k+1}^{\text{left}} C_{k+1}^{-1} \quad , \tag{B.10}$$

where now the superscript index has increased as we have renormalised the quantities. This process can be iterated for the remaining layers, progressively working through the device and at the boundary between partitions renormalising every quantity.

In Ref [43] they show that

$$\mathcal{G}_{i,j} = T_i \Theta \check{T}_j \ , \text{ for } i \geq j \tag{B.11}$$

Using the superscript notation, assuming that the i^{th} layer is contained within the l^{th} partition and that the j^{th} layer is contained within the m^{th} partition, then we can express the inverse as

$$\mathcal{G}_{i,j} = -T_i^{(0)} \left[A_1 T_1^{(0)} + B_1 T_2^{(0)} \right]^{-1} \check{T}_j^{(0)} \ , \text{ for } i \geq j \tag{B.12}$$

where all of the superscript indices are identically zero as in the initial transfer matrix approach none of the quantities are ever renormalised. Although this appears reasonable, the presence of terms such as $T_1^{(0)}$ in Eq. (B.11) pose some difficulties as in the truncated transfer matrix approach (TTM) we compute quantities that have been renormalised multiple times such as $T_1^{(p-1)}$. However, by comparing Eqs. (B.3) and (B.9) we observe that

$$T_{n-k-1}^{(1)} = T_{n-k-1}^{(0)} \left[T_{n-k}^{(0)} \right]^{-1} \quad . \tag{B.13}$$

Hence there is a relationship between matrices of different partitions. Generalising this, and assuming that the i^{th} layer is contained within the l^{th} partition, we find

$$T_i^{(l-1)} = T_i^{(0)} \prod_{q=1}^{l-1} \left[T_{n-qk}^{(q-1)} \right]^{-1} \quad , \tag{B.14}$$

where the ordering of the product is taken as $\prod_{i=1}^{n} A_i \equiv A_1 \dots A_n$.

From Eq. (B.11), we have that

$$\mathcal{G}_{n,mk+j} = -\left[A_1 T_1^{(0)} + B_1 T_2^{(0)} \right]^{-1} \check{T}_{mk+j}^{(0)} \text{ , for } 1 \leq j < k \quad . \tag{B.15}$$

However, by renormalising the $mk+1$ layer to factor in all layers to its left as

$$A_{mk+1} \to A_{k+1}^{\text{left}} \equiv A_{mk+1} + \left[\check{T}_{mk+1}^{(m)} \right]^{-1} \check{T}_{mk}^{(m)} B_k \quad , \tag{B.16}$$

then an application of the RGF states that

$$\mathcal{G}_{n,mk+j} = -\left[A_{mk+1}^{\text{left}} T_{mk+1}^{(0)} + B_{mk+1} T_{mk+2}^{(0)} \right]^{-1} \check{T}_{mk+j}^{(m)} \text{ , for } 1 \leq j < k \quad . \tag{B.17}$$

Hence, for $j, i \in [1, k)$ we can use Eq. (B.14) to write Eq. (B.18) as

$$\begin{aligned}
\mathcal{G}_{lk+i,mk+j} &= -T_{lk+i}^{(0)} \left[A_{mk+1}^{\text{left}} T_{mk+1}^{(0)} + B_{mk+1} T_{mk+2}^{(0)} \right]^{-1} \check{T}_{mk+j}^{(m)} \\
&= -T_{lk+i}^{(p-l-1)} \prod_{q=p-l-1}^{1} T_{(p-q)k}^{(q-1)} \Big[\Big(A_{mk+1}^{\text{left}} T_{mk+1}^{(p-m-1)} \\
&\qquad + B_{mk+1} T_{mk+2}^{(p-m-1)} \Big) \prod_{q=p-m-1}^{1} T_{(p-q)k}^{(q-1)} \Big]^{-1} \check{T}_{mk+j}^{(m)} \\
&= -T_{lk+i}^{(p-l-1)} \prod_{q=p-l-1}^{p-m-2} \left[T_{(p-q)k}^{(q-1)} \right]^{-1} \left[A_{mk+1}^{\text{left}} T_{mk+1}^{(p-m-1)} + B_{mk+1} T_{mk+2}^{(p-m-1)} \right]^{-1} \check{T}_{mk+j}^{(m)}
\end{aligned} \tag{B.18}$$

We can now drop the superscript indices as the subscript index contains all the required information to write

$$\mathcal{G}_{lk+i,mk+j} = T_{lk+i} \mathcal{G}_{lk+1,mk+1} \check{T}_{mk+j}^{(m)} \quad , \tag{B.19}$$

where

$$\mathcal{G}_{lk+1,mk+1} = [T_{lk}]^{-1} \mathcal{G}_{(l-1)k+1,mk+1} \quad , \tag{B.20}$$

where

$$\mathcal{G}_{1,mk+1} = -\left[A_{mk+1}^{\text{left}} T_{mk+1} + B_{mk+1} T_{mk+2} \right]^{-1} \quad . \tag{B.21}$$

and for completeness $\mathcal{G}_{0,mk+1} = I$.

B.2 Chebychev Approximation

We begin by assuming that $2X$ is an $N \times N$ matrix, and hence has N eigenvalues – the set of which we denote by $\{\lambda_i\}$. We introduce another critical parameter ξ, which denotes the spread of the eigenvalues $\xi \equiv |\max(\{\lambda_i\}) - \min(\{\lambda_i\})|$. From Fig. 5.5, we see that for $x \in (-1, 1)$, the Chebyshev polynomials oscillates somewhat sinusoidally, but for $|x| > 1$ it appears to grow exponentially.

We now look to estimating the ratio

$$\frac{\max(U_k(\{\lambda_i\}))}{\min(U_k(\{\lambda_i\}))} \quad , \tag{B.22}$$

for some set of eigenvalues $\{\lambda_i\}$. To do so, we note that for $|x| < 1$, U_k is bounded, whilst for $x > 1$ it grows exponentially, hence we can obtain a rough bound to the ratio by letting $\min(U_k(\{\lambda_i\}))$ be near the right most zero of the function, whilst $\max(U_k(\{\lambda_i\})) \sim \max(U_k(\{\xi\}))$ – namely as far right as possible whilst having at least one eigenvalue near the the right most zero.

As a result, by assuming that distance an eigenvalue is to a zero is proportional to the density of eigenvalues, then $\min(U_n(\{e\})) \sim 1/N$. We now look to estimate

We can parameterise $U_k(x)$ by [94]

$$U_k(x) = \begin{cases} \frac{\sin((k+1)\,\mathrm{acos}(x))}{\sin(\mathrm{acos}(x))} & |x| < 1 \\ \frac{\sinh\left((k+1)\cosh^{-1}(x)\right)}{\sinh\left(\cosh^{-1}(x)\right)} & |x| \geq 1 \end{cases} \tag{B.23}$$

We shall focus on the case of $x > 1$, to this end we parameterise x by some w by

$$x = \frac{w + w^{-1}}{2} \quad . \tag{B.24}$$

As a result,

$$\begin{aligned} U_k(w) &= \frac{\sinh((k+1)\ln(w))}{\sinh(\ln(w))} \\ &= \frac{\sinh\left(\ln(w)^{k+1}\right)}{\sinh(\ln(w))} \\ &= \frac{\exp\left[\ln\left(w^{k+1}\right)\right] - \exp\left[-\ln\left(w^{k+1}\right)\right]}{2} \frac{2}{w - w^{-1}} \\ &= \frac{w^{k+1} - w^{-(k+1)}}{w - w^{-1}} \end{aligned} \tag{B.25}$$

As a result, for a reasonably large k, we have that

$$U_k(w) = \frac{w^{k+1}}{w - w^{-1}} \tag{B.26}$$

Appendix C

Chapters Six and Seven

C.1 Baker-Campbell-Hausdorff Identity

An identity of the Baker-Campbell-Hausdorff relation is that

$$e^X Y e^{-X} = \sum_{n=0}^{\infty} \frac{[(X)^n, Y]}{n!} \quad , \tag{C.1}$$

where

$$(X)^n \equiv \underbrace{[X, \ldots, [X, [X}_{n \text{ times}}, Y]] \ldots] \tag{C.2}$$

We consider the case of $X = iA\sigma_i$ and $Y = B\sigma_j$. We progressively compute the commutators as [1]

$$\begin{aligned}
[iA\sigma_i, B\sigma_j] &= (-1)^0 (iA)(B)(2i)\epsilon_{ijk}\sigma_k \\
[iA\sigma_i, (iA)(B)(2i\epsilon_{ijk})\sigma_k] &= (-1)^0 (iA)^2 (B)(2i)^2 \epsilon_{ijk}\epsilon_{ikj}\sigma_j \\
&= (-1)^1 (iA)^2 (B)(2i)^2 \sigma_j \\
\left[iA\sigma_i, (-1)^1 (iA)^2 (B)(2i)^2 \sigma_j\right] &= (-1)^1 (iA)^3 (B)(2i)^3 \epsilon_{ijk}\sigma_k \\
\left[iA\sigma_i, (-1)^1 (iA)^3 (B)(2i)^3 \epsilon_{ijk}\sigma_k\right] &= (-1)^1 (iA)^4 (B)(2i)^4 \epsilon_{ijk}\epsilon_{ikj}\sigma_j \\
&= (-1)^2 (iA)^4 (B)(2i)^4 \sigma_j
\end{aligned} \tag{C.3}$$

[1] Note in the following the indices are never being summed over.

As a result

$$\begin{aligned} e^{iA\sigma_i} B\sigma_j e^{-iA\sigma_i} &= \sum_{n=0}^{\infty} \left\{ \frac{\Big[(X)^{(2n)}, Y\Big]}{(2n)!} + \frac{\Big[(X)^{(2n+1)}, Y\Big]}{(2n+1)!} \right\} \\ &= \sum_{n=0}^{\infty} B \left\{ \frac{(-1)^n (iA)^{2n} (2i)^{2n}}{(2n)!} \sigma_j + \frac{(-1)^n (iA)^{2n+1} (2i)^{2n+1}}{(2n+1)!} \epsilon_{ijk} \sigma_k \right\} \\ &= \sum_{n=0}^{\infty} B \left\{ \frac{(-1)^n (2A)^{2n}}{(2n)!} \sigma_j - \frac{(-1)^n (2A)^{2n+1}}{(2n+1)!} \epsilon_{ijk} \sigma_k \right\} \\ &= B(\cos(2A)\sigma_j - \sin(2A)\epsilon_{ijk}\sigma_k) \quad . \end{aligned} \tag{C.4}$$

C.2 Spin-orbit dispersion relation

We follow the procedure and notation of Ref [95]; repeating it here for convenience but also to explicitly work with our more general Hamiltonian. We denote the wavefunction by the state $|\psi\rangle \equiv \sum_\sigma \sum_{lm} \chi^\sigma_{lm} |l\, m\, \sigma\rangle$ where $|l\, m\, \sigma\rangle \equiv c^\dagger_{l\, m\, \sigma} |0\rangle$ for some vacuum state $|0\rangle$; l and m denote lattice sites on the 2D lattice, whilst σ is the spin-index.

We can write out the full Hamiltonian as

$$\begin{aligned} H = \sum_{lm\sigma} \epsilon n_{lm\sigma} - \sum_{lm} c^\dagger_{l,m,\sigma} \left(g\mu_B B \sigma_y\right)^\sigma_{\sigma'} c_{l,m,\sigma'} - t \sum_{lm\sigma} \Big(c^\dagger_{l+1,m,\sigma} c_{l,m,\sigma} + c^\dagger_{l,m+1,\sigma} c_{l,m,\sigma} + \text{h.c.} \Big) \\ - t_\alpha \sum_{lm\sigma\sigma'} \Big(c^\dagger_{l,m+1,\sigma} \left(i\sigma_x\right)^\sigma_{\sigma'} c_{l,m,\sigma'} - c^\dagger_{l+1,m,\sigma} \left(i\sigma_y\right)^\sigma_{\sigma'} c_{l,m,\sigma'} + \text{h.c.} \Big) \end{aligned} \tag{C.5}$$

where $\epsilon = 4t - \mu$. Schrödinger's equation now states that

$$H\,|\Psi\rangle = E\,|\Psi\rangle \tag{C.6}$$

Left multiplying Eq. (C.6) by $\langle i\, j\, s|$ we find that

$$\begin{aligned} (\epsilon - E)\,\chi^\pm_{lm} \mp ig\mu_B B \chi^\mp_{lm} - t\big(\chi^\pm_{l-1,m} + \chi^\pm_{l+1,m} + \chi^\pm_{l,m-1} + \chi^\pm_{l,m+1}\big) \\ - it_\alpha\big(\chi^\mp_{l,m-1} - \chi^\mp_{l,m+1}\big) \mp t_\alpha\big(\chi^\mp_{l-1,m} - \chi^\mp_{l+1,m}\big) = 0 \end{aligned} \tag{C.7}$$

We also pause to define the vector

$$A^\sigma_l = \begin{pmatrix} \chi^\sigma_{l,1} \\ \chi^\sigma_{l,2} \\ \vdots \\ \chi^\sigma_{l,n_y} \end{pmatrix} \tag{C.8}$$

and the matrices

$$H_0 = \begin{pmatrix} \epsilon & -t & 0 & \cdots & 0 \\ -t & \epsilon & -t & \cdots & 0 \\ 0 & -t & \epsilon & \ddots & 0 \\ \vdots & \vdots & \ddots & \ddots & \ddots \\ 0 & 0 & 0 & \ddots & \epsilon \end{pmatrix} \tag{C.9}$$

$$T_\alpha^{\mp} = \begin{pmatrix} \mp ig\mu_B B & it_\alpha & 0 & \cdots & 0 \\ -it_\alpha & \mp ig\mu_B B & it_\alpha & \cdots & 0 \\ 0 & -it_\alpha & \mp ig\mu_B B & \ddots & 0 \\ \vdots & \vdots & \ddots & \ddots & \ddots \\ 0 & 0 & 0 & \ddots & \mp ig\mu_B B \end{pmatrix} \tag{C.10}$$

Additionally, as our system has translation symmetry along the x-axis, we know that $A_{l+1}^\sigma = \lambda A_l^\sigma$, where $\lambda = e^{ik_x a}$. Finally, we can rewrite Eq. (C.7) as the matrix equation

$$\big(H_0^\pm - E\big)A_l^\pm - t\lambda A_l^\pm - tA_{l-1}^\pm + T_\alpha A_l^\mp \mp t_\alpha A_{l-1}^\mp \pm \lambda t_\alpha A_l^\mp = 0 \tag{C.11}$$

Which we can write as

$$\begin{pmatrix} H_0^+ - E & T_\alpha^- & -t & -t_\alpha \\ T_\alpha^+ & H_0^- - E & t_\alpha & -t \\ 1 & 0 & 0 & 0 \\ 0 & 1 & 0 & 0 \end{pmatrix} \begin{pmatrix} A_l^+ \\ A_l^- \\ A_{l-1}^+ \\ A_{l-1}^- \end{pmatrix} = \lambda \begin{pmatrix} t & -t_\alpha & 0 & 0 \\ t_\alpha & t & 0 & 0 \\ 0 & 0 & 1 & 0 \\ 0 & 0 & 0 & 1 \end{pmatrix} \begin{pmatrix} A_l^+ \\ A_l^- \\ A_{l-1}^+ \\ A_{l-1}^- \end{pmatrix} \tag{C.12}$$

By solving this generalised eigenvalue problem we can extract the values of λ for each energy E. Checking $|\lambda| = 1$ such that it corresponds to a phase, we can extract $k_y a$ as required. From this we can plot the resulting dispersion relation.

C.3 Anomalous current in superconducting constriction

In Chapter 7 we discussed the anomalous Josephson effect in the context of S-N-S junctions where there was a non-superconducting material separating the two superconductors. However, here we will discuss the same effect for junctions formed from superconducting constrictions, or weak links where the normal region is small relative to the coherence length. Critically we will see that the effect is due to a net phase that the condensate picks up by traversing the junction due to the spin-orbit coupling and the Zeeman field.

To begin, we will consider a 1D Josephson junction formed from a superconducting constriction and tuned such that the dominant energy contribution comes from the spin-orbit coupling. We let the constriction lie in the $\hat{l}$ direction and assume

a generic $SU(2)$ gauge field of the form $\boldsymbol{\rho} = k_\alpha \boldsymbol{\sigma} \times \hat{d}$, where $\hat{d}$ is the directional vector of the spin-polarisation. From Section 7.4.3, we note that we can decouple the Hamiltonian into 'external' and 'internal' systems where

$$H_{\text{in/ext}} = \int \mathrm{d}x \begin{pmatrix} \psi^\dagger_{\text{in/ext}} & \psi^\top_{\text{in/ext}} \end{pmatrix} \begin{pmatrix} h_{\text{in/ext}} & \Delta i\sigma_y \\ -\Delta i\sigma_y & -h^*_{\text{in/ext}} \end{pmatrix} \begin{pmatrix} \psi_{\text{in/ext}} \\ \psi^*_{\text{in/ext}} \end{pmatrix} \quad , \tag{C.13}$$

where the contribution from the kinetic term of $h_{\text{in/ext}}$ is given by the expanding out the covariant derivative $\mathbf{D}$ to order $\mathcal{O}(k_\alpha^0)$:

$$\text{K.E.} \propto \left(\mathbf{D}^2 + \boldsymbol{\rho}^2\right) \sim ik_\alpha \Big(\boldsymbol{\sigma} \times \hat{d}\Big) \cdot \nabla - k_\alpha^2 + \mathcal{O}(k_\alpha^0) \quad . \tag{C.14}$$

As a thought experiment, we let the order parameter possess a helical phase along the axis of the nanowire $\hat{l}$:

$$\Delta_0 \to \Delta_0 \exp\Big(2iq\hat{l} \cdot \boldsymbol{r}\Big) \quad . \tag{C.15}$$

and that there are no external magnetic fields. From Section 6.3.1, this implies that the condensate flows in the direction $\hat{l}$ – down the nanowire – with a centre of momentum of $2\hbar q$. Physically we will have current flow through the device, even in the absence of a bulk phase difference – we can recognise this lack of phase bias as indicating an anomalous current. We now perform a $U(1)$ gauge transform to remove the helical phase

$$\psi_{\text{in/ext}} \to \exp\Big(-iq\hat{l} \cdot \mathbf{r}\Big)\psi_{\text{in/ext}} \quad . \tag{C.16}$$

As a result, the covariant derivative also transforms as

$$\mathbf{D} \to \nabla - iq\hat{l} + ik_\alpha \boldsymbol{\sigma} \times \hat{d} \quad . \tag{C.17}$$

As before, in this linearised model the kinetic contribution to the Hamiltonian can be computed by expanding out the covariant derivative to order $\mathcal{O}(k_\alpha^0)$, resulting in:

$$\text{K.E.} \propto \left(\mathbf{D}^2 + \boldsymbol{\rho}^2\right) \to qk_\alpha \Big(\boldsymbol{\sigma} \times \hat{d}\Big) \cdot \hat{l} + ik_\alpha \Big(\boldsymbol{\sigma} \times \hat{d}\Big) \cdot \nabla - k_\alpha^2 + \mathcal{O}(k_\alpha^0) \quad . \tag{C.18}$$

We note the second term in Eq. (C.18) is the usual coupling between the kinetic momentum and the spin-orbit field, whilst the first term, due to the coupling between the $U(1)$ and $SU(2)$ gauge fields, is an effective magnetic field introduced by the change in $U(1)$ gauge. Indeed by rewriting this term we can see the gauge equivalence between these two picture:

$$\underbrace{\arg(\Delta_0) = 2q\hat{l} \cdot \boldsymbol{r} \ \text{ and } \ \mathbf{B} = 0}_{\text{Current flows down nanowire}} \quad \Leftrightarrow \quad \underbrace{\arg(\Delta_0) = 0 \ \text{ and } \ \mathbf{B} = -\frac{\hbar^2 q k_\alpha}{2m}\hat{d} \times \hat{l}}_{\text{Current flows down nanowire}}$$

where we have highlighted that as they simply correspond to a different choice in $U(1)$ gauge, they necessarily correspond to the same physical system – namely, anomalous current flowing down the nanowire.

Returning to our original system, as the leads connected to the device are bulk systems then they supply an order parameter with a constant phase; the order parameter is *not* in a helical phase [96]. However, we now note that if a magnetic field $\mathbf{B} = |\mathbf{B}|\hat{B}$ is applied to the system such that

$$\left(\hat{d} \times \hat{l}\right) \cdot \hat{B} \neq 0 \quad , \tag{C.19}$$

then as per the previous thought experiment current will flow down the nanowire – precisely the anomalous Josephson effect. As a result, Eq. (C.19) is the oft-cited condition that must be met such that one will measure an anomalous Josephson effect [81]. Although this was in the context of superconducting constrictions, the condition Eq. (C.19) must be satisfied to see the anomalous current as can be argued from purely symmetry arguments as in Ref [90].

Returning to the spin-orbit coupled nanowires of Section 7.4.3, we note that we partitioned the Hamiltonian into two uncoupled inner and outer bands. From Eqs. (7.46) and (7.47), the fundamental difference between the single particle Hamiltonians between the two bands was the sign difference in the kinetic terms: $\pm i\alpha\partial_x\sigma_z$. As a result, for the *same* phase difference across the junction, the two resulting pairs of ABS will carry current in *different* directions. Although this seems to indicate anomalous current will always cancel pairwise, as the magnetic field along the direction of the nanowire increases in strength, from Fig. 7.20 the superconducting gap of the inner spinors decreases. Indeed, when in the topological phase the inner bound states vanish entirely, as a result there will be a net anomalous current carried by the exterior states [86]. Hence in the nanowire model, there is a direct link between the appearance of an anomalous phase and whether the wire is in a topological or trivial phase. Finally, we note that in Ref [96] they determined that the maximum anomalous current, which we denote by I_h, is given by the formula

$$\max(I_{\text{an}}) \equiv I_h = \frac{eg\mu_B \mathbf{B} \cdot \hat{d}}{\hbar} \quad . \tag{C.20}$$

When plotting the anomalous current we will regularly normalise with respect to I_h.

Bibliography

[1] P Danielewicz. Quantum theory of nonequilibrium processes, i. *Annals of Physics*, 152(2):239–304, 1984.

[2] B.D. Josephson. Possible new effects in superconductive tunnelling. *Physics Letters*, 1(7):251–253, 1962.

[3] Jason Alicea. New directions in the pursuit of majorana fermions in solid state systems. *Reports on Progress in Physics*, 75(7):076501, jun 2012.

[4] Jürg Fröhlich and Urban M. Studer. Gauge invariance and current algebra in nonrelativistic many-body theory. *Rev. Mod. Phys.*, 65:733–802, Jul 1993.

[5] James D Bjorken and Sidney David Drell. *Relativistic quantum mechanics*. International series in pure and applied physics. McGraw-Hill, New York, NY, 1964.

[6] I. V. Tokatly. Equilibrium spin currents: Non-abelian gauge invariance and color diamagnetism in condensed matter. *Phys. Rev. Lett.*, 101:106601, Sep 2008.

[7] Bertrand Berche and Ernesto Medina Dagger. Classical yang-mills theory in condensed matter physics. *European Journal of Physics*, 34, 09 2012.

[8] H Kleinert. *Gauge Fields in Condensed Matter*. WORLD SCIENTIFIC, 1989.

[9] Morten Willatzen and Lok C. Lew Yan Voon. *The k p Method: Electronic Properties of Semiconductors*. Springer, 2009.

[10] Alexander Altland and Ben D. Simons. *Condensed Matter Field Theory*. Cambridge University Press, 2 edition, 2010.

[11] Mikio Nakahara. *Geometry, topology and physics*. Graduate student series in physics. Hilger, Bristol, 1990.

[12] Michel Le Bellac. *Thermal Field Theory*. Cambridge Monographs on Mathematical Physics. Cambridge University Press, 1996.

[13] Jørgen Rammer. *Quantum Field Theory of Non-equilibrium States*. Cambridge University Press, 2007.

[14] Gianluca Stefanucci and Robert van Leeuwen. *Nonequilibrium Many-Body Theory of Quantum Systems: A Modern Introduction*. Cambridge University Press, Cambridge, 2013.

[15] M. C. M. Wright. Green function or green's function? *Nature Physics*, 2(10):646–646, Oct 2006.

[16] Hubert Mabilat. Derivation of the real-time formalism from first principles in thermal field theory. *Zeitschrift für Physik C Particles and Fields*, 75(1):155–166, Mar 1997.

[17] J Maciejko. Lecture notes in an introduction to nonequilibrium many-body theory, October 2007.

[18] D. Semkat, D. Kremp, and M. Bonitz. Kadanoff-baym equations with initial correlations. *Phys. Rev. E*, 59:1557–1562, Feb 1999.

[19] Nikolai Kopnin. *Theory of Nonequilibrium Superconductivity*. International Series of Monographs on Physics. Oxford University Press, Oxford, 2001.

[20] W. L. McMillan. Theory of superconductor-normal-metal interfaces. *Phys. Rev.*, 175:559–568, Nov 1968.

[21] François Konschelle. Transport equations for superconductors in the presence of spin interaction. *The European Physical Journal B*, 87(5), May 2014.

[22] J. A. Sauls. Andreev bound states and their signatures. *Philosophical Transactions of the Royal Society A: Mathematical, Physical and Engineering Sciences*, 376(2125):20180140, 2018.

[23] C. W. J. Beenakker. Universal limit of critical-current fluctuations in mesoscopic josephson junctions. *Phys. Rev. Lett.*, 67:3836–3839, Dec 1991.

[24] Zhao Yang Zeng, Baowen Li, and F. Claro. Electronic transport in hybrid mesoscopic structures: A nonequilibrium green function approach. *Phys. Rev. B*, 68:115319, Sep 2003.

[25] Antti-Pekka Jauho, Ned S. Wingreen, and Yigal Meir. Time-dependent transport in interacting and noninteracting resonant-tunneling systems. *Phys. Rev. B*, 50:5528–5544, Aug 1994.

[26] Thomas Rylander, Pär Ingelström, and Anders Bondeson. *Finite Differences*, pages 19–42. Springer New York, New York, NY, 2013.

[27] Supriyo Datta. *Quantum Transport: Atom to Transistor*. Cambridge University Press, 2005.

[28] G. P. Lepage. Lattice QCD for novices. In *13th Annual HUGS AT CEBAF (HUGS 98)*, pages 49–90, 5 1998.

[29] Douglas R. Hofstadter. Energy levels and wave functions of bloch electrons in rational and irrational magnetic fields. *Phys. Rev. B*, 14:2239–2249, Sep 1976.

[30] Samuel D. Escribano, Alfredo Levy Yeyati, and Elsa Prada. Improved effective equation for the rashba spin-orbit coupling in semiconductor nanowires. *Phys. Rev. Research*, 2:033264, Aug 2020.

[31] A. Manchon, H. C. Koo, J. Nitta, S. M. Frolov, and R. A. Duine. New perspectives for rashba spin–orbit coupling. *Nature Materials*, 14(9):871–882, Sep 2015.

[32] Jie Liu, Andrew C. Potter, K. T. Law, and Patrick A. Lee. Zero-bias peaks in the tunneling conductance of spin-orbit-coupled superconducting wires with and without majorana end-states. *Phys. Rev. Lett.*, 109:267002, Dec 2012.

[33] A Wills. Magnetic structures and their determination using group theory. *Le Journal de Physique IV*, 11(PR9):Pr9–133, 2001.

[34] C. R. Dean, L. Wang, P. Maher, C. Forsythe, F. Ghahari, Y. Gao, J. Katoch, M. Ishigami, P. Moon, M. Koshino, T. Taniguchi, K. Watanabe, K. L. Shepard, J. Hone, and P. Kim. Hofstadter's butterfly and the fractal quantum hall effect in moiré superlattices. *Nature*, 497(7451):598–602, May 2013.

[35] Yi Yang, Bo Zhen, John D. Joannopoulos, and Marin Soljačić. Non-abelian generalizations of the hofstadter model: spin–orbit-coupled butterfly pairs. *Light: Science & Applications*, 9(1):177, Oct 2020.

[36] L. A. Ponomarenko, R. V. Gorbachev, G. L. Yu, D. C. Elias, R. Jalil, A. A. Patel, A. Mishchenko, A. S. Mayorov, C. R. Woods, J. R. Wallbank, M. Mucha-Kruczynski, B. A. Piot, M. Potemski, I. V. Grigorieva, K. S. Novoselov, F. Guinea, V. I. Fal'ko, and A. K. Geim. Cloning of dirac fermions in graphene superlattices. *Nature*, 497(7451):594–597, May 2013.

[37] Gérard Meurant. A review on the inverse of symmetric tridiagonal and block tridiagonal matrices. *SIAM Journal on Matrix Analysis and Applications*, 13(3):707–728, 1992.

[38] Roger Lake, Gerhard Klimeck, R. Chris Bowen, and Dejan Jovanovic. Single and multiband modeling of quantum electron transport through layered semiconductor devices. *Journal of Applied Physics*, 81(12):7845–7869, 1997.

[39] Christoph W Groth, Michael Wimmer, Anton R Akhmerov, and Xavier Waintal. Kwant: a software package for quantum transport. *New Journal of Physics*, 16(6):063065, jun 2014.

[40] C Caroli, R Combescot, P Nozieres, and D Saint-James. Direct calculation of the tunneling current. *Journal of Physics C: Solid State Physics*, 4(8):916–929, jun 1971.

[41] P. Concus, G. H. Golub, and G. Meurant. Block preconditioning for the conjugate gradient method. *SIAM Journal on Scientific and Statistical Computing*, 6(1):220–252, 1985.

[42] E Asplund. Inverse of matrices a_{ij} which satisy $a_{ij} = 0$ for $j > i + p$. *Mathematica Scandinavica*, 7(1):57–60, 1959.

[43] Roberto Bevilacqua, Bruno Codenotti, and Francesco Romani. Parallel solution of block tridiagonal linear systems. *Linear Algebra and its Applications*, 104:39–57, 1988.

[44] P. Concus and G. Meurant. On computing inv block preconditionings for the conjugate gradient method. *BIT Numerical Mathematics*, 26(4):493–504, Dec 1986.

[45] Stephen Demko, William F. Moss, and Philip W. Smith. Decay rates for inverses of band matrices. *Mathematics of Computation*, 43(168):491–499, 1984.

[46] M Y Azbel. Residual resistance, quantum scattering and free energy. *Journal of Physics C: Solid State Physics*, 13(29):L797–L801, oct 1980.

[47] E Abrahams and M J Stephen. Resistance fluctuations in disordered one-dimensional conductors. *Journal of Physics C: Solid State Physics*, 13(15):L377–L381, may 1980.

[48] Daniel S. Fisher and Patrick A. Lee. Relation between conductivity and transmission matrix. *Phys. Rev. B*, 23:6851–6854, Jun 1981.

[49] Luca Molinari. Transfer matrices, non-hermitian hamiltonians and resolvents: some spectral identities. *Journal of Physics A: Mathematical and General*, 31(42):8553–8562, oct 1998.

[50] J. H. Wilkinson. Modern error analysis. *SIAM Review*, 13(4):548–568, 1971.

[51] M P Lopez Sancho, J M Lopez Sancho, and J Rubio. Quick iterative scheme for the calculation of transfer matrices: application to mo (100). *Journal of Physics F: Metal Physics*, 14(5):1205–1215, may 1984.

[52] M P Lopez Sancho, J M Lopez Sancho, J M L Sancho, and J Rubio. Highly convergent schemes for the calculation of bulk and surface green functions. *Journal of Physics F: Metal Physics*, 15(4):851–858, apr 1985.

[53] A. A. Golubov, M. Yu. Kupriyanov, and E. Il'ichev. The current-phase relation in josephson junctions. *Rev. Mod. Phys.*, 76:411–469, Apr 2004.

[54] Steven Weinberg. Superconductivity for Particular Theorists. *Progress of Theoretical Physics Supplement*, 86:43–53, 01 1986.

[55] John David Jackson. *Classical electrodynamics*. Wiley, New York, NY, 3rd ed. edition, 1999.

[56] A A Abrikosov. Fundamentals of the theory of metals, 1988. 1(1), 1 1988.

[57] Aleksandr F. Andreev. Electron spectrum of the intermediate state of superconductors. *Soviet Journal of Experimental and Theoretical Physics*, 22(2):455–458, February 1966.

[58] G. E. Blonder, M. Tinkham, and T. M. Klapwijk. Transition from metallic to tunneling regimes in superconducting microconstrictions: Excess current, charge imbalance, and supercurrent conversion. *Phys. Rev. B*, 25:4515–4532, Apr 1982.

[59] Philip F. Bagwell. Suppression of the josephson current through a narrow, mesoscopic, semiconductor channel by a single impurity. *Phys. Rev. B*, 46:12573–12586, Nov 1992.

[60] K. K. Likharev. Superconducting weak links. *Rev. Mod. Phys.*, 51:101–159, Jan 1979.

[61] B. van Heck, J. I. Väyrynen, and L. I. Glazman. Zeeman and spin-orbit effects in the andreev spectra of nanowire junctions. *Phys. Rev. B*, 96:075404, Aug 2017.

[62] John Bardeen and Jared L. Johnson. Josephson current flow in pure superconducting-normal-superconducting junctions. *Phys. Rev. B*, 5:72–78, Jan 1972.

[63] D. D. Johnson. Modified broyden's method for accelerating convergence in self-consistent calculations. *Phys. Rev. B*, 38:12807–12813, Dec 1988.

[64] A. Levy Yeyati, A. Martín-Rodero, and F. J. García-Vidal. Self-consistent theory of superconducting mesoscopic weak links. *Phys. Rev. B*, 51:3743–3753, Feb 1995.

[65] P. W. Anderson. Considerations on the flow of superfluid helium. *Rev. Mod. Phys.*, 38:298–310, Apr 1966.

[66] J. S. Langer and Vinay Ambegaokar. Intrinsic resistive transition in narrow superconducting channels. *Phys. Rev.*, 164:498–510, Dec 1967.

[67] Allen Hatcher. *Algebraic topology*. Cambridge Univ. Press, Cambridge, 2000.

[68] A. Martín-Rodero, F. J. García-Vidal, and A. Levy Yeyati. Microscopic theory of josephson mesoscopic constrictions. *Phys. Rev. Lett.*, 72:554–557, Jan 1994.

[69] R. Mélin, F. S. Bergeret, and A. Levy Yeyati. Self-consistent microscopic calculations for nonlocal transport through nanoscale superconductors. *Phys. Rev. B*, 79:104518, Mar 2009.

[70] Jorge L. D'Amato and Horacio M. Pastawski. Conductance of a disordered linear chain including inelastic scattering events. *Phys. Rev. B*, 41:7411–7420, Apr 1990.

[71] P. L. Pernas, A. Martin-Rodero, and F. Flores. Electrochemical-potential variations across a constriction. *Phys. Rev. B*, 41:8553–8556, Apr 1990.

[72] Tomohiro Yokoyama, Mikio Eto, and Yuli V. Nazarov. Anomalous josephson effect induced by spin-orbit interaction and zeeman effect in semiconductor nanowires. *Phys. Rev. B*, 89:195407, May 2014.

[73] A I Buzdin, L N Bulaevskii, and S V Panyukov. Critical-current oscillations as a function of the exchange field and thickness of the ferromagnetic metal (f) in an s-f-s josephson junction. *JETP Lett. (Engl. Transl.); (United States)*, 35:3, 2 1982.

[74] V. V. Ryazanov, V. A. Oboznov, A. Yu. Rusanov, A. V. Veretennikov, A. A. Golubov, and J. Aarts. Coupling of two superconductors through a ferromagnet: Evidence for a π junction. *Phys. Rev. Lett.*, 86:2427–2430, Mar 2001.

[75] S. M. Frolov, D. J. Van Harlingen, V. A. Oboznov, V. V. Bolginov, and V. V. Ryazanov. Measurement of the current-phase relation of superconductor/ferromagnet/superconductor π josephson junctions. *Phys. Rev. B*, 70:144505, Oct 2004.

[76] A. Buzdin. Direct coupling between magnetism and superconducting current in the josephson φ_0 junction. *Phys. Rev. Lett.*, 101:107005, Sep 2008.

[77] D. B. Szombati, S. Nadj-Perge, D. Car, S. R. Plissard, E. P. A. M. Bakkers, and L. P. Kouwenhoven. Josephson ϕ_0-junction in nanowire quantum dots. *Nature Physics*, 12(6):568–572, Jun 2016.

[78] Elia Strambini, Andrea Iorio, Ofelia Durante, Roberta Citro, Cristina Sanz-Fernández, Claudio Guarcello, Ilya V. Tokatly, Alessandro Braggio, Mirko Rocci, Nadia Ligato, Valentina Zannier, Lucia Sorba, F. Sebastián Bergeret, and Francesco Giazotto. A josephson phase battery. *Nature Nanotechnology*, 15(8):656–660, Aug 2020.

[79] I. V. Krive, L. Y. Gorelik, R. I. Shekhter, and M. Jonson. Chiral symmetry breaking and the josephson current in a ballistic superconductor–quantum wire–superconductor junction. *Low Temperature Physics*, 30(5):398–404, 2004.

[80] Silvano De Franceschi, Leo Kouwenhoven, Christian Schönenberger, and Wolfgang Wernsdorfer. Hybrid superconductor–quantum dot devices. *Nature Nanotechnology*, 5(10):703–711, Oct 2010.

[81] F. S. Bergeret and I. V. Tokatly. Theory of diffusive φ_0 josephson junctions in the presence of spin-orbit coupling. *EPL (Europhysics Letters)*, 110(5):57005, jun 2015.

[82] A. V. Samokhvalov, A. A. Kopasov, A. G. Kutlin, S. V. Mironov, A. I. Buzdin, and A. S. Mel'nikov. Spontaneous currents and topologically protected states in superconducting hybrid structures with the spin–orbit coupling (brief review). *JETP Letters*, 113(1):34–46, Jan 2021.

[83] T. Ando. Quantum point contacts in magnetic fields. *Phys. Rev. B*, 44:8017–8027, Oct 1991.

[84] V. P. Mineev and K. V. Samokhin. Helical phases in superconductors. *Journal of Experimental and Theoretical Physics*, 78(3):401–409, 1994.

[85] Yuval Oreg, Gil Refael, and Felix von Oppen. Helical liquids and majorana bound states in quantum wires. *Phys. Rev. Lett.*, 105:177002, Oct 2010.

[86] Konstantin N. Nesterov, Manuel Houzet, and Julia S. Meyer. Anomalous josephson effect in semiconducting nanowires as a signature of the topologically nontrivial phase. *Phys. Rev. B*, 93:174502, May 2016.

[87] Chaitanya Murthy, Vladislav D. Kurilovich, Pavel D. Kurilovich, Bernard van Heck, Leonid I. Glazman, and Chetan Nayak. Energy spectrum and current-phase relation of a nanowire josephson junction close to the topological transition. *Physical Review B*, 101(22), jun 2020.

[88] S. Nadj-Perge, V. S. Pribiag, J. W. G. van den Berg, K. Zuo, S. R. Plissard, E. P. A. M. Bakkers, S. M. Frolov, and L. P. Kouwenhoven. Spectroscopy of spin-orbit quantum bits in indium antimonide nanowires. *Phys. Rev. Lett.*, 108:166801, Apr 2012.

[89] Henry F. Legg, Daniel Loss, and Jelena Klinovaja. Superconducting diode effect due to magnetochiral anisotropy in topological insulator and rashba nanowires, 2022.

[90] Asbjørn Rasmussen, Jeroen Danon, Henri Suominen, Fabrizio Nichele, Morten Kjaergaard, and Karsten Flensberg. Effects of spin-orbit coupling and spatial symmetries on the josephson current in sns junctions. *Phys. Rev. B*, 93:155406, Apr 2016.

[91] R. Haag, N. M. Hugenholtz, and M. Winnink. On the equilibrium states in quantum statistical mechanics. *Communications in Mathematical Physics*, 5(3):215 – 236, 1967.

[92] Alex Kamenev. Many-body theory of non-equilibrium systems, 2005.

[93] A A Abrikosov, I Dzyaloshinskii, L P Gorkov, and Richard A Silverman. *Methods of quantum field theory in statistical physics*. Dover, New York, NY, 1975.

[94] J. Mason and D. Handscomb. *Chebyshev polynomials*. Chapman & Hall/CRC, Boca Raton, Fla., 2003.

[95] Francisco Mireles and George Kirczenow. Ballistic spin-polarized transport and rashba spin precession in semiconductor nanowires. *Phys. Rev. B*, 64:024426, Jun 2001.

[96] Fabrizio Dolcini, Manuel Houzet, and Julia S. Meyer. Topological josephson ϕ_0 junctions. *Phys. Rev. B*, 92:035428, Jul 2015.